# Describing the macroscopic behavior of surfaces based on atomistic models

von der Fakultät Maschinenbau
der Technischen Universität Dortmund
zur Erlangung des akademischen Grades

**Doktor-Ingenieur (Dr.-Ing.)**

genehmigte Dissertation

von

**Christian Sievers**

aus Bochum

| | |
|---|---|
| Referent: | Prof. Dr.-Ing. J. Mosler |
| Korreferenten: | Prof. Dr. A. Hartmaier |
| | Prof. Dr.-Ing. W. Tillmann |
| Tag der Einreichung: | 30.06.2020 |
| Tag der mündlichen Prüfung: | 07.10.2020 |

**Bibliografische Information Der Deutschen Bibliothek**
Die Deutsche Bibliothek verzeichnet diese Publikation in der Deutschen Nationalbibliografie; detaillierte bibliografische Daten sind im Internet über **http://dnb.ddb.de** abrufbar.

**Bibliographic information published by Die Deutsche Bibliothek**
Die Deutsche Bibliothek lists this publication in the Deutsche Nationalbibliografie; detailed bibliographic data is available in the Internet at **http://dnb.ddb.de**.

Schriftenreihe des Instituts für Mechanik

Herausgeber: Institut für Mechanik
Fakultät Maschinenbau
Technische Universität Dortmund
Leonhard-Euler-Str. 5
D-44227 Dortmund

Druck: Koffler DruckManagement GmbH



Als Manuskript gedruckt. Printed in Germany.

ISSN 2191-0022
ISBN 978-3-947323-24-1

*To my grandma*

# Acknowledgements

This thesis has been accomplished during my employment as a scientific assistant at the Institute of Mechanics at TU Dortmund University and afterwards from 2014 until 2020. I would like to use this occasion to mention and thank some of the people who have accompanied and contributed to my work during this time.

First of all, I would like to thank my mentor and doctoral thesis supervisor Professor Jörn Mosler. He gave me the opportunity to write my doctoral thesis after finishing my master thesis in 2014. I enjoyed the benefit of his inspired ideas and extensive knowledge as well as revealing discussions. However, he especially impressed me with his scientific way of thinking and working.

Furthermore, my thanks go to Professor Alexander Hartmaier for his interest in my research as well as for acting as co-referee of my doctoral thesis. Similarly, I want to thank Professor Wolfgang Tillmann for acting as third referee of my doctoral thesis. Moreover, I should thank Professor Andreas Menzel who agreed to serve as the chairman of the examination committee.

Special thanks also go to Dr. Patrick Kurzeja. I was really happy when he joined out team since I know him from exercises at Ruhr-Universität Bochum. He helped me to understand the field of molecular simulations and supported my publications as a co-author. I also thank Dr. Lothar Brendel and Professor Dietrich Wolf for stimulating discussions.

Further special thanks go to the whole team of the Institute of Mechanics. Due to a pleasant and friendly working atmosphere created by Professor Jörn Mosler and Professor Andreas Menzel as well as by my awesome colleagues, I enjoyed the time at the institute. I will definitely miss it. To some of my fantastic colleagues I should express special thanks. First of all, our dream team Kerstin Walter and Christina McDonagh for their outstanding support at administrative issues and organizing various events, e.g. Christmas parties and institute trips, as well as Matthias Weiss for his professional software and hardware support. Thanks also go to assistant professor Sandra Klinge who has accompanied me since my Semesterarbeit and my time as student research assistant at Ruhr-Universität Bochum.

Subsequently, I would like to express my sincere gratitude to my colleagues for their cordiality and friendship. Apart from the scientific exchange and the mutual support during the work, we had many "funny" moments besides (and during) work, deviating me from mechanical problems and being an additional motivation for my thesis. For this, special thanks go to Serhat Aygün, Dr. Thorsten Bartel, Dr. Alexander Bartels (best office colleague ever), Dr. Rolf Berthelsen, Dr. Karsten Buckmann, Dr. Dinesh

Dusthakar, Volker Fohrmeister, Tim Furlan, Dr. Raphael Holtermann, Dr. Tim Heitbreder, Dr. Tobias Kaiser, Henning Lammen, Kai Langenfeld, Isabelle Noll, Dr. Richard Ostwald, Robin Schulte and Hendrik Wilbuer. I will definitely keep you in mind and hopefully we stay in touch.

I would also like to thank to my other and former colleagues Dr. Till Clausmeyer, Professor Ralf Denzer, Ph.D. Guillermo Díaz, Ph.D. Krishnendu Haldar, Professor Ali Javili, Professor Björn Kiefer, Ph.D. César Polindara, Lars Rose, Leon Sprave and Tillmann Wiegold for their helpful and engaged teamwork.

Most of all, I would like to thank my family and friends for their support during my time working on this thesis. Finally, I gratefully thank my parents and my grandmother for their support during my whole education process.

Dortmund, November 2020 Christian Sievers

# Zusammenfassung

Diese Arbeit beschreibt die Modellierung von Grenz- und Oberflächen. Ein neuartiger Multiskalen-Modellierungsrahmen, basierend auf molekulardynamischen Simulationen, dient zur Bestimmung von Materialeigenschaften freier Oberflächen auf der Makroskala. Ein wesentlicher Aspekt dafür ist die Entwicklung eines thermodynamisch konsistenten Homogenisierungsansatzes auf Basis des Prinzips der Energieminimierung. Dabei werden die Parameter, welche die Energie auf der Makroskala beschreiben, aus dem Vergleich mit der Energie auf der atomistischen Skala ermittelt. Dieser Homogenisierungsansatz wird zudem auch auf thermoelastische Materialien erweitert. Danach liegt der Fokus auf einer kontinuumsmechanischen Modellierung von Oberflächen und einer starken Kopplung zwischen der Physik des Bulk- und Oberflächenmaterials. Dazu wird die Oberflächenverzerrung direkt aus der grundlegenden, dreidimensionalen Verzerrung des Bulkmaterials bestimmt. Dieses Vorgehen wird anhand zweier Ansätze implementiert. Schließlich wird für beide Ansätze eine numerische Implementierung in die Finite-Elemente Methode hergeleitet.

# Abstract

This work describes the modeling of interface and surface materials. A novel multiscale framework determines continuum material properties of free surfaces on the macroscale based on molecular dynamics simulations. A key aspect is the derivation of a thermodynamically consistent homogenization approach by the principle of energy minimization. The parameters describing the energy on the macroscale are determined from the comparison with the corresponding energy on the atomistic scale. In addition, this Ritz-homogenization approach is enlarged to thermoelastic materials. Afterwards, the work focuses on the continuum mechanically surface modeling and a strong coupling between bulk and surface physics. To be more precise, the surface deformation is directly determined from the underlying three-dimensional bulk deformation. Therefore, two approaches of the surface deformation are implemented. Finally, a numerical implementation of both approaches in a finite-element framework is derived.

# Publications

The following articles were carried out during the preparation of this thesis. The article of Ch. 3 is accepted and the article of Ch. 5 is submitted.

**Chapter 2:** C. Sievers, J. Mosler, L. Brendel, P. Kurzeja: *Computational homogenization of material surfaces: From atomistic simulations to continuum models*, Computational Materials Science, 175:109431, 2020. (cf. [58])

**Chapter 4:** C. Sievers, J. Mosler, P. Kurzeja: *Projection vs. relaxation for surface modeling: theoretical and numerical aspects*, submitted, 2020.

The above articles have been published together with one or more authors. The author of this thesis contributed essential parts of the underlying theory to the articles and carried out all the numerical implementations and simulations. The contents of the articles were complemented by unpublished results as well as by further details concerning the theory and numerical implementation.

# Contents

# 1 Motivation and state of the art

This thesis focuses on material surfaces. On the one hand, the material properties of the surface are determined from molecular dynamic simulations by a novel homogenization approach and, on the other hand, different approaches for the modeling of mechanical surfaces are deduced and compared.

## 1.1 Computational homogenization review for a atomistic-to-continuum transition of material properties

The effective macroscopic properties of a broad variety of materials are defined by their material surfaces. The surface behavior ranges from elasticity [15, 26, 53] to cohesive zones [19, 42] and typically adds a new length scale to the classic bulk behavior. Surfaces also drive contact crystallization and thus the elasticity of cohesive powders under cyclic loading [68]. Remarkable surface phenomena have been particularly observed on small length scales, for instance, in nano-wires [33] and nano-tubes [15].

Only a few numerical techniques have been developed in recent works to identify mechanical surface parameters directly from the atomistic scale. The universal binding energy relation model (UBER) developed by Rose et al. [53] studies the perturbation of a relaxed bulk material by a vacuum gap. Shenoy [56] developed analytical expressions for the surface parameters based on the interatomic potential and points out the relevance of a post-relaxation after applying strain. Existing research shows a rich spectrum of materials in the form of atomistic potentials. However, little attention has been paid to the continuum model. Surface elastic parameters are often found in the pure form of surface energy and its strain derivative. Second-order derivatives, i.e. stiffness contributions, are more seldom, see the works of Shenoy [56] and Dingreville & Qu [13]. Existing data thus allows for a simple Hooke-type description (linearized elasticity theory), but neglects the broad spectrum of continuum models such as (finite strain) hyperelastic materials, let alone plasticity or damage. The latter require a framework that guarantees thermodynamic consistency and compatibility with modern material descriptions, e.g., energy potentials formulated in invariants. It is aimed at contributing to the implementation of more general continuum surface models by providing a framework that links the atomistic observations to a thermodynamically consistent continuum description.

The first objective of this work is the derivation of a novel homogenization framework informed by molecular dynamics simulations. For that purpose, the principle of energy equivalence between the atomistic and continuum model is applied. With this novel framework at hand, the free surface elastic parameters will be determined. Moreover, the suitability of the homogenization approach to thermoelastic materials will be investigated. These issues are treated in Ch. 3 and 4.

## 1.2 Continuum surface modeling

Mechanical modeling of surfaces adds to the complexity of bulk modeling in various geometrical, physical and computational aspects. Geometrically, even a constant surface energy can alter the curvature as it is well known from capillary effects [16, 30, 31]. Physically, surfaces can induce special phenomena such as scale effects [25] or provide additional information on capillary hysteresis [28, 29]. Computationally, a broad spectrum of approaches has been proposed for the variety of surface and interface mechanics, e.g., the implementation of rank-one relaxation for membrane stresses, fiber-like unloading of cohesive zones or homogenization of diffuse interfaces by means of phase field descriptions [2, 3, 6, 18, 48–50].

Little attention has been explicitly paid to the near-surface coupling of bulk and surface mechanics, although this coupling influences all aforementioned aspects. For instance, bulk and surface elasticity in pure metals do not only derive from the same molecular potential. As one additional result, interatomic relaxation near the surface couples surface and bulk deformation within a finite range, see [56] and [13]. Also oxygen incorporation [1] and anchoring [27] yield reconstruction and relaxation within a finite boundary of the bulk. Such detailed look on phase boundaries generally poses the question whether the assumption of a sharp surface or interface is a reliable approximation or whether the surface deformation has to be treated as part of the bulk deformation. It is well known that sharp interface limits must be treated with special care, e.g., considering kinematic compatibility or objectivity principles [18]. The same applies to the computational implementation of surfaces, which can be costly and add yet another motivation to harness a coupling with the bulk mechanics.

The second objective of this issue is the derivation of a surface model based on the bulk material models. For that purpose, two approaches – one based on a relaxation technique and another one based on projection ansatz – are discussed in Ch. 5.

# 2 Introduction to continuum mechanics

This chapter comprises an introduction to continuum mechanics as well as one into the finite element framework. It starts with a brief introduction to the underlying tensor operations in Sec. 2.1. Subsequently, the kinematics of the geometrically non-linear theory at finite strains is given in Sec. 2.2. Sec. 2.3 summarizes the basic balance equations. Hyperelastic and thermoelastic materials with its underlying constitutive equations are derived in Sec. 2.3. Finally, the implementation of the constitutive equations is shown in a nutshell in Sec. 2.5.

Certainly, the presented equations and relations in this section are well-known and they are not new. Detailed information on the presented equations and relations can be found for example in [21, 23, 54, 69].

## 2.1 Notation

The following notation has been used throughout the entire thesis. The Euclidean space $\mathbb{R}^3$ is spanned by the Cartesian vectors $\mathbf{e}_i$ for $i = \{1, 2, 3\}$ with its center $\mathcal{O}$. Scalar variables are denoted by italic letters, e.g., $a, b$. First order tensors, i.e. vectors, are represented by boldfaced lowercase letters, e.g., $\mathbf{a}, \mathbf{b}$, second order tensor are denoted by boldfaced uppercase letters, e.g., $\mathbf{A}, \mathbf{B}$ and fourth order tensors are symbolized by blackboard letters, e.g., $\mathbb{A}, \mathbb{B}$. Where necessary, tensors are denoted by index notation and Einstein summation rule is used. All vectors and higher order tensors are spanned by Cartesian basis vectors and, accordingly, whenever possible the basis vectors are omitted.

$$\mathbf{a} = \{\mathbf{a}\}_i \mathbf{e}_i = a_i \mathbf{e}_i \tag{2.1}$$

$$\mathbf{A} = \{\mathbf{A}\}_{ij} \mathbf{e}_i \otimes \mathbf{e}_j = A_{ij} \mathbf{e}_i \otimes \mathbf{e}_j \tag{2.2}$$

$$\mathbb{A} = \{\mathbb{A}\}_{ijkl} \mathbf{e}_i \otimes \mathbf{e}_j \otimes \mathbf{e}_k \otimes \mathbf{e}_l = \mathbb{A}_{ijkl} \mathbf{e}_i \otimes \mathbf{e}_j \otimes \mathbf{e}_k \otimes \mathbf{e}_l \tag{2.3}$$

In the following, basic algebraic operations between tensors are presented.

- Scalar products

$$\mathbf{a} \cdot \mathbf{b} = a_i \, b_i \tag{2.4}$$
$$\mathbf{A} : \mathbf{B} = A_{ij} \, B_{ij} \tag{2.5}$$

- Inner tensor products

$$\{\mathbf{a} \overset{(2)}{\cdot} \mathbb{B}\}_{ijk} = a_l \, \mathbb{B}_{iljk} \tag{2.6}$$
$$\{\mathbf{A} \cdot \mathbf{b}\}_{i} = A_{ij} \, b_j \tag{2.7}$$
$$\{\mathbf{A} \cdot \mathbf{B}\}_{ij} = A_{ik} \, B_{kj} \tag{2.8}$$
$$\{\mathbb{A} \cdot \mathbf{b}\}_{ijk} = \mathbb{A}_{ijkl} \, b_l \tag{2.9}$$
$$\{\mathbb{A} : \mathbf{B}\}_{ij} = \mathbb{A}_{ijkl} \, B_{kl} \tag{2.10}$$
$$\{\mathbb{A} : \mathbb{B}\}_{ijkl} = \mathbb{A}_{ijmn} \, \mathbb{B}_{mnkl} \tag{2.11}$$

- Outer tensor products

$$\{\mathbf{a} \otimes \mathbf{b}\}_{ij} = a_i \, b_j \tag{2.12}$$
$$\{\mathbf{a} \,\overline{\otimes}\, \mathbf{B}\}_{ijk} = a_j \, B_{ik} \tag{2.13}$$
$$\{\mathbf{A} \otimes \mathbf{B}\}_{ijkl} = A_{ij} \, B_{kl} \tag{2.14}$$
$$\{\mathbf{A} \,\underline{\otimes}\, \mathbf{B}\}_{ijkl} = A_{il} \, B_{jk} \tag{2.15}$$
$$\{\mathbf{A} \,\overline{\otimes}\, \mathbf{B}\}_{ijkl} = A_{ik} \, B_{jl} \tag{2.16}$$

The definitions of the operators ($\underline{\otimes}$) and ($\overline{\otimes}$) are not standard in continuum mechanics.

- Identity tensors

$$\{\mathbf{I}\}_{ij} = \delta_{ij} \tag{2.17}$$
$$\{\mathbb{I}\}_{ijkl} = \{\mathbf{I} \,\overline{\otimes}\, \mathbf{I}\}_{ijkl} = \delta_{ik} \, \delta_{jl} \tag{2.18}$$

$\delta_{ij}$ denotes the Kronecker Delta and has the following identity properties:

$$\delta_{ij} = \begin{cases} 0 & \text{if} \quad i \neq j \\ 1 & \text{if} \quad i = j \end{cases} \tag{2.19}$$

- Trace operations

$$\operatorname{tr}\mathbf{A} = \mathbf{A} : \mathbf{I} \tag{2.20}$$
$$\mathbb{I} : \mathbf{A} = \mathbf{A} \tag{2.21}$$

Therein, $\operatorname{tr}\mathbf{A}$ denotes the trace of the second order tensor $\mathbf{A}$.

## 2.2 Kinematics

This section briefly summarizes the motion of continuous body $\mathcal{B}$ (Boltzmann continuum) in the Euclidean space $\mathbb{R}^3$. At time $t_0$ the undeformed body is defined by a set of material points belonging to the reference or undeformed configuration $\mathcal{B}_0$. Quantities with a subscript 0 belong to the reference configuration, and a subscript $t$ indicates quantities being a part of the current configuration. The position of a material point $P$ within the body $\mathcal{B}_0$ is described by position vector $\mathbf{X}$ in material coordinates. After deformation due to, e.g., body forces, tractions or prescribed displacements, each material point undergoes a displacement $\mathbf{u} = \mathbf{u}(t)$. The moved material point $P$ is identified by position vector $\mathbf{x}(\mathbf{X}, t)$ in spatial coordinates. The deformed body belongs to the current or deformed configuration and is denoted by $\mathcal{B}_t$ at the time $t > t_0$ with $t \in \mathbb{R}^+$. The motion of material points is characterized by the deformation mapping

$$\boldsymbol{\varphi} : \mathcal{B}_0 \times \mathbb{R}^+ \to \mathcal{B}_t \quad \text{and} \tag{2.22}$$
$$(\mathbf{X}, t) \to \mathbf{x} = \boldsymbol{\varphi}(\mathbf{X}, t)\,. \tag{2.23}$$

Thus, each material point $P$ with coordinates $\mathbf{X}$ within the reference configuration is mapped to the current configuration by $\mathbf{x} = \boldsymbol{\varphi}(\mathbf{X}, t)$ (cf. [8]). Fig. 2.1 shows the deformation mapping between the reference and current configuration. The displacement vector denotes the difference between the reference and current configuration and reads

$$\mathbf{u} = \mathbf{u}(t) = \mathbf{x} - \mathbf{X}. \tag{2.24}$$

The deformation between both configurations is aproximated (first-order) by deformation gradient $\mathbf{F}$ as

$$\mathbf{F} = \frac{\partial \mathbf{x}}{\partial \mathbf{X}} = \frac{\partial \boldsymbol{\varphi}(\mathbf{X}, t)}{\partial \mathbf{X}} = \operatorname{Grad} \boldsymbol{\varphi}(\mathbf{X}, t) \quad \text{with} \quad \operatorname{Grad}(\bullet) = \frac{\partial(\bullet)}{\partial \mathbf{X}}. \tag{2.25}$$

It maps vectors from the reference configuration onto vectors in the current configuration. It bears emphasis that the first index of the deformation gradient belongs to the current configuration and the second index to the reference configuration.

The definition of the deformation gradient allows mapping of line, surface and volume elements (see Fig. 2.1) from the reference to the current configuration and vice versa.

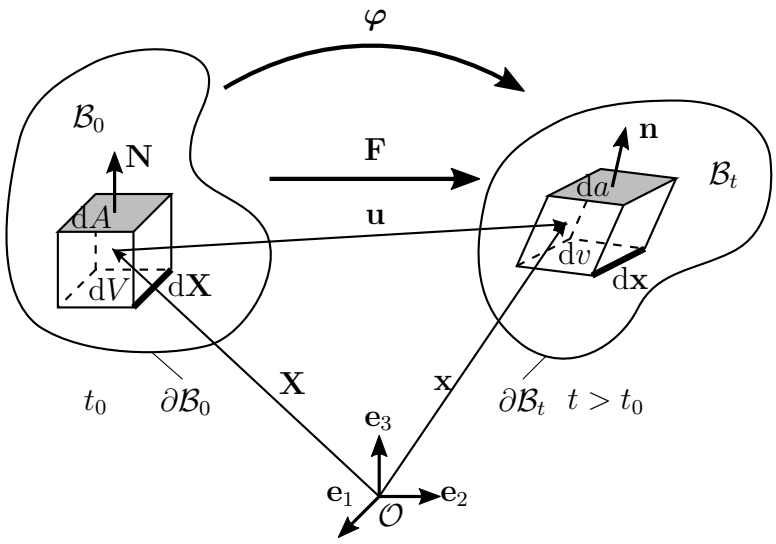


**Figure 2.1:** Kinematics of continuous body $\mathcal{B}$. Reference (time $t_0$) and current configuration (time $t > t_0$).

Supposing $\mathrm{d}\mathbf{X}$ is a material line element in the reference configuration, it is mapped to the current configuration by the relation

$$\mathrm{d}\mathbf{x} = \mathbf{F} \cdot \mathrm{d}\mathbf{X} \tag{2.26}$$

and its inverse formulation reads

$$\mathrm{d}\mathbf{X} = \mathbf{F}^{-1} \cdot \mathrm{d}\mathbf{x}. \tag{2.27}$$

Due to this invertibility, $\mathbf{F}$ has to be a non-singular tensor. Thus, the determinate of the deformation gradient, also known as the Jacobian of $\mathbf{F}$, combining with initial conditions is restricted to

$$J = \det \mathbf{F} > 0. \tag{2.28}$$

This relation is also known as local invertibility condition. By the use of Eq. (2.26), an orientated surface element within the reference configuration $\mathrm{d}\mathbf{A} = \mathrm{d}\mathbf{X}_1 \times \mathrm{d}\mathbf{X}_2$ is mapped to an orientated surface element within the current configuration $\mathrm{d}\mathbf{a} = \mathrm{d}\mathbf{x}_1 \times \mathrm{d}\mathbf{x}_2$ ($\mathrm{d}\mathbf{X}_1$ and $\mathrm{d}\mathbf{X}_2$ denote line elements in the reference configuration and $\mathrm{d}\mathbf{x}_1$ and $\mathrm{d}\mathbf{x}_2$ are line elements in the current configuration) by the relation

$$\mathrm{d}\mathbf{a} = J\, \mathbf{F}^{-\mathrm{T}} \cdot \mathrm{d}\mathbf{A}. \tag{2.29}$$

The orientated surface elements are defined by their normal vectors in the reference and current configuration, $\mathbf{N}$ and $\mathbf{n}$, as: $\mathrm{d}\mathbf{A} = \mathbf{N}\,\mathrm{d}A$ and $\mathrm{d}\mathbf{a} = \mathbf{n}\,\mathrm{d}a$, where $\mathrm{d}A$ and $\mathrm{d}a$ constitute the area of the surface elements in the reference and current configuration.

Using the scalar triple product and Eq. (2.26), volume elements in the reference and current configuration $\mathrm{d}V$ and $\mathrm{d}V$ are connected by

$$\mathrm{d}v = J\,\mathrm{d}V. \tag{2.30}$$

The lengths of line elements $\mathrm{d}L$ in the reference configuration and $\mathrm{d}l$ in the current configuration are defined as

$$\mathrm{d}L^2 = ||\mathrm{d}\mathbf{X}||^2 = \mathrm{d}\mathbf{X}\cdot\mathrm{d}\mathbf{X} \quad \text{and} \quad \mathrm{d}l^2 = ||\mathrm{d}\mathbf{x}||^2 = \mathrm{d}\mathbf{x}\cdot\mathrm{d}\mathbf{x}. \tag{2.31}$$

Using the push forward for line elements, the right Cauchy-Green strain tensor $\mathbf{C}$ is introduced as

$$\mathrm{d}l^2 = \mathrm{d}\mathbf{X}\cdot\left(\mathbf{F}^{\mathrm{T}}\cdot\mathbf{F}\right)\cdot\mathrm{d}\mathbf{X} \tag{2.32}$$

$$\mathrm{d}l^2 = \mathrm{d}\mathbf{X}\cdot\mathbf{C}\cdot\mathrm{d}\mathbf{X} \tag{2.33}$$

The right Cauchy-Green strain tensor thus reads

$$\mathbf{C} = \mathbf{F}^{\mathrm{T}}\cdot\mathbf{F}. \tag{2.34}$$

In order to follow the standard continuum mechanics notation, quantities belonging to the reference configuration are denoted with uppercase letters, and quantities belonging to the current configuration are denoted by lowercase letters (cf. [21, 23] and others).

Considering curvilinear coordinates $\theta^i$ for $i \in \{1,2,3\}$, a material point with respect to the reference configuration is denoted as

$$\mathbf{X} = \mathbf{X}\left(\theta^i\right) \tag{2.35}$$

and a material point with respect to the current configuration reads

$$\mathbf{x} = \mathbf{x}\left(\theta^i\right). \tag{2.36}$$

Due to the connection of both points, the deformation mapping is achieved as

$$\mathbf{x} = \boldsymbol{\varphi}\left(\theta^i\right). \tag{2.37}$$

By defining a canonical (local) coordinate system, the covariant basis vectors, also known as tangent vectors, are introduced as

$$\mathbf{g}_i = \frac{\partial\mathbf{x}}{\partial\theta^i} \quad \text{and} \quad \mathbf{G}_i = \frac{\partial\mathbf{X}}{\partial\theta^i} \tag{2.38}$$

and the contravariant basis vectors read

$$\mathbf{g}^i = \frac{\partial\theta^i}{\partial\mathbf{x}} \quad \text{and} \quad \mathbf{G}^i = \frac{\partial\theta^i}{\partial\mathbf{X}}. \tag{2.39}$$

Therein, $\mathbf{G}_i$ and $\mathbf{G}^i$ denote basis vectors with respect to the reference configuration and $\mathbf{g}_i$ and $\mathbf{g}^i$ are basis vectors with respect to the current configuration. Unlike Cartesian coordinates, the covariant basis vectors have the following properties: $||\mathbf{g}_i|| \neq 1$ and $\mathbf{g}_i \cdot \mathbf{g}_j \neq 0$. Orthogonality is given by their dual basis. To be more precise

$$\mathbf{g}_i \cdot \mathbf{g}^j = \delta_{ij} \tag{2.40}$$
$$\mathbf{G}_i \cdot \mathbf{G}^j = \delta_{ij} \tag{2.41}$$

The co- and contravariant bases are coupled by the metrics. The covariant metrics of the reference and current configuration read

$$G_{ij} = \mathbf{G}_i \cdot \mathbf{G}_j, \quad [G_{ij}] = \begin{bmatrix} G_{11} & G_{12} & G_{13} \\ G_{21} & G_{22} & G_{23} \\ G_{31} & G_{32} & G_{33} \end{bmatrix} \tag{2.42}$$

and

$$g_{ij} = \mathbf{g}_i \cdot \mathbf{g}_j, \quad [g_{ij}] = \begin{bmatrix} g_{11} & g_{12} & g_{13} \\ g_{21} & g_{22} & g_{23} \\ g_{31} & g_{32} & g_{33} \end{bmatrix}. \tag{2.43}$$

Computing the inverse, the contravariant metrics of the reference and current configuration are obtained as

$$\left[G^{ij}\right] = [G_{ij}]^{-1} \quad \text{and} \quad \left[g^{ij}\right] = [g_{ij}]^{-1}. \tag{2.44}$$

Finally, the contravariant bases of the reference and current configuration can also be defined as

$$\mathbf{G}^i = G^{ij}\,\mathbf{G}_j \quad \text{and} \quad \mathbf{g}^i = g^{ij}\,\mathbf{g}_j. \tag{2.45}$$

With the curvilinear basis vectors at hand, the deformation gradient can be rewritten as

$$\mathbf{F} = \frac{\partial \mathbf{x}}{\partial \mathbf{X}} = \frac{\partial \mathbf{x}}{\partial \theta^i} \otimes \frac{\partial \theta^i}{\partial \mathbf{X}} = \mathbf{g}_i \otimes \mathbf{G}^i. \tag{2.46}$$

As can be seen, the bases of deformation gradient are associated with the deformed and undeformed configuration. It is thus a so-called two-point tensor. The mapping of line elements $\mathrm{d}\mathbf{X}$ and $\mathrm{d}\mathbf{x}$ is reformulated as

$$\mathrm{d}\mathbf{X} = \frac{\partial \mathbf{X}}{\partial \theta^i}\,\mathrm{d}\theta^i = \mathbf{G}_i\,\mathrm{d}\theta^i \quad \text{and} \quad \mathrm{d}\mathbf{x} = \frac{\partial \mathbf{x}}{\partial \theta^i}\,\mathrm{d}\theta^i = \mathbf{g}_i\,\mathrm{d}\theta^i. \tag{2.47}$$

The tangent vectors can also be used to rewrite the identity mapping in the undeformed

and deformed configuration as

$$\mathbf{I} = \mathbf{G}_i \otimes \mathbf{G}^i \quad \text{and} \quad \mathbf{i} = \mathbf{g}_i \otimes \mathbf{g}^i. \tag{2.48}$$

From Eqs. (2.46) and (2.47) it can be seen that deformation gradient $\mathbf{F}$ maps the covariant basis vector in the reference configuration $\mathbf{G}_i$ to the covariant basis vector in the current configuration $\mathbf{g}_i$, such as

$$\mathbf{g}_i = \mathbf{F} \cdot \mathbf{G}_i. \tag{2.49}$$

## 2.3 Balance equations

This section summarizes the balance equations of continuum mechanics. Based on the integral formulation, the local balance equations of linear momentum and energy are derived. The integral formulation contains a control volume and control surface of the reference body $\Omega_0 \subset \mathcal{B}_0$ and $\partial\Omega_0 \subset \partial\mathcal{B}_0$ (within a Boltzmann continuum).

This work only gives a short overview of the balance equations. For detailed information, the interested reader is referred to [9, 10, 22, 44, 66].

### 2.3.1 Conservation of linear momentum

The balance law of linear momentum predicts that the sum of external forces $\mathbf{K}$ acting on body $\mathcal{B}_0$ equals the time rate of linear momentum $\dot{\mathbf{L}}$. The external forces read

$$\mathbf{K} = \int_{\Omega_0} \rho_0 \, \mathbf{B} \, \mathrm{d}V + \int_{\partial\Omega_0} \mathbf{T}_0 \, \mathrm{d}A, \tag{2.50}$$

where $\rho_0$ denotes the mass density per unit volume, $\mathbf{B}$ the body force per unit mass and $\mathbf{T}_0$ the prescribed tractions on the boundary per unit area. The linear momentum reads

$$\mathbf{L} = \frac{\mathrm{d}}{\mathrm{d}t} \int_{\Omega_0} \rho_0 \, \boldsymbol{\varphi} \, \mathrm{d}V = \int_{\Omega_0} \rho_0 \, \dot{\boldsymbol{\varphi}} \, \mathrm{d}V, \tag{2.51}$$

where the superposed dot presents the material time derivative $\mathrm{d}(\bullet)/\mathrm{d}t = \dot{\bullet}$. By application of mass closed systems, i.e. $\dot{\rho}_0 = 0$, the equality $\mathbf{K} = \dot{\mathbf{L}}$ leads to

$$\int_{\Omega_0} \rho_0 \, \ddot{\boldsymbol{\varphi}} \, \mathrm{d}V = \int_{\Omega_0} \rho_0 \, \mathbf{B} \, \mathrm{d}V + \int_{\partial\Omega_0} \mathbf{T}_0 \, \mathrm{d}A. \tag{2.52}$$

In order to apply the integral law of balance of linear momentum on material points, it is converted into a local form by using the Cauchy theorem and the Gauß theorem[1].

[1] The divergence theorem (cf. Eq. (1.294) in [21]), also known as Gauß's divergence theorem, relates an outward flux of a vector field $\mathbf{a}$ or a second order tensor field $\mathbf{B}$ through the closed surface $\partial\Omega$

The Cauchy theorem states that the traction $\mathbf{T}$ depends only on the normal vector $\mathbf{N}$. It can be shown that this implies a linear dependency which, in turn, allows to define the first Piola-Kirchhoff stress tensor $\mathbf{P}$ by $\mathbf{T} = \mathbf{P} \cdot \mathbf{N}$. By localization, this leads to the local form of the balance of linear momentum

$$\operatorname{Div} \mathbf{P} + \rho_0 \mathbf{B} = \rho_0 \ddot{\boldsymbol{\varphi}} \quad \forall \mathbf{X} \in \mathcal{B}_0 \quad \text{with} \quad \operatorname{Div}(\bullet) = \operatorname{Grad}(\bullet) : \mathbf{I}. \tag{2.53}$$

Since this thesis deals with static problems only, dynamic effects can be neglected and thus, the inertia term vanishes:

$$\operatorname{Div} \mathbf{P} + \rho_0 \mathbf{B} = \mathbf{0} \quad \forall \mathbf{X} \in \mathcal{B}_0. \tag{2.54}$$

**Remark 1** *The conservation of angular momentum is not considered in this section. It is equivalent to the condition that the Cauchy stress tensor* $\boldsymbol{\sigma} = J^{-1} \mathbf{P} \cdot \mathbf{F}^T$ *as well as the second Piola-Kirchhoff stress tensor* $\mathbf{S} = \mathbf{F}^{-1} \cdot \mathbf{P}$ *are symmetric. Due to* $\boldsymbol{\sigma} = \boldsymbol{\sigma}^T$, $\mathbf{P} \cdot \mathbf{F}^T = \mathbf{F} \cdot \mathbf{P}^T$ *has to hold.*

The solution of thermomechanically coupled initial boundary value problems requires suitable boundary conditions and initial conditions. For that purpose, the boundary $\partial\mathcal{B}_0$ of the body $\mathcal{B}_0$ is decomposed into Dirichlet boundary $\partial\mathcal{B}_{0,\boldsymbol{\varphi}}$ and Neumann boundary $\partial\mathcal{B}_{0,\mathbf{T}}$

$$\partial\mathcal{B}_0 = \partial\mathcal{B}_{0,\boldsymbol{\varphi}} \cup \partial\mathcal{B}_{0,\mathbf{T}} \quad \text{and} \quad \partial\mathcal{B}_{0,\boldsymbol{\varphi}} \cap \partial\mathcal{B}_{0,\mathbf{T}} = \emptyset. \tag{2.55}$$

The boundary conditions are defined as

$$\boldsymbol{\varphi} = \bar{\boldsymbol{\varphi}} \; \forall \mathbf{X} \in \partial\mathcal{B}_{0,\boldsymbol{\varphi}} \quad \text{and} \quad \mathbf{P} \cdot \mathbf{N} = \mathbf{T} \; \forall \mathbf{X} \in \partial\mathcal{B}_{0,\mathbf{T}}, \tag{2.56}$$

where $\bar{\boldsymbol{\varphi}}$ denotes the prescribed deformation field on the Dirichlet boundary and where $\mathbf{T}$ denotes the prescribed tractions on the Neumann boundary. The initial deformation field is prescribed by $\boldsymbol{\varphi}(\mathbf{X}, t_0) = \boldsymbol{\varphi}_0(\mathbf{X})$ at time $t_0$.

### 2.3.2 Conservation of energy

The balance law of energy is also known as the first law of thermodynamics. It balances the mechanical and thermodynamic energies inside and from outside of a body. The

to the volume integral of the divergence of the tensor field inside the surface region

$$\begin{aligned} \int_{\partial\Omega} \mathbf{a} \cdot \mathbf{N} \, \mathrm{d}A &= \int_{\Omega} \operatorname{Div} \mathbf{a} \, \mathrm{d}V \quad \text{and} \\ \int_{\partial\Omega} \mathbf{B} \cdot \mathbf{N} \, \mathrm{d}A &= \int_{\Omega} \operatorname{Div} \mathbf{B} \, \mathrm{d}V, \end{aligned}$$

where $\mathbf{N}$ denotes the outward surface vector and $\Omega$ the body enclosed by the surface region $\partial\Omega$.

total energy of the body can be split into four different contributions: power due to externally applied forces $\mathcal{P}_{\text{ext}}$, heat power $\mathcal{P}_\Theta$, kinetic energy $K$ and internal energy $E$.

$$\dot{K} + \dot{E} = \mathcal{P}_{\text{ext}} + \mathcal{P}_\Theta \tag{2.57}$$

The external power consists of the body forces $\rho_0 \mathbf{B}$ and tractions acting on the surface $\mathbf{T}$. It is defined as

$$\mathcal{P}_{\text{ext}} = \int_{\Omega_0} \rho_0 \mathbf{B} \cdot \dot{\boldsymbol{\varphi}} \, \mathrm{d}V + \int_{\partial\Omega_0} \dot{\boldsymbol{\varphi}} \cdot \mathbf{T} \, \mathrm{d}A. \tag{2.58}$$

The heat power reads

$$\mathcal{P}_\Theta = \int_{\Omega_0} \rho_0 R \, \mathrm{d}V - \int_{\partial\Omega_0} \mathbf{H} \cdot \mathbf{N} \, \mathrm{d}A, \tag{2.59}$$

in which $R$ denotes the heat source density and $\mathbf{H}$ is the outward heat material flux vector depending linearly on the normal vector $\mathbf{N}$. Considering dynamic systems, the kinetic energy has the form

$$K = \int_{\Omega_0} \frac{1}{2} \rho_0 \left|\left|\dot{\boldsymbol{\varphi}}\right|\right|^2 \mathrm{d}V, \tag{2.60}$$

where $||\bullet|| = \sqrt{\{\bullet\}_i \{\bullet\}_i}$ denotes the Euclidean norm. By means of an internal energy density $U$ per unit mass, the internal energy $E$ is expressed as

$$E = \int_{\Omega_0} \rho_0 U \, \mathrm{d}V. \tag{2.61}$$

Finally, after applying the Gauß divergence theorem and, inserting the balance law of linear momentum (Eq. (2.53)) into the integral form Eq. (2.57), the local form of the balance law of energy reads

$$\rho_0 \dot{U} = \mathbf{P} : \dot{\mathbf{F}} - \operatorname{Div} \mathbf{H} + \rho_0 R \quad \forall \mathbf{X} \in \mathcal{B}_0, \tag{2.62}$$

where $\mathcal{P} = \mathbf{P} : \dot{\mathbf{F}}$ is the stress power.

Similarly to the mechanical boundary value problem, the thermal boundary is split into

$$\partial\mathcal{B}_0 = \partial\mathcal{B}_{0,\Theta} \cup \partial\mathcal{B}_{0,\mathbf{H}} \quad \text{and} \quad \partial\mathcal{B}_{0,\Theta} \cap \partial\mathcal{B}_{0,\mathbf{H}} = \emptyset. \tag{2.63}$$

The Dirichlet boundary $\mathcal{B}_{0,\Theta}$ defines the prescribed temperature $\theta$ and the Neumann boundary $\mathcal{B}_{0,\mathbf{H}}$ enforces the prescribed heat flux $H$ in the form

$$\Theta = \theta \; \forall \mathbf{X} \in \partial\mathcal{B}_{0,\Theta} \quad \text{and} \quad \mathbf{H} \cdot \mathbf{N} = H \; \forall \mathbf{X} \in \partial\mathcal{B}_{0,\mathbf{H}}. \tag{2.64}$$

The initial condition for the temperature field at time $t_0$ is denoted as $\Theta(\mathbf{X}, t_0) = \Theta_0(\mathbf{X})$.

### 2.3.3 Second law of thermodynamics

The second law of thermodynamics, also known as the entropy inequality, gives the direction of a thermodynamical process. In comparison to the described conservations laws, the balance law of entropy presents only a conservation law for reversible processes. The entropy $S$ of the control volume $\Omega_0 \in \mathcal{B}_0$ is defined as

$$S = \int_{\Omega_0} \rho_0 \, N \, \mathrm{d}V, \tag{2.65}$$

where $N$ denotes the entropy density per unit mass. The entropy inequality of a control volume $\Omega \in \mathcal{B}_0$ has the form

$$\frac{\mathrm{d}}{\mathrm{d}t} \int_{\Omega_0} \rho_0 \, N \, \mathrm{d}V \geq \int_{\Omega_0} \frac{\rho_0 \, R}{\Theta} \, \mathrm{d}V - \int_{\partial\Omega_0} \frac{\mathbf{H} \cdot \mathbf{N}}{\Theta} \, \mathrm{d}A, \tag{2.66}$$

in which $\Theta$ denotes the absolute temperature in Kelvin with $\Theta > 0\mathrm{K}$. The rate of entropy measures the energy transformed due to irreversible processes. The entropy inequality states that the rate of entropy is never smaller than the one associated with the external entropy supply resulting from heat sources and fluxes. Applying the Gauß theorem, the local form of the entropy inequality, also known as Clausius-Duhem inequality, is obtained as

$$\rho_0 \, \dot{N} - \frac{\rho_0 \, R}{\Theta} + \operatorname{Div} \frac{\mathbf{H}}{\Theta} \geq 0. \tag{2.67}$$

Using the product rule of the divergence and gradient[2] and multiplying Ineq. (2.67) by $\Theta$, the so-called dissipation inequality (dissipation $\mathcal{D}$) is achieved

$$\mathcal{D} = \operatorname{Div} \mathbf{H} + \rho_0 \left[ \Theta \, \dot{N} - R \right] + \mathbf{H} \cdot \mathbf{G} \geq 0 \quad \forall \mathbf{X} \in \mathcal{B}_0. \tag{2.68}$$

where $\mathbf{G} = -1/\Theta \operatorname{Grad} \Theta$ denotes the generalized temperature gradient. The term $\operatorname{Div} \mathbf{H} - \rho_0 \, R$ is replaced by the first law of thermodynamics (cf. Eq. (2.62)) and the

[2] Being $\mathbf{A}$ a second-order tensor field, $\mathbf{b}$ a vector field and $c$ a scalar field, the following identities (cf. [21]) hold

$$\begin{aligned} \operatorname{Div}(c\,\mathbf{b}) &= \mathbf{b} \cdot \operatorname{Grad} c + c \operatorname{Div} \mathbf{b}, \\ \operatorname{Div}(c\,\mathbf{A}) &= \mathbf{A} \cdot \operatorname{Grad} c + c \operatorname{Div} \mathbf{A} \quad \text{and} \\ \operatorname{Grad} c^n &= n \, c^{n-1} \operatorname{Grad} c. \end{aligned}$$

dissipation inequality reads

$$\mathcal{D} = \mathbf{P} : \dot{\mathbf{F}} + \rho_0 \left[ \Theta \, \dot{N} - \dot{U} \right] + \mathbf{H} \cdot \mathbf{G} \geq 0 \quad \forall \mathbf{X} \in \mathcal{B}_0. \tag{2.69}$$

An alternative form depending on the Helmholtz free energy $\psi_0$ can be formulated by introducing the Legendre transformation

$$U(N, \bullet) = \psi_0(\Theta, \bullet) + \Theta \, N. \tag{2.70}$$

Finally, by applying the time derivative of the Legendre transformation $\dot{U} - \Theta \, \dot{N} = \dot{\psi}_0 + \dot{\Theta} \, N$, an alternative form of the dissipation inequality is obtained:

$$\mathcal{D} = \mathbf{P} : \dot{\mathbf{F}} - \rho_0 \left[ \dot{\Theta} \, N + \dot{\psi}_0 \right] + \mathbf{H} \cdot \mathbf{G} \geq 0 \quad \forall \mathbf{X} \in \mathcal{B}_0. \tag{2.71}$$

Following Clausius-Planck, the dissipation inequality (2.71) can be formulated in a stronger form. To be more precise, with the internal dissipation $\mathcal{D}_{\text{int}}$ and dissipation caused by heat conduction $\mathcal{D}_{\text{con}}$ one postulates

$$\mathcal{D}_{\text{int}} = \mathbf{P} : \dot{\mathbf{F}} - \rho_0 \left[ \dot{\Theta} \, N + \dot{\psi}_0 \right] \geq 0 \quad \text{and} \quad \mathcal{D}_{\text{con}} = \mathbf{H} \cdot \mathbf{G} \geq 0. \tag{2.72}$$

## 2.4 Constitutive modeling

The material response of a body is described by constitutive relations. In the following, the constitutive model of an isothermal and a thermoelastic material at finite strains will be presented. Each model will be characterized by a Helmholtz free energy density $\psi_0$.

### 2.4.1 Hyperelasticity

This section focuses on isothermal processes. In the sense of Cauchy materials, the stress tensor depends only on the deformation gradient $\mathbf{P} = \mathbf{P}(\mathbf{F})$. Focussing on hyperelastic materials, the integral of stress power $\mathcal{P} = \mathbf{P} : \dot{\mathbf{F}}$ is path-independent. Hence, a potential depending on the deformation gradient $\Psi = \Psi(\mathbf{F})$, such as

$$\mathbf{P} = \frac{\partial \Psi(\mathbf{F})}{\partial \mathbf{F}} \quad \text{and} \quad \dot{\Psi}(\mathbf{F}) = \mathbf{P} : \dot{\mathbf{F}} = \mathcal{P} \tag{2.73}$$

exists. In this case, the time derivative of the potential $\dot{\Psi}$ is equal to the stress power $\mathcal{P}$. Inserting the definition of $\mathbf{P}$ into the internal dissipation in Ineq. (2.72), the potential reads

$$\Psi(\mathbf{F}) = \rho_0 \, \psi_0(\mathbf{F}) \, . \tag{2.74}$$

Therein, $\psi_0(\mathbf{F})$ denotes the Helmholtz free energy density. The hyperelastic material fulfills a priori the second law of thermodynamics represented in Ineq. (2.71) and it reads

$$\mathbf{P} : \dot{\mathbf{F}} - \rho_0 \, \dot{\Psi}(\mathbf{F}) = 0 \quad \Rightarrow \quad \dot{N} = 0. \tag{2.75}$$

Postulating that the material fulfills objectivity,

$$\Psi(\mathbf{F}) = \Psi(\mathbf{Q} \cdot \mathbf{F}) \tag{2.76}$$

has to hold, where the material is independent of any rigid body rotation $\mathbf{Q} \in S \subset SO(3)$ applied to the deformed configuration (cf. [34]). Thus, the stored energy can be expressed as a function of the symmetric right Cauchy-Green tensor

$$\mathbf{C} = \mathbf{F}^{\mathrm{T}} \cdot \mathbf{F} \quad \text{with} \quad \mathbf{C} = \mathbf{C}^{\mathrm{T}} \tag{2.77}$$

as $\Psi(\mathbf{F}) = \Psi(\mathbf{C})$. In this case, the first Piola Kirchoff stress tensor reads

$$\mathbf{P} = \frac{\partial \Psi(\mathbf{C})}{\partial \mathbf{C}} : \frac{\partial \mathbf{C}}{\partial \mathbf{F}} = 2 \, \mathbf{F} \cdot \frac{\partial \Psi(\mathbf{C})}{\partial \mathbf{C}} = 2 \, \rho_0 \, \mathbf{F} \cdot \frac{\partial \psi_0(\mathbf{C})}{\partial \mathbf{C}}. \tag{2.78}$$

Without loss of generality, the derivative $\partial \psi_0(\mathbf{C}) / \partial \mathbf{C}$ is represented by a symmetric tensor. It is referred to as the second Piola-Kirchhoff stress tensor

$$\mathbf{S} = 2 \, \frac{\partial \psi_0(\mathbf{C})}{\partial \mathbf{C}} \quad \text{with} \quad \mathbf{S} = \mathbf{S}^{\mathrm{T}}. \tag{2.79}$$

In this case balance of angular momentum is a priori fulfilled. To be more precise,

$$\mathbf{P} \cdot \mathbf{F}^{\mathrm{T}} = 2 \, \mathbf{F} \cdot \frac{\partial \Psi(\mathbf{C})}{\partial \mathbf{C}} \cdot \mathbf{F}^{\mathrm{T}} = \mathbf{F} \cdot \mathbf{P}^{\mathrm{T}}. \tag{2.80}$$

**Remark 2** *In general, objectivity means that the constitutive equations are independent of the motion of an observer. Under an observer transformation, the deformation gradient reads* $\mathbf{F}^* = \mathbf{Q} \cdot \mathbf{F}$. $\mathbf{Q} \in S \subset SO(3)$ *is the rotation tensor with* $\mathbf{Q}^T = \mathbf{Q}^{-1}$. *Accordingly, the right Cauchy-Green tensor transforms as* $\mathbf{C}^* = \mathbf{F}^T \cdot \mathbf{Q}^T \cdot \mathbf{Q} \cdot \mathbf{F} = \mathbf{C}$.

**Remark 3** *The principle of material symmetry requires a transformation in the form of* $\tilde{\mathbf{X}} = \mathbf{Q} \cdot \mathbf{X} \; \forall \mathbf{Q} \in S \subset SO(3)$. *Thus, the transformation of the deformation gradient reads* $\tilde{\mathbf{F}} = \mathbf{F} \cdot \mathbf{Q}^T$. *Assuming an energy potential as a function of the right Cauchy-Green tensor* $\Psi = \Psi(\mathbf{C})$, *it is called isotropic, if* $\Psi(\mathbf{C}) = \Psi(\tilde{\mathbf{C}})$ *and* $\tilde{\mathbf{C}} = \mathbf{Q} \cdot \mathbf{C} \cdot \mathbf{Q}^T$ $\forall \mathbf{Q} \in SO(3)$ *is fulfilled.*

### 2.4.2 Thermoelasticity

Potential $\Psi$ of the thermoelastic material depends on the deformation gradient $\mathbf{F}$ and the temperature $\Theta$, such as

$$\Psi = \Psi(\mathbf{F}, \Theta) \quad \text{with} \quad \Psi(\mathbf{F}, \Theta) = \rho_0 \, \psi_0(\mathbf{F}, \Theta) \,, \tag{2.81}$$

where $\psi_0(\mathbf{F}, \Theta)$ denotes the Helmholtz free energy density. The second law of thermodynamics provides the basis (cf. Ineq. (2.72)) for the constitutive relations of the thermoelastic material. For thermoelastic materials $\mathcal{D}_{\text{int}} = 0$ holds true. In order to obtain the constitutive relations, Ineq. (2.72) is rewritten as

$$\mathcal{D}_{\text{int}} = \left[ \mathbf{P} - \frac{\partial \Psi(\mathbf{F}, \Theta)}{\partial \mathbf{F}} \right] : \dot{\mathbf{F}} - \left[ \rho_0 \, N + \frac{\partial \Psi(\mathbf{F}, \Theta)}{\partial \Theta} \right] \dot{\Theta} = 0, \tag{2.82}$$

where the time derivative of the Helmholtz free energy reads

$$\dot{\Psi}(\mathbf{F}, \Theta) = \frac{\partial \Psi(\mathbf{F}, \Theta)}{\partial \mathbf{F}} : \dot{\mathbf{F}} + \frac{\partial \Psi(\mathbf{F}, \Theta)}{\partial \Theta} \, \dot{\Theta}. \tag{2.83}$$

Application of the Coleman and Noll procedure yields

$$\mathbf{P} = \frac{\partial \Psi(\mathbf{F}, \Theta)}{\partial \mathbf{F}} = \rho_0 \, \frac{\partial \psi_0(\mathbf{F}, \Theta)}{\partial \mathbf{F}} \tag{2.84}$$

and

$$N = -\frac{1}{\rho_0} \, \frac{\partial \Psi(\mathbf{F}, \Theta)}{\partial \Theta} = -\frac{\partial \psi_0(\mathbf{F}, \Theta)}{\partial \Theta}, \tag{2.85}$$

where the entropy $N$ is thermodynamically conjugated to the temperature $\Theta$ and vice versa.

Since the first law of thermodynamics does not define the process direction of the temperature, the temperature equation is derived from the Clausius-Duhem inequality. For that purpose, the rate of the entropy $\dot{N}$ is inserted into Ineq. (2.67). It can be written as

$$\dot{N} = -\frac{\partial \dot{\psi}_0(\mathbf{F}, \Theta)}{\partial \Theta} = -\left[ \frac{\partial^2 \psi_0(\mathbf{F}, \Theta)}{\partial \Theta^2} \, \dot{\Theta} + \frac{\partial^2 \psi_0(\mathbf{F}, \Theta)}{\partial \Theta \, \partial \mathbf{F}} : \dot{\mathbf{F}} \right]. \tag{2.86}$$

By doing so, the temperature equation has the form

$$\operatorname{Div} \mathbf{H} - \rho_0 \, R + c \, \dot{\Theta} + \mathcal{H} = 0, \tag{2.87}$$

where $c$ denotes the heat capacity and is restricted to the constraint $c > 0$. $\mathcal{H}$ is the structural heating and describes the thermoelastic response of the material. It is also

known as Gough-Joule effect. $c$ and $\mathcal{H}$ are defined as

$$c = -\rho_0\,\Theta\,\frac{\partial^2\psi_0(\mathbf{F},\Theta)}{\partial\Theta^2} \quad \text{and} \quad \mathcal{H} = -\rho_0\,\Theta\,\frac{\partial^2\psi_0(\mathbf{F},\Theta)}{\partial\Theta\,\partial\mathbf{F}} : \dot{\mathbf{F}}. \tag{2.88}$$

Considering the special case of an adiabatic system without internal heat sources ($\mathbf{H} = 0$ and $R = 0$), the temperature equation reduces to

$$c\,\dot{\Theta} + \mathcal{H} = 0. \tag{2.89}$$

In general, the anisotropic heat flux vector is defined by the use of the thermal conductivity tensor $\mathbb{H}$ in the reference configuration as

$$\mathbf{H} = -\mathbb{H} \cdot \operatorname{Grad}\Theta. \tag{2.90}$$

In order to fulfill the dissipation inequality or, to be more precise, the dissipation caused by conductivity $\mathcal{D}_{\text{con}} \geq 0$ (Ineq. (2.72)), the thermal conductivity tensor has to be positive semi-definite. In the special case of an isotropic conductivity $\mathbb{H} = \lambda\,\mathbf{I}$, the heat flux vector is expressed as

$$\mathbf{H} = -\lambda\,\operatorname{Grad}\Theta. \tag{2.91}$$

Thus, the dissipation caused by heat conduction is automatically satisfied

$$\mathcal{D}_{\text{con}} = \frac{\lambda}{\Theta}\,\operatorname{Grad}\Theta \cdot \operatorname{Grad}\Theta. \tag{2.92}$$

## 2.5 Numerical implementation

This section describes the numerical implementation of the balance equations into the finite element framework. For that purpose, balance of linear momentum and balance of energy are first rewritten into their weak forms, and test functions $\delta\boldsymbol{\varphi}$ (virtual velocity field) and $\delta\Theta$ (virtual temperature field) are introduced. By doing so one obtains (see Eq. (2.54))

$$\delta W_{\boldsymbol{\varphi}} = \int_{\mathcal{B}_0} \delta\boldsymbol{\varphi} \cdot \operatorname{Div}\mathbf{P}\,\mathrm{d}V + \int_{\mathcal{B}_0} \delta\boldsymbol{\varphi} \cdot \rho_0\,\mathbf{B}\,\mathrm{d}V = 0 \tag{2.93}$$

and (see Eq. (2.87))

$$\delta W_{\Theta} = \int_{\mathcal{B}_0} \Big[\operatorname{Div}\mathbf{H} - \rho_0\,R + c\,\dot{\Theta} + \mathcal{H}\Big]\,\delta\Theta\,\mathrm{d}V = 0. \tag{2.94}$$

By using the product rule[3] and the Gauß theorem,

$$\int_{\mathcal{B}_0} \delta\boldsymbol{\varphi} \cdot \operatorname{Div} \mathbf{P} \, \mathrm{d}V = \int_{\partial\mathcal{B}_{0,\mathbf{T}}} \mathbf{P}^{\mathrm{T}} \cdot \delta\boldsymbol{\varphi} \cdot \mathbf{N} \, \mathrm{d}A - \int_{\mathcal{B}_0} \mathbf{P} : \operatorname{Grad} \delta\boldsymbol{\varphi} \, \mathrm{d}V, \tag{2.95}$$

together with the Cauchy theorem $\mathbf{P}\cdot\mathbf{N} = \mathbf{T}$, and kinematic admissibility of test function $\delta\boldsymbol{\varphi}$, Eq. (2.93) is rewritten as

$$\delta W_{\boldsymbol{\varphi}} = \int_{\mathcal{B}_0} \left[\mathbf{P} : \operatorname{Grad} \delta\boldsymbol{\varphi} - \rho_0 \, \mathbf{B}\right] \mathrm{d}V - \int_{\partial\mathcal{B}_{0,\mathbf{T}}} \mathbf{T} \cdot \delta\boldsymbol{\varphi} \, \mathrm{d}A = 0. \tag{2.96}$$

Similarly, using the product rule and the divergence theorem, one obtains

$$\int_{\mathcal{B}_0} \operatorname{Div} \mathbf{H} \, \delta\Theta \, \mathrm{d}V = \int_{\partial\mathcal{B}_0} H \, \delta\Theta \, \mathrm{d}A - \int_{\mathcal{B}_{0,\mathbf{T}}} \mathbf{H} \cdot \operatorname{Grad} \delta\Theta \, \mathrm{d}V \tag{2.97}$$

with the heat flux $H = \mathbf{H} \cdot \mathbf{N}$. The integral form of the temperature equation Eq. (2.94) reads

$$\delta W_{\Theta} = \int_{\mathcal{B}_0} \left[ -\mathbf{H} \cdot \operatorname{Grad} \delta\Theta - \left[ \rho_0 \, R - c \, \dot{\Theta} + \Theta \, \frac{\partial \mathbf{P}}{\partial \Theta} : \dot{\mathbf{F}} \right] \delta\Theta \right] \mathrm{d}V + \int_{\partial\mathcal{B}_{0,\mathbf{T}}} H \, \delta\Theta \, \mathrm{d}A = 0. \tag{2.98}$$

In order to apply the finite element discretization, the referential body $\mathcal{B}_0$ is approximated by

$$\mathcal{B}_0 \approx \mathcal{B}_0^{\mathrm{h}} = \bigcup_{e=1}^{n_{\mathrm{el}}} \mathcal{B}_0^e, \tag{2.99}$$

where $\mathcal{B}_0^{\mathrm{h}}$ denotes the set of all elements, $n_{\mathrm{el}}$ is the number of elements belonging to the set $\mathcal{B}_0^{\mathrm{h}}$ and $\mathcal{B}_0^e$ is the element $e$ within the set $\mathcal{B}_0^{\mathrm{h}}$. Within the framework of the isoparametric concept, position vector $\mathbf{X}$ and primary field variables $\boldsymbol{\varphi}$ and $\Theta$ (certainly, the isoparametric concept does not apply to $\Theta$) are approximated within one element $e$

[3] Being $\mathbf{A}$ a second-order tensor field and $\mathbf{b}$ a vector field, the following identity (cf. [21]) holds

$$\operatorname{Div}\left(\mathbf{A}^{\mathrm{T}} \cdot \mathbf{b}\right) = \operatorname{Div}(\mathbf{A}) \cdot \mathbf{b} + \mathbf{A} : \operatorname{Grad} \mathbf{b}.$$

by

$$\mathbf{X}|_{\mathcal{B}_0^e} \approx \mathbf{X}^{\mathrm{h}} = \sum_{a=1}^{n_{\mathrm{en}}} N^a(\boldsymbol{\xi})\ \mathbf{X}^a, \tag{2.100}$$

$$\boldsymbol{\varphi}|_{\mathcal{B}_0^e} \approx \boldsymbol{\varphi}^{\mathrm{h}} = \sum_{a=1}^{n_{\mathrm{en}}} N^a(\boldsymbol{\xi})\ \boldsymbol{\varphi}^a \quad \text{and} \tag{2.101}$$

$$\Theta|_{\mathcal{B}_0^e} \approx \Theta^{\mathrm{h}} = \sum_{a=1}^{n_{\mathrm{en}}} N^a(\boldsymbol{\xi})\ \Theta^a. \tag{2.102}$$

Therein, $\mathbf{X}^a$ denotes the position vectors with respect to the reference configuration at local node $a$. $\boldsymbol{\varphi}^a$ and $\Theta^a$ are the field variables at the local node $a$. $n_{\mathrm{en}}$ is the total number of the local nodes belonging to the element $e$. $N^a(\boldsymbol{\xi})$ describes the shape function of the local node $a$ with respect to the natural coordinates $\boldsymbol{\xi}$ within the reference element. The approximations of the virtual quantities are chosen in line with Bubnov-Galerkin method, i.e.,

$$\delta\boldsymbol{\varphi}|_{\mathcal{B}_0^e} \approx \delta\boldsymbol{\varphi}^{\mathrm{h}} = \sum_{a=1}^{n_{\mathrm{en}}} N^a(\boldsymbol{\xi})\ \delta\boldsymbol{\varphi}^a \quad \text{and} \tag{2.103}$$

$$\delta\Theta|_{\mathcal{B}_0^e} \approx \delta\Theta^{\mathrm{h}} = \sum_{a=1}^{n_{\mathrm{en}}} N^a(\boldsymbol{\xi})\ \delta\Theta^a. \tag{2.104}$$

According to these approximations, the gradients of the deformation field and of the temperature field are expressed as

$$\operatorname{Grad}\boldsymbol{\varphi}^{\mathrm{h}} = \sum_{a=1}^{n_{\mathrm{en}}} \boldsymbol{\varphi}^a \otimes \operatorname{Grad} N^a \quad \text{and} \quad \operatorname{Grad}\Theta^{\mathrm{h}} = \sum_{a=1}^{n_{\mathrm{en}}} \Theta^a\ \operatorname{Grad} N^a. \tag{2.105}$$

Similarly, the gradients of the virtual fields have the form

$$\operatorname{Grad}\delta\boldsymbol{\varphi}^{\mathrm{h}} = \sum_{a=1}^{n_{\mathrm{en}}} \delta\boldsymbol{\varphi}^a \otimes \operatorname{Grad} N^a \quad \text{and} \quad \operatorname{Grad}\delta\Theta^{\mathrm{h}} = \sum_{a=1}^{n_{\mathrm{en}}} \delta\Theta^a\ \operatorname{Grad} N^a. \tag{2.106}$$

Hence, the deformation gradient and the virtual deformation gradient read $\mathbf{F}^{\mathrm{h}} = \operatorname{Grad}\boldsymbol{\varphi}^{\mathrm{h}}$ and $\delta\mathbf{F}^{\mathrm{h}} = \operatorname{Grad}\delta\boldsymbol{\varphi}^{\mathrm{h}}$, respectively. Introducing the Jacobian matrix

$$\mathbf{J} = \frac{\partial\mathbf{X}}{\partial\boldsymbol{\xi}} = \sum_{a=1}^{n_{\mathrm{en}}} \mathbf{X}^a \otimes \frac{\partial N^a(\boldsymbol{\xi})}{\partial\boldsymbol{\xi}}, \tag{2.107}$$

the gradient of the shape function yields

$$\operatorname{Grad} N^a = \frac{\partial N^a(\boldsymbol{\xi})}{\partial \mathbf{X}} = \frac{\partial N^a(\boldsymbol{\xi})}{\partial \boldsymbol{\xi}} \cdot \frac{\partial \boldsymbol{\xi}}{\partial \mathbf{X}} = \frac{\partial N^a(\boldsymbol{\xi})}{\partial \boldsymbol{\xi}} \cdot \mathbf{J}^{-1}. \tag{2.108}$$

With the previous equations (2.99) – (2.108) at hand, the contribution of element $e$ to the balance laws are expressed in the discretized form as

$$\delta W_{\boldsymbol{\varphi}}|_{\mathcal{B}_0^e} = \sum_{a=1}^{n_{\text{en}}} \delta\boldsymbol{\varphi}^a \left[\mathbf{f}^a_{\boldsymbol{\varphi},\text{int}} + \mathbf{f}^a_{\boldsymbol{\varphi},\text{sur}} + \mathbf{f}^a_{\boldsymbol{\varphi},\text{vol}}\right] \quad \text{and} \tag{2.109}$$

$$\delta W_{\Theta}|_{\mathcal{B}_0^e} = \sum_{a=1}^{n_{\text{en}}} \delta\Theta^a \left[f^a_{\Theta,\text{int}} + f^a_{\Theta,\text{sur}} + f^a_{\Theta,\text{vol}}\right], \tag{2.110}$$

where $\mathbf{f}^a_{\boldsymbol{\varphi},\bullet}$ and $f^a_{\Theta,\bullet}$ denote (generalized) nodal forces. The forces are decomposed into internal (int), surface (sur) and body (vol) parts. In detail they read

$$\mathbf{f}^a_{\boldsymbol{\varphi},\text{int}} = \int_{\mathcal{B}_0} \mathbf{P} \cdot \operatorname{Grad} N^a \,\mathrm{d}V, \tag{2.111}$$

$$\mathbf{f}^a_{\boldsymbol{\varphi},\text{sur}} = -\int_{\partial\mathcal{B}_0} N^a \,\mathbf{T} \,\mathrm{d}A, \tag{2.112}$$

$$\mathbf{f}^a_{\boldsymbol{\varphi},\text{vol}} = -\int_{\mathcal{B}_0} N^a \,\rho_0 \,\mathbf{B} \,\mathrm{d}V, \tag{2.113}$$

$$f^a_{\Theta,\text{int}} = \int_{\mathcal{B}_0} \left[-\mathbf{H} \cdot \operatorname{Grad} N^a + c\,\dot{\Theta} - \Theta \frac{\partial \mathbf{P}}{\partial \Theta} : \dot{\mathbf{F}}\right] \mathrm{d}V, \tag{2.114}$$

$$f^a_{\Theta,\text{sur}} = \int_{\partial\mathcal{B}_0} N^a \,H \,\mathrm{d}A \quad \text{and} \tag{2.115}$$

$$f^a_{\Theta,\text{vol}} = -\int_{\mathcal{B}_0} N^a \,\rho_0 \,R \,\mathrm{d}V. \tag{2.116}$$

Time derivatives $\dot{(\bullet)}$ are approximated by the Backward Euler rule

$$\dot{(\bullet)} = \frac{\mathrm{d}(\bullet)}{\mathrm{d}t} \approx \frac{1}{\Delta t}\left[(\bullet)_{n+1} - (\bullet)_n\right], \tag{2.117}$$

where $n$ denotes the previous time step and $n+1$ indicates the current time step. $\Delta t = t_{n+1} - t_n$ describes the time increment between two time steps. Consequently, the rate of the temperature and deformation gradient are expressed as

$$\dot{\Theta} = \frac{\mathrm{d}\Theta}{\mathrm{d}t} \approx \frac{\Theta_{n+1} - \Theta_n}{\Delta t} \quad \text{and} \quad \dot{\mathbf{F}} = \frac{\mathrm{d}\mathbf{F}}{\mathrm{d}t} \approx \frac{\mathbf{F}_{n+1} - \mathbf{F}_n}{\Delta t}. \tag{2.118}$$

In order to shorten the equations, in the following the $\dot{(\bullet)}$-notation is used.

The residual vector $\mathbf{R}_e^a$ of a local node $a$ at element $e$ is defined as

$$\mathbf{R}_e^a = \begin{bmatrix} \mathbf{R}_{e,\boldsymbol{\varphi}}^a \\ R_{e,\Theta}^a \end{bmatrix} = \begin{bmatrix} \mathbf{f}_{\boldsymbol{\varphi},\mathrm{int}}^a + \mathbf{f}_{\boldsymbol{\varphi},\mathrm{sur}}^a + \mathbf{f}_{\boldsymbol{\varphi},\mathrm{vol}}^a \\ f_{\Theta,\mathrm{int}}^a + f_{\Theta,\mathrm{sur}}^a + f_{\Theta,\mathrm{vol}}^a \end{bmatrix}. \tag{2.119}$$

The global residuum is constituted by the use of global assembly operator $\mathbf{A}_{e=1}^{n_{\mathrm{el}}}$

$$\mathbf{R}^A = \mathop{\mathbf{A}}_{e=1}^{n_{\mathrm{el}}} \mathbf{R}_e^a. \tag{2.120}$$

The assembly operator maps the local node $a$ of the element $e$ to the global node $A$. $\mathbf{R}^A$ denotes the global residuum with respect to the global node $A$. The total number of global nodes is $n_{\mathrm{np}}$. The consistent linearization of the resulting system of equations is

$$\mathbf{R} + \left.\frac{\partial \mathbf{R}}{\partial \boldsymbol{\eta}}\right|_n \cdot \Delta\boldsymbol{\eta} = \mathbf{0} \quad \text{with} \quad \boldsymbol{\eta}_{n+1} = \boldsymbol{\eta}_n + \Delta\boldsymbol{\eta}, \tag{2.121}$$

where $n$ denotes the iteration step. The degrees of freedom (deformation and temperature field) are summarized in

$$\boldsymbol{\eta} = \begin{bmatrix} \boldsymbol{\varphi} \\ \Theta \end{bmatrix}. \tag{2.122}$$

$\mathbf{R}$ and $\boldsymbol{\eta}$ are the global vectors of residual and degrees of freedom. They are defined as

$$\mathbf{R} = \begin{bmatrix} \mathbf{R}^1 \\ \vdots \\ \mathbf{R}^A \\ \vdots \\ \mathbf{R}^{n_{\mathrm{np}}} \end{bmatrix} \quad \text{and} \quad \boldsymbol{\eta} = \begin{bmatrix} \boldsymbol{\eta}^1 \\ \vdots \\ \boldsymbol{\eta}^A \\ \vdots \\ \boldsymbol{\eta}^{n_{\mathrm{np}}} \end{bmatrix}. \tag{2.123}$$

Subsequently, the local algorithmic tangent modulus matrix $\mathbf{K}_e^{ab}$ of the element $e$ being identical to the derivative of the local residual $\mathbf{R}_e^a$ with respect to the degrees of freedom $\delta\boldsymbol{\eta}^b$ is constituted as

$$\mathbf{K}_e^{ab} = \frac{\mathrm{d}\mathbf{R}_e^a}{\mathrm{d}\boldsymbol{\eta}^b} = \begin{bmatrix} \dfrac{\mathrm{d}\mathbf{R}_{e,\boldsymbol{\varphi}}^a}{\mathrm{d}\boldsymbol{\varphi}^b} & \dfrac{\mathrm{d}\mathbf{R}_{e,\boldsymbol{\varphi}}^a}{\mathrm{d}\Theta^b} \\ \dfrac{\mathrm{d}R_{e,\Theta}^a}{\mathrm{d}\boldsymbol{\varphi}^b} & \dfrac{\mathrm{d}R_{e,\Theta}^a}{\mathrm{d}\Theta^b} \end{bmatrix} = \begin{bmatrix} \mathbf{K}_{\boldsymbol{\varphi}\boldsymbol{\varphi}}^{ab} & \mathbf{K}_{\boldsymbol{\varphi}\Theta}^{ab} \\ \mathbf{K}_{\Theta\boldsymbol{\varphi}}^{ab} & K_{\Theta\Theta}^{ab} \end{bmatrix} \tag{2.124}$$

with its sub-matrices

$$\mathbf{K}^{ab}_{\boldsymbol{\varphi}\boldsymbol{\varphi}} = \int_{\mathcal{B}_0} \operatorname{Grad} N^a \overset{(2)}{\cdot} \frac{\mathrm{d}\mathbf{P}}{\mathrm{d}\mathbf{F}} \cdot \operatorname{Grad} N^b \,\mathrm{d}V, \tag{2.125}$$

$$\mathbf{K}^{ab}_{\boldsymbol{\varphi}\Theta} = \int_{\mathcal{B}_0} N^b \frac{\mathrm{d}\mathbf{P}}{\mathrm{d}\Theta} \cdot \operatorname{Grad} N^a \,\mathrm{d}V, \tag{2.126}$$

$$\mathbf{K}^{ab}_{\Theta\boldsymbol{\varphi}} = -\int_{\mathcal{B}_0} N^a \,\Theta \frac{\mathrm{d}}{\mathrm{d}\mathbf{F}} \left( \frac{\partial \mathbf{P}}{\partial \Theta} : \dot{\mathbf{F}} \right) \cdot \operatorname{Grad} N^b \,\mathrm{d}V \quad \text{and} \tag{2.127}$$

$$\begin{aligned} K^{ab}_{\Theta\Theta} = \int_{\mathcal{B}_0} \Big[ & \lambda \operatorname{Grad} N^a \cdot \operatorname{Grad} N^b \\ & + N^a \frac{\mathrm{d}}{\mathrm{d}\Theta} \left( c\,\dot{\Theta} - \Theta \left[ \frac{\partial \mathbf{P}}{\partial \Theta} : \dot{\mathbf{F}} \right] + H \right) N^b \Big] \,\mathrm{d}V. \end{aligned} \tag{2.128}$$

$\mathrm{d}\mathbf{P}/\mathrm{d}\mathbf{F}$ is the so-called tangent and in the following it is denoted as $\mathbb{A}$. At the end, the global tangent matrix $\mathbf{K}^{AB}$ is assembled analogously to the global residual vector (see Eq. (2.119))

$$\mathbf{K}^{AB} = \mathop{\mathsf{A}}_{e=1}^{n_{\mathrm{el}}} \mathbf{K}^{ab}_e. \tag{2.129}$$

Further details on the derivation and numerical implementation of the finite element framework can be founded in [54] and [69].

In order to execute finite element simulations, the finite element code FEAP (cf. [65]) is used. It permits the implementation of an arbitrary material model. Conceptually, an interface passes the elemental residual vector $\mathbf{R}_e$ and the elemental tangent matrix $\mathbf{K}_e$.

# 3 Computational homogenization of material surfaces: from atomistic simulations to continuum models

The objective of this chapter is a numerical multiscale framework that determines mechanical continuum properties of material surfaces based on molecular statics. The key idea is the coupling of representative volume elements in the atomistic and in the continuum model by the principle of energy equivalence. This allows a thermodynamically consistent implementation of various material models and boundary conditions, e.g., to capture size effects in nano scale materials. For the present example of copper, a very good match with literature data is observed. Only the results for the surface stiffness still deviate in the same range as existing data sources do. The presented results concurrently indicate a drastic strain sensitivity. Further, a methodological bulk to surface error propagation by an appropriate strain limit and thickness extrapolation is eliminated. The latter is calculated by always allowing for fully developed surface regions. Additionally, this method reveals a strain dependence of higher order that is caused by the anharmonic potential and not captured by standard bulk models. The presented multiscale framework finally serves two purposes: validating the reasonableness of a material surface model and determining its parameters.

In this work, the material parameters will be determined by a novel homogenization method, i.e., the principle of energy equivalence between the atomistic and the continuum model. Within the proposed framework of energy equivalence, the energy obtained from atomistic simulations is compared to the energy obtained from continuum simulations. The (change in) total energy is employed because this observability is well defined in both models and its value must be model independent, making the difference between both a suitable measure to be minimized. This coupling between the models is straightforward in the present case of elasticity, but will require more attention if other energy contributions are present, e.g., thermoelasticity, plasticity and damage modeling. With the total energies at hand, an optimal set of surface material parameters is determined from Ritz-type minimization of the energy difference between the models. The material parameters to be determined are defined by an underlying prototype constitutive continuum material model which defines the space of approximations in the sense of the Ritz method. Given the reported unconventional behavior of material surfaces [13, 53, 56]

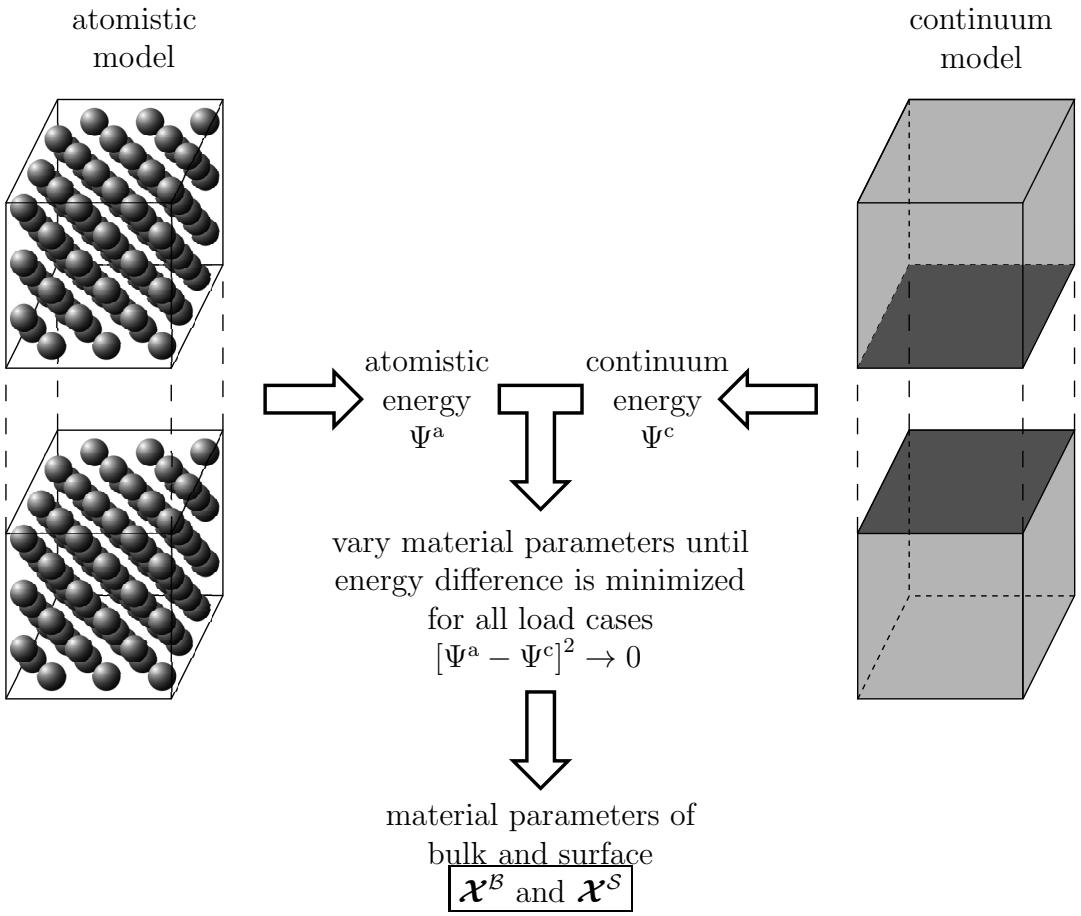


**Figure 3.1:** Sketch of the representative atomistic volume element $\Omega^{\mathrm{a}}$ (left) and the continuum representative volume element $\Omega^{\mathrm{c}}$ (right) as used to obtain the material surface parameters $\boldsymbol{\mathcal{X}}^{\mathcal{S}}$ using the Ritz method, i.e., minimizing the difference between the atomistic energy $\Psi^{\mathrm{a}}$ and the continuum energy $\Psi^{\mathrm{c}}$. The gray area illustrates the 2d-surface material in the continuum model.

special emphasis is put on two influences on the material parameters, namely, strain amplitude and bulk thickness. Compared to the boundary conditions in other literature, this work focuses on the most fundamental situation of free surfaces, where atoms at and near the surface are allowed to relax in all spatial directions, see Fig. 3.1 for an illustration.

The present chapter is structured into four sections. The determination of atomistic and continuum energies are presented in Sec. 3.1 together with a prototype continuum material model. Subsequently, Sec. 3.2 introduces the key idea of the novel Ritz-type homogenization approach for surfaces using energy equivalence. The numerical example for copper in Sec. 3.3 then illustrates the application and interpretation of the new framework, discussing the validity and peculiarities of the prototype material model. Sec. 3.4 concludes this work with a summary of the key features of the modeling framework.

## 3.1 Constitutive frameworks

The presented homogenization approach involves two views: an atomistic model and a continuum model. The energy modeling is introduced for both in the following, with quantities of the atomistic and the continuum model being marked with $^{\mathrm{a}}$ and $^{\mathrm{c}}$, respectively.

### 3.1.1 Atomistic scale

The atomistic body of interest $\Omega^{\mathrm{a}}$ is chosen to be a representative volume element (RVE) with periodic boundary conditions, containing $n_{\mathrm{atoms}}$ atoms at positions $\mathbf{x}_1, \ldots, \mathbf{x}_{n_{\mathrm{atoms}}}$ (cf. Fig. 3.1 and the fcc structure of copper in Fig. 3.2a). The volume is deformed into a parallelepiped, specified by the homogeneous deformation gradient $\bar{\mathbf{F}}$, which will be laid out in more detail in Sec. 3.2. The atoms' positions change upon this deformation, which are restricted to be elastic, i.e. small enough as to avoid "drastic" displacements like slip planes. The energy of a single atom $\alpha$ inside the body under deformation is modeled by an ansatz of the embedded-atom method (EAM) developed by Daw and Baskes [12] as

$$\Psi_\alpha^{\mathrm{a}}(\mathbf{x}_1, \ldots, \mathbf{x}_{n_{\mathrm{atoms}}}) = G(\rho_\alpha) + \frac{1}{2} \sum_{\beta \neq \alpha} \phi_{\alpha\beta}\left(\mathbf{x}_{\alpha\beta}\right). \tag{3.1}$$

Therein, $G(\rho_\alpha)$ is the energy to embed atom $\alpha$ into the electron density

$$\rho_\alpha = \sum_{\beta \neq \alpha} f_{\mathrm{e}} \exp(-\delta\left(x_{\alpha\beta}/x_{\mathrm{eq}} - 1\right)), \tag{3.2}$$

while

$$\phi_{\alpha\beta}\left(\mathbf{x}_{\alpha\beta}\right) = \phi_{\mathrm{e}} \exp(-\gamma\left(x_{\alpha\beta}/x_{\mathrm{eq}} - 1\right)) \tag{3.3}$$

is a two-body potential (see Oh-Johnson potential [45]) between the atoms $\alpha$ and $\beta$ separated by the distance $x_{\alpha\beta} = |\mathbf{x}_{\alpha\beta}|$ with $\mathbf{x}_{\alpha\beta} = \mathbf{x}_\alpha - \mathbf{x}_\beta$. The equilibrium interatomic separation distance $x_{\mathrm{eq}}$ is a model parameter just as $f_{\mathrm{e}}, \delta, \phi_{\mathrm{e}}$, and $\gamma$.

Since some of the neighbor atoms $\beta$ in Eq. (3.1) will be periodic images, the positions of which are affected by $\bar{\mathbf{F}}$, the energy $\Psi_\alpha^{\mathrm{a}}$ depends on $\bar{\mathbf{F}}$, as well. The total equilibrium energy $\Psi_{\mathrm{eq}}^{\mathrm{a}}$ of the entire atomistic body $\Omega^{\mathrm{a}}$ is then defined as the minimum energy over variations of the atoms' positions within the deformed periodic cell as

$$\Psi_{\mathrm{eq}}^{\mathrm{a}}\big(\bar{\mathbf{F}}\big) = \min_{\mathbf{x}_1, \ldots, \mathbf{x}_{n_{\mathrm{atoms}}}} \sum_{\alpha=1}^{n_{\mathrm{atoms}}} \Psi_\alpha^{\mathrm{a}}\big(\mathbf{x}_1, \ldots, \mathbf{x}_{n_{\mathrm{atoms}}}, \bar{\mathbf{F}}\big). \tag{3.4}$$

This work uses different lengths in order to describe the dimensions of the RVE. The

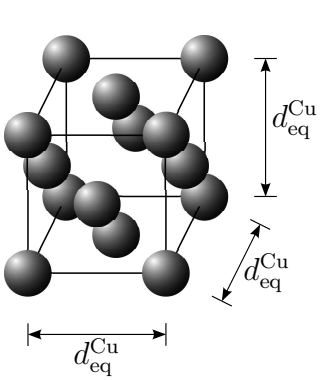


**(a)** Fcc unit cell of copper and its lattice constant $d_{\mathrm{eq}}^{\mathrm{Cu}}$.

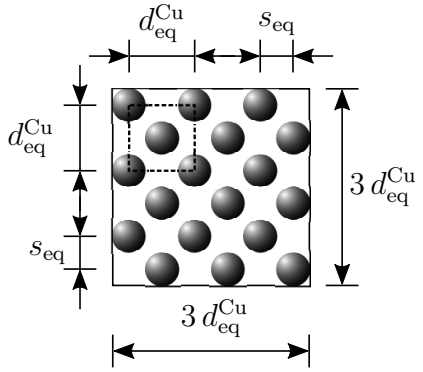


**(b)** Two-dimensional cross section (edge length $3\,n_{\mathrm{uc}} = 3\,d_{\mathrm{eq}}^{\mathrm{Cu}}$) of RVE with three periodic images of fcc unit cell in each spatial direction. A single fcc unit cell is highlighted by the dashed square.

**Figure 3.2:** Fcc unit cell and two-dimensional cross section of periodic arrangement of fcc unit cells defining the lattice constant $d_{\mathrm{eq}}^{\mathrm{Cu}}$ and the lattice spacing $s_{\mathrm{eq}} = 0.5\,d_{\mathrm{eq}}^{\mathrm{Cu}}$.

edge length of the fcc unit cell in the equilibrium configuration (undeformed configuration) is defined by the lattice constant $d_{\mathrm{eq}}^{\mathrm{Cu}}$ (cf. Fig. 3.2a). Due to periodic arrangement of the fcc unit cell, different layers arise. Fig. 3.2b shows the two-dimensional cross section being the periodic arrangement of fcc unit cells. The distance between two layers in the undeformed configuration is defined as the layer spacing $s_{\mathrm{eq}}$ and is half of the lattice constant in the equilibrium configuration: $s_{\mathrm{eq}} = 0.5\,d_{\mathrm{eq}}^{\mathrm{Cu}}$. In the deformed configuration it is denoted as $s$. In order to describe the length independently of its configuration, the dimensionless quantity number of unit cells $n_{\mathrm{uc}}$ is introduced. It describes the length dependently on the number of periodic arrangements of the unit cell. Thus, its current length varies conditionally upon the deformation.

## 3.1.2 Continuum scale

### 3.1.2.1 Fundamentals

The energy density of a material point in the continuum description is given as

$$\psi^{\mathrm{c}}(\mathbf{F})\,, \tag{3.5}$$

where the dependence on the local deformation gradient $\mathbf{F}$ is explicitly stated. The latter depends on the deformation field of the undeformed domain $\mathbf{x}(\mathbf{X})$ as $\mathbf{F} = \partial\mathbf{x}(\mathbf{X})/\partial\mathbf{X}$. The specific choice of this function determines the physical behavior that can be captured and thus depends on the material of interest. A prototype model is described in the following Sec. 3.1.2.2.

The total equilibrium energy $\Psi_{\mathrm{eq}}^{\mathrm{c}}$ is determined from integrating the energy density $\psi^{\mathrm{c}}$

over the undeformed bulk and surface domains, $\Omega_{\mathcal{B}}$ and $\Omega_{\mathcal{S}}$, respectively. It is eventually also formulated as a minimum energy among all deformation fields $\mathbf{x}-\mathbf{X}$ which are continuously differentiable (also across the periodic boundaries) and compatible with the prescribed deformation of the periodic cell $\bar{\mathbf{F}}$:

$$\Psi^{\mathrm{c}}\big(\bar{\mathbf{F}}\big) = \min_{\substack{\text{cont. diff. } \mathbf{x} \\ \text{compatible with } \bar{\mathbf{F}}}} \left\{ \int_{\Omega_{\mathcal{B}}} \psi^{\mathrm{c}}_{\mathcal{B}}(\mathbf{F}(\mathbf{X}))\,\mathrm{d}V + \int_{\Omega_{\mathcal{S}}} \psi^{\mathrm{c}}_{\mathcal{S}}(\mathbf{F}(\mathbf{X}))\,\mathrm{d}A \right\}. \tag{3.6}$$

**Remark 4** *Another equilibrium condition that is typically found in the context of continuum mechanics is the local stress equilibrium, being equivalent to the vanishing energy variation. In the continuum model, it means a divergence free stress tensor, provided external forces are not present. Its atomistic counterpart is the vanishing of all net forces (see [63]). In this work energy formulations are preferred, because of their scale-independent meaning, the possibility of a thermodynamic interpretation and their tradition in the modeling of solids, e.g., metals and polymers.*

#### 3.1.2.2 Prototype constitutive continuum material model

For comparison with available literature data [13, 56] and to focus on the key aspects of the framework, the example of a standard Hooke-type material model is investigated. The energy of this model depends on the linearized strain tensor field $\boldsymbol{\varepsilon} = (\mathbf{F}^{\mathrm{T}}+\mathbf{F})/2-\mathbf{I}$ and reads for the continuum bulk $\mathcal{B}$ and a plane-stress surface $\mathcal{S}$, respectively,

$$\psi^{\mathrm{c}}_{\mathcal{B}}\big(\psi^{\mathcal{B}}_0, \boldsymbol{\sigma}^{\mathcal{B}}_0, \mathbb{C}^{\mathcal{B}}, \boldsymbol{\varepsilon}\big) = \psi^{\mathcal{B}}_0 + \boldsymbol{\sigma}^{\mathcal{B}}_0 : \boldsymbol{\varepsilon} + \frac{1}{2}\,\boldsymbol{\varepsilon} : \mathbb{C}^{\mathcal{B}} : \boldsymbol{\varepsilon} \quad \text{and} \tag{3.7a}$$

$$\psi^{\mathrm{c}}_{\mathcal{S}}\big(\psi^{\mathcal{S}}_0, \boldsymbol{\sigma}^{\mathcal{S}}_0, \mathbb{C}^{\mathcal{S}}, \boldsymbol{\varepsilon}\big) = \psi^{\mathcal{S}}_0 + \boldsymbol{\sigma}^{\mathcal{S}}_0 : \boldsymbol{\varepsilon} + \frac{1}{2}\,\boldsymbol{\varepsilon} : \mathbb{C}^{\mathcal{S}} : \boldsymbol{\varepsilon}. \tag{3.7b}$$

Thus, the model contains constant, linear and quadratic contributions in terms of the linearized strain tensor field $\boldsymbol{\varepsilon}$. They are defined as:

$$\psi^{\mathrm{c},\mathcal{S}}_{\mathrm{const}} = \psi^{\mathcal{S}}_0, \tag{3.8}$$

$$\psi^{\mathrm{c},\mathcal{S}}_{\mathrm{lin}} = \boldsymbol{\sigma}^{\mathcal{S}}_0 : \boldsymbol{\varepsilon}, \tag{3.9}$$

$$\psi^{\mathrm{c},\mathcal{S}}_{\mathrm{quad}} = \frac{1}{2}\,\boldsymbol{\varepsilon} : \mathbb{C}^{\mathcal{S}} : \boldsymbol{\varepsilon}. \tag{3.10}$$

Therein, the initial energy densities $\psi_0$, the initial stress tensors $\boldsymbol{\sigma}_0$ and the material stiffness tensors $\mathbb{C}$ define the general set of model parameters to be determined for the bulk and surface material of interest

$$\boldsymbol{\mathcal{X}}^{\mathcal{B}} = \big\{\psi^{\mathcal{B}}_0, \boldsymbol{\sigma}^{\mathcal{B}}_0, \mathbb{C}^{\mathcal{B}}\big\} \quad \text{and} \quad \boldsymbol{\mathcal{X}}^{\mathcal{S}} = \big\{\psi^{\mathcal{S}}_0, \boldsymbol{\sigma}^{\mathcal{S}}_0, \mathbb{C}^{\mathcal{S}}\big\}. \tag{3.11}$$

Due to major and minor symmetries of the material stiffness tensors ($\mathbb{C}_{ijkl} = \mathbb{C}_{jikl}$, $\mathbb{C}_{ijkl} = \mathbb{C}_{ijlk}$ and $\mathbb{C}_{ijkl} = \mathbb{C}_{klij}$ as valid for a potential depending on symmetric strain

tensors), the number of independent components reduces from 81 to 21. Moreover it is assumed that a relaxed bulk configuration starts with no initial bulk stress, $\boldsymbol{\sigma}_0^{\mathcal{B}} = \mathbf{0}$. Thus, the set of bulk material parameters

$$\boldsymbol{\mathcal{X}}^{\mathcal{B}} = \left\{ \psi_0^{\mathcal{B}}, \mathbb{C}^{\mathcal{B}} \right\} = \left\{ \mathcal{X}_1^{\mathcal{B}}, \ldots, \mathcal{X}_{22}^{\mathcal{B}} \right\} \tag{3.12}$$

encompasses 22 unknowns (1 for the energy constant and 21 for the stiffness tensor). The set of material surface parameters

$$\boldsymbol{\mathcal{X}}^{\mathcal{S}} = \left\{ \psi_0^{\mathcal{S}}, \boldsymbol{\sigma}_0^{\mathcal{S}}, \mathbb{C}^{\mathcal{S}} \right\} = \left\{ \mathcal{X}_1^{\mathcal{S}}, \ldots, \mathcal{X}_{10}^{\mathcal{S}} \right\} \tag{3.13}$$

reduces to 10 unknowns when assuming plane stress (1 for the initial energy density, 3 for the initial stress tensor and 6 for the stiffness tensor).

For the sake of readability and clarity, it seems to be useful to denote the material parameters by the Voigt-notation [38]. Numbers above tensors denote their order if they deviate from their standard format (e.g. $\mathbb{C} = \overset{4}{\mathbb{C}}$, $\boldsymbol{\sigma} = \overset{2}{\boldsymbol{\sigma}}$). Although this part is only important for the surface material, the surface index $\mathcal{S}$ will be omitted for simplification. The stress calculation is transformed from $\boldsymbol{\sigma} = \mathbb{C} : \boldsymbol{\varepsilon}$ to $\overset{1}{\boldsymbol{\sigma}} = \overset{2}{\mathbb{C}} \cdot \overset{1}{\boldsymbol{\varepsilon}}$. Taking into account the minor and major symmetries of $\mathbb{C}$,

$$\underbrace{\begin{bmatrix} \sigma_{11} \\ \sigma_{22} \\ \sigma_{33} \\ \sigma_{23} \\ \sigma_{13} \\ \sigma_{12} \end{bmatrix}}_{\overset{1}{\boldsymbol{\sigma}}} = \underbrace{\begin{bmatrix} C_{1111} & C_{1122} & C_{1133} & C_{1123} & C_{1113} & C_{1112} \\ C_{1122} & C_{2222} & C_{2233} & C_{2223} & C_{2213} & C_{2212} \\ C_{1133} & C_{2233} & C_{3333} & C_{3323} & C_{3313} & C_{3312} \\ C_{1123} & C_{2223} & C_{3323} & C_{2323} & C_{2313} & C_{2312} \\ C_{1113} & C_{2213} & C_{3313} & C_{2313} & C_{1313} & C_{1312} \\ C_{1112} & C_{2212} & C_{3312} & C_{2312} & C_{1312} & C_{1212} \end{bmatrix}}_{\overset{2}{\mathbb{C}}} \cdot \underbrace{\begin{bmatrix} \varepsilon_{11} \\ \varepsilon_{22} \\ \varepsilon_{33} \\ 2\,\varepsilon_{23} \\ 2\,\varepsilon_{13} \\ 2\,\varepsilon_{12} \end{bmatrix}}_{\overset{1}{\boldsymbol{\varepsilon}}} \tag{3.14}$$

holds in the new notation. Due to the assumption of plane stress, stresses perpendicular to the surface, i.e. in $\mathbf{e}_3$-direction, vanish:

$$\boldsymbol{\sigma} = \begin{bmatrix} \sigma_{11} & \sigma_{12} & 0 \\ \sigma_{12} & \sigma_{22} & 0 \\ 0 & 0 & 0 \end{bmatrix} \quad \text{and} \quad \boldsymbol{\varepsilon} = \begin{bmatrix} \varepsilon_{11} & \varepsilon_{12} & 0 \\ \varepsilon_{12} & \varepsilon_{22} & 0 \\ 0 & 0 & \varepsilon_{33} \end{bmatrix}. \tag{3.15}$$

Changing the gap size (excluding surface-surface contact) does not contribute to the

energy. Accordingly to Eq. (3.14), the fully occupied surface stiffness tensor reads

$$\overset{2}{\mathbb{C}} = \begin{bmatrix} \tilde{C}_{1111} & \tilde{C}_{1122} & \tilde{C}_{1133} & \tilde{C}_{1123} & \tilde{C}_{1113} & \tilde{C}_{1112} \\ \tilde{C}_{1122} & \tilde{C}_{2222} & \tilde{C}_{2233} & \tilde{C}_{2223} & \tilde{C}_{2213} & \tilde{C}_{2212} \\ \tilde{C}_{1133} & \tilde{C}_{2233} & \tilde{C}_{3333} & \tilde{C}_{3323} & \tilde{C}_{3313} & \tilde{C}_{3312} \\ \tilde{C}_{1123} & \tilde{C}_{2223} & \tilde{C}_{3323} & \tilde{C}_{2323} & \tilde{C}_{2313} & \tilde{C}_{2312} \\ \tilde{C}_{1113} & \tilde{C}_{2213} & \tilde{C}_{3313} & \tilde{C}_{2313} & \tilde{C}_{1313} & \tilde{C}_{1312} \\ \tilde{C}_{1112} & \tilde{C}_{2212} & \tilde{C}_{3312} & \tilde{C}_{2312} & \tilde{C}_{1312} & \tilde{C}_{1212} \end{bmatrix}. \tag{3.16}$$

The simplification of $\overset{2}{\mathbb{C}}$ under the assumption of plane stress perpendicular to the $\mathbf{e}_3$-direction has the form (Eq. (3.15)):

$$\overset{2}{\mathbb{C}} = \begin{bmatrix} \tilde{C}_{1111} - \dfrac{\left[\tilde{C}_{1133}\right]^2}{\tilde{C}_{3333}} & \tilde{C}_{1122} - \dfrac{\tilde{C}_{1133}\,\tilde{C}_{2233}}{\tilde{C}_{3333}} & 0 & 0 & 0 & \tilde{C}_{1112} - \dfrac{\tilde{C}_{1133}\,\tilde{C}_{3312}}{\tilde{C}_{3333}} \\ \tilde{C}_{1122} - \dfrac{\tilde{C}_{1133}\,\tilde{C}_{2233}}{\tilde{C}_{3333}} & \tilde{C}_{2222} - \dfrac{\left[\tilde{C}_{2233}\right]^2}{\tilde{C}_{3333}} & 0 & 0 & 0 & \tilde{C}_{2212} - \dfrac{\tilde{C}_{2233}\,\tilde{C}_{3312}}{\tilde{C}_{3333}} \\ 0 & 0 & 0 & 0 & 0 & 0 \\ 0 & 0 & 0 & 0 & 0 & 0 \\ 0 & 0 & 0 & 0 & 0 & 0 \\ \tilde{C}_{1112} - \dfrac{\tilde{C}_{1133}\,\tilde{C}_{3312}}{\tilde{C}_{3333}} & \tilde{C}_{2212} - \dfrac{\tilde{C}_{2233}\,\tilde{C}_{3312}}{\tilde{C}_{3333}} & 0 & 0 & 0 & \tilde{C}_{1212} - \dfrac{\left[\tilde{C}_{3312}\right]^2}{\tilde{C}_{3333}} \end{bmatrix}. \tag{3.17}$$

With these conditions for plane stress at hand and eliminating the $C_{3333}$-component, $\overset{2}{\mathbb{C}}^{\mathcal{S}}$ of the surface material simplifies to a tensor with six independent components in the form

$$\overset{2}{\mathbb{C}}^{\mathcal{S}} = \begin{bmatrix} C^{\mathcal{S}}_{1111} & C^{\mathcal{S}}_{1122} & 0 & 0 & 0 & C^{\mathcal{S}}_{1112} \\ C^{\mathcal{S}}_{1122} & C^{\mathcal{S}}_{2222} & 0 & 0 & 0 & C^{\mathcal{S}}_{2212} \\ 0 & 0 & 0 & 0 & 0 & 0 \\ 0 & 0 & 0 & 0 & 0 & 0 \\ 0 & 0 & 0 & 0 & 0 & 0 \\ C^{\mathcal{S}}_{1112} & C^{\mathcal{S}}_{2212} & 0 & 0 & 0 & C^{\mathcal{S}}_{1212} \end{bmatrix}. \tag{3.18}$$

In accordance with Eq. (3.15), $\boldsymbol{\sigma}^{\mathcal{S}}_0$ has 3 independent components:

$$\boldsymbol{\sigma}^{\mathcal{S}}_0 = \begin{bmatrix} \sigma^{\mathcal{S}}_{0,11} & \sigma^{\mathcal{S}}_{0,12} & 0 \\ \sigma^{\mathcal{S}}_{0,12} & \sigma^{\mathcal{S}}_{0,22} & 0 \\ 0 & 0 & 0 \end{bmatrix}. \tag{3.19}$$

Before proceeding with the key homogenization scheme, it has to be emphasized

that the proposed model serves as a prototype model for the sake of illustration and comparison with literature. It can be replaced by more comprehensive models depending on the application of interest. Following [26], for instance, the asymmetric, linearized surface Piola-Kirchhoff stress tensor of an arbitrary objective Helmholtz free energy density $\psi(\mathbf{C})$ as a function of the right Cauchy-Green strain tensor $\mathbf{C}$ reads

$$\boldsymbol{\Pi}^{\mathcal{S}} = \boldsymbol{\Pi}_0^{\mathcal{S}} + \mathbb{C}^{\mathcal{S}} : \boldsymbol{\varepsilon}^{\mathcal{S}} + \operatorname{Grad} \mathbf{u}^{\mathcal{S}} \cdot \boldsymbol{\Pi}_0^{\mathcal{S}}, \tag{3.20}$$

where $\boldsymbol{\Pi}_0^{\mathcal{S}}$ denotes the initial energy density, $\mathbb{C}^{\mathcal{S}}$ the material stiffness tensor and $\operatorname{Grad} \mathbf{u}^{\mathcal{S}} \cdot \boldsymbol{\Pi}_0^{\mathcal{S}}$ is the product of the surface deformation gradient and the initial, linearized surface stress. The initial stresses and the material stiffness tensor are defined as

$$\boldsymbol{\Pi}_0^{\mathcal{S}} := \mathbf{S}^{\mathcal{S}}\big|_{\mathbf{F}=\mathbf{I}} = 2 \left.\frac{\partial \psi^{\mathcal{S}}}{\partial \mathbf{C}^{\mathcal{S}}}\right|_{\mathbf{F}=\mathbf{I}} \quad \text{and} \tag{3.21}$$

$$\mathbb{C}^{\mathcal{S}} := 2 \left.\frac{\partial \mathbf{S}^{\mathcal{S}}}{\partial \mathbf{C}^{\mathcal{S}}}\right|_{\mathbf{F}=\mathbf{I}} = 4 \left.\frac{\partial^2 \psi^{\mathcal{S}}}{\partial \mathbf{C}^{\mathcal{S}} \, \partial \mathbf{C}^{\mathcal{S}}}\right|_{\mathbf{F}=\mathbf{I}}. \tag{3.22}$$

Therein, $\mathbf{S}^{\mathcal{S}}$ denotes the second Piola-Kirchhoff stress tensor of the surface. More generally, the presented framework is also compatible with – but not limited to – temperature effects, dissipation, finite strain plasticity as well as internal variables and incrementally defined potentials [7, 70] for both the bulk and the surface. This compatibility is achieved by the following Ritz-type energy approach that imposes no constraints on the formerly listed physical phenomena.

#### 3.1.2.3 Implementation in finite element framework

The implementation of prototype material models into the finite element framework (see Sec. 2.5) requires the global residual vector $\mathbf{R}$ and the global tangent matrix $\mathbf{K}$. Considering Sec. 2.5, for a purely mechanical problem the local residual vector reduces to $\mathbf{R}_e^a = \mathbf{R}_{e,\boldsymbol{\varphi}}^a = \mathbf{f}_{\boldsymbol{\varphi},\mathrm{int}}^a$ and the local tangent matrix reduces to $\mathbf{K}_e^{ab} = \mathbf{K}_{\boldsymbol{\varphi}\boldsymbol{\varphi}}^{ab} = \mathrm{d}\mathbf{f}_{\boldsymbol{\varphi},\mathrm{int}}^a / \mathrm{d}\boldsymbol{\varphi}^b$. According to Eqs. (2.111) and (2.125) only the stress tensor $\mathbf{P}$ and its derivative $\mathrm{d}\mathbf{P}/\mathrm{d}\mathbf{F}$ have to be computed. However, due to focusing on small strains within the prototype material models, $\mathbf{P}$ and $\mathbf{F}$ are replaced by $\boldsymbol{\sigma}$ and $\boldsymbol{\varepsilon}$ with $\boldsymbol{\varepsilon} = \left[\mathbf{F} + \mathbf{F}^{\mathrm{T}}\right]/2 - \mathbf{I}$. With Eqs. (3.7a) and (3.7b) in mind, $\boldsymbol{\sigma} = \mathrm{d}\psi/\mathrm{d}\boldsymbol{\varepsilon}$ and $\mathrm{d}\boldsymbol{\sigma}/\mathrm{d}\boldsymbol{\varepsilon}$ read

$$\frac{\mathrm{d}\psi^{\bullet}}{\mathrm{d}\boldsymbol{\varepsilon}} = \boldsymbol{\sigma}_0^{\bullet} + \mathbb{C}^{\bullet} : \boldsymbol{\varepsilon} \quad \text{and} \tag{3.23}$$

$$\frac{\mathrm{d}\boldsymbol{\sigma}^{\bullet}}{\mathrm{d}\boldsymbol{\varepsilon}} = \mathbb{C}^{\bullet}, \tag{3.24}$$

where $\bullet$ has to be replaced either by $\mathcal{B}$ or $\mathcal{S}$.

## 3.2 A novel Ritz-type homogenization approach: material parameter transition from the atomistic model to the continuum model

### 3.2.1 Ritz's method applied to materials with surfaces

The Ritz method (cf. [5]) is adopted to identify the set of material parameters of the bulk and the surface, $\boldsymbol{\mathcal{X}}^{\mathcal{B}}$ and $\boldsymbol{\mathcal{X}}^{\mathcal{S}}$. In general, the Ritz method minimizes an energy residuum $\mathcal{R}$ of a boundary value problem. Here, the energy residuum to be minimized is the difference between the energy of the atomistic model $\Psi^{\mathrm{a}}$ and the energy of the continuum model $\Psi^{\mathrm{c}}$ that should ideally vanish as $\Psi^{\mathrm{c}} - \Psi^{\mathrm{a}} = 0$.

To identify a set of unknown material parameters, various load cases are applied and the related atomistic and continuum energies are compared. Each load case $1 \leq i \leq n_{\mathrm{lc}}$ is prescribed by the corresponding macroscopic deformation gradient $\bar{\mathbf{F}}^{(i)}$ of a periodic RVE in the form

$$\bar{\mathbf{F}}^{(i)}(\epsilon) = \mathbf{I} + \epsilon\, \Delta\bar{\mathbf{F}}^{(i)}, \tag{3.25}$$

where $\Delta\bar{\mathbf{F}}^{(i)}$ are representative mixtures of axial and shear deformations which are then scaled by $\epsilon$. $n_{\mathrm{lc}}$ denotes the total number of load cases. The difference between the energies on the continuum and the atomistic model must become minimal for each individual load case

$$\left[\Psi^{\mathrm{c}} - \Psi^{\mathrm{a}}\right]^2\Big|_{\bar{\mathbf{F}}^{(i)}} \rightarrow \min \quad \text{for} \quad 1 \leq i \leq n_{\mathrm{lc}}, \tag{3.26}$$

$$\Leftrightarrow \quad \mathcal{R} := \sum_{i=1}^{n_{\mathrm{lc}}} \left[\Psi^{\mathrm{c}} - \Psi^{\mathrm{a}}\right]^2\Big|_{\bar{\mathbf{F}}^{(i)}} \rightarrow \min\,. \tag{3.27}$$

The adapted Ritz method hence aims at the minimization of the residuum $\mathcal{R}$ by variations of the material parameters. The central relationship for determination of the material parameters can be eventually formulated by

$$\boldsymbol{\mathcal{X}}^{\mathcal{B}} = \arg\, \min_{\boldsymbol{\mathcal{X}}^{\mathcal{B}}} \mathcal{R}(\boldsymbol{\mathcal{X}}^{\mathcal{B}}) \quad \text{followed by} \quad \boldsymbol{\mathcal{X}}^{\mathcal{S}} = \arg\, \min_{\boldsymbol{\mathcal{X}}^{\mathcal{S}}} \mathcal{R}(\boldsymbol{\mathcal{X}}^{\mathcal{S}}, \boldsymbol{\mathcal{X}}^{\mathcal{B}}). \tag{3.28}$$

That means, the application of the Ritz method is now split and described in two steps:

1. Determination of the bulk material parameters $\boldsymbol{\mathcal{X}}^{\mathcal{B}}$ by application of Ritz's method to the pure bulk.

2. Determination of the surface material parameters $\boldsymbol{\mathcal{X}}^{\mathcal{S}}$ by application of Ritz's method to the bulk with a free surface, incorporating the results from step one.

If the continuum model was chosen comprehensively enough to allow full energetic equivalence, the minimum reached would be $\mathcal{R} = 0$. A compromise between accuracy and

applicability for complex materials can prevent this ideal case, though. As a consequence, the solution of the material parameters by the adapted Ritz method can depend on the strain amplitude $\epsilon$, and on the bulk thickness $a_{\mathcal{B}}$ measured by the dimensionless quantity $n_{\mathrm{uc}}$ (number of unit cells, see Secs. 3.1.1 and 3.2.3) if surfaces are present. This dependency is denoted by the symbols $\hat{\boldsymbol{\mathcal{X}}}^{\mathcal{B}}(\epsilon)$ and $\hat{\boldsymbol{\mathcal{X}}}^{\mathcal{S}}(\epsilon, a_{\mathcal{B}})$. With actually constant material parameters $\boldsymbol{\mathcal{X}}^{\mathcal{B}}$ and $\boldsymbol{\mathcal{X}}^{\mathcal{S}}$ in mind, four, partially conflicting, constraints are identified: (i) approximation of the linear-elastic limit, $\epsilon \to 0$; (ii) numerical resolvability of the energy variations with $\epsilon$, requiring sufficient strain increments; (iii) a fully developed surface boundary region, requiring enough atom layers, $a_{\mathcal{B}} \gg 1\, n_{\mathrm{uc}}$; (iv) avoidance of numerical cancellation errors due to too large total energies of too much bulk.

Eventually, a bulk size of $a_{\mathcal{B}} = 20\, n_{\mathrm{uc}}$ unit cell layers is chosen to guarantee a fully developed surface boundary region and determine the zero-strain limit from a third-order interpolation, see Sec. 3.3.2 for a quantitative validation of these assumptions. In contrast to this physically motivated limit, a second, more mathematical motivated limit for a zero thickness surface with $a_{\mathcal{B}} \to 0$ is chosen:

$$\boldsymbol{\mathcal{X}}^{\mathcal{S}}_{a_{\mathcal{B}}=20\, n_{\mathrm{uc}}} = \lim_{\epsilon \to 0} \hat{\boldsymbol{\mathcal{X}}}^{\mathcal{S}}(\epsilon, a_{\mathcal{B}} = 20\, n_{\mathrm{uc}}) \quad \text{and} \tag{3.29a}$$

$$\boldsymbol{\mathcal{X}}^{\mathcal{S}}_{a_{\mathcal{B}}\to 0} = \lim_{\substack{a_{\mathcal{B}}\to 0 \\ \epsilon \to 0}} \hat{\boldsymbol{\mathcal{X}}}^{\mathcal{S}}(\epsilon, a_{\mathcal{B}}) \tag{3.29b}$$

However, this work will focus on the physically motivated limit $a_{\mathcal{B}} = 20\, n_{\mathrm{uc}}$, because it is the more reasonable limit and due to the restriction to one bulk thickness, the numerical cost is lower. The mathematically motivated limit seems to be more meaningful in terms of the mathematical understanding of limits in general and serves as an additional comparison only.

All atomistic systems are simulated with the molecular dynamics code LAMMPS and the continuum systems are simulated using the finite element software FEAP, see Sec. A.1 for more details on the numerical settings.

### 3.2.2 Bulk parameters

A cubic homogeneous RVE $\Omega^{\mathrm{a}}_{\mathcal{B}}$ with periodic boundaries is studied to determine the bulk material parameters. It covers 20 unit cells in each spatial direction and consists of a single domain with 32.000 atoms, see Fig. 3.3. Relaxation of the bulk atoms is performed by energy minimization under zero-load. The relaxed RVE $\Omega^{\mathrm{a}}_{\mathcal{B}}$ with edge lengths $b_i$ then constitutes the initial configuration for all following load cases in the atomistic and the continuum model.

22 load cases $\bar{\mathbf{F}}^{(i)}(\epsilon)$ are required and used to identify the set of material parameters $\boldsymbol{\mathcal{X}}^{\mathcal{B}}$ of the bulk material. They are characterized by axial loading and shear of the periodic RVE as well as combinations of them. A detailed overview can be found in Tab. 3.1. 20 different strain amplitudes between $-0.001$ and $0.001$ are studied, not taking into ac-

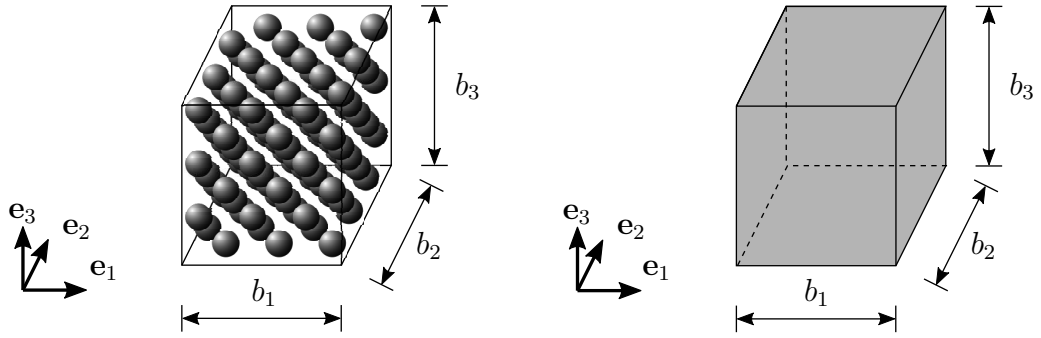


**(a)** Illustration of the relaxed initial RVE $\Omega^{\mathrm{a}}_{\mathcal{B}}$ of the atomistic model.

**(b)** Illustration of the relaxed initial RVE $\Omega^{\mathrm{c}}_{\mathcal{B}}$ of the continuum model.

**Figure 3.3:** Periodic cells of the atomistic (a) and continuum model (b) including a single bulk domain. Deviating from the simulations the figure shows a bulk RVE with $b_1 = b_2 = b_3 = 3\,n_{\mathrm{uc}}$.

count the initial relaxed state, i.e., $\epsilon \in \boldsymbol{\epsilon}$ with $\boldsymbol{\epsilon} = \{-0.001, -0.0009, \ldots, 0.001\} \setminus \{0\}$. The zero-strain limit is obtained from a linear regression in the form

$$\hat{\mathcal{X}}_i^{\mathcal{B}}(\epsilon) = m_i^{\mathcal{B}}\,\epsilon + \mathcal{X}_i^{\mathcal{B}}. \tag{3.30}$$

**Remark 5** *The choice of load cases can have an influence on the resulting material parameters like in other order reduction schemes [40]. This effect is tried to be minimized by a symmetric choice and weighting of the load types and a consistency check with literature, isolated simple tension and material symmetry.*

### 3.2.3 Surface parameters

A bulk domain and a vacuum gap, providing two surfaces, form the periodic RVE that is used to determine the surface parameters. Correspondingly, a two-dimensional material surface is added to the continuum model between the vacuum gap and the bulk (gray areas in Fig. 3.5). Hence, this system involves three types of domains: bulk $\mathcal{B}^{\mathrm{a/c}}$, a vacuum gap $\mathcal{V}^{\mathrm{a/c}}$ and two material surfaces $\mathcal{S}^{\mathrm{c}}_{\mathrm{d/u}}$ which are exclusively added to the continuum model. The size of the vacuum gap in $\mathbf{e}_3$-direction is approximately twenty times the lattice constant ($\approx 20\,d^{\mathrm{Cu}}_{\mathrm{eq}}$). The lattice constant $d^{\mathrm{Cu}}_{\mathrm{eq}}$ is determined from the relaxation simulation of the bulk material (see Sec. 3.3.1). Width and depth of the surface RVE span five lattice constants ($a_1 = a_2 = 5\,d^{\mathrm{Cu}}_{\mathrm{eq}}$). The boundary atoms at the surface between the vacuum gap and the bulk material are unconstrained and thus free of normal stress in $\mathbf{e}_3$-direction, which is the (001) crystal face in crystallographic notation.

In order to represent surface materials belonging to relaxed bulk materials, the spacing between atoms within the surface layer (rectangular to the surface normal) has to equal the spacing between atoms in the equilibrium configuration, $s_{\mathrm{eq}} = 0.5\,d^{\mathrm{Cu}}_{\mathrm{eq}}$. For this

| type | $i$ | $\Delta\bar{\mathbf{F}}^{(i)}$ |
|---|---|---|
| relaxation | 1 | $\mathbf{0}$ |
| axial | 2 | $\mathbf{e}_1 \otimes \mathbf{e}_1$ |
| | 3 | $\mathbf{e}_2 \otimes \mathbf{e}_2$ |
| | 4 | $\mathbf{e}_3 \otimes \mathbf{e}_3$ |
| shear | 5 | $\mathbf{e}_1 \otimes \mathbf{e}_2$ |
| | 6 | $\mathbf{e}_1 \otimes \mathbf{e}_3$ |
| | 7 | $\mathbf{e}_2 \otimes \mathbf{e}_3$ |
| biaxial | 8 | $\mathbf{e}_1 \otimes \mathbf{e}_1 + \mathbf{e}_2 \otimes \mathbf{e}_2$ |
| | 9 | $\mathbf{e}_1 \otimes \mathbf{e}_1 + \mathbf{e}_3 \otimes \mathbf{e}_3$ |
| | 10 | $\mathbf{e}_2 \otimes \mathbf{e}_2 + \mathbf{e}_3 \otimes \mathbf{e}_3$ |
| axial & shear | 11 | $\mathbf{e}_1 \otimes \mathbf{e}_1 + \mathbf{e}_1 \otimes \mathbf{e}_2$ |
| | 12 | $\mathbf{e}_1 \otimes \mathbf{e}_1 + \mathbf{e}_1 \otimes \mathbf{e}_3$ |
| | 13 | $\mathbf{e}_1 \otimes \mathbf{e}_1 + \mathbf{e}_2 \otimes \mathbf{e}_3$ |
| | 14 | $\mathbf{e}_2 \otimes \mathbf{e}_2 + \mathbf{e}_1 \otimes \mathbf{e}_2$ |
| | 15 | $\mathbf{e}_2 \otimes \mathbf{e}_2 + \mathbf{e}_1 \otimes \mathbf{e}_3$ |
| | 16 | $\mathbf{e}_2 \otimes \mathbf{e}_2 + \mathbf{e}_2 \otimes \mathbf{e}_3$ |
| | 17 | $\mathbf{e}_3 \otimes \mathbf{e}_3 + \mathbf{e}_1 \otimes \mathbf{e}_2$ |
| | 18 | $\mathbf{e}_3 \otimes \mathbf{e}_3 + \mathbf{e}_1 \otimes \mathbf{e}_3$ |
| | 19 | $\mathbf{e}_3 \otimes \mathbf{e}_3 + \mathbf{e}_2 \otimes \mathbf{e}_3$ |
| shear combinations | 20 | $\mathbf{e}_1 \otimes \mathbf{e}_2 + \mathbf{e}_1 \otimes \mathbf{e}_3$ |
| | 21 | $\mathbf{e}_1 \otimes \mathbf{e}_2 + \mathbf{e}_2 \otimes \mathbf{e}_3$ |
| | 22 | $\mathbf{e}_1 \otimes \mathbf{e}_3 + \mathbf{e}_2 \otimes \mathbf{e}_3$ |

**Table 3.1:** Types of deformation $\Delta\bar{\mathbf{F}}^{(i)}$ belonging to the macroscopic deformation gradient $\bar{\mathbf{F}}^{(i)}(\epsilon) = \mathbf{I} + \epsilon\,\Delta\bar{\mathbf{F}}^{(i)}$ (cf. Eq. (3.25)) to determine the bulk parameters.

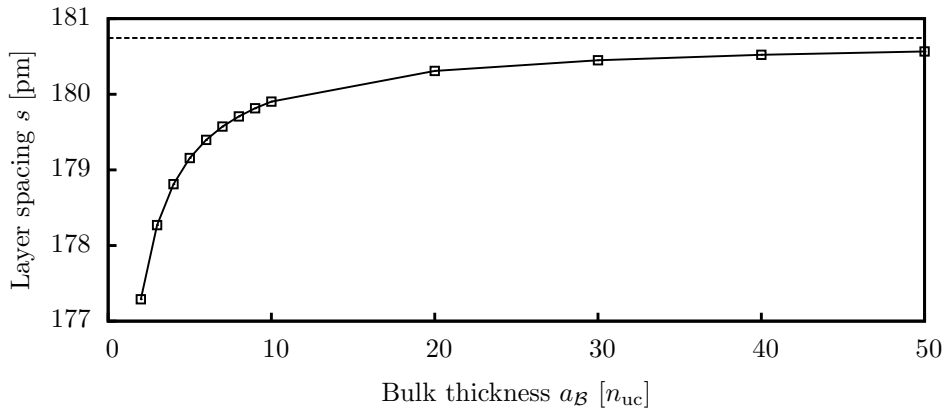


**Figure 3.4:** Layer spacing $s$ of the fully relaxed surface RVE (under zero-load) in $\mathbf{e}_1$- and $\mathbf{e}_2$-direction over the bulk thickness $a_{\mathcal{B}}$ in $\mathbf{e}_3$-direction measured by the number of unit cells $n_{\mathrm{uc}}$ (square symbols) and the half of the lattice constant $s_{\mathrm{eq}} = 0.5\,d_{\mathrm{eq}}^{\mathrm{Cu}}$ (dashed line).

purpose, two boundary conditions of surface RVEs will be discussed in the following: (i) relaxation with zero-load and (ii) prescribed width and depth ($a_1$ and $a_2$ according to Fig. 3.5). Due to the gap, the height $a_3$ has to be prescribed in both cases. Regardless of whether the width and depth are fixed or not, the atoms are still allowed to relax in direction of the surface normal.

As shown in Fig. 3.4, zero-load boundary conditions lead to a relaxation of the atom layer spacing in $\mathbf{e}_1$- and $\mathbf{e}_2$-direction of the surface RVE. Only for thicker bulk materials a convergence of the layer spacing in $\mathbf{e}_1$- and $\mathbf{e}_2$-direction, $s$, with half of the lattice constant, $0.5\, d_{\mathrm{eq}}^{\mathrm{Cu}} = s_{\mathrm{eq}}$, can be observed. Thus, surface RVEs with zero-load boundary conditions do not represent surfaces of relaxed bulk materials and finally, the width and depth of surface RVEs will be prescribed ($a_1 = a_2 = 5\, d_{\mathrm{eq}}^{\mathrm{Cu}}$).

To determine the surface material parameters $\boldsymbol{\mathcal{X}}^{\mathcal{S}}$, again various load cases $\bar{\mathbf{F}}^{(i)}(\epsilon)$ are applied. A detailed overview can be found in Tab. 3.2. Changing the gap size without surface-surface contact are zero-energy modes and thus neglected for parameter identification. Although at least ten load cases are necessary, twelve combinations of axial and shear deformations are used to achieve a symmetric weighting of the deformation modes. Like for the bulk parameters, 20 different strain amplitudes between $-0.001$ and $0.001$ are studied, not taking into account the initial relaxed state, i.e., $\epsilon \in \boldsymbol{\epsilon}$ with $\boldsymbol{\epsilon} = \{-0.001, -0.0009, \ldots, 0.001\} \setminus \{0\}$. In order to weight the $\mathbf{e}_1$- and $\mathbf{e}_2$-direction equally for a given strain amplitude, some load cases have to be distinguished with respect to the positive and the negative strain amplitude.

| type | $i$ | $\Delta\bar{\mathbf{F}}^{(i)}$ |
|---|---|---|
| relaxation | 1 | $\mathbf{0}$ |
| axial | 2 | $\mathbf{e}_1 \otimes \mathbf{e}_1$ |
| | 3 | $\mathbf{e}_2 \otimes \mathbf{e}_2$ |
| shear | 4 | $\mathbf{e}_1 \otimes \mathbf{e}_2$ |
| biaxial | 5 | $\mathbf{e}_1 \otimes \mathbf{e}_1 + \mathbf{e}_2 \otimes \mathbf{e}_2$ |
| | 6 | $\mathbf{e}_1 \otimes \mathbf{e}_1 - \mathbf{e}_2 \otimes \mathbf{e}_2$ |
| | 7 | $-\mathbf{e}_1 \otimes \mathbf{e}_1 + \mathbf{e}_2 \otimes \mathbf{e}_2$ |
| | 8 | $-\mathbf{e}_1 \otimes \mathbf{e}_1 - \mathbf{e}_2 \otimes \mathbf{e}_2$ |
| axial & shear | 9 | $\mathbf{e}_1 \otimes \mathbf{e}_1 + \mathbf{e}_1 \otimes \mathbf{e}_2$ |
| | 10 | $\mathbf{e}_1 \otimes \mathbf{e}_1 - \mathbf{e}_1 \otimes \mathbf{e}_2$ |
| | 11 | $\mathbf{e}_2 \otimes \mathbf{e}_2 + \mathbf{e}_1 \otimes \mathbf{e}_2$ |
| | 12 | $\mathbf{e}_2 \otimes \mathbf{e}_2 - \mathbf{e}_1 \otimes \mathbf{e}_2$ |

**Table 3.2:** Types of deformation $\Delta\bar{\mathbf{F}}^{(i)}$ belonging to the macroscopic deformation gradient $\bar{\mathbf{F}}^{(i)}(\epsilon) = \mathbf{I} + \epsilon\, \Delta\bar{\mathbf{F}}^{(i)}$ (cf. Eq. (3.25)) to determine the surface parameters.

In addition to the pure bulk setting, the influence of the bulk domain thickness is further examined. The bulk domain thickness is a function of the number of unit cells in $\mathbf{e}_3$-direction: $a_{\mathcal{B}} = a_{\mathcal{B}}(n_{\mathrm{uc}})$. Since the molecular dynamics code provides only the

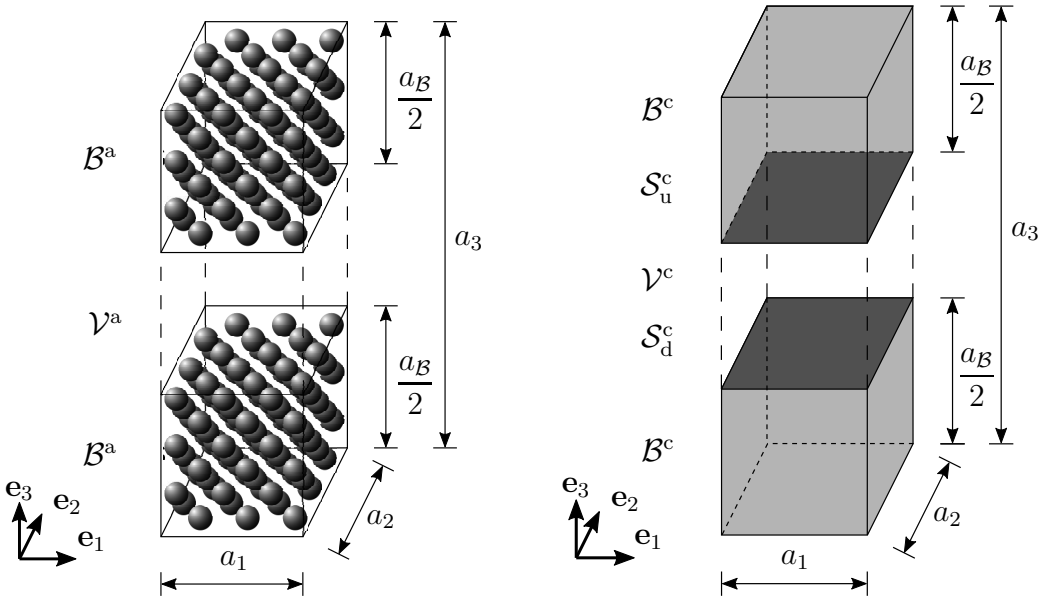


**(a)** RVE $\Omega^{\mathrm{a}}_{\mathcal{B}+\mathcal{S}}$ of the atomistic model after energy relaxation.

**(b)** Reference configuration of the RVE $\Omega^{\mathrm{c}}_{\mathcal{B}+\mathcal{S}}$ of the continuum model.

**Figure 3.5:** Periodic cells of the atomistic (a) and continuum model (b) including subdomains. Deviating from the simulations the figure shows a surface RVE with $a_1 = a_2 = 3\,n_{\mathrm{uc}}$ and $a_{\mathcal{B}} = 6\,n_{\mathrm{uc}}$.

atoms' positions and no thicknesses (apart from the RVE itself) as required for the continuum computations, the bulk material thickness $a_{\mathcal{B}}$ has to be determined under some assumptions for the first and last atom layers as explained in what follows. The bulk thickness is computed by summing up the atom layer thicknesses $s_j$ being identical with the layer spacing (see Fig. 3.6):

$$a_{\mathcal{B}} = 2\left[s_1 + \sum_{j=1}^{n_j} s_j + s_{n_j}\right] \quad \text{with} \quad \sum_{j=1}^{n_j} s_j = z_{n_j-1} - z_1 \tag{3.31}$$

$$s_j = \begin{cases} z_2 - z_1, & j = 1, \\ z_{n_j} - z_{n_j-1}, & j = n_j, \\ \dfrac{1}{2}\left[z_{j+1} - z_{j-1}\right], & \text{else.} \end{cases} \tag{3.32}$$

Therein, $j$ denotes the numbering of the atom layers and $n_j$ is the total number of atom layers within the upper and lower part of the bulk domain $\mathcal{B}^{\mathrm{a}}$. One unit cell layer corresponds to two atom layers in each spatial direction for an fcc material such as copper (cf. Fig. 3.2a). To be more precise, the total number of unit cell layers in $\mathbf{e}_3$-direction is twice the number of atom layers: $n_{\mathrm{uc}} = 2\,n_j$. In Fig. 3.5a the bulk domain seems to be decomposed into two parts: an upper and a lower part. The apparent decomposition is based only on the choice of the RVE with an internal vacuum gap.

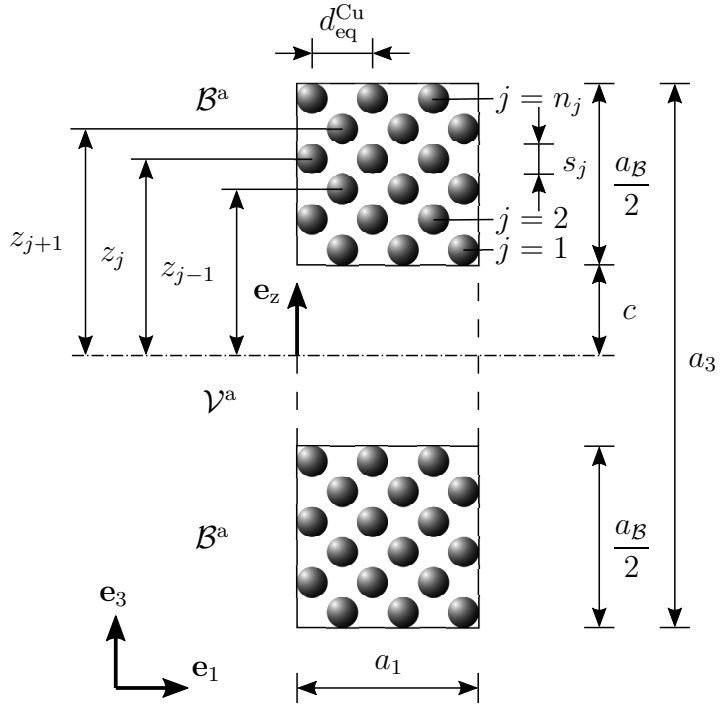


**Figure 3.6:** Two-dimensional cross section area in the global $\mathbf{e}_1$-$\mathbf{e}_3$-plane (cf. Fig. 3.5) of the atomistic RVE $\Omega^{\mathrm{a}}_{\mathcal{B}+\mathcal{S}}$ with parameters used for calculation of the layer thickness or layer spacing $s_j$, respectively. Coordinate $\mathbf{e}_{\mathrm{z}}$ has its origin at the symmetry plane. Deviating from the simulations this figure shows a surface RVE with $a_1 = 3\, d_{\mathrm{eq}}^{\mathrm{Cu}}$ and $a_{\mathcal{B}} = 6\, n_{\mathrm{uc}}$.

However, due to the periodic boundary conditions and the arrangement of the atoms inside the RVE, only one domain with the length $a_{\mathcal{B}}$ exists. Other arrangements of the atoms within the RVE, e.g., a plate with a sandwich-like configuration locating the bulk in the middle and a vacuum outside can also be chosen. During the energy minimization with LAMMPS some atoms can penetrate the walls of the RVE and appear on its opposite wall. Thereby, the number of atom layers in the upper and lower part of the bulk can differ in $\mathbf{e}_3$-direction. However, in this work it is assumed that the number of atom layers is identical in both parts. Thus, both bulk parts are mirror-symmetrical at the middle of the vacuum gap and their thickness is $a_{\mathcal{B}}/2$. The numbering of the atom layers is carried out for each bulk part separately and starts with $j = 1$ at the vacuum gap. The thickness $s_j$ of the atom layer $j$ depends on the positions $z_{j-1}$ and $z_{j+1}$ of the atom layers $j-1$ and $j+1$. Only for the first ($j = 1$) and last atom layers ($j = n_j$) special cases have to be considered in Eq. (3.32). The atom layers' positions are defined in Fig. 3.6 by the coordinate $\mathbf{e}_{\mathrm{z}}$ in the middle of the vacuum gap between both surfaces, where the distance $c$ is defined as

$$c = \frac{1}{2}\left[a_3 - 2\, a_{\mathcal{B}}\right]. \tag{3.33}$$

The number of unit cells $n_{\mathrm{uc}}$ is preferred to use as a measure of the bulk thickness in $\mathbf{e}_3$-direction, because the length $a_{\mathcal{B}}$ differs between the states of a pure bulk and a relaxed surface and thus does not provide an appropriate reference length. This study covers thicknesses of $\mathbf{n}_{\mathrm{uc}} = \{2, 3, \ldots, 10, 20, \ldots, 50\}$ unit cells. The zero-strain limit of the surface parameters $\mathcal{X}_i^{\mathcal{S}}$ is finally obtained for a fully developed surface boundary from the interpolation function

$$\hat{\mathcal{X}}_i^{\mathcal{S}}(\epsilon, a_{\mathcal{B}} = 20\, n_{\mathrm{uc}}) = \mathcal{X}^{\mathcal{S}}_{a_{\mathcal{B}}=20\, n_{\mathrm{uc}},i} + c^{\mathcal{S}}_{1,i}\, \epsilon + c^{\mathcal{S}}_{2,i}\, \epsilon^2 + c^{\mathcal{S}}_{3,i}\, \epsilon^3. \tag{3.34}$$

The polynomial degrees of the interpolation function have been chosen based on the results found in literature and the present work [13, 53, 56]. In comparison to the physically motivated limit at $a_{\mathcal{B}} = 20\, n_{\mathrm{uc}}$, the mathematically motivated limit at $a_{\mathcal{B}} \to 0$ reads

$$\hat{\mathcal{X}}_i^{\mathcal{S}}(\epsilon, a_{\mathcal{B}} \to 0) = \mathcal{X}^{\mathcal{S}}_{a_{\mathcal{B}}\to 0,i} + c^{\mathcal{S}}_{1,i}\, \epsilon + c^{\mathcal{S}}_{2,i}\, \epsilon^2 + c^{\mathcal{S}}_{3,i}\, \epsilon^3 \quad \text{with} \tag{3.35}$$

$$\hat{\mathcal{X}}_i^{\mathcal{S}}(\epsilon, a_{\mathcal{B}}) = \hat{\mathcal{X}}_i^{\mathcal{S}}(\epsilon, a_{\mathcal{B}} \to 0) + m_i^{\mathcal{S}}\, a_{\mathcal{B}}. \tag{3.36}$$

Therein, first a linear regression over the bulk thickness $a_{\mathcal{B}}$ is performed in Eq. (3.36), in which $\hat{\mathcal{X}}_i^{\mathcal{S}}(\epsilon, a_{\mathcal{B}} \to 0)$ provides the material parameters for each strain amplitude $\epsilon$ at $a_{\mathcal{B}} \to 0$. Eventually, the polynomial fit over the strain amplitude $\epsilon$ analogous to Eq. (3.34) is executed in Eq. (3.35).

## 3.3 Results and Discussion

The example of copper is now investigated using the presented novel Ritz-type approach (Sec. 3.2.1) in combination with a Hooke-type prototype material model (Sec. 3.1.2.2). Sec. 3.3.1 focuses on the bulk material and Sec. 3.3.2 on the surface material.

### 3.3.1 Bulk material

All bulk parameters, the equilibrium energy density and the stiffness tensor, show an excellent match with less than 0.5% difference compared to [32], see Tab. 3.3 for detailed numbers. Moreover, accordance with an orthotropic material is observed, as expected for the copper crystal. The difference between stiffness components due to further anisotropy is less than 1 GPa or $\leq 0.27\%$ of the largest stiffness component $C^{\mathcal{B}}_{1111}$. Also the underlying atomistic simulations closely match the literature data, e.g., a lattice constant for relaxed bulk copper of $d_{\mathrm{eq}}^{\mathrm{Cu}} = b_i / n_{\mathrm{uc}} = 361.49\,\mathrm{pm}$ is observed compared to 361.47 pm at 293 K [59] and 360.25 pm for a low-temperature approximation [55]. With respect to the numerical evaluation procedure, extremely small strains $|\epsilon| \leq 0.0002$ resulted in small fluctuations, which are due to round-off errors and thus to be interpreted as numerically unreliable. Hence, the corresponding data points from the evaluation procedure are excluded but they are plotted for full illustration in Fig. 3.7.

A pronounced linearity in strain for the majority of the elastic bulk parameters is observed, see the middle graph in Fig. 3.7. The absolute correlation factor underlines this very good fit of the linear regression being $> 0.99$ throughout all parameters (except $C^{\mathcal{B}}_{1212}$, $C^{\mathcal{B}}_{1313}$, $C^{\mathcal{B}}_{2323}$, $C^{\mathcal{B}}_{1213}$, $C^{\mathcal{B}}_{1223}$ and $C^{\mathcal{B}}_{1323}$, which are already strain-independent with a standard deviation smaller than 0.34% of $C^{\mathcal{B}}_{1111}$). This is due to an anharmonic atomistic potential for copper [20] and the absence of a third-order strain component in the continuum prototype model Eq. (3.7a). Being usually neglected in standard bulk continuum models, this error has a significant impact on the surface parameters that are sensitive to small changes in the overall energy as will be seen in the following.

| Variable | $\psi^{\mathcal{B}}_0$ | $C^{\mathcal{B}}_{1111}$ | $C^{\mathcal{B}}_{2222}$ | $C^{\mathcal{B}}_{3333}$ | $C^{\mathcal{B}}_{1122}$ | $C^{\mathcal{B}}_{1133}$ | $C^{\mathcal{B}}_{2233}$ | $C^{\mathcal{B}}_{1212}$ | $C^{\mathcal{B}}_{1313}$ | $C^{\mathcal{B}}_{2323}$ |
|---|---|---|---|---|---|---|---|---|---|---|
| Ledbetter & Naimon [32] | | 169.1 | | | 122.2 | | | 75.42 | | |
| present framework | -48.0 | 169.6 | 169.6 | 169.6 | 122.3 | 122.3 | 122.3 | 75.9 | 75.9 | 75.9 |
| slope of interpolation in $\epsilon$ | 0.0 | -340.5 | -340.5 | -340.5 | -808.5 | -808.5 | -808.5 | 0.0 | 0.0 | 0.0 |

**Table 3.3:** Selected results of the bulk material parameters as determined by the proposed Ritz-type homogenization approach and in comparison to literature data [32]. $\psi^{\mathcal{B}}_0$ and $C^{\mathcal{B}}_{ijkl}$ in $[10^9\,\mathrm{J/m^3}] = [1\,\mathrm{GPa}]$.

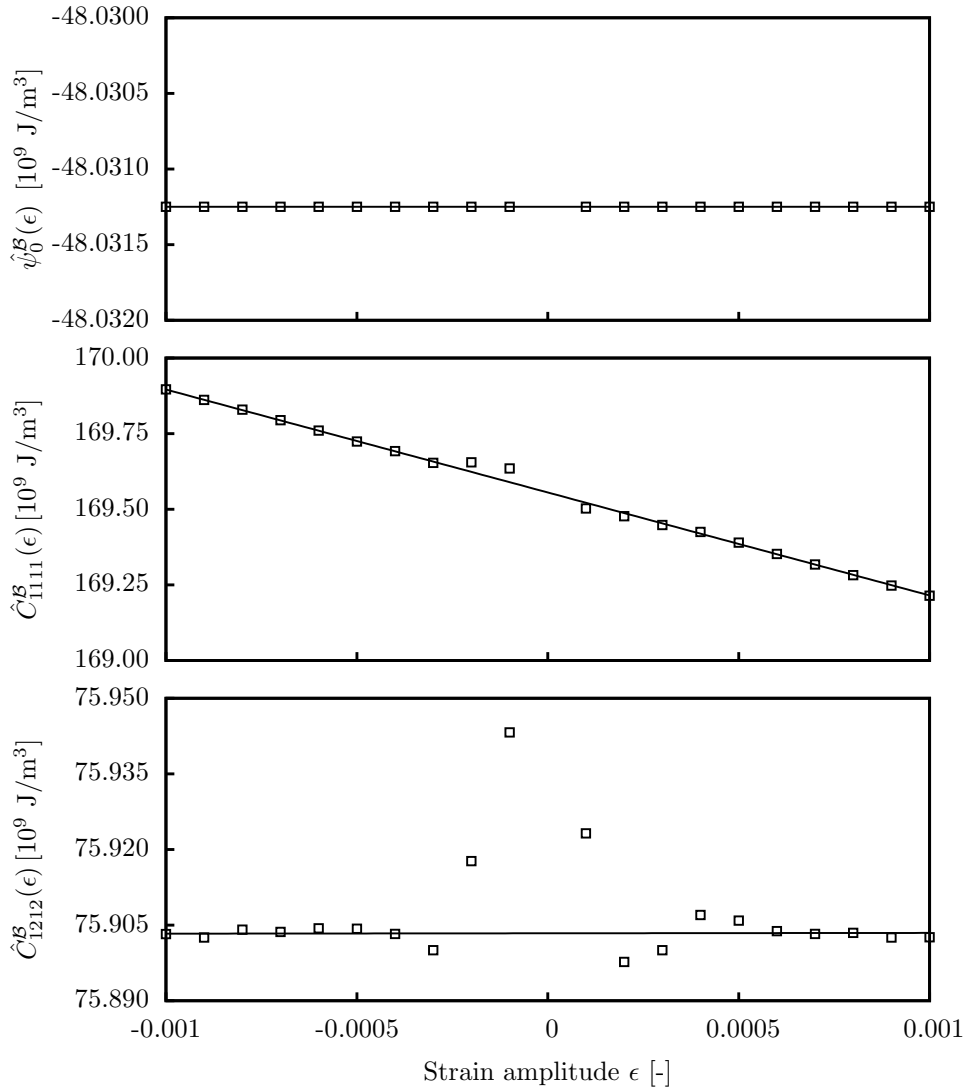


**Figure 3.7:** Results of selected bulk material parameters (square symbols) and their linear fits (lines) as a function of the strain amplitude $\epsilon$: the initial energy density $\hat{\psi}_0^{\mathcal{B}}$ as well as the material stiffness tensor components $\hat{C}^{\mathcal{B}}_{1111}$ and $\hat{C}^{\mathcal{B}}_{1212}$. Deviations at extremely small strains, $|\epsilon| \leq 0.0002$, are considered numerically unreliable and excluded from evaluation.

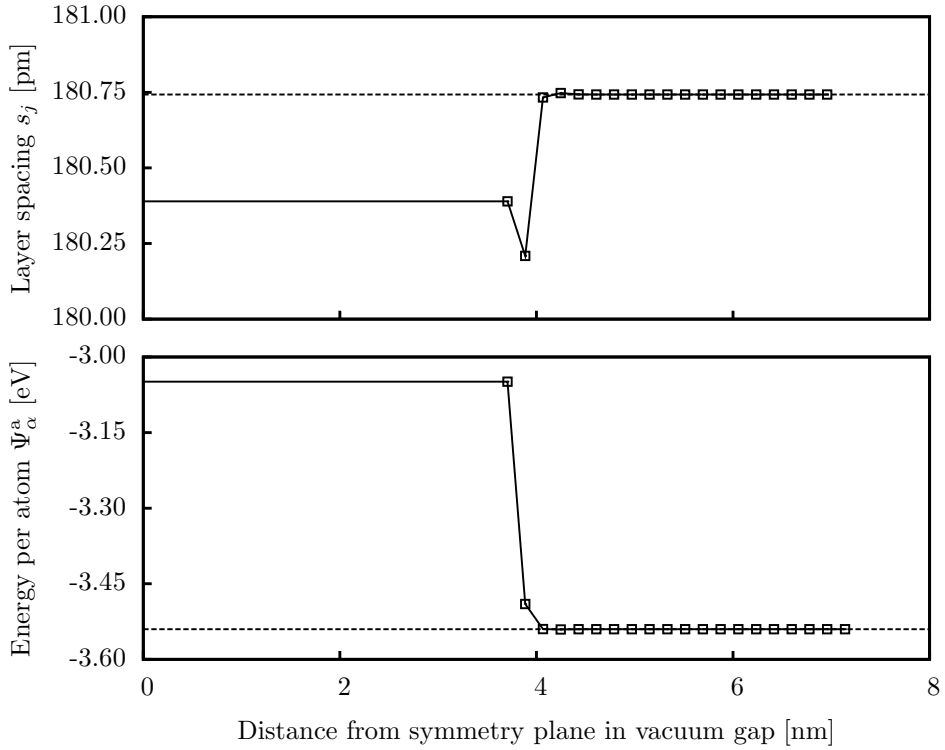


**Figure 3.8:** Layer spacing $s_j$ and total energy per atom $\Psi^{\mathrm{a}}_{\alpha}$ along the thickness of the upper bulk domain over the distance from the symmetry plane in the vacuum gap. The dashed lines mark the equilibrium layer spacing ($s_{\mathrm{eq}} = 0.5\, d^{\mathrm{Cu}}_{\mathrm{eq}} = 180.743\,\mathrm{pm}$, top) and the equilibrium energy per atom ($\Psi^{\mathrm{a}}_{\alpha,\mathrm{eq}} = -3.540201\,\mathrm{eV}$, bottom). Each square symbol represents an average over the respective atomistic planes (for $a_{\mathcal{B}} = 20\, n_{\mathrm{uc}}$).

## 3.3.2 Surface material

This section is structured as: (i) unless otherwise stated, the validation with literature data is performed by the physically motivated limit $\lim_{\epsilon\to 0} \hat{\boldsymbol{\mathcal{X}}}^{\mathcal{S}}(\epsilon, a_{\mathcal{B}} = 20\, n_{\mathrm{uc}})$ and (ii), subsequently, this limit is compared to the mathematically motivated limit $\lim_{a_{\mathcal{B}}\to 0,\epsilon\to 0} \hat{\boldsymbol{\mathcal{X}}}^{\mathcal{S}}(\epsilon, a_{\mathcal{B}})$.

As already explained in Sec. 3.2.3, the initial system for the determination of surface parameters consists of a bulk part with the previously determined bulk parameters $\boldsymbol{\mathcal{X}}^{\mathcal{B}}$ and a vacuum gap, connected via periodic boundary conditions, cf. Fig. 3.5. The creation of a new surface induces further relaxation of the near surface atoms. This relaxation reaches a depth of six atom layers, where layer spacing and atomistic energy $\Psi^{\mathrm{a}}_{\alpha}$ deviate between 0.01% and 14% from the inner bulk situation (cf. Fig. 3.8 for visualization and Tab. 3.4).

This validates the choice of 20 unit cell layers being sufficient for fully developed boundary regions as used in the limit $\lim_{\epsilon\to 0} \hat{\boldsymbol{\mathcal{X}}}^{\mathcal{S}}(\epsilon, a_{\mathcal{B}} = 20\, n_{\mathrm{uc}})$ in Eq. (3.29a). This limit

| | $a_{\mathcal{B}} = 20\, n_{\mathrm{uc}}$ | | | $a_{\mathcal{B}} = 1000\, n_{\mathrm{uc}}$ | | |
|---|---|---|---|---|---|---|
| layer number $j$ | $z_j$ [nm] | $\Psi^{\mathrm{a}}_{\alpha,j}$ [eV] | $s_j$ [pm] | $z_j$ [nm] | $\Psi^{\mathrm{a}}_{\alpha,j}$ [eV] | $s_j$ [pm] |
| 1 | 3.70612 | -3.048932 | 180.390 | 3.70609 | -3.048932 | 180.390 |
| 2 | 3.88651 | -3.490214 | 180.209 | 3.88648 | -3.490214 | 180.209 |
| 3 | 4.06672 | -3.540018 | 180.733 | 4.06669 | -3.540018 | 180.733 |
| 4 | 4.24746 | -3.540630 | 180.748 | 4.24742 | -3.540630 | 180.748 |
| 5 | 4.42820 | -3.540213 | 180.743 | 4.42817 | -3.540213 | 180.743 |
| 6 | 4.60895 | -3.540198 | 180.743 | 4.60891 | -3.540198 | 180.743 |
| 7 | 4.78969 | -3.540201 | 180.743 | 4.78966 | -3.540201 | 180.743 |
| 8 | 4.97043 | -3.540201 | 180.743 | 4.97040 | -3.540201 | 180.743 |
| 9 | 5.15118 | -3.540201 | 180.743 | 5.15114 | -3.540201 | 180.743 |
| 10 | 5.33192 | -3.540201 | 180.743 | 5.33189 | -3.540201 | 180.743 |
| ⋮ | | | | | | |
| $n_j - 1$ | 6.77786 | -3.540201 | 180.743 | 184.08675 | -3.540201 | 180.743 |
| $n_j$ | 6.95861 | -3.540201 | | 184.26749 | -3.540201 | |

**Table 3.4:** Position $z_j$ (distance from symmetry plane in vacuum gap), total energy per atom $\Psi^{\mathrm{a}}_{\alpha,j}$ and layer spacing $s_j$ for selected atom layers $j$ of one bulk domain $\mathcal{B}^{\mathrm{a}}$ containing 20 and 1000 unit cell layers in $\mathbf{e}_3$-direction ($a_{\mathcal{B}} = 20\, n_{\mathrm{uc}}$ and $a_{\mathcal{B}} = 1000\, n_{\mathrm{uc}}$).

definition for surface parameters proves to be well defined and is furthermore checked for consistency by comparison with a zero-thickness extrapolation see Fig. 3.9 for a quantitative comparison. It is observed that such a zero-thickness limit provides similar results, but of course only if extrapolated from states with fully developed boundary regions.

The equilibrium surface energy and the initial surface stresses eventually match the literature data [13, 56] very well, where available (see Tab. 3.5). Analogous to the bulk material, the material surface shows a two-dimensional orthotropic behavior as expected from its regular lattice structure. Components on the principal diagonal of $\mathbb{C}^{\mathcal{S}}$ and $\boldsymbol{\sigma}^{\mathcal{S}}_0$ are very close to each other. They deviate only by 0.015% between $C^{\mathcal{S}}_{1111}$ and $C^{\mathcal{S}}_{2222}$ or are identical with $\sigma^{\mathcal{S}}_{0,11} = \sigma^{\mathcal{S}}_{0,22}$ within the range of numerical precision.

Some components of the stiffness tensor capture the same order of magnitude but vary in a greater range, though. This discrepancy between the presented example and [56] as well as [13] stays in contrast to the previous matching and in contrast to the supposed similar conditions, i.e., the similar atomistic potential, boundary conditions and relaxation conditions. To minimize methodological differences, the limit definition with a zero-thickness extrapolation is checked successfully, see Fig. 3.9 and cf. [56]. The influence of possible typos in [56] (missing minus in his Eq. (9) and a symmetric version of the second term on the right hand side in his Eq. (17)) is also tested. In order to obtain symmetrical stiffness parameters, the following quadratic energy, motivated by

the quadratic approximation of $\det \bar{\mathbf{F}}$ and $\gamma$, is used:

$$\psi^{\mathrm{quad}} = \gamma + \frac{\partial \gamma}{\partial \varepsilon_{ij}}\,\varepsilon_{ij} + \frac{1}{2}\,\varepsilon_{ij}\,\frac{\partial^2 \gamma}{\partial \varepsilon_{ij}\,\partial \varepsilon_{kl}}\,\varepsilon_{kl} + \gamma\,\delta_{ij}\,\varepsilon_{ij} + \frac{\partial \gamma}{\partial \varepsilon_{ij}}\,\varepsilon_{ij}\,\delta_{kl}\,\varepsilon_{kl} + \frac{1}{2}\,\gamma\,[\delta_{ij}\,\delta_{kl} - 2\,\delta_{ik}\,\delta_{jl}]\,\varepsilon_{ij}\,\varepsilon_{kl}, \quad (3.37)$$

where $\gamma$ is Shenoy's notation of $\psi_0^{\mathcal{S}}$ and both notations are identical. The derivatives with respect to the strain are determined from Eqs. (13) and (17) in [56]. The second derivative of $\psi^{\mathrm{quad}}$ with respect to $\boldsymbol{\varepsilon}$ corresponds to the surface stiffness material parameters:

$$\frac{\partial^2 \psi^{\mathrm{quad}}}{\partial \boldsymbol{\varepsilon}^2} = \mathbb{C}^{\mathcal{S}}. \quad (3.38)$$

Furthermore, a minus seems to be missing in Eq. (9) in [56]. However, this is not considered.

Nevertheless, neither check could explain the discrepancies of the surface stiffness values. It is also important to note that these discrepancies already exist between the two data bases found in literature [56] and [13]. Unfortunately, [13] did not discuss the results from [56]. A few potential methodological differences remain that cannot be assessed quantitatively, except checking the obtained results for convergence and sensitivity. This includes, for example, the termination conditions of the atomistic simulations (note the sensitivity with respect to the choice of the atomistic model as shown in [51]) or the strain discretization on the continuum scale (the calculation of energy derivatives cannot be compared one-to-one to the present numerical minimization scheme containing multiple load types at once). It can be stated from this study, though, that the largest differences appear for surface stiffness parameters that are very sensitive to strain. This is summarized in Tabs. 3.5 and 3.6 and discussed in the following with emphasis on propagating bulk errors.

Noting the strain-dependence observed for the continuum bulk, the strain-dependence of the continuum surface is also explicitly examined. Interpolation functions of third order in strain, reading $\hat{\mathcal{X}}_i^{\mathcal{S}}(\epsilon,\, a_{\mathcal{B}} = 20\, n_{\mathrm{uc}}) = \mathcal{X}_i^{\mathcal{S}} + c_{1,i}^{\mathcal{S}}\,\epsilon + c_{2,i}^{\mathcal{S}}\,\epsilon^2 + c_{3,i}^{\mathcal{S}}\,\epsilon^3$ are used. Again, the strain values have been chosen as a compromise between the linear-elastic limit and a strain energy that is large enough to exceed the limit of numerical inaccuracy. This is particularly important for the surface stiffness tensor, because the quadratic energy contribution is relatively small in the present example of copper. For strains up to $\epsilon \leq 0.01$, linear and quadratic surface strains result in 0.808% and 0.008% energy contribution, respectively, see the comparisons in Tab. 3.7 and Fig. 3.10 for simple tension. It has to be emphasized that the present framework considers only strain amplitudes $\epsilon$ within the dimension of 0.0001 and 0.001. The contribution of the quadratic term – containing the stiffness components – with 0.000003% to the total energy density

| Variable | Shenoy [56] | Dingreville & Qu [13] | present framework $\boldsymbol{\mathcal{X}}^{\mathcal{S}}_{a_{\mathcal{B}}=20\,n_{\mathrm{uc}}}$ | present framework $\boldsymbol{\mathcal{X}}^{\mathcal{S}}_{a_{\mathcal{B}}\to 0}$ |
|---|---|---|---|---|
| $\psi_0^{\mathcal{S}}$ | 1326.6 | 1288 | 1275.31 | 1275.31 |
| $\sigma^{\mathcal{S}}_{0,11}$ | 1039.8 | 1396 | 1039.26 | 1039.26 |
| $\sigma^{\mathcal{S}}_{0,22}$ | 1039.8 | | 1039.26 | 1039.26 |
| $\sigma^{\mathcal{S}}_{0,12}$ | 0.0 | | 0.00 | 0.00 |
| $C^{\mathcal{S}}_{1111}$ | -8432.3 | -712 | -2006.31 | -2004.38 |
| $C^{\mathcal{S}}_{2222}$ | -8432.3 | | -2006.00 | -2005.29 |
| $C^{\mathcal{S}}_{1212}$ | -6315.8 | -992 | 104.45 | 107.24 |
| $C^{\mathcal{S}}_{1122}$ | 5349.7 | 5914 | 5380.95 | 5381.56 |
| $C^{\mathcal{S}}_{1112}$ | | | 2.84 | 0.03 |
| $C^{\mathcal{S}}_{2212}$ | | | 0.77 | 0.04 |

**Table 3.5:** Initial surface energy $\psi_0^{\mathcal{S}}$, initial surface stress $\sigma^{\mathcal{S}}_{0,ij}$ and surface stiffness $C^{\mathcal{S}}_{ijkl}$ as determined by the present framework in comparison with literature. The present framework represents the results from the physically and mathematically motivated limits ($\lim_{\epsilon\to 0}\hat{\boldsymbol{\mathcal{X}}}^{\mathcal{S}}(\epsilon, a_{\mathcal{B}}=20\,n_{\mathrm{uc}})$ and $\lim_{a_{\mathcal{B}}\to 0,\epsilon\to 0}\hat{\boldsymbol{\mathcal{X}}}^{\mathcal{S}}(\epsilon, a_{\mathcal{B}})$). All values are given in $[10^{-3}\ \mathrm{J/m^2}]$. Notes on data transformation from [56]: Shenoy used another stress definition with respect to the deformed configuration that was calculated back to the present form. The present stiffness is the second strain derivative of $\gamma\, d\mathrm{A}/d\mathrm{A}_0$ as used in Shenoy's notation. Among Shenoy's two methods, the so-called relaxed values as they correspond to the presented boundary conditions are compared.

$\psi^{\mathrm{c}}_{\mathcal{S}}$ is nearly negligibly small (cf. Tab. 3.7). Even though the influence of the quadratic term rises at a strain amplitude beyond 0.01, the elastic region will be left and, due to plasticity, non-linear effects in the bulk and surface material will occur.

Like for the bulk material (cf. Fig. 3.7), higher order effects in the form of a linear strain dependency of the surface stiffness tensor and, in accordance with the energy formulation, a quadratic dependence of the initial stresses as well as a cubic dependence of the equilibrium energy density, Fig. 3.11 (influence of the constants is given in Tab. 3.6) are observed.

| | $\lim_{\epsilon\to 0} \hat{\boldsymbol{\mathcal{X}}}^{\mathcal{S}}(\epsilon, a_{\mathcal{B}} = 20\, n_{\mathrm{uc}})$ | | | $\lim_{\substack{a_{\mathcal{B}}\to 0 \\ \epsilon\to 0}} \hat{\boldsymbol{\mathcal{X}}}^{\mathcal{S}}(\epsilon, a_{\mathcal{B}})$ | | |
|---|---|---|---|---|---|---|
| Variable | $c^{\mathcal{S}}_{1,i}$ | $c^{\mathcal{S}}_{2,i}$ | $c^{\mathcal{S}}_{3,i}$ | $c^{\mathcal{S}}_{1,i}$ | $c^{\mathcal{S}}_{2,i}$ | $c^{\mathcal{S}}_{3,i}$ |
| $\psi^{\mathcal{S}}_0$ | −9.23E−6 | −4.49E−1 | 8.11E+5 | −7.38E−5 | −1.32E−1 | −7.38E+3 |
| $\sigma^{\mathcal{S}}_{0,11}$ | −9.12E−3 | −1.41E+6 | −3.29E+4 | −7.19E−2 | 8.52E+3 | 1.22E+5 |
| $\sigma^{\mathcal{S}}_{0,22}$ | −2.28E−2 | −1.41E+6 | −1.00E+5 | −3.96E−2 | 8.52E+3 | 1.05E+4 |
| $\sigma^{\mathcal{S}}_{0,12}$ | −2.04E−2 | −6.54E+5 | −1.34E+6 | −1.57E−1 | 1.29E+4 | 2.72E+5 |
| $C^{\mathcal{S}}_{1111}$ | −4.80E+5 | 5.31E+5 | 3.04E+8 | 7.88E+3 | −1.56E+5 | −2.62E+7 |
| $C^{\mathcal{S}}_{2222}$ | −7.37E+5 | 4.00E+6 | 6.95E+8 | 3.74E+3 | 1.07E+6 | −4.52E+8 |
| $C^{\mathcal{S}}_{1212}$ | −3.12E+5 | 2.19E+6 | −1.23E+9 | −1.04E+4 | −7.81E+4 | −6.79E+8 |
| $C^{\mathcal{S}}_{1122}$ | −1.48E+2 | 5.52E+6 | 1.86E+8 | −9.89E+1 | 8.96E+4 | 1.60E+8 |
| $C^{\mathcal{S}}_{1112}$ | 6.55E+5 | −6.31E+5 | −1.46E+9 | −1.30E+4 | −1.21E+5 | 7.90E+7 |
| $C^{\mathcal{S}}_{2212}$ | 6.55E+5 | −4.93E+5 | −1.61E+9 | −1.30E+4 | −7.67E+4 | 7.56E+7 |

**Table 3.6:** Constants of the polynomial fit belonging to the physically and mathematically motivated zero-strain limits ($\lim_{\epsilon\to 0} \hat{\boldsymbol{\mathcal{X}}}^{\mathcal{S}}(\epsilon, a_{\mathcal{B}} = 20\, n_{\mathrm{uc}})$ and $\lim_{a_{\mathcal{B}}\to 0,\epsilon\to 0} \hat{\boldsymbol{\mathcal{X}}}^{\mathcal{S}}(\epsilon, a_{\mathcal{B}})$, cf. Eqs. (3.34) and (3.35)).

| $\varepsilon_{11}$ | $\lvert\psi^{\mathrm{c},\mathcal{S}}_{\mathrm{const}}/\psi^{\mathrm{c}}_{\mathcal{S}}\rvert$ | $\lvert\psi^{\mathrm{c},\mathcal{S}}_{\mathrm{lin}}/\psi^{\mathrm{c}}_{\mathcal{S}}\rvert$ | $\lvert\psi^{\mathrm{c},\mathcal{S}}_{\mathrm{quad}}/\psi^{\mathrm{c}}_{\mathcal{S}}\rvert$ |
|---|---|---|---|
| 0.0001 | 0.99992 | 0.00008 | 3E−8 |
| 0.001 | 0.99919 | 0.00081 | 3E−6 |
| 0.01 | 0.99199 | 0.00808 | 0.00008 |
| 0.1 | 0.93142 | 0.07590 | 0.00733 |

**Table 3.7:** Ratio of the constant, linear and quadratic contributions $\psi^{\mathrm{c},\mathcal{S}}_{\mathrm{const}}$, $\psi^{\mathrm{c},\mathcal{S}}_{\mathrm{lin}}$ and $\psi^{\mathrm{c},\mathcal{S}}_{\mathrm{quad}}$ of the surface Helmholtz free energy density of the prototype constitutive material model computed with parameters of the novel Ritz-type homogenization approach ($\boldsymbol{\mathcal{X}}^{\mathcal{S}}_{a_{\mathcal{B}}=20\, n_{\mathrm{uc}}}$) under simple tension $\boldsymbol{\varepsilon} = \varepsilon_{11}\, \mathbf{e}_1 \otimes \mathbf{e}_1$ for $\varepsilon_{11} \in \{0.0001, 0.001, 0.01, 0.1\}$.

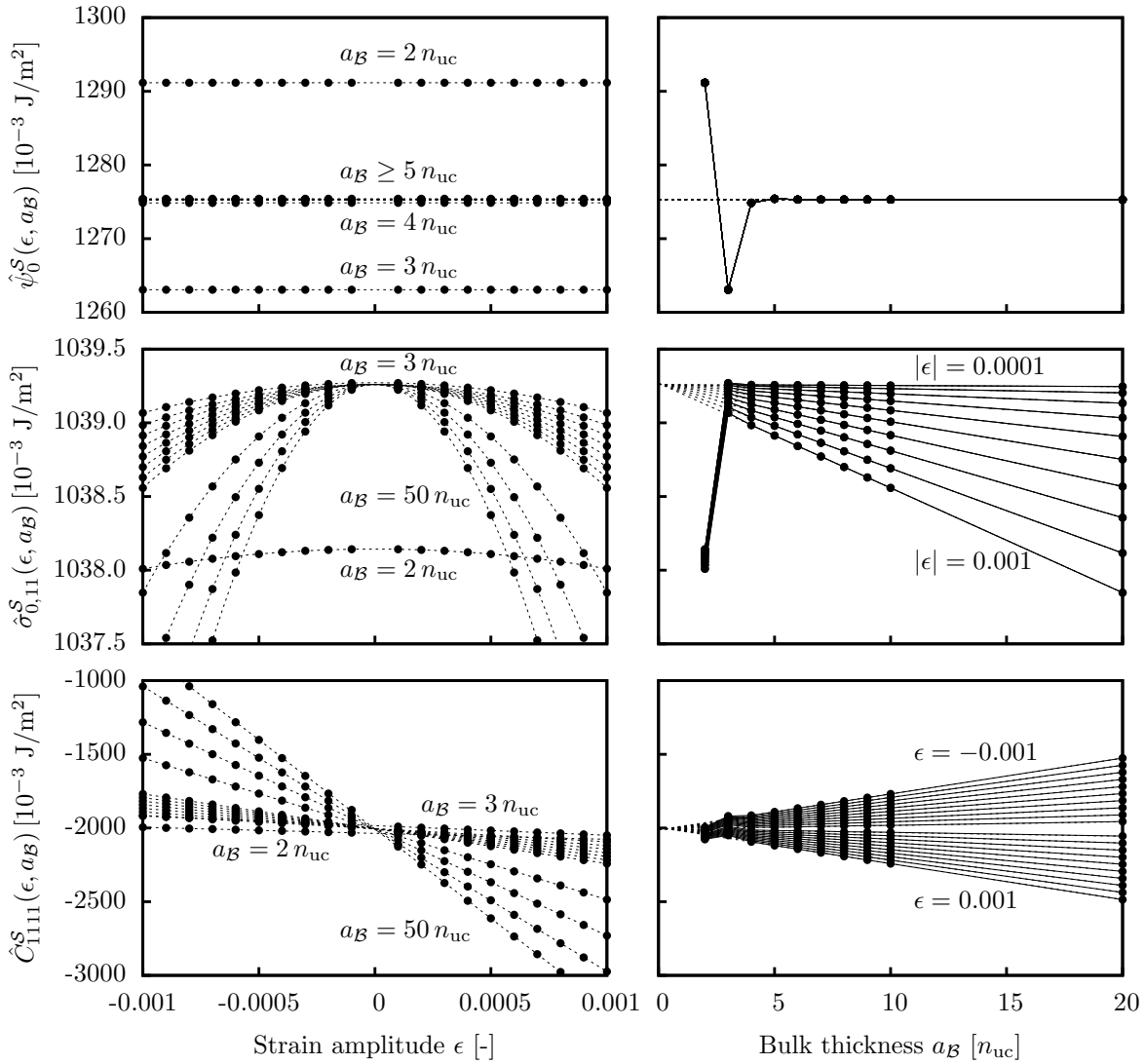


**Figure 3.9:** Two different limits to determine thickness and strain-independent material parameters for the example of initial surface energy density $\psi_0^{\mathcal{S}}$, initial surface stress $\sigma_{0,11}^{\mathcal{S}}$ and surface stiffness $C_{1111}^{\mathcal{S}}$: a third-order zero-strain interpolation (left) and a linear zero-thickness extrapolation (right, extrapolated from states with fully developed surface regions for comparison). The right diagrams are cut at $a_{\mathcal{B}} = 20\,n_{\mathrm{uc}}$ in order to focus on the surface effects. The curves are strongly linear between $a_{\mathcal{B}} = 10\,n_{\mathrm{uc}}$ and $a_{\mathcal{B}} = 50\,n_{\mathrm{uc}}$ (cf. Fig. 3.12). Dashed lines denote either a polynomial fit (left) or linear interpolation (right) and continuous lines connect results belonging to the same strain amplitude. In the left diagrams bulk thicknesses for $a_{\mathcal{B}} \geq 5\,n_{\mathrm{uc}}$ overlap (top) or the thickness rises between $a_{\mathcal{B}} = 3\,n_{\mathrm{uc}}$ and $a_{\mathcal{B}} = 50\,n_{\mathrm{uc}}$ (middle and bottom). In the right diagrams all strain amplitudes overlap (top) or increase (middle and bottom). Positive and negative strains overlap in the right middle.

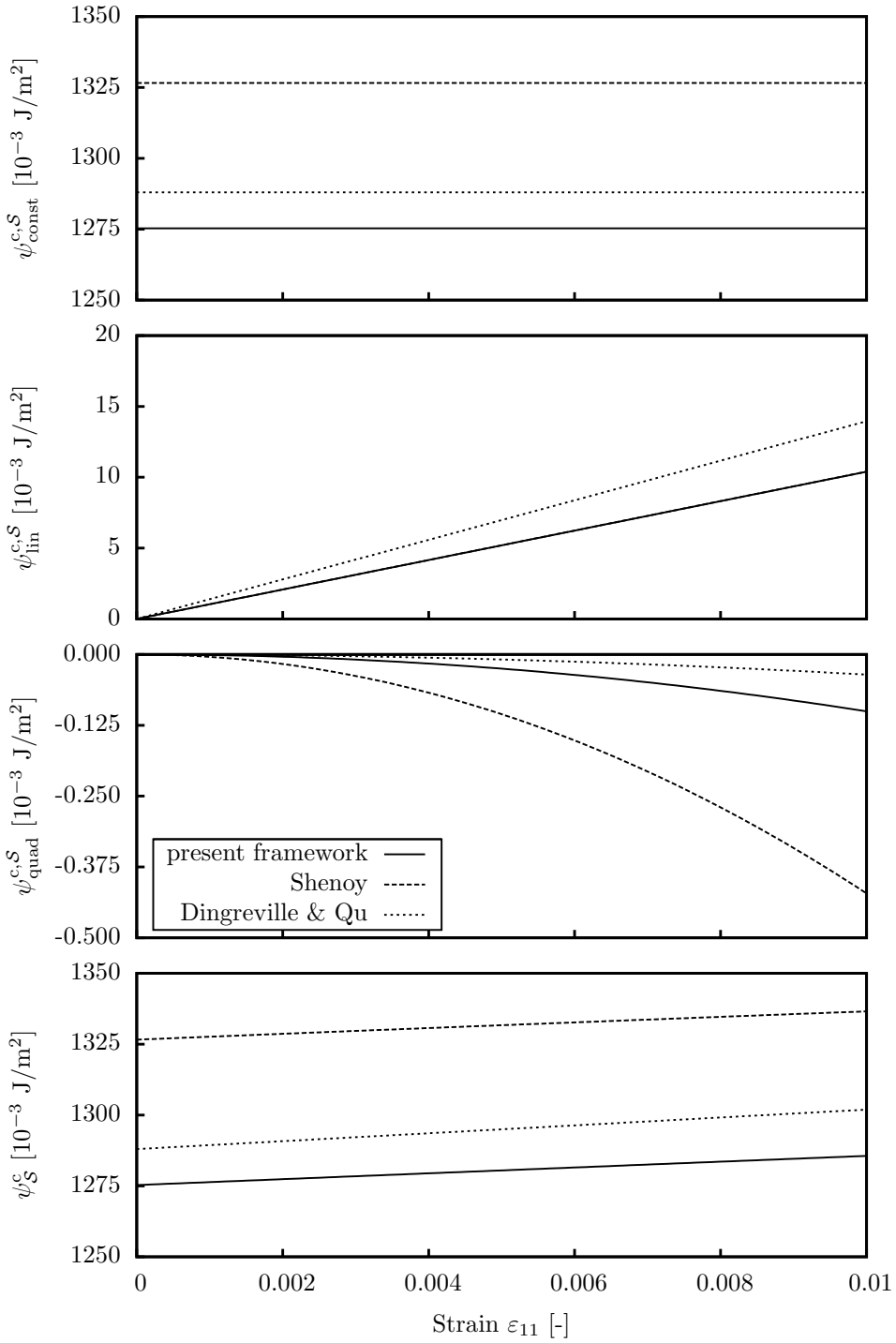


**Figure 3.10:** Constant, linear and quadratic contributions $\psi^{c,\mathcal{S}}_{\text{const}}$, $\psi^{c,\mathcal{S}}_{\text{lin}}$ and $\psi^{c,\mathcal{S}}_{\text{quad}}$ of the surface Helmholtz free energy density $\psi^{c}_{\mathcal{S}}$ of the prototype constitutive continuum material model computed with parameters of the novel Ritz-type homogenization approach ($\boldsymbol{\mathcal{X}}^{\mathcal{S}}_{a_{\mathcal{B}}=20\,n_{\text{uc}}}$), Shenoy [56] and Dingreville & Qu [13] under simple tension $\boldsymbol{\varepsilon} = \varepsilon_{11}\,\mathbf{e}_1 \otimes \mathbf{e}_1$. The lines of the present framework and Shenoy virtually overlap in the middle graph.

A very important factor for the surface model is the error of the bulk approximation that propagates to the surface approximation, $\psi^{\mathrm{c}}_{\mathcal{S}} = \psi^{\mathrm{c}} - \psi^{\mathrm{c}}_{\mathcal{B}}$ + bulk error. Indeed it is obvious that the strain dependence of the surface parameters decreases significantly if the amount of the bulk is reduced. This dependence of the surface material parameters on the bulk thickness is strongly linear (absolute correlation factors $\geq 0.999$ except for $\hat{C}^{\mathcal{S}}_{1122}(a_{\mathcal{B}})$ that can be approximated remarkably well by a constant value of 5381.6 $10^{-3}$ J/m$^2$ $\pm$ 0.0026% standard deviation), see Fig. 3.12. The bulk model thus strongly dictates the data quality used for the surface model in the present example. This propagating error deserves special emphasis in the context of continuum modeling. A fundamental goal is the continuum description of the entire system, including bulk phases as well as their interfaces, surfaces, contact lines etc. The pioneering reference literature [13, 56] provided pure surface parameters, ideally eliminating the bulk contribution already on the molecular scale. As a next step towards continuum applications and because a surface does not exist without a bulk, an approximating bulk model together with the surface model is intentionally incorporated and handled. One application, for instance, is later verification with experiments. However, only few experiments will allow to reproduce the pure bulk deformation state independently and thus eliminate its contribution from the overall energy, e.g., simple uniaxial strain compared to shear of notched plates. Also, the exploration of new materials depends on the variation of both bulk and surface models.

The propagating bulk error can be reduced by three options: a reduced thickness, an improved bulk model or a reduced strain amplitude. Based on the observations, the suitability of the bulk model is recommended to check and to evaluate the propagating error by correlating the strain-dependent deviation with the thickness of the bulk phase. Both tasks can be achieved by the presented framework that allows to implement more general bulk and surface models.

In addition to the validation of the present framework with literature data restricted to results achieved from the physically motivated limit, the applications of the physically and mathematically motivated limits, $\lim_{\epsilon\to 0} \hat{\boldsymbol{\chi}}^{\mathcal{S}}(\epsilon, n_{\mathrm{uc}} = 20)$ and $\lim_{n_{\mathrm{uc}}\to 0,\epsilon\to 0} \hat{\boldsymbol{\chi}}^{\mathcal{S}}(\epsilon, n_{\mathrm{uc}})$, are compared. The mathematically motivated limit is first performed by a linear regression over the bulk thickness $a_{\mathcal{B}}$, and afterwards, a polynomial fit over the strain amplitude $\epsilon$ is executed. Finally, material parameters and constants of the polynomial fits achieved by the application of both limits are shown in Tabs. 3.5 and 3.6. It becomes obvious that both limits lead to identical initial energy densities $\psi^{\mathcal{S}}_0$ and to initial stress tensor components of $\boldsymbol{\sigma}^{\mathcal{S}}_0$. Only the stiffness components differ in a barely considerable range. The visualization of the polynomial fits is illustrated in Fig. 3.11. Although the curves of the mathematically motivated limit ($\hat{\boldsymbol{\chi}}^{\mathcal{S}}(\epsilon, n_{\mathrm{uc}} \to 0)$) seem to be constant, they are still polynomials of third order. It has to be emphasized that these curves correspond to intersections in Figs. 3.9 (right diagrams) and 3.12 with strain amplitudes at $a_{\mathcal{B}} \to 0$ and $a_{\mathcal{B}} = 20\, n_{\mathrm{uc}}$.

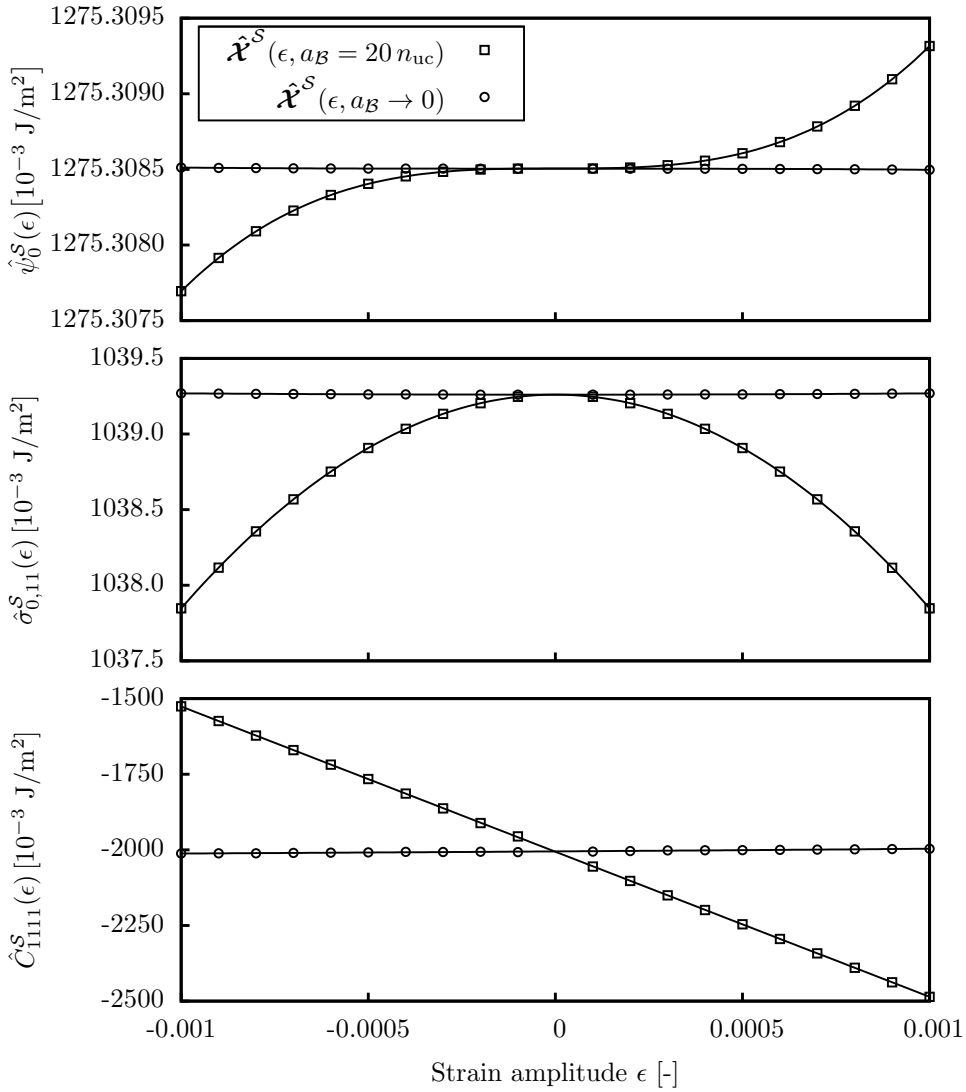


**Figure 3.11:** Results of surface material parameters $\hat{\boldsymbol{\mathcal{X}}}^{\mathcal{S}}(\epsilon, a_{\mathcal{B}} = 20\, n_{\mathrm{uc}})$ (square symbols), $\hat{\boldsymbol{\mathcal{X}}}^{\mathcal{S}}(\epsilon, a_{\mathcal{B}} \to 0)$ (circle symbols) and their polynomial fits (solid lines) as a function of strain amplitude $\epsilon$ for a thickness of $a_{\mathcal{B}} = 20\, n_{\mathrm{uc}}$ and $a_{\mathcal{B}} \to 0$: the equilibrium energy density $\hat{\psi}_0^{\mathcal{S}}(\epsilon)$, the initial stress tensor component $\hat{\sigma}_{0,11}^{\mathcal{S}}(\epsilon)$ and the material stiffness tensor component $\hat{C}_{1111}^{\mathcal{S}}(\epsilon)$.

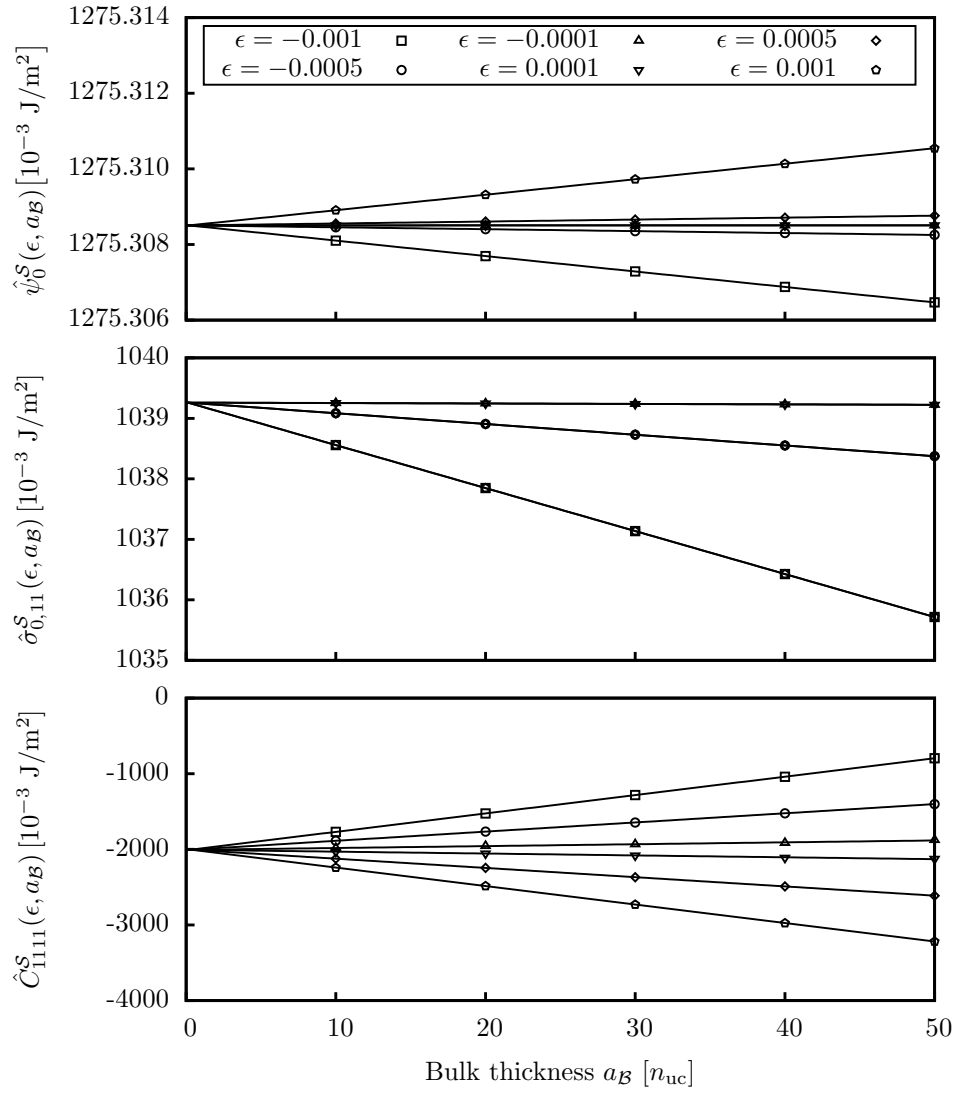


**Figure 3.12:** Results of selected surface material parameters $\hat{\boldsymbol{\mathcal{X}}}^{\mathcal{S}}$ (square symbols) and their polynomial fits (solid lines) as a function of the bulk thickness $a_{\mathcal{B}}$: the equilibrium energy density $\hat{\psi}_0^{\mathcal{S}}$, the initial stress component $\hat{\sigma}_{0,11}^{\mathcal{S}}$ and the material stiffness component $\hat{C}_{1111}^{\mathcal{S}}$. Results are given for various strains, and solid lines denote the respective linear fit. The results of the initial stresses overlap for equal strain amplitudes $|\epsilon|$.

## 3.4 Conclusion

A novel Ritz-type homogenization model has been presented that determines mechanical bulk and surface material parameters from molecular simulations. The material parameters are determined by an energetically consistent comparison of microscopic and macroscopic energies. Existing literature provides surface parameters in the form of energy values and strain derivatives up to second order, allowing to compare the presented framework for a Hooke-like energy approach. The example of copper shows an excellent match with literature data for both bulk and surface properties. Deviations only appear for the surface stiffness parameters, as they already do among existing literature [13, 56]. The presented framework aims at supporting future unification by allowing a broader class of material models that exceed the pure energy derivatives around the relaxed state. This is particularly important for the minimization of a bulk error that affects the data quality used for subsequent surface modeling. For instance, the anharmonic potential inevitably causes a higher-order strain influence that cannot be captured by standard bulk models. The detailed energetic consideration was thus used to evaluate the propagating bulk error in the form of strain dependence compared to a zero-thickness extrapolation under consideration of fully developed surface boundaries.

Future investigations will focus on the application of the presented framework to other material classes, e.g., non-linear, dissipative or plastic surfaces. The Ritz-type homogenization approach guarantees a thermodynamically consistent implementation of modern material formulations, e.g., in the form of invariant-based potentials. This extension shall enrich continuum surface modeling the same way atomistic potentials already provide for molecular descriptions.

# 4 Atomistic-to-continuum homogenization approach suitable for thermoelastic material

The thermoelastic properties of continua are defined by their underlying atomistic structure. A general homogenization framework for the determination of such properties based on molecular dynamics is presented. The method is variationally consistent and is based on the principle of energy equivalence. More explicitly speaking, the Ritz-type homogenization approach introduced in Ch. 3 is extended to thermomechanics. The atomistic and continuum models consist of periodic RVEs as illustrated in Fig. 4.1. The system is assumed to be adiabatic and has no internal heat source.

This chapter is structured as follows. Sec. 4.1 represents the determination of the atomistic and continuum energies in connection with the underlying constitutive prototype material model. Subsequently, the extended Ritz-type homogenization approach for thermoelastic materials is introduced in Sec. 4.2. Afterwards, a numerical example using copper as material is shown in Sec. 4.3. Sec. 4.4 closes the chapter with a short conclusion.

## 4.1 Constitutive frameworks

### 4.1.1 Atomistic scale

The atomistic body $\Omega^{\mathrm{a}}$ of interest is chosen to be an RVE with periodic boundary conditions, containing $n_{\mathrm{atoms}}$ atoms at positions $\mathbf{x}_1, \ldots, \mathbf{x}_{n_{\mathrm{atoms}}}$ (cf. Fig. 4.1). The total atomistic energy within this RVE $\Omega^{\mathrm{a}}$ is determined by the use of Nosé-Hoover-style time integration of non-Hamiltonian equations of motion. They are designed in order to describe positions and velocities of particles within a closed system. Thermostatting and barostatting allow a temperature and pressure regulation of the system. In this work, the equations of motion introduced by Shinoda et al. [57] in combination with the hydrostatic equations of Martyna et al. [36] and the strain energy derived by Parrinello and Rahman [46] are applied by the use of the molecular dynamics code LAMMPS

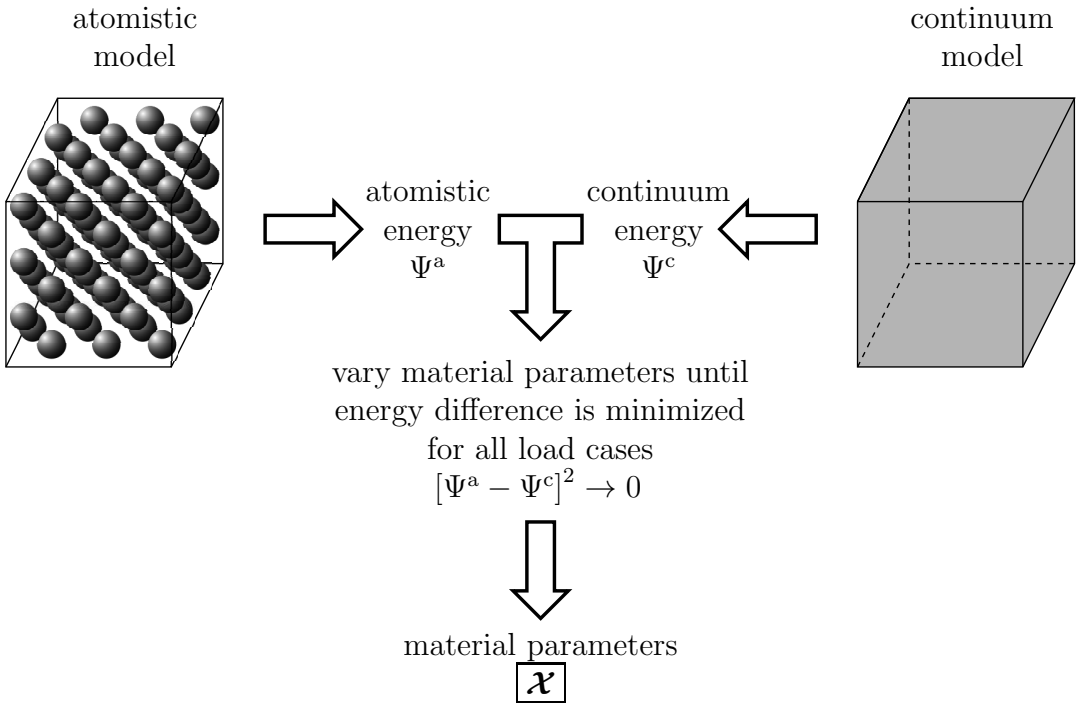


**Figure 4.1:** Sketch of the representative atomistic volume element $\Omega^{\mathrm{a}}$ (left) and the continuum representative volume element $\Omega^{\mathrm{c}}$ (right) as used to obtain the material parameters $\boldsymbol{\mathcal{X}}$ by the Ritz method, i.e., minimizing the difference between the atomistic energy $\Psi^{\mathrm{a}}$ and the continuum energy $\Psi^{\mathrm{c}}$.

(cf. [11]). According to [57], these equations have the form:

$$\dot{\mathbf{x}}_\alpha = \frac{\mathbf{p}_\alpha}{m_\alpha} + \frac{\mathbf{p}_{\mathrm{g}} \cdot \mathbf{x}_\alpha}{W_{\mathrm{g}}}, \tag{4.1}$$

$$\dot{\mathbf{p}}_\alpha = \mathbf{f}_\alpha - \frac{\mathbf{p}_{\mathrm{g}} \cdot \mathbf{p}_\alpha}{W_{\mathrm{g}}} - \frac{1}{N_{\mathrm{f}}} \frac{\mathrm{tr}\big(\mathbf{p}_{\mathrm{g}}\big)}{W_{\mathrm{g}}} \mathbf{p}_\alpha - \frac{p_\xi}{Q} \mathbf{p}_\alpha, \tag{4.2}$$

$$\dot{\mathbf{h}} = \frac{\mathbf{p}_{\mathrm{g}} \cdot \mathbf{h}}{W_{\mathrm{g}}}, \tag{4.3}$$

$$\dot{\mathbf{p}}_{\mathrm{g}} = V \left[\mathbf{P}_{\mathrm{int}} - P_{\mathrm{ext}}\, \mathbf{I}\right] - \mathbf{h} \cdot \boldsymbol{\Sigma} \cdot \mathbf{h}^{\mathrm{T}} + \left[\frac{1}{N_{\mathrm{f}}} \sum_{\alpha=1}^{n_{\mathrm{atoms}}} \frac{\mathbf{p}_1^2}{m_\alpha}\right] \mathbf{I} - \frac{p_{\xi_1}}{Q_1} \mathbf{p}_{\mathrm{g}}, \tag{4.4}$$

$$\dot{\xi}_k = \frac{p_{\xi_k}}{Q_k} \quad \text{for } k = 1, \ldots, M, \tag{4.5}$$

$$\dot{p}_{\xi_1} = \sum_{\alpha=1}^{n_{\mathrm{atoms}}} \frac{\mathbf{p}_\alpha^2}{m_\alpha} + \frac{1}{W_{\mathrm{g}}}\, \mathrm{tr}\big(\mathbf{p}_{\mathrm{g}}^{\mathrm{T}} \cdot \mathbf{p}_{\mathrm{g}}\big) - \big[N_{\mathrm{f}} + d^2\big]\; k_{\mathrm{B}}\, \Theta - p_{\xi_1} \frac{p_{\xi_2}}{Q_2}, \tag{4.6}$$

$$\dot{p}_{\xi_k} = \left[\frac{p_{\xi_{k-1}}^2}{Q_{k-1}} - k_{\mathrm{B}}\, \Theta\right] - p_{\xi_k} \frac{p_{\xi_{k+1}}}{Q_{k+1}} \quad \text{for } k = 2, \ldots, M-1 \quad \text{and} \tag{4.7}$$

$$\dot{p}_{\xi_M} = \frac{p_{\xi_{M-1}}}{Q_{M-1}} - k_{\mathrm{B}}\, \Theta, \tag{4.8}$$

with

$$\boldsymbol{\Sigma} = \mathbf{h}_0^{-1} \cdot [\mathbf{t} - P_{\text{ext}}\, \mathbf{I}] \cdot \mathbf{h}_0^{-\text{T}}, \tag{4.9}$$

where $\mathbf{x}_\alpha$ denotes the position, $\mathbf{p}_\alpha$ is the momentum and $m_\alpha$ is the mass of particle $\alpha$. $\mathbf{p}_\text{g}$ is the modularly invariant form of the cell momenta of the barostat (cf. [39]). It is a second order tensor that modulates the particle velocities to adapt to the prescribed pressure boundary condition. $W_\text{g}$ is an associated material parameter. The cell momenta $\mathbf{p}_\text{g}$ can be understood as a scaling matrix in order to the represent pressure and $W_\text{g}$ as its correction value. $\xi_k$ describes the thermostat variable, $p_{\xi_k}$ is the conjugated momentum and $Q_k$ is the material parameter of the $k$th thermostat of the Nosé-Hoover chain (cf. [35]). Similar to the barostat, the conjugated momentum $p_{\xi_k}$ acts as the temperature controlling of the cell and $Q_k$ is the correction value. In general, the correction values, $W_\text{g}$ and $Q_k$, serve to fulfill the balance laws after their violation due to pressure or temperature controlling and they are used to tune the frequency at which these variables fluctuate (cf. [37]). The constant $N_\text{f} (= 3\, n_\text{atoms})$ denotes the number of system degrees of freedom, $d$ is the dimension of the system and $k_\text{B}$ is the Boltzmann constant. Volume $V$ is defined by the determinate of the cell matrix's edge vectors $\mathbf{a}_1, \mathbf{a}_2, \mathbf{a}_3$: $V = \det \mathbf{h}$, while $\mathbf{h} = (\mathbf{a}_1, \mathbf{a}_2, \mathbf{a}_3)$ can be expressed as a column matrix and resembles the deformation gradient $\mathbf{F}$. Variable $\Theta$ is the external temperature, $\mathbf{t}$ denotes the stress applied to the system, $P_\text{ext}$ is the external hydrostatic pressure and $\mathbf{P}_\text{int}$ is the internal pressure defined as

$$\mathbf{P}_\text{int} = \frac{1}{V} \left[ \sum_{\alpha=1}^{n_\text{atoms}} \frac{\mathbf{p}_\alpha \otimes \mathbf{p}_\alpha}{m_\alpha} + \sum_{\alpha=1}^{n_\text{atoms}} \mathbf{f}_\alpha \otimes \mathbf{x}_\alpha - \frac{\partial \phi(\mathbf{x}, \mathbf{h})}{\partial \mathbf{h}} \cdot \mathbf{h}^\text{T} \right], \tag{4.10}$$

where $\phi$ denotes the applied potential. For that purpose, the Mishin potential [41] for copper is applied. $\mathbf{f}_\alpha$ denotes the force of particle $\alpha$ and is defined as $\mathbf{f}_\alpha = \partial \phi(\mathbf{x}, V) / \partial \mathbf{x}_\alpha$ (cf. [36]). Finally, the above equations of motion, Eqs. (4.1) – (4.8), lead to the conserved quantity (a Hamiltonian that is extended by the numerical implementations of prescribed pressure and temperature)

$$\begin{aligned} \mathcal{H} = \underbrace{\sum_{\alpha=1}^{n_\text{atoms}} \frac{\mathbf{p}_\alpha^2}{2\, m_\alpha}}_{\text{I}} + \underbrace{\phi(\mathbf{x}, \mathbf{h})}_{\text{II}} + \underbrace{P_\text{ext} \det \mathbf{h}}_{\text{III}} + \underbrace{\frac{1}{2} \operatorname{tr}(\boldsymbol{\Sigma} \cdot \mathbf{G})}_{\text{IV}} + \underbrace{\frac{1}{2\, W_\text{g}} \operatorname{tr}\!\left(\mathbf{p}_\text{g}^\text{T} \cdot \mathbf{p}_\text{g}\right)}_{\text{V}} \\ + \underbrace{\left[N_\text{f} + d^2\right] k_\text{B}\, \Theta\, \xi_1}_{\text{VI}} + \underbrace{\sum_{k=2}^{M} k_\text{B}\, \Theta\, \xi_k}_{\text{VII}} + \underbrace{\sum_{k=1}^{M} \frac{p_{\xi_k}^2}{2\, Q_k}}_{\text{VIII}}, \end{aligned} \tag{4.11}$$

where $\mathbf{G} = \mathbf{h}^\text{T} \cdot \mathbf{h}$ denotes the metric tensor. The conserved quantity is split into eight terms marked by Roman numerals. Term I describes the kinetic energy of all particles.

Term II employs only the atomic potential. Subsequently, term III contains the external pressure. After that, term IV describes the stress work. Term V is the contribution from the pressure boundary conditions to deform the cell uniformly. Terms VI, VII and VIII denote the temperature influence from the Nosé-Hoover chain and its correction value.

The time integration schemes closely follow the time-reversible measure-preserving Verlet and rRESPA integrators derived by Tuckerman et al. [67]. Therein, the constraints of the time integration scheme are given. They are divided into different ensembles: the canonical ($NVT$), isothermal-isobaric ($N\mathbf{t}T$) and isenthalpic ($N\mathbf{t}h$) ensembles. The abbreviation of each ensemble ($NVT$, $N\mathbf{t}T$ and $N\mathbf{t}h$) describes the fixed quantities ($N$, $V$, $T$, $\mathbf{t}$, or $h$). $N$ ($= n_{\text{atoms}}$) denotes the number of atoms, $V$ is the volume, $T$ is the temperature $\Theta$, $\mathbf{t}$ is the stress tensor applied to the system and $h$ stands for the enthalpy. For instance, the canonical ensemble fixes the number of atoms $N$, the volume $V$ and the temperature $\Theta$ in the control volume defined by the RVE $\Omega^{\text{a}}$. Controlling the volume is synonymous with the macroscopic deformation of the RVE. Other quantities, e.g., the stress tensor $\mathbf{t}$, are free and will be determined at each time step. The $NVT$ and $N\mathbf{t}T$ ensembles allow a temperature regulation, the $N\mathbf{t}T$ and $N\mathbf{t}h$ ensembles allow a regulation of the stress tensor being synonymous with the continuum mechanics first Piola-Kirchhoff stress tensor $\mathbf{P}$.

Analogous to Sec. 3.1.1, the total potential equilibrium energy depending on the deformation $\bar{\mathbf{F}}$ and the temperature $\Theta$ of the atomistic body $\Omega^{\text{a}}$ is obtained as

$$\Psi^{\text{a}}_{\text{eq}}\big(\bar{\mathbf{F}},\Theta\big) = \mathcal{H}\big(\mathbf{x}_1,\ldots,\mathbf{x}_{n_{\text{atoms}}},\bar{\mathbf{F}},\Theta\big)\,. \tag{4.12}$$

For a detailed study, the interested reader is referred to Tadmor & Miller [64].

## 4.1.2 Continuum scale

### 4.1.2.1 Fundamentals

The internal energy density of a material point in the continuum description is denoted as $U^{\text{c}}(\mathbf{F},\Theta)$. It depends on the deformation gradient $\mathbf{F}$ and the temperature field $\Theta$. According to Sec. 2.3.3, the internal energy is defined by the Legendre transformation as a function of the Helmholtz free energy density $\psi^{\text{c}}$ and the dual variables $\Theta$ and $N$ as

$$U^{\text{c}}(\mathbf{F},N(\Theta)) = \psi^{\text{c}}(\mathbf{F},\Theta) + \Theta\, N. \tag{4.13}$$

Using its derivative with respect to the temperature

$$\frac{\partial U^{\text{c}}}{\partial\Theta} = \frac{\partial\psi^{\text{c}}}{\partial\Theta} + N = 0 \quad\Leftrightarrow\quad N(\Theta) = -\frac{\partial\psi^{\text{c}}}{\partial\Theta}, \tag{4.14}$$

one obtains

$$U^{\mathrm{c}}(\mathbf{F},\Theta) = \psi^{\mathrm{c}}(\mathbf{F},\Theta) - \Theta\,\frac{\partial \psi^{\mathrm{c}}}{\partial \Theta}. \tag{4.15}$$

A prototype constitutive material model for $\psi^{\mathrm{c}}$ is described in the following section.

The total equilibrium energy is achieved by integrating the internal energy density $U^{\mathrm{c}}$ over the undeformed body $\Omega^{\mathrm{c}}$ for a relaxed state (equilibrium). Finally, it is formulated as a minimum energy considering the deformation fields $\mathbf{x}-\mathbf{X}$ being continuously differentiable for the prescribed deformation field $\bar{\mathbf{F}}$ and the prescribed temperature field $\bar{\Theta}$ of the periodic cell:

$$\Psi^{\mathrm{c}}\big(\bar{\mathbf{F}},\bar{\Theta}\big) = \min_{\substack{\text{cont. diff. } \mathbf{x} \\ \text{compatible with } \bar{\mathbf{F}},\bar{\Theta}}} \left\{ \int_{\Omega} U^{\mathrm{c}}(\mathbf{F}(\mathbf{X})\,,\Theta(\mathbf{X}))\,\mathrm{d}V \right\}. \tag{4.16}$$

#### 4.1.2.2 Prototype material model

In what follows, a thermoelastic Helmholtz free energy $\psi(\mathbf{F},\Theta)$ depending on the deformation gradient $\mathbf{F}$ and the temperature $\Theta$ is chosen, such as

$$\psi(\mathbf{F},\Theta) = W\big(\bar{\mathbf{C}}\big) + U(J) + M(J,\Theta) + T(\Theta) + \psi_0 \tag{4.17}$$

with

$$\bar{\mathbf{C}} = J^{-2/3}\,\mathbf{F}^{\mathrm{T}}\cdot\mathbf{F}, \tag{4.18}$$

where $W\big(\bar{\mathbf{C}}\big)$ denotes the purely mechanical deviatoric material response, $U(J)$ the purely mechanical volumetric material response, $M(J,\Theta)$ the thermomechanically coupled potential, $T(\Theta)$ the purely thermal potential and $\psi_0$ the ground state energy density at 0 K. The different energy contributions read

$$W\big(\bar{\mathbf{C}}\big) = \frac{1}{2}\,\mu\big[\operatorname{tr}\bar{\mathbf{C}} - 3\big]\,, \tag{4.19}$$

$$U(J) = \frac{1}{2}\,\kappa\left[\frac{1}{2}\big[J^2-1\big] - \log J\right], \tag{4.20}$$

$$M(J,\Theta) = [\Theta-\Theta_0]\left[-3\,\alpha_0\,\frac{\partial U}{\partial J}\right] \quad \text{and} \tag{4.21}$$

$$T(\Theta) = c_0\left[[\Theta-\Theta_0] - \Theta\log\frac{\Theta}{\Theta_0}\right]. \tag{4.22}$$

Therein, $\kappa$ and $\mu$ represent the bulk and shear modulus, $\alpha_0$ the thermal expansion coefficient, $c_0$ the thermal heat capacity and $\Theta_0$ the reference temperature. These parameters are also the material parameters to be optimized by the Ritz-type homogenization ap-

proach and they are summarized in the set of material parameters $\boldsymbol{\mathcal{X}}$:

$$\boldsymbol{\mathcal{X}} = \{\psi_0, \kappa, \mu, \alpha_0, c_0\} = \{\mathcal{X}_1, \ldots, \mathcal{X}_5\}\,. \tag{4.23}$$

In order to obtain the internal energy density $U^{\mathrm{c}}$, the derivative of the Helmholtz free energy with respect to the temperature is required:

$$\frac{\partial \psi^{\mathrm{c}}}{\partial \Theta} = -\frac{3}{2}\,\alpha_0\,\kappa\left[J - \frac{1}{J}\right] - c_0\,\ln\!\left(\frac{\Theta}{\Theta_0}\right). \tag{4.24}$$

Finally, the internal energy density has the form

$$\begin{aligned} U^{\mathrm{c}}(\mathbf{F}, \Theta) = \frac{\mu}{2}\left[\left[J^{-2/3}\,\mathbf{F}^{\mathrm{T}}\cdot\mathbf{F}\right] : \mathbf{I} - 3\right] + \frac{\kappa}{2}\left[\frac{1}{2}\left[J^2 - \frac{1}{J}\right] - \ln J\right] \\ + \frac{3}{2}\,\Theta_0\,\alpha_0\,\kappa\left[J - \frac{1}{J}\right] + c_0\,[\Theta - \Theta_0] + \psi_0. \end{aligned} \tag{4.25}$$

#### 4.1.2.3 Numerical implementation

According to Sec. 2.5, the implementation of the constitutive prototype material model into the finite element framework requires the global residual vector $\mathbf{R}$ and the global tangent matrix $\mathbf{K}$. Due to the assumption of an adiabatic system and the absence of heat sources, i.e., $\mathbf{H} = \mathbf{0}$ and $R = 0$, the local residual vector reduces to $\mathbf{R}_e^a = [\mathbf{f}_{\boldsymbol{\varphi},\mathrm{int}}\; f_{\Theta,\mathrm{int}}]^{\mathrm{T}}$. Thus, the implementation is based on Eqs. (2.111), (2.114), (2.125) – (2.128) only. Therefore, the first Piola-Kirchhoff stress tensor $\mathbf{P} = \partial\psi^{\mathrm{c}}/\partial\mathbf{F}$ as well as its derivatives with respect to the deformation gradient and the temperature, i.e. $\mathrm{d}\mathbf{P}/\mathrm{d}\mathbf{F}$ and $\mathrm{d}\mathbf{P}/\mathrm{d}\Theta = \partial\mathbf{P}/\partial\Theta$, are required.

The first derivative of the Helmholtz free energy with respect to the deformation $\mathbf{P} = \partial\psi^{\mathrm{c}}/\partial\mathbf{F}$ reads

$$\begin{aligned} \mathbf{P} = \left[-\frac{1}{3}\,\mu\,J^{-\frac{2}{3}}[\mathbf{F} : \mathbf{F}] + \frac{1}{2}\,\kappa\big[J^2 - 1\big] + [\Theta - \Theta_0]\left[-\frac{3}{2}\,\alpha_0\,\kappa\left[J + \frac{1}{J}\right]\right]\right]\mathbf{F}^{-\mathrm{T}} \\ + \mu\,J^{-\frac{2}{3}}\,\mathbf{F}. \end{aligned} \tag{4.26}$$

Finally, the derivatives of $\mathbf{P}$ with respect to the deformation gradient and the tempera-

ture are expressed as

$$\begin{aligned}\frac{\partial \mathbf{P}}{\partial \mathbf{F}} &= -\frac{2}{3}\,\mu\, J^{-2/3}\,\mathbf{F}^{-\mathrm{T}}\otimes\mathbf{F} + \mu\, J^{-2/3}\,\mathbf{I}\,\overline{\otimes}\,\mathbf{I} - \frac{2}{3}\,\mu\, J^{-2/3}\,\mathbf{F}\otimes\mathbf{F}^{-1} \\ &\quad -\left[-\frac{1}{3}\,\mu\, J^{-2/3}\,\mathbf{F}:\mathbf{F} + \frac{1}{2}\,\kappa\left[J^2-1\right] + [\Theta-\Theta_0]\left[-\frac{3}{2}\,\alpha_0\,\kappa\left[J+\frac{1}{J}\right]\right]\right]\mathbf{F}^{-\mathrm{T}}\,\underline{\otimes}\,\mathbf{F}^{-1} \\ &\quad +\left[\frac{2}{9}\,\mu\, J^{1/3}\,\mathbf{F}:\mathbf{F} + \kappa\, J^2 + [\Theta-\Theta_0]\left[-\frac{3}{2}\,\alpha_0\,\kappa\left[J-\frac{1}{J}\right]\right]\right]\mathbf{F}^{-\mathrm{T}}\otimes\mathbf{F}^{-1}, \qquad (4.27)\\ \frac{\partial \mathbf{P}}{\partial \Theta} &= -\frac{3}{2}\,\alpha_0\,\kappa\left[J+\frac{1}{J}\right]\mathbf{F}^{-\mathrm{T}}. \qquad (4.28)\end{aligned}$$

# 4.2 A Ritz-type homogenization approach: material parameter transition from the atomistic model to the continuum model

## 4.2.1 Ritz's method applied to thermoelastic materials

The novel Ritz-type approach introduced in Sec. 3.2 is applied to a thermoelastic material in order to identify the set of material parameters $\boldsymbol{\mathcal{X}}$ of the constitutive prototype material model. Again, the Ritz-type homogenization approach minimizes the energy residuum under a certain set of load cases applied to the periodic RVE. Each load case $(i)$ is described by means of a macroscopic deformation gradient $\bar{\mathbf{F}}^{(i)}$ and a temperature field $\bar{\Theta}^{(i)}$ for $1 \leq i \leq n_{\mathrm{lc}}$, where $n_{\mathrm{lc}}$ is the total number of applied load cases. The energy residuum $\mathcal{R}$ is the sum of the energy difference between the atomistic and continuum model over all load cases and is defined as

$$\mathcal{R} := \sum_{i=1}^{n_{\mathbf{lc}}} \left[\Psi^{\mathrm{c}} - \Psi^{\mathrm{a}}\right]^2\Big|_{\bar{\mathbf{F}}^{(i)},\bar{\Theta}^{(i)}} \rightarrow \min. \qquad (4.29)$$

Therein, the energy of the continuum model depends on the set of material parameters summarized in $\boldsymbol{\mathcal{X}}$ (see Eq. (4.23)), i.e. $\Psi^{\mathrm{c}} = \Psi^{\mathrm{c}}(\boldsymbol{\mathcal{X}})$. Thus, the optimization problem considered for the determination of material parameters reads

$$\boldsymbol{\mathcal{X}} = \arg\min_{\boldsymbol{\mathcal{X}}} \mathcal{R}(\boldsymbol{\mathcal{X}}). \qquad (4.30)$$

## 4.2.2 Simulation details

A cubic homogeneous RVE $\Omega^{\mathrm{a}}$ with periodic boundaries is studied to determine the material parameters. It covers $10\,n_{\mathrm{uc}}$ (unit cells, see Sec. 3.1.1) in each spatial direction and consists of a single domain with 4.000 atoms, see Fig. 4.2. Relaxation at the desired temperature $\Theta_0$ is implemented by the use of the isothermal-isobaric $(N\mathbf{t}T)$ ensemble

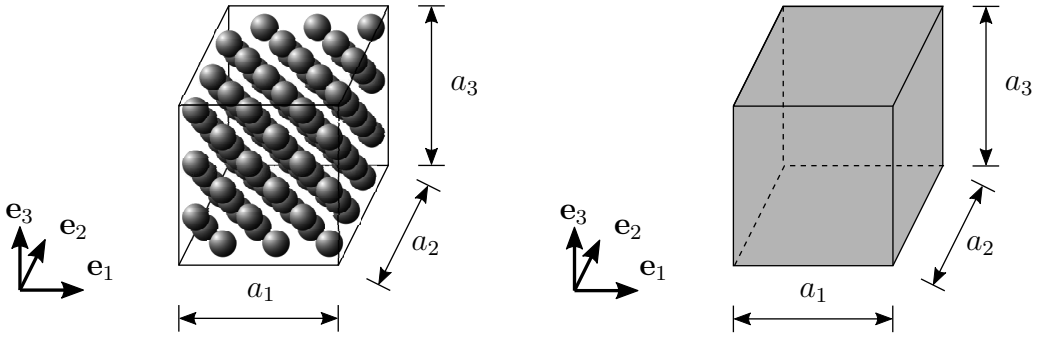


**(a)** Illustration of the relaxed initial RVE $\Omega^{\mathrm{a}}$ of the atomistic model.

**(b)** Illustration of the relaxed initial RVE $\Omega^{\mathrm{c}}$ of the continuum model.

**Figure 4.2:** Periodic cells of the atomistic (a) and continuum model (b) including a single bulk domain. Deviating from the simulations the figure shows an RVE with $a_1 = a_2 = a_3 = 3\,n_{\mathrm{uc}}$.

under zero-load. Subsequently, the relaxed RVE $\Omega^{\mathrm{a}}$ with edge lengths $a_i$ constitutes the initial configuration for the following load cases of the atomistic and the continuum model. Concerning the molecular dynamics model, load cases based on relaxation are performed by the canonical ($NVT$) ensemble.

Although at least five load cases are required to determine the set of five material parameters $\mathcal{X}$, six load cases are used. The macroscopic deformation gradient $\bar{\mathbf{F}}^{(i)}$ is expressed as

$$\bar{\mathbf{F}}^{(i)} = \mathbf{I} + \epsilon\,\Delta\bar{\mathbf{F}}^{(i)}, \tag{4.31}$$

where $\epsilon$ denotes the strain amplitude and $\Delta\bar{\mathbf{F}}^{(i)}$ is the deformation type characterized by simple volumetric expansion or shear. The macroscopic temperature field $\bar{\Theta}^{(i)}$ has the form

$$\bar{\Theta}^{(i)} = \Theta_0 + \Delta\bar{\Theta}^{(i)}. \tag{4.32}$$

Therein, $\Theta_0$ denotes the reference temperature (see Sec. 4.1.2.2) and $\Delta\bar{\Theta}^{(i)}$ is the thermal heating of the load case $(i)$. A detailed overview over the types of load cases can be found in Tab. 4.1. For this study, two strain amplitudes and three initial temperatures are investigated: $\boldsymbol{\epsilon} = \{0.002, 0.01\}$ and $\boldsymbol{\Theta}_0 = \{1, 273, 293\}$ (in K) with a thermal heating $\Delta\bar{\Theta}^{(i)}$ of 10 K.

## 4.3 Results and Discussion

Tab. 4.2 shows the thermoelastic material parameters determined by the Ritz-type homogenization approach in comparison to literature data for copper. Comparative values for the initial energy density have not been found and are thus only compared to the results presented in Sec. 3.3.2 for atomistic simulations based on molecular statics and

| $i$ | $\Delta\bar{\mathbf{F}}^{(i)}$ | $\Delta\bar{\Theta}^{(i)}$ | ensemble |
|---|---|---|---|
| 1 | $\mathbf{0}$ | 0 | $N\mathbf{t}T$ |
| 2 | $\mathbf{e}_1 \otimes \mathbf{e}_1 + \mathbf{e}_2 \otimes \mathbf{e}_2 + \mathbf{e}_3 \otimes \mathbf{e}_3$ | 0 | $NVT$ |
| 3 | $2\left[\mathbf{e}_1 \otimes \mathbf{e}_1 + \mathbf{e}_2 \otimes \mathbf{e}_2 + \mathbf{e}_3 \otimes \mathbf{e}_3\right]$ | 0 | $NVT$ |
| 4 | $\mathbf{e}_1 \otimes \mathbf{e}_2 + \mathbf{e}_1 \otimes \mathbf{e}_3 + \mathbf{e}_2 \otimes \mathbf{e}_3$ | 0 | $NVT$ |
| 5 | $\mathbf{0}$ | 10 | $NVT$ |
| 6 | $\mathbf{e}_1 \otimes \mathbf{e}_1 + \mathbf{e}_2 \otimes \mathbf{e}_2 + \mathbf{e}_3 \otimes \mathbf{e}_3$ | 10 | $NVT$ |

**Table 4.1:** Types of deformation $\Delta\bar{\mathbf{F}}^{(i)}$, thermal heating $\Delta\bar{\Theta}^{(i)}$ (in [K]) and the chosen ensemble belonging to the macroscopic deformation gradient $\bar{\mathbf{F}}^{(i)}(\epsilon) = \mathbf{I} + \epsilon\,\Delta\bar{\mathbf{F}}^{(i)}$ (cf. Eq. (4.31)) and the macroscopic temperature field $\bar{\Theta}^{(i)} = \Theta_0 + \Delta\bar{\Theta}^{(i)}$ (cf. Eq. (4.32)) to determine the parameters of the continuum model at the macroscopic scale.

a different pair-to-pair potential. However, the deviation is very small (2.1%) for a reference temperature of $\Theta_0 = 1\,\mathrm{K}$. Bulk and shear modulus deviate to a larger extent from the literature data, i.e., between 0.8% and 12.4% for the bulk modulus and 8.5% to 94.0% for the shear modulus. Without considering the temperature at $\Theta_0 = 1\,\mathrm{K}$, the thermal heat expansion coefficient deviates up to 12.9%. Eventually, the thermal heat capacity matches the literature data very closely with a maximum deviation of 2.0%.

| $\epsilon$ | $\Theta_0$ | $\kappa$ | $\mu$ | $\alpha_0$ | $c_0$ | $\psi_0$ |
|---|---|---|---|---|---|---|
| Ref. [47] | | 140 | 48 | 16.5 | 3.44 | |
| Ref. [17] | | 137.8 | | 17.0 | 3.45 | |
| 0.002 | 1 | 136.7 | 76.4 | 0.1 | 3.51 | -47.0 |
| 0.002 | 273 | 136.7 | 93.1 | 14.8 | 3.45 | -46.4 |
| 0.002 | 293 | 122.6 | 52.1 | 18.6 | 3.44 | -46.4 |
| 0.01 | 1 | 129.7 | 76.8 | 0.9 | 3.51 | -47.0 |
| 0.01 | 273 | 126.6 | 74.9 | 17.0 | 3.46 | -46.4 |
| 0.01 | 293 | 125.7 | 73.9 | 18.6 | 3.44 | -46.4 |

**Table 4.2:** Results of the material parameters determined by the Ritz-type homogenization approach for different strain amplitudes $\epsilon$ and temperatures $\Theta_0$ in comparison to literature data for copper. In [47] and [17] only the specific thermal heat capacity $\bar{c} = 384.4\,\mathrm{J/(K\,kg)}$ or $\bar{c} = 385\,\mathrm{J/(K\,kg)}$ and the density $\rho = 8.96\,\mathrm{kg/m^3}$ are given. Thus, the thermal heat capacity is calculated as $c_0 = \bar{c}\,\rho = 3.4442\,\mathrm{MPa/K}$ or $c_0 = \bar{c}\,\rho = 3.4496\,\mathrm{MPa/K}$, respectively. $\Theta_0$ in [K], $\kappa$ and $\mu$ in [GPa], $\alpha_0$ in $[10^{-6}\,\mathrm{K}]$, $c_0$ in [MPa/K] and $\psi_0$ in $[10^9\,\mathrm{J/m^3}] = [1\,\mathrm{GPa}]$.

## 4.4 Conclusion

An extended Ritz-type homogenization approach for thermoelastic applications has been presented. For that purpose, the atomistic simulations are extended by using the canonical and the isothermal-isobaric ensemble. Within the continuum model, the standard

Hooke-type material model has been replaced by a thermoelastic prototype constitutive material model. Some of the identified thermoelastic material parameters are very close to the literature data, other parameters deviated in a large scale and they seem to be inconsistently.

# 5 Designing material models for surfaces based on bulk constitutive models

Motivated by a strong coupling between bulk and surface physics, two approaches to derive surface models from a three-dimensional deformation state are presented: projection and relaxation. In contrast to conventional *ad-hoc* models, properties like the surface stress are consistently derived from a thermodynamic potential. While the projection approach captures classic in-plane stresses, the relaxation approach can further relax normal-normal and normal-shear coupling. A projection onto the surface is indeed always a relaxation if anisotropy is superficial, but not *vice versa*. The distinct behavior of projection and relaxation is theoretically discussed and highlighted by specific examples. Numerical implementation in a finite-element framework is subsequently elaborated. Its performance is illustrated by isotropic and anisotropic surface energies of a free cube and a beam under tension. Finally, both projection and relaxation constitute valuable alternatives to conventional surface models in terms of physics, geometry and computation.

In view of the strong interaction between bulk and surface, particularly in the near-surface regions, the aim of this work is to derive a surface model that utilizes the underlying bulk deformation state. First, the basic kinematics, balance laws and the conventional modeling approach with invariants will be introduced within Sec. 5.1. Afterwards, two approaches to derive a thermodynamically consistent model from the bulk deformation state will be presented in Sec. 5.2: projection and relaxation. The numerical implementation is presented in Sec. 5.3. The key discussion in Sec. 5.4 compares projection and relaxation. It considers the theoretical aspects as well as numerical examples before concluding and giving an outlook in Sec. 5.5.

## 5.1 Introduction

### 5.1.1 Kinematics of material surfaces

Denoting curvilinear coordinates as $\Theta^i$ with $i \in \{1, 2, 3\}$, a material point of a bulk body is denoted as $\mathbf{X} = \mathbf{X}(\Theta^i)$ with respect to the undeformed configuration and as

$\mathbf{x} = \mathbf{x}(\Theta^i)$ with respect to the deformed configuration. Both points are connected by the deformation mapping $\mathbf{x} = \boldsymbol{\varphi}(\mathbf{X})$. The deformation gradient $\mathbf{F}$ maps line elements as

$$\mathrm{d}\mathbf{x} = \mathbf{F} \cdot \mathrm{d}\mathbf{X}. \tag{5.1}$$

By introducing tangent vectors $\mathbf{g}_i := \partial\mathbf{x}/\partial\Theta^i$ and $\mathbf{G}_i := \partial\mathbf{X}/\partial\Theta^i$, the deformation gradient can be written as

$$\mathbf{F} = \mathbf{g}_i \otimes \mathbf{G}^i, \quad i \in \{1,2,3\}. \tag{5.2}$$

Similarly, the deformation mapping $\overline{\boldsymbol{\varphi}}$ of material points belonging to a surface can be introduced. Denoting the position of the point with respect to the undeformed and deformed configuration as $\overline{\mathbf{X}}$ and $\overline{\mathbf{x}}$, respectively, tangent vectors in the surface parametrization read $\overline{\mathbf{g}}_\alpha = \partial\overline{\mathbf{x}}/\partial\Theta^\alpha$ and $\overline{\mathbf{G}}_\alpha = \partial\overline{\mathbf{X}}/\partial\Theta^\alpha$ and require only two coordinates $\Theta^\alpha$, thus $\alpha \in \{1,2\}$. In the following, only material surfaces are considered, i.e., surfaces which follow the motion of the neighboring bulk. In this case, it is convenient to use the same coordinates for the bulk and the surface description. Accordingly, a parametrization such that $\overline{\mathbf{g}}_\alpha = \mathbf{g}_\alpha$ and $\overline{\mathbf{G}}_\alpha = \mathbf{G}_\alpha$ can be chosen. Analogous to the standard identity mapping $\mathbf{I} = \mathbf{G}_i \otimes \mathbf{G}^i$ for the bulk with respect to the undeformed configuration, the standard identity mapping $\overline{\mathbf{I}}$ for the surface with respect to the undeformed configuration has the form

$$\overline{\mathbf{I}} = \mathbf{G}_\alpha \otimes \mathbf{G}^\alpha = \mathbf{I} - \mathbf{N} \otimes \mathbf{N} \quad \text{with} \quad \mathbf{N} = \frac{\mathbf{G}_1 \times \mathbf{G}_2}{||\mathbf{G}_1 \times \mathbf{G}_2||}. \tag{5.3}$$

A push-forward of $\mathbf{I}$ yields the surface identity with respect to the deformed configuration $\mathbf{i} = \mathbf{g}_i \otimes \mathbf{g}^i$. The same holds for the spatial projection operator of the surface

$$\overline{\mathbf{i}} = \mathbf{g}_\alpha \otimes \mathbf{g}^\alpha = \mathbf{i} - \mathbf{n} \otimes \mathbf{n} \quad \text{with} \quad \mathbf{n} = \frac{\mathbf{g}_1 \times \mathbf{g}_2}{||\mathbf{g}_1 \times \mathbf{g}_2||} = \frac{\mathbf{F}^{-\mathrm{T}} \cdot \mathbf{N}}{\left|\left|\mathbf{F}^{-\mathrm{T}} \cdot \mathbf{N}\right|\right|}. \tag{5.4}$$

Analogous to the bulk material, the surface deformation gradient maps line elements belonging to the tangent space spanned by the surface as

$$\mathrm{d}\overline{\mathbf{x}} = \overline{\mathbf{F}} \cdot \mathrm{d}\overline{\mathbf{X}}. \tag{5.5}$$

The surface deformation gradient reads in curvilinear coordinates

$$\overline{\mathbf{F}} = \mathbf{g}_\alpha \otimes \mathbf{G}^\alpha, \quad \alpha \in \{1,2\} \tag{5.6}$$

and can be understood as a projection of the bulk deformation gradient onto the surface in the sense [25]

$$\overline{\mathbf{F}} = \mathbf{F} \cdot \overline{\mathbf{I}}. \tag{5.7}$$

In line with the bulk material, suitable strain measures can be defined by means of the deformation gradient $\overline{\mathbf{F}}$. The right Cauchy-Green tensor $\mathbf{C}$ will be used for the bulk and $\overline{\mathbf{C}}$ for the surface, reading

$$\mathbf{C} = \mathbf{F}^{\mathrm{T}} \cdot \mathbf{F} = g_{ij}\, \mathbf{G}^i \otimes \mathbf{G}^j \quad \text{and} \quad \overline{\mathbf{C}} = \overline{\mathbf{F}}^{\mathrm{T}} \cdot \mathbf{F} = \overline{\mathbf{I}} \cdot \mathbf{C} \cdot \overline{\mathbf{I}} = g_{\alpha\beta}\, \mathbf{G}^\alpha \otimes \mathbf{G}^\beta. \tag{5.8}$$

The coordinates of the metric tensor are defined as $g_{\alpha\beta} = \mathbf{g}_\alpha \cdot \mathbf{g}_\beta$.

Before proceeding, three special notations will be emphasized. First, the same energy $\psi$ may operate on a bulk deformation, on a projected surface deformation or on a relaxed surface deformation, $\mathbf{C}$, $\overline{\mathbf{C}}$ or $\widetilde{\mathbf{C}}$. Second, energies depending on the right Cauchy-Green tensors or on the deformation gradients, $\mathbf{C}$ or $\mathbf{F}$, will be employed as they are useful for illustrating examples or general proofs, respectively. Third, different conjugate pairs of stresses and strains will be discussed accordingly. The physical interpretation of individual relationships strongly benefits from these various formulations. The mathematical formulation that seems most beneficial for the example, the proof or the literature reference at hand will be chosen. For the sake of comprehensibility, the variants are introduced in detail in the theory section 5.2. Subsequently, for brevity and clarity the arguments of functions in definite and obvious cases will be omitted and they will be explicitly stated otherwise.

### 5.1.2 Balance laws

The following derivatives closely follow the well-known concepts in rational continuum mechanics of bulk phases with boundary surfaces, lines and points, e.g., see [25, 62]. $\mathcal{B}_0$ denotes the body, $\mathcal{S}_0 = \partial\mathcal{B}_0$ denotes the surface and $\partial\mathcal{S}_0$ is the surface boundary in the reference configuration. The elastic energy of the system ($\Psi_{\mathrm{tot}}$) splits into the integral of the bulk energy density ($\psi$) and the surface energy density ($\psi_{\mathcal{S}}$), both initially depending on the bulk deformation gradient $\mathbf{F}$

$$\Psi_{\mathrm{tot}} = \int_{\mathcal{B}_0} \psi(\mathbf{F})\, \mathrm{d}V + \int_{\mathcal{S}_0} \psi_{\mathcal{S}}(\mathbf{F})\, \mathrm{d}A. \tag{5.9}$$

Accordingly, hyperelasticity is considered, although one could also work with reduced potentials allowing to incorporate dissipative mechanisms.

The key aspect of this investigation is to explore different realizations of the surface energy $\psi_{\mathcal{S}}$. Many common approaches directly restrict the energy to in-plane contributions in the familiar form of $\psi_{\mathcal{S}}(\mathbf{F}_{\mathcal{S}})$ [25]. The present work, in contrast, approaches the surface model based on the idea that it actually approximates a three-dimensional boundary region. Therefore, the possibilities of deriving a surface deformation $\mathbf{F}_{\mathcal{S}}$ from a fully three-dimensional deformation state, $\mathbf{F} \mapsto \mathbf{F}_{\mathcal{S}}$, will be discussed later. Accordingly, also the energy shall derive from a three-dimensional origin. For comparison, it will be further distinguished between energy formulations that inherently contain the transformation to a two-dimensional state, $\mathbf{F} \mapsto \psi_{\mathcal{S}}$, from energy formulations that act

on already transformed deformation states, $(\mathbf{F} \mapsto \mathbf{F}_{\mathcal{S}}) \mapsto \psi_{\mathcal{S}}$, and interpret the respective stress measures. For now, however, surface properties will be generally indicated by index $\mathcal{S}$ and possible specifications will be introduced at a later stage.

The balance equations can be derived from minimization of a functional $\mathcal{I}$, see [25, 62]. The rate of the time-continuous potential contains the elastic bulk and surface energy and a power term $\mathcal{P}_{\mathbf{F}}(\dot{\boldsymbol{\varphi}})$ resulting from external forces, reading

$$\dot{\mathcal{I}} = \dot{\Psi}_{\text{tot}} - \mathcal{P}_{\mathbf{F}}(\dot{\boldsymbol{\varphi}}) = \int_{\mathcal{B}_0} \dot{\psi}(\mathbf{F}) \, \mathrm{d}V + \int_{\mathcal{S}_0} \dot{\psi}_{\mathcal{S}}(\mathbf{F}) \, \mathrm{d}A - \mathcal{P}_{\mathbf{F}}(\dot{\boldsymbol{\varphi}}) \tag{5.10}$$

with

$$\mathcal{P}_{\mathbf{F}}(\dot{\boldsymbol{\varphi}}) = \int_{\mathcal{B}_0} \dot{\boldsymbol{\varphi}} \cdot \mathbf{B}_0 \, \mathrm{d}V + \int_{\mathcal{S}_0} \dot{\boldsymbol{\varphi}} \cdot \mathbf{T}_0 \, \mathrm{d}A + \int_{\mathcal{S}_0} \dot{\boldsymbol{\varphi}} \cdot \mathbf{B}_{\mathcal{S},0} \, \mathrm{d}A + \int_{\partial\mathcal{S}_0} \dot{\boldsymbol{\varphi}} \cdot \mathbf{T}_{\mathcal{S},0} \, \mathrm{d}L, \tag{5.11}$$

where $\mathbf{B}_0$ denotes the body force density per unit reference volume of the bulk and $\mathbf{B}_{\mathcal{S},0}$ the body force density per unit reference area of the surface in the reference configuration. Similarly, $\mathbf{T}_0$ denotes the traction density per unit reference area of the bulk and $\mathbf{T}_{\mathcal{S},0}$ the traction density per unit reference length of the surface in the reference configuration.

The dissipation inequality for such an elastic system of bulk and surface yields the dissipation inequality as shown in [25, 62]

$$\mathcal{D} = \left[ \mathbf{P} - \frac{\partial \psi(\mathbf{F})}{\partial \mathbf{F}} \right] : \dot{\mathbf{F}} \geq 0 \quad \text{on } \mathcal{B}_0 \quad \text{and} \tag{5.12}$$

$$\mathcal{D}_{\mathcal{S}} = \left[ \mathbf{P}_{\mathcal{S}} - \frac{\partial \psi_{\mathcal{S}}(\mathbf{F})}{\partial \mathbf{F}} \right] : \dot{\mathbf{F}} \geq 0 \quad \text{on } \mathcal{S}_0, \tag{5.13}$$

where $\mathbf{P}$ and $\mathbf{P}_{\mathcal{S}}$ denote the first Piola-Kirchhoff stress tensors of the bulk and surface material. Satisfying the dissipation inequality for arbitrary deformation gradients by application of the classic Coleman & Noll procedure yields constitutive relations

$$\mathbf{P} = \frac{\partial \psi(\mathbf{F})}{\partial \mathbf{F}} \quad \text{and} \quad \mathbf{P}_{\mathcal{S}} = \frac{\partial \psi_{\mathcal{S}}(\mathbf{F})}{\partial \mathbf{F}}. \tag{5.14}$$

In order to achieve material symmetry, the response of the constitutive material has to be independent of rotations belonging to the symmetry group $S \subset SO(3)$. This is fulfilled if the material response is formulated as a function of the right Cauchy-Green tensor $\psi = \psi(\mathbf{C})$. Accordingly, the first and the second Piola-Kirchhoff stress tensors for bulk and surface can be derived as

$$\mathbf{P} = 2\,\mathbf{F} \cdot \frac{\partial \psi(\mathbf{C})}{\partial \mathbf{C}}, \quad \mathbf{S} = 2\,\frac{\partial \psi(\mathbf{C})}{\partial \mathbf{C}} \tag{5.15}$$

and

$$\mathbf{P}_{\mathcal{S}} = 2\,\mathbf{F}\cdot\frac{\partial\psi_{\mathcal{S}}(\mathbf{C})}{\partial\mathbf{C}},\quad \mathbf{S}_{\mathcal{S}} = 2\,\frac{\partial\psi_{\mathcal{S}}(\mathbf{C})}{\partial\mathbf{C}}. \tag{5.16}$$

By application of the time integration on Eq. (5.10) and using the constitutive relations from Eq. (5.14), the respective stationarity conditions are achieved as

$$\begin{aligned}\delta\mathcal{I} &= \int_{\mathcal{B}_0}\mathbf{P}:\delta\mathbf{F}-\delta\boldsymbol{\varphi}\cdot\mathbf{B}_0\,\mathrm{d}V-\int_{\mathcal{S}_0}\delta\boldsymbol{\varphi}\cdot\mathbf{T}_0\,\mathrm{d}A\\ &\quad+\int_{\mathcal{S}_0}\mathbf{P}_{\mathcal{S}}:\delta\mathbf{F}-\delta\boldsymbol{\varphi}\cdot\mathbf{B}_{\mathcal{S},0}\,\mathrm{d}A-\int_{\partial\mathcal{S}_0}\delta\boldsymbol{\varphi}\cdot\mathbf{T}_{\mathcal{S},0}\,\mathrm{d}L \qquad (5.17)\\ &= -\int_{\mathcal{B}_0}[\mathrm{Div}\,\mathbf{P}+\mathbf{B}_0]\cdot\delta\boldsymbol{\varphi}\,\mathrm{d}V+\int_{\mathcal{S}_0}[\mathbf{P}\cdot\mathbf{N}-\mathbf{T}_0]\cdot\delta\boldsymbol{\varphi}\,\mathrm{d}A\\ &\quad-\int_{\mathcal{S}_0}[\mathrm{Div}_{\mathcal{S}}\,\mathbf{P}_{\mathcal{S}}+\mathbf{B}_{\mathcal{S},0}]\cdot\delta\boldsymbol{\varphi}\,\mathrm{d}A+\int_{\partial\mathcal{S}_0}\left[\mathbf{P}_{\mathcal{S}}\cdot\widehat{\mathbf{N}}-\mathbf{T}_{\mathcal{S},0}\right]\cdot\delta\boldsymbol{\varphi}\,\mathrm{d}L \qquad (5.18)\end{aligned}$$

with the virtual deformations $\delta\mathbf{F}=\mathrm{Grad}\,\delta\boldsymbol{\varphi}$. Reformulation using divergence theorems for bulk and surface (cf. [62]), the individual variations yield the local balances of linear momentum

$$\mathrm{Div}\,\mathbf{P}+\mathbf{B}_0=0\quad\text{on }\mathcal{B}_0\quad\text{and} \tag{5.19}$$

$$\mathrm{Div}_{\mathcal{S}}\,\mathbf{P}_{\mathcal{S}}+\mathbf{B}_{\mathcal{S},0}=0\quad\text{on }\mathcal{S}_0 \tag{5.20}$$

and the Neumann boundary conditions

$$\mathbf{T}_0=\mathbf{P}\cdot\mathbf{N}\quad\text{on }\mathcal{S}_0\quad\text{and} \tag{5.21}$$

$$\mathbf{T}_{\mathcal{S},0}=\mathbf{P}_{\mathcal{S}}\cdot\widehat{\mathbf{N}}\quad\text{on }\partial\mathcal{S}_0, \tag{5.22}$$

where $\mathbf{N}$ is the outward unit normal vector of the boundary $\mathcal{S}_0$ of the bulk and $\widehat{\mathbf{N}}$ the outward unit normal vector of the surface $\partial\mathcal{S}_0$ being tangential in the surface $\partial\mathcal{S}_0$ in the reference configuration.

The local balances of angular momentum are achieved from Eq. (5.11). Finally, this implies symmetry of the stress tensor in the sense

$$\epsilon:\left[\mathbf{F}\cdot\mathbf{P}^{\mathrm{T}}\right]=\mathbf{0}\quad\Leftrightarrow\quad\mathbf{P}\cdot\mathbf{F}^{\mathrm{T}}=\mathbf{F}\cdot\mathbf{P}^{\mathrm{T}}\quad\text{and} \tag{5.23}$$

$$\epsilon:\left[\mathbf{F}\cdot\mathbf{P}_{\mathcal{S}}^{\mathrm{T}}\right]=\mathbf{0}\quad\Leftrightarrow\quad\mathbf{P}_{\mathcal{S}}\cdot\mathbf{F}^{\mathrm{T}}=\mathbf{F}\cdot\mathbf{P}_{\mathcal{S}}^{\mathrm{T}}, \tag{5.24}$$

where $\epsilon$ denotes the Levi-Civita symbol. More details about the derivation of the angular momentum are given in [25].

### 5.1.3 Conventional surface elasticity using surface invariants

A common modern approach to material modeling is the formulation of energies in terms of invariants. This formulation is briefly recapitulated for later examples and evaluation of the projection and the relaxation approaches. Without loss of generality, the focus is on the Helmholtz free energy per area of the undeformed configuration, $\psi$. Balance of linear momentum is enforced by minimizing the total energy of the considered body as a function of the deformation gradient $\psi(\mathbf{F})$. In order to fulfill the principle of material frame indifference, $\psi$ depends on the right Cauchy-Green tensor $\mathbf{C}$ (also guaranteeing balance of angular momentum). For an isotropic bulk, this dependence reduces to the invariants of $\mathbf{C}$. We can identify three principal invariants

$$I_{\mathbf{C}} = \operatorname{tr}\mathbf{C}, \quad II_{\mathbf{C}} = \frac{1}{2}\left[I_{\mathbf{C}}^2 - \operatorname{tr}\left(\mathbf{C}^2\right)\right], \quad III_{\mathbf{C}} = \det\mathbf{C} \tag{5.25}$$

as well as three basis invariants

$$J_{\mathbf{C}}^{(1)} = \operatorname{tr}\mathbf{C}, \quad J_{\mathbf{C}}^{(2)} = \operatorname{tr}\left(\mathbf{C}^2\right), \quad J_{\mathbf{C}}^{(3)} = \operatorname{tr}\left(\mathbf{C}^3\right). \tag{5.26}$$

Turning the view towards surfaces, the surface deformation gradient is rank-deficient and its three-dimensional determinate is zero. Consequently, the two remaining principal invariants characterizing an isotropic surface energy are

$$I_{\overline{\mathbf{C}}} = \overline{\operatorname{tr}}\,\overline{\mathbf{C}} = \overline{\mathbf{C}} : \overline{\mathbf{I}}, \quad II_{\overline{\mathbf{C}}} = \frac{1}{2}\left[I_{\overline{\mathbf{C}}}^2 - \overline{\operatorname{tr}}\left(\overline{\mathbf{C}}^2\right)\right] \tag{5.27}$$

and the two basis invariants for isotropic surfaces read

$$J_{\overline{\mathbf{C}}}^{(1)} = \overline{\operatorname{tr}}\,\overline{\mathbf{C}}, \quad J_{\overline{\mathbf{C}}}^{(2)} = \overline{\operatorname{tr}}\left(\overline{\mathbf{C}}^2\right). \tag{5.28}$$

The material behavior of an isotropic surface can thus be formulated in the two invariants $\{I_{\overline{\mathbf{C}}}, II_{\overline{\mathbf{C}}}\}$ or $\{J_{\overline{\mathbf{C}}}^{(1)}, J_{\overline{\mathbf{C}}}^{(2)}\}$, which is a common approach neglecting special extensions such as curvature effects or out-of-plane stresses [16, 25, 61, 71]. $II_{\overline{\mathbf{C}}}$ plays a prominent role for surfaces as it is the squared ratio of deformed to undeformed surface area. In line with the determinant for the bulk, it is also equal to the two-dimensional determinant of $\overline{\mathbf{C}}$, which is proven in Sec. C.1.

Anisotropic materials can be accounted for by using so-called pseudo invariants, if the symmetry group of the considered material is known (cf. [60]). For the sake of illustration, an orthotropic material is considered here. Its material axes are denoted as ${}^{(i)}\mathbf{d}_0$ yielding the structural tensors ${}^{(i)}\mathbf{M} = {}^{(i)}\mathbf{d}_0 \otimes {}^{(i)}\mathbf{d}_0$. The zero subscript indicates that both belong to the undeformed configuration. According to [60], every orthotropic Helmholtz free energy can be written in terms of the principle or basis invariants as well

as in terms of the pseudo invariants

$$J_{\mathbf{C}}^{(4)} = \mathbf{C} : {}^{(1)}\mathbf{M}, \quad J_{\mathbf{C}}^{(5)} = \mathbf{C}^2 : {}^{(1)}\mathbf{M}, \quad J_{\mathbf{C}}^{(6)} = \mathbf{C} : {}^{(2)}\mathbf{M}, \quad J_{\mathbf{C}}^{(7)} = \mathbf{C}^2 : {}^{(2)}\mathbf{M}. \tag{5.29}$$

In the special case of ${}^{(1)}\mathbf{d}_0$ and ${}^{(2)}\mathbf{d}_0$ belonging to the tangent space and ${}^{(3)}\mathbf{d}_0$ corresponding to the normal direction, two dependencies can be formulated between the invariants

$$J_{\overline{\mathbf{C}}}^{(4)} + J_{\overline{\mathbf{C}}}^{(6)} = \overline{\mathbf{C}} : \left[ {}^{(1)}\mathbf{M} + {}^{(2)}\mathbf{M} \right] = \overline{\mathbf{C}} : \overline{\mathbf{I}} = \overline{\mathrm{tr}}(\overline{\mathbf{C}}) = J_{\overline{\mathbf{C}}}^{(1)}, \tag{5.30}$$

$$J_{\overline{\mathbf{C}}}^{(5)} + J_{\overline{\mathbf{C}}}^{(7)} = \overline{\mathbf{C}}^2 : \left[ {}^{(1)}\mathbf{M} + {}^{(2)}\mathbf{M} \right] = \overline{\mathbf{C}}^2 : \overline{\mathbf{I}} = \overline{\mathrm{tr}}(\overline{\mathbf{C}}^2) = J_{\overline{\mathbf{C}}}^{(2)}. \tag{5.31}$$

In this case, only four (pseudo-)invariants of the surface are independent and the surface Helmholtz free energy takes the form

$$\psi = \psi\left( J_{\overline{\mathbf{C}}}^{(1)}, J_{\overline{\mathbf{C}}}^{(2)}, J_{\overline{\mathbf{C}}}^{(4)}, J_{\overline{\mathbf{C}}}^{(5)} \right). \tag{5.32}$$

The work continues with surface models that are not derived from pure surface invariants. Instead the underlying three-dimensional deformation state will be harnessed. As mentioned in the introduction, this approach is motivated by several physical observations such as finite-thickness phase boundaries, near surface relaxation, anchoring effects as well as computational and mathematical approaches such as rank-one relaxation in membrane models. Thus, the question can be formulated as to how a suitable surface energy and thermodynamically suitable surface stress response can be derived, see Fig. 5.1 for illustration. Namely, projection and relaxation will be employed.

## 5.2 Deriving surface elasticity models from a three-dimensional deformation

### 5.2.1 Surface energies by projection

The probably most straightforward transformation of a three-dimensional bulk model to a two-dimensional surface model is a projection onto the surface tangent space. The projection is not uniquely defined, though. The projection $\overline{\mathbf{I}}$ is applied at the initial stage of the modeling framework, i.e. $\mathbf{F} \to \mathbf{F} \cdot \overline{\mathbf{I}} = \overline{\mathbf{F}}$ and $\mathbf{C} \to \overline{\mathbf{I}} \cdot \mathbf{C} \cdot \overline{\mathbf{I}} = \overline{\mathbf{C}}$, allowing only surface deformations to contribute to the surface Helmholtz free energy

$$\psi_{\mathrm{p}}(\mathbf{C}) := \psi\big(\overline{\mathbf{C}}\big) = \psi\big(\overline{\mathbf{I}} \cdot \mathbf{C} \cdot \overline{\mathbf{I}}\big). \tag{5.33}$$

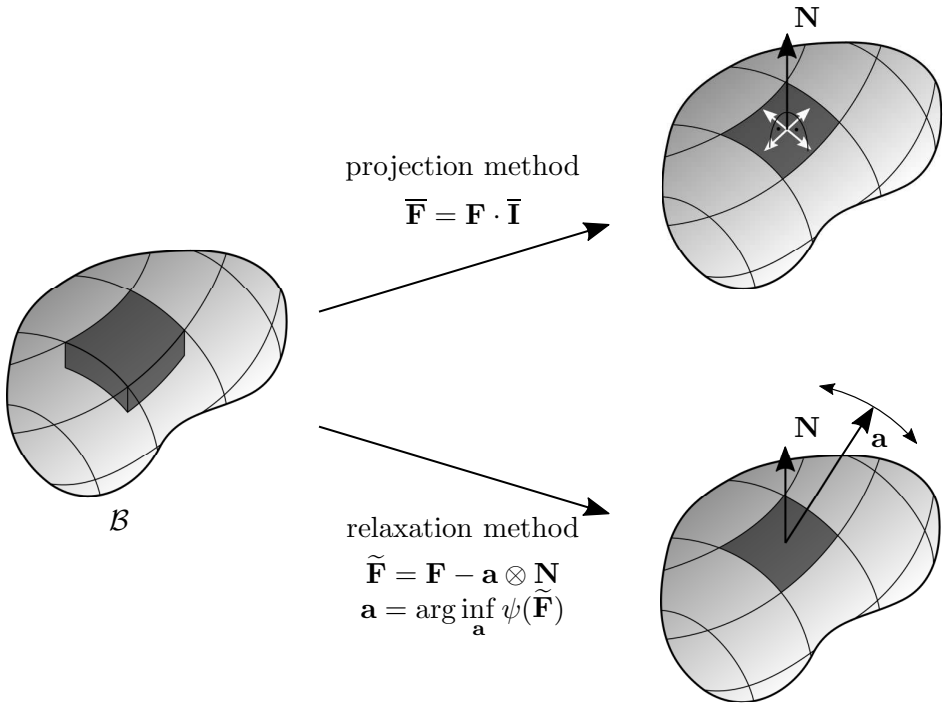


**Figure 5.1:** Comparison between projection and relaxation method: surface deformation is either determined by a surface projection of the deformation gradient $\overline{\mathbf{F}} = \mathbf{F} \cdot \overline{\mathbf{I}}$ or by relaxation of the deformation gradient $\widetilde{\mathbf{F}} = \mathbf{F} - \mathbf{a} \otimes \mathbf{N}$ that minimizes the energy as $\inf_{\mathbf{a}} \psi(\widetilde{\mathbf{F}})$.

Based on this frame-indifferent energy, the first and the second Piola-Kirchoff stress tensors are obtained as

$$\mathbf{P}_{\mathrm{p}} = \frac{\partial \psi_{\mathrm{p}}(\mathbf{F})}{\partial \mathbf{F}} = \frac{\partial \psi\big(\overline{\mathbf{F}}\big)}{\partial \mathbf{F}} = \frac{\partial \psi\big(\overline{\mathbf{F}}\big)}{\partial \overline{\mathbf{F}}} : \frac{\partial \overline{\mathbf{F}}}{\partial \mathbf{F}} = \frac{\partial \psi\big(\overline{\mathbf{F}}\big)}{\partial \overline{\mathbf{F}}} : \big[\mathbf{i} \overline{\otimes} \overline{\mathbf{I}}\big] = \frac{\partial \psi\big(\overline{\mathbf{F}}\big)}{\partial \overline{\mathbf{F}}} \cdot \overline{\mathbf{I}}, \tag{5.34}$$

$$\mathbf{S}_{\mathrm{p}} = 2\,\frac{\partial \psi_{\mathrm{p}}(\mathbf{C})}{\partial \mathbf{C}} = 2\,\frac{\partial \psi\big(\overline{\mathbf{C}}\big)}{\partial \overline{\mathbf{C}}} : \frac{\partial \overline{\mathbf{C}}}{\partial \mathbf{C}} = 2\,\frac{\partial \psi\big(\overline{\mathbf{C}}\big)}{\partial \overline{\mathbf{C}}} : \big[\overline{\mathbf{I}} \overline{\otimes} \overline{\mathbf{I}}\big] = 2\,\overline{\mathbf{I}} \cdot \frac{\partial \psi\big(\overline{\mathbf{C}}\big)}{\partial \overline{\mathbf{C}}} \cdot \overline{\mathbf{I}}, \tag{5.35}$$

$$\mathbf{P}_{\mathrm{p}} = 2\,\overline{\mathbf{F}} \cdot \frac{\partial \psi\big(\overline{\mathbf{C}}\big)}{\partial \overline{\mathbf{C}}} \cdot \overline{\mathbf{I}} = \mathbf{F} \cdot \mathbf{S}_{\mathrm{p}}. \tag{5.36}$$

The present stress tensors are initially defined to be conjugate to bulk deformation, $\mathbf{F}$ and $\mathbf{C}$, respectively, within a thermodynamically consistent framework. A characteristic property that derives from this approach is a pure in-plane stress-tensor in the sense that

$$\mathbf{S}_{\mathrm{p}} = \mathbf{S}\big(\overline{\mathbf{C}}\big) : \big[\overline{\mathbf{I}} \overline{\otimes} \overline{\mathbf{I}}\big] = \mathbf{S}\big(\overline{\mathbf{I}} \cdot \mathbf{C} \cdot \overline{\mathbf{I}}\big) : \big[\overline{\mathbf{I}} \overline{\otimes} \overline{\mathbf{I}}\big] = \overline{\mathbf{I}} \cdot \mathbf{S}\big(\overline{\mathbf{I}} \cdot \mathbf{C} \cdot \overline{\mathbf{I}}\big) \cdot \overline{\mathbf{I}}. \tag{5.37}$$

The present formulation of the projection approach implicitly contains the projection of the deformation state as part of the energy formulation. An alternative is given by

the split into the mere projection operator and an energy that acts on already projected deformation states, writing

$$\overline{\psi}\big(\overline{\mathbf{C}}\big) := \psi\big(\overline{\mathbf{C}}\big) \tag{5.38}$$

with

$$\psi_{\mathrm{p}}(\mathbf{C}) = \underbrace{\psi \circ \mathrm{projection}}_{\psi_{\mathrm{p}}}(\mathbf{C}) = \psi \circ \underbrace{\mathrm{projection}(\mathbf{C})}_{\overline{\mathbf{C}}} = \psi\big(\overline{\mathbf{C}}\big) = \overline{\psi}\big(\overline{\mathbf{C}}\big) \tag{5.39}$$

or $\overline{\psi}\big(\overline{\mathbf{F}}\big) := \psi\big(\overline{\mathbf{F}}\big)$, respectively. Despite the seemingly small difference in notation, the different formulations of the dual stress tensors should be pointed, because this split into projection and energy can be found frequently in literature, for instance in [25]. The respective first and second Piola-Kirchhoff stress tensors can be expressed as

$$\overline{\mathbf{P}} = \frac{\partial\overline{\psi}\big(\overline{\mathbf{F}}\big)}{\partial\overline{\mathbf{F}}} = \frac{\partial\psi\big(\overline{\mathbf{F}}\big)}{\partial\overline{\mathbf{F}}} \quad \text{and} \quad \overline{\mathbf{S}} = 2\,\frac{\partial\overline{\psi}\big(\overline{\mathbf{C}}\big)}{\partial\overline{\mathbf{C}}} = 2\,\frac{\partial\psi\big(\overline{\mathbf{C}}\big)}{\partial\overline{\mathbf{C}}} \quad \text{with} \quad \overline{\mathbf{P}} = \overline{\mathbf{F}}\cdot\overline{\mathbf{S}}. \tag{5.40}$$

and relate to the above variants as

$$\mathbf{P}_{\mathrm{p}} = \overline{\mathbf{P}} : \big[\mathbf{i}\,\overline{\otimes}\,\overline{\mathbf{I}}\big] = \overline{\mathbf{P}}\cdot\overline{\mathbf{I}} \quad \text{and} \quad \mathbf{S}_{\mathrm{p}} = \overline{\mathbf{S}} : \big[\overline{\mathbf{I}}\,\overline{\otimes}\,\overline{\mathbf{I}}\big] = \overline{\mathbf{I}}\cdot\overline{\mathbf{S}}\cdot\overline{\mathbf{I}}. \tag{5.41}$$

Both formulations, $\mathbf{P}_{\mathrm{p}}$ and $\overline{\mathbf{P}}$, are equivalent if the projected stress tensor $\overline{\mathbf{P}}$ is invariant under contraction with $\overline{\mathbf{I}}$. This is the case for surface Helmholtz free energies depending on the four invariants as introduced in this treatise, $\psi = \psi(I_{\overline{\mathbf{F}}}, II_{\overline{\mathbf{F}}}, J^{(4)}_{\overline{\mathbf{F}}}, J^{(5)}_{\overline{\mathbf{F}}})$, because the derivatives of these invariants with respect to $\overline{\mathbf{F}}$ are invariant under contraction with $\overline{\mathbf{I}}$ themselves:

$$\begin{aligned}
\mathbf{P}_{\mathrm{p}} &= \overline{\mathbf{P}}\cdot\overline{\mathbf{I}} && (5.42)\\
&= \left[\frac{\partial\psi}{\partial I_{\overline{\mathbf{F}}}}\frac{\partial I_{\overline{\mathbf{F}}}}{\partial\overline{\mathbf{F}}} + \frac{\partial\psi}{\partial II_{\overline{\mathbf{F}}}}\frac{\partial II_{\overline{\mathbf{F}}}}{\partial\overline{\mathbf{F}}} + \frac{\partial\psi}{\partial J^{(4)}_{\overline{\mathbf{F}}}}\frac{\partial J^{(4)}_{\overline{\mathbf{F}}}}{\partial\overline{\mathbf{F}}} + \frac{\partial\psi}{\partial J^{(5)}_{\overline{\mathbf{F}}}}\frac{\partial J^{(5)}_{\overline{\mathbf{F}}}}{\partial\overline{\mathbf{F}}}\right]\cdot\overline{\mathbf{I}} && (5.43)\\
&= \overline{\mathbf{P}}. && (5.44)
\end{aligned}$$

The same analogy is applied to the tangent being the second derivative of an arbitrary

projected surface energy $\psi(\overline{\mathbf{F}})$ with respect to the deformation gradient $\mathbf{F}$ and yields

$$
\begin{aligned}
\mathrm{d}\mathbf{P}_{\mathrm{p}} &= \frac{\partial}{\partial \mathbf{F}}\left(\frac{\partial \psi(\overline{\mathbf{F}})}{\partial \mathbf{F}}\right) : \mathrm{d}\mathbf{F} && (5.45)\\
&= \frac{\partial}{\partial \mathbf{F}}\left(\frac{\partial \psi(\overline{\mathbf{F}})}{\partial \overline{\mathbf{F}}} : \frac{\partial \overline{\mathbf{F}}}{\partial \mathbf{F}}\right) : \mathrm{d}\mathbf{F} && (5.46)\\
&= \left[\frac{\partial}{\partial \mathbf{F}}\left(\frac{\partial \psi(\overline{\mathbf{F}})}{\partial \overline{\mathbf{F}}}\right) : \frac{\partial \overline{\mathbf{F}}}{\partial \mathbf{F}} + \frac{\partial \psi(\overline{\mathbf{F}})}{\partial \overline{\mathbf{F}}} : \frac{\partial}{\partial \mathbf{F}}\left(\frac{\partial \overline{\mathbf{F}}}{\partial \mathbf{F}}\right)\right] : \mathrm{d}\mathbf{F} && (5.47)\\
&= \left[\frac{\partial \overline{\mathbf{F}}}{\partial \mathbf{F}} : \frac{\partial^2 \psi(\overline{\mathbf{F}})}{\partial \overline{\mathbf{F}}^2} : \frac{\partial \overline{\mathbf{F}}}{\partial \mathbf{F}} + \frac{\partial \psi(\overline{\mathbf{F}})}{\partial \overline{\mathbf{F}}} : \underbrace{\frac{\partial^2 \overline{\mathbf{F}}}{\partial \mathbf{F}^2}}_{=\mathbf{0}}\right] : \mathrm{d}\mathbf{F} && (5.48)\\
&= \frac{\partial \overline{\mathbf{F}}}{\partial \mathbf{F}} : \frac{\partial^2 \psi(\overline{\mathbf{F}})}{\partial \overline{\mathbf{F}}^2} : \frac{\partial \overline{\mathbf{F}}}{\partial \mathbf{F}} : \mathrm{d}\mathbf{F} && (5.49)\\
\Rightarrow \mathbb{A}_{\mathrm{p}} &= \frac{\mathrm{d}\mathbf{P}_{\mathrm{p}}}{\mathrm{d}\mathbf{F}} = \frac{\partial^2 \psi(\overline{\mathbf{F}})}{\partial \mathbf{F}^2} = \frac{\partial \overline{\mathbf{F}}}{\partial \mathbf{F}} : \frac{\partial^2 \psi(\overline{\mathbf{F}})}{\partial \overline{\mathbf{F}}^2} : \frac{\partial \overline{\mathbf{F}}}{\partial \mathbf{F}} && (5.50)\\
&= \left[\mathbf{i} \overline{\otimes} \overline{\mathbf{I}}\right] : \frac{\partial^2 \psi(\overline{\mathbf{F}})}{\partial \overline{\mathbf{F}}^2} : \left[\mathbf{i} \overline{\otimes} \overline{\mathbf{I}}\right] && (5.51)\\
\Leftrightarrow \mathbb{A}_{\mathrm{p}} &= \left[\mathbf{i} \overline{\otimes} \overline{\mathbf{I}}\right] : \overline{\mathbb{A}} : \left[\mathbf{i} \overline{\otimes} \overline{\mathbf{I}}\right] = \overline{\mathbf{I}} \overset{(2)}{\cdot} \overline{\mathbb{A}} \cdot \overline{\mathbf{I}} && (5.52)
\end{aligned}
$$

Again, for a special surface Helmholtz free energy depending on the four invariants as mentioned above, such as $\psi = \psi(I_{\overline{\mathbf{F}}}, II_{\overline{\mathbf{F}}}, J^{(4)}_{\overline{\mathbf{F}}}, J^{(5)}_{\overline{\mathbf{F}}})$, the derivative of the invariants with respect to $\overline{\mathbf{F}}$ are invariant under the contraction with $\overline{\mathbf{I}}$:

$$
\mathbb{A}_{\mathrm{p}} = \overline{\mathbf{I}} \overset{(2)}{\cdot} \overline{\mathbb{A}} \cdot \overline{\mathbf{I}} = \overline{\mathbb{A}}. \tag{5.53}
$$

Further note, however, that many alternative and non-equivalent *ad-hoc* projections exist that may even lead to physically incompatible results. Thus, it is enlightening to illustrate the challenges of other projections at this point. Alternative and obvious tempting *ad-hoc* choices are: $\overline{\mathbf{P}} = \mathbf{P} \cdot \overline{\mathbf{I}}$, $\overline{\mathbf{P}} = \overline{\mathbf{i}} \cdot \mathbf{P} \cdot \overline{\mathbf{I}}$ and $\overline{\mathbf{P}} = \mathbf{F} \cdot \overline{\mathbf{I}} \cdot \mathbf{S} \cdot \overline{\mathbf{I}}$, being equivalent to $\overline{\mathbf{S}} = \overline{\mathbf{I}} \cdot \mathbf{S} \cdot \overline{\mathbf{I}}$ and $\overline{\mathbf{P}} = \mathbf{F} \cdot \overline{\mathbf{S}}$. However, all such choices are physically not sound, to be more precise:

- $\overline{\mathbf{P}} = \mathbf{P} \cdot \overline{\mathbf{I}}$ does not fulfill angular momentum, since $\overline{\mathbf{P}} \cdot \mathbf{F}^{\mathrm{T}} = \mathbf{P} \cdot \overline{\mathbf{F}}^{\mathrm{T}} \neq \overline{\mathbf{F}} \cdot \mathbf{P}^{\mathrm{T}} = [\overline{\mathbf{P}} \cdot \mathbf{F}^{\mathrm{T}}]^{\mathrm{T}}$. Similarly, $\overline{\mathbf{P}} \cdot \overline{\mathbf{F}}^{\mathrm{T}} = \mathbf{P} \cdot \overline{\mathbf{F}}^{\mathrm{T}} \neq \overline{\mathbf{F}} \cdot \mathbf{P}^{\mathrm{T}} = [\overline{\mathbf{P}} \cdot \overline{\mathbf{F}}^{\mathrm{T}}]^{\mathrm{T}}$. A counterexample showing this explicitly is the transversally isotropic Helmholtz free energy $\psi = 1/2\, \mathbf{C} : [\mathbf{d}_0 \otimes \mathbf{d}_0]$, where the vector $\mathbf{d}_0$ is neither orthogonal nor belonging to the tangent space of the surface, i.e., $\mathbf{d}_0 \cdot \mathbf{N} \neq 0$ and $\mathbf{d}_0 \cdot \mathbf{G}_\alpha \neq 0$.

- $\overline{\mathbf{P}} = \overline{\mathbf{i}} \cdot \mathbf{P} \cdot \overline{\mathbf{I}}$ cannot be derived from a potential, since the derivative of $\overline{\mathbf{P}}$ with respect to $\mathbf{F}$ does not show major symmetry. Accordingly, this is a Cauchy-elastic material showing non-vanishing dissipation in general. The proof of non-existing symmetry reads: $\partial\overline{\mathbf{P}}/\partial\mathbf{F} : \mathrm{d}\mathbf{F} = [\overline{\mathbf{i}} \overline{\otimes} \overline{\mathbf{I}}] : \partial\mathbf{P}/\partial\mathbf{F} : \mathrm{d}\mathbf{F} \neq [\partial\overline{\mathbf{P}}/\partial\mathbf{F}]^{\mathrm{T}} : \mathrm{d}\mathbf{F} = \mathrm{d}\mathbf{F} : [\overline{\mathbf{i}} \overline{\otimes} \overline{\mathbf{I}}] : \partial\mathbf{P}/\partial\mathbf{F}$.
- $\overline{\mathbf{P}} = \mathbf{F} \cdot \overline{\mathbf{I}} \cdot \mathbf{S} \cdot \overline{\mathbf{I}} = \mathbf{F} \cdot \overline{\mathbf{S}}$ cannot be derived from a potential, since the derivative of $\overline{\mathbf{P}}$ with respect to $\mathbf{F}$ does not show major symmetry, again, yielding is a dissipative Cauchy-elastic material. For the proof of non-existing symmetry, it is sufficient to show that $\partial\overline{\mathbf{S}}/\partial\mathbf{C}$ is non-symmetric. That can be shown in a straightforward manner: $\partial\overline{\mathbf{S}}/\partial\mathbf{C} : \mathrm{d}\mathbf{C} = [\overline{\mathbf{I}} \overline{\otimes} \overline{\mathbf{I}}] : \partial\mathbf{S}/\partial\mathbf{C} : \mathrm{d}\mathbf{C} \neq \mathrm{d}\mathbf{C} : [\overline{\mathbf{I}} \overline{\otimes} \overline{\mathbf{I}}] : \partial\mathbf{S}/\partial\mathbf{C} = [\partial\overline{\mathbf{S}}/\partial\mathbf{C}]^{\mathrm{T}} : \mathrm{d}\mathbf{C}$.

The results are not surprising, since postulating a stress response is equivalent to introducing a Cauchy-elastic material model. Such models are known to be inconsistent with the second law of thermodynamics in general. For this reason, the presented projection applies to the original deformation state and further properties are derived from a thermodynamic potential.

### 5.2.2 Surface energies by relaxation

Relaxation of a fully three-dimensional bulk model is another possibility to obtain a two-dimensional surface model. Motivations for energetic relaxation are rank-one relaxation in membrane models, surface reconstruction and anchoring effects [1, 27, 48], which exceed a simple projection onto tangential deformation components. Again, starting at the initial stage of the energy formulation that now depends on the relaxed deformation gradient $\widetilde{\mathbf{F}}$ or strain tensor $\widetilde{\mathbf{C}}$, respectively, it reads

$$\psi_{\mathrm{r}}(\mathbf{C}) = \inf_{\mathbf{a}} \psi\Big(\widetilde{\mathbf{C}}(\mathbf{C}, \mathbf{F}, \mathbf{a})\Big)\,, \tag{5.54}$$

$$\widetilde{\mathbf{F}} = \mathbf{F} - \mathbf{a} \otimes \mathbf{N}, \tag{5.55}$$

$$\widetilde{\mathbf{C}} = \widetilde{\mathbf{F}}^{\mathrm{T}} \cdot \widetilde{\mathbf{F}} = \mathbf{C} - \mathbf{N} \otimes \mathbf{a} \cdot \mathbf{F} - \mathbf{a} \cdot \mathbf{F} \otimes \mathbf{N} + [\mathbf{a} \cdot \mathbf{a}]\ \mathbf{N} \otimes \mathbf{N}. \tag{5.56}$$

The surface energy is derived by variationally fulfilling the Cauchy-Hadamard compatibility condition between the bulk deformation gradient $\mathbf{F}$ and the relaxed deformation gradient $\widetilde{\mathbf{F}}$. Vector $\mathbf{a}$ defines the jump of the deformation gradient and follows from the relaxation of the bulk energy. It is determined, though not necessarily uniquely, for the respective deformation by

$$\mathbf{a}_{\mathrm{inf}}(\mathbf{C}) = \arg\inf_{\mathbf{a}} \psi\Big(\widetilde{\mathbf{C}}(\mathbf{C}, \mathbf{F}, \mathbf{a})\Big)\,. \tag{5.57}$$

In line with the projection approach, the relaxed surface stresses and the bulk deformation are conjugate within the relaxed energy. The relaxed first and second Piola-

Kirchhoff stress tensors read

$$\mathbf{P}_{\mathrm{r}} = \frac{\partial \psi_{\mathrm{r}}}{\partial \mathbf{F}} = \frac{\partial \inf\limits_{\mathbf{a}} \psi\Big(\widetilde{\mathbf{C}}(\mathbf{C},\mathbf{F},\mathbf{a})\Big)}{\partial \mathbf{F}} \tag{5.58}$$

$$\mathbf{S}_{\mathrm{r}} = 2\,\frac{\partial \psi_{\mathrm{r}}}{\partial \mathbf{C}} = 2\,\frac{\partial \inf\limits_{\mathbf{a}} \psi\Big(\widetilde{\mathbf{C}}(\mathbf{C},\mathbf{F},\mathbf{a})\Big)}{\partial \mathbf{C}}, \tag{5.59}$$

$$\mathbf{P}_{\mathrm{r}} = \mathbf{F}\cdot\mathbf{S}_{\mathrm{r}}. \tag{5.60}$$

An alternative conjugate pair that provides a more convenient mathematical structure of the stress tensors for analytical studies can yet be derived. For that reason, the already relaxed deformation as an argument to the surface energy $\widetilde{\psi}$ is passed as

$$\widetilde{\psi}(\widetilde{\mathbf{C}}) := \psi(\widetilde{\mathbf{C}}) \tag{5.61}$$

with

$$\psi_{\mathrm{r}}(\widetilde{\mathbf{C}}) = \underbrace{\psi \circ \mathrm{relaxation}}_{\psi_{\mathrm{r}}}(\mathbf{C}) = \psi \circ \underbrace{\mathrm{relaxation}(\mathbf{C})}_{\widetilde{\mathbf{C}}} = \psi(\widetilde{\mathbf{C}}) = \widetilde{\psi}(\widetilde{\mathbf{C}}) \tag{5.62}$$

and $\widetilde{\psi}(\widetilde{\mathbf{F}}) := \psi(\widetilde{\mathbf{F}})$, respectively. This formulation yields the stresses

$$\begin{aligned} \widetilde{\mathbf{P}} &= \frac{\partial \widetilde{\psi}(\widetilde{\mathbf{F}})}{\partial \widetilde{\mathbf{F}}} = \frac{\partial \psi(\widetilde{\mathbf{F}})}{\partial \widetilde{\mathbf{F}}} \quad \text{and} \\ \widetilde{\mathbf{S}} &= 2\,\frac{\partial \widetilde{\psi}(\widetilde{\mathbf{C}})}{\partial \widetilde{\mathbf{C}}} = 2\,\frac{\partial \psi(\widetilde{\mathbf{C}})}{\partial \widetilde{\mathbf{C}}} \quad \text{with} \quad \widetilde{\mathbf{P}} = \widetilde{\mathbf{F}}\cdot\widetilde{\mathbf{S}} \end{aligned} \tag{5.63}$$

and obeys to the stationarity of the relaxation in the particular form

$$\mathbf{0} = \frac{\partial \psi(\widetilde{\mathbf{F}}(\mathbf{F},\mathbf{a}))}{\partial \mathbf{a}} = \frac{\partial \psi(\widetilde{\mathbf{F}})}{\partial \widetilde{\mathbf{F}}} : \frac{\partial \widetilde{\mathbf{F}}(\mathbf{F},\mathbf{a})}{\partial \mathbf{a}} = \widetilde{\mathbf{P}} : [\mathbf{N} \overline{\otimes} \mathbf{I}] = \widetilde{\mathbf{P}}\cdot\mathbf{N}. \tag{5.64}$$

The surface stress formulation $\widetilde{\mathbf{P}}$ thus vanishes in normal direction, $\widetilde{\mathbf{P}}\cdot\mathbf{N} = \mathbf{0}$, due to the very definition of the relaxation condition. However, note that $\widetilde{\mathbf{P}}\cdot\mathbf{N} = \mathbf{0}$ does not necessarily imply $\widetilde{\mathbf{S}}\cdot\mathbf{N} = 0$, as the transformation $\widetilde{\mathbf{F}}$ can be rank deficient. The general

stationarity condition for $\widetilde{\mathbf{S}}$ instead reads

$$\begin{aligned}\mathbf{0} &= \frac{\partial \psi}{\partial \mathbf{a}} = \frac{\partial \psi}{\partial \widetilde{\mathbf{C}}} : \frac{\partial \widetilde{\mathbf{C}}}{\partial \widetilde{\mathbf{F}}} : \frac{\partial \widetilde{\mathbf{F}}}{\partial \mathbf{a}} = \left[\frac{1}{2}\,\widetilde{\mathbf{S}}\right] : \left[\mathbf{I} \underline{\otimes} \widetilde{\mathbf{F}} + \widetilde{\mathbf{F}}^{\mathrm{T}} \overline{\otimes} \mathbf{I}\right] : [\mathbf{N} \overline{\otimes} \mathbf{I}] \\ &= \frac{1}{2}\left[\widetilde{\mathbf{F}} \cdot \widetilde{\mathbf{S}}^{\mathrm{T}} \cdot \mathbf{N} + \widetilde{\mathbf{F}} \cdot \widetilde{\mathbf{S}} \cdot \mathbf{N}\right] = \widetilde{\mathbf{F}} \cdot \widetilde{\mathbf{S}} \cdot \mathbf{N} = [\mathbf{F} - \mathbf{a} \otimes \mathbf{N}] \cdot \widetilde{\mathbf{S}} \cdot \mathbf{N} \\ \Leftrightarrow \quad & \mathbf{F} \cdot \widetilde{\mathbf{S}} \cdot \mathbf{N} = \left[\mathbf{N} \cdot \widetilde{\mathbf{S}} \cdot \mathbf{N}\right] \mathbf{a}. \end{aligned} \tag{5.65}$$

Consistency of the above stress formulations is moreover given in the following sense (see Sec. C.2 for details): (i) symmetry of $\widetilde{\mathbf{S}}$, (ii) balance of angular momentum, (iii) stress power originates purely from the surface deformation rate.

## 5.3 Numerical implementation

Following [24, 62], the energy functional introduced in Eq. (5.17) is discretized into a set of bulk elements $\mathcal{B}_0^{\mathrm{h}}$ and surface elements $\mathcal{S}_0^{\mathrm{h}}$

$$\mathcal{B}_0 \approx \mathcal{B}_0^{\mathrm{h}} = \bigcup_{e_{\mathrm{b}}=1}^{n_{\mathrm{be}}} \mathcal{B}_0^{e_{\mathrm{b}}} \quad \text{and} \quad \mathcal{S}_0 \approx \mathcal{S}_0^{\mathrm{h}} = \bigcup_{e_{\mathrm{s}}=1}^{n_{\mathrm{se}}} \mathcal{S}_0^{e_{\mathrm{s}}}, \tag{5.66}$$

where $n_{\mathrm{be}}$ denotes the number of bulk elements and $n_{\mathrm{se}}$ the number of surface elements. The geometry for each bulk element is written as a function of natural coordinates $\boldsymbol{\xi} = (\xi_1, \xi_2, \xi_3)$ by using interpolation functions $N$ as

$$\mathbf{X}(\boldsymbol{\xi}) \approx \mathbf{X}^{\mathrm{h}} = \sum_{e_{\mathrm{b}}=1}^{n_{\mathrm{be}}} N^{e_{\mathrm{b}}}(\boldsymbol{\xi})\, \mathbf{X}^{e_{\mathrm{b}}} \quad \text{and} \quad \boldsymbol{\varphi}(\boldsymbol{\xi}) \approx \boldsymbol{\varphi}^{\mathrm{h}} = \sum_{e_{\mathrm{b}}=1}^{n_{\mathrm{be}}} N^{e_{\mathrm{b}}}(\boldsymbol{\xi})\, \boldsymbol{\varphi}^{e_{\mathrm{b}}}. \tag{5.67}$$

The geometry of the surface elements are expressed as a function of natural surface coordinates $\overline{\boldsymbol{\xi}} = \left(\overline{\xi}_1, \overline{\xi}_2\right)$ by using standard two-dimensional interpolation functions $\overline{N}$:

$$\overline{\mathbf{X}}\left(\overline{\boldsymbol{\xi}}\right) \approx \overline{\mathbf{X}}^{\mathrm{h}} = \sum_{e_{\mathrm{s}}=1}^{n_{\mathrm{se}}} \overline{N}^{e_{\mathrm{s}}}\left(\overline{\boldsymbol{\xi}}\right) \mathbf{X}^{e_{\mathrm{s}}} \quad \text{and} \quad \overline{\boldsymbol{\varphi}}\left(\overline{\boldsymbol{\xi}}\right) \approx \overline{\boldsymbol{\varphi}}^{\mathrm{h}} = \sum_{e_{\mathrm{s}}=1}^{n_{\mathrm{se}}} \overline{N}^{e_{\mathrm{s}}}\left(\overline{\boldsymbol{\xi}}\right) \boldsymbol{\varphi}^{e_{\mathrm{s}}}. \tag{5.68}$$

Due to minimization of the energy functional $\delta \mathcal{I} = 0$ in Eq. (5.17) and neglecting body forces, the virtual work reads

$$\int_{\mathcal{B}_0} \mathbf{P} : \operatorname{Grad} \delta\boldsymbol{\varphi}\, \mathrm{d}V + \int_{\mathcal{S}_0} \mathbf{P}_{\mathcal{S}} : \operatorname{Grad} \delta\boldsymbol{\varphi}\, \mathrm{d}A = 0. \tag{5.69}$$

Based on this general weak form, the numerical implementation of the projection and the relaxation approach is carried out in the following.

### 5.3.1 Surface energies by projection

The numerical implementation of the projection approach employs two-dimensional surface elements located on the surface $\mathcal{S}_0$ of the bulk $\mathcal{B}_0$. When introducing the projection approach in Sec. 5.2, two possible formulations and stress-strain pairs were discussed: $\mathbf{P}_\mathrm{p} \leftrightarrow \mathbf{F}$ and $\overline{\mathbf{P}} \leftrightarrow \overline{\mathbf{F}}$. The latter is chosen for the numerical implementation, because the simplifying projection can be applied before further calculations are performed and the implementation can be compared to existing frameworks such as [25]. Stress and deformation terms of the general weak form in Eq. (5.69) are thus replaced by

$$\mathbf{P}_\mathcal{S} \rightarrow \overline{\mathbf{P}} \quad \text{and} \quad \operatorname{Grad} \delta\boldsymbol{\varphi} \rightarrow \overline{\operatorname{Grad}}\, \delta\overline{\boldsymbol{\varphi}} = \frac{\partial \delta\overline{\boldsymbol{\varphi}}}{\partial \Theta^\alpha} \otimes \mathbf{G}^\alpha. \tag{5.70}$$

The residual vector for a local node $i$ of the element $e$ reads

$$\mathbf{R}_e^i = \int_{\mathcal{B}_0^e} \mathbf{P} \cdot \operatorname{Grad} N^i \,\mathrm{d}V + \int_{\mathcal{S}_0^e} \overline{\mathbf{P}} \cdot \overline{\operatorname{Grad}}\, \overline{N}^i \,\mathrm{d}A \tag{5.71}$$

and the global residual at the global node $I$ has the form

$$\mathbf{R}^I = \mathop{\mathbf{A}}_{e=1}^{n_\mathrm{el}} \mathbf{R}_e^i. \tag{5.72}$$

$\mathbf{A}_{e=1}^{n_\mathrm{el}}$ denotes the assembly of all bulk and surface element contributions at the global node $I = 1, \ldots, n_\mathrm{np}$, where $n_\mathrm{np}$ denotes the total number of nodes and $n_\mathrm{el}$ denotes the total number of elements. For the projection method the total number of elements $n_\mathrm{el}$ is defined by the sum over the bulk and surface elements: $n_\mathrm{el} = n_\mathrm{be} + n_\mathrm{se}$. The local tangent stiffness $\mathbf{K}_e^{ij}$ of element $e$ at the local nodes $i$ and $j$ reads

$$\begin{aligned}\left\{\mathbf{K}_e^{ij}\right\}_{ac} = \int_{\mathcal{B}_0^e} \left\{\operatorname{Grad} N^i\right\}_b \left\{\frac{\partial \mathbf{P}}{\partial \mathbf{F}}\right\}_{abcd} \left\{\operatorname{Grad} N^i\right\}_d \mathrm{d}V \\ + \int_{\mathcal{S}_0^e} \left\{\overline{\operatorname{Grad}}\, \overline{N}^i\right\}_b \left\{\frac{\partial \overline{\mathbf{P}}}{\partial \overline{\mathbf{F}}}\right\}_{abcd} \left\{\overline{\operatorname{Grad}}\, \overline{N}^i\right\}_d \mathrm{d}A,\end{aligned} \tag{5.73}$$

where $\partial\mathbf{P}/\partial\mathbf{F}$ is identical to the bulk tangent $\mathbb{A}$ and $\partial\mathbf{P}_\mathrm{p}/\partial\mathbf{F}$ is identical with the tangent $\mathbb{A}_\mathrm{p}$ of the projected surface energy. Finally, the global tangent stiffness is assembled to the global node numbers $I$ and $J$ by

$$\mathbf{K}^{IJ} = \mathop{\mathbf{A}}_{e=1}^{n_\mathrm{el}} \mathbf{K}_e^{ij}. \tag{5.74}$$

An arbitrary element $e$ consists either of a bulk domain $\mathcal{B}_0$ or a surface domain $\mathcal{S}_0$, but never of both. Further information about the surface elements and the determination of

the deformation gradient can be found in [24, 25].

## 5.3.2 Surface energies by relaxation

The numerical implementation of the relaxed deformation gradient does not require surface elements. The key aspect is using a new set of quadrature points within the surface domain. To be more precise, the new set of quadrature points is only activated on the surface of bulk elements belonging to the surface $\mathcal{S}_0$. Sec. 5.3.2.1 describes the novel tetrahedral and hexahedral bulk elements in order to compute the deformation gradient on its surface. Finally, Sec. 5.3.2.2 presents the implementation of the relaxed surface deformation gradient into the finite element framework.

### 5.3.2.1 Bulk elements for surface deformation

This section describes the computation of the deformation gradient on the surface of three-dimensional elements. For that purpose, quadrature points of a two-dimensional element are transformed on the surface of a three-dimensional element. This procedure is presented for tetrahedral and hexahedral elements. Due to neighboring bulk elements, the standard three-dimensional interpolation functions are still employed and can be found in [4, 69]. After the determination of the bulk deformation gradient at the surface, $\mathbf{F}$, a Newton scheme solves the minimization $\inf_{\mathbf{a}} \psi(\widetilde{\mathbf{F}}(\mathbf{F}, \mathbf{a}))$ and finally, the relaxed deformation gradient, $\widetilde{\mathbf{F}}$, is obtained.

The transformation of triangular quadrature points (number of quadrature points $n_{\text{qp}} = 6$) onto the surface of tetrahedral elements is illustrated in the following. For this purpose, the quadrature points and their positions within a triangular element are shown in Fig. 5.2a. Their positions $\boldsymbol{\xi}^q_{\text{qp,tri}}$ are determined by the use of barycentric coordinates $\mathbf{v}_q = [v_1^q, v_2^q, v_3^q]$ with $q = 1, \ldots, n_{\text{qp}}$ (cf. [14]):

$$\boldsymbol{\xi}^q_{\text{qp,tri}}(\mathbf{v}_q) = \frac{1}{v_1^q + v_2^q + v_3^q} \left[ v_1^q \, \boldsymbol{\xi}^1_{\text{tri}} + v_2^q \, \boldsymbol{\xi}^2_{\text{tri}} + v_3^q \, \boldsymbol{\xi}^3_{\text{tri}} \right], \tag{5.75}$$

where the three vertex nodes are

$$\boldsymbol{\xi}^1_{\text{tri}} = \begin{bmatrix} 0 \\ 0 \end{bmatrix}, \quad \boldsymbol{\xi}^2_{\text{tri}} = \begin{bmatrix} 1 \\ 0 \end{bmatrix} \quad \text{and} \quad \boldsymbol{\xi}^3_{\text{tri}} = \begin{bmatrix} 0 \\ 1 \end{bmatrix}. \tag{5.76}$$

The barycentric coordinates and their weights are summarized in Tab. 5.1.

Similarly, the quadrature points' positions on a surface of the tetrahedral element are computed (see Fig. 5.2b). Therefore, Eq. (5.75) is rewritten as

$$\boldsymbol{\xi}^q_{\text{qp,tet}}\left(\boldsymbol{\xi}^A_{\text{tet}}, \boldsymbol{\xi}^B_{\text{tet}}, \boldsymbol{\xi}^C_{\text{tet}}, \mathbf{v}_q\right) = \frac{1}{v_1^q + v_2^q + v_3^q} \left[ v_1^q \, \boldsymbol{\xi}^A_{\text{tet}} + v_2^q \, \boldsymbol{\xi}^B_{\text{tet}} + v_3^q \, \boldsymbol{\xi}^C_{\text{tet}} \right], \tag{5.77}$$

where $\boldsymbol{\xi}^A_{\text{tet}}$, $\boldsymbol{\xi}^B_{\text{tet}}$ and $\boldsymbol{\xi}^C_{\text{tet}}$ denote the vertex nodes of the surface triangular $ABC$. Accord-

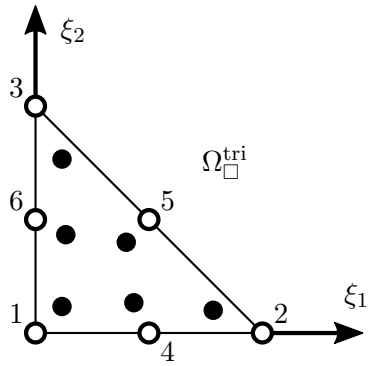


**(a)** Two-dimensional 6-node triangular element $\Omega_\square^{\text{tri}}$ with its natural coordinates $\boldsymbol{\xi} = [\xi_1, \xi_2]$ and the surface area $A_\square^{\text{tri}} = 0.5$.

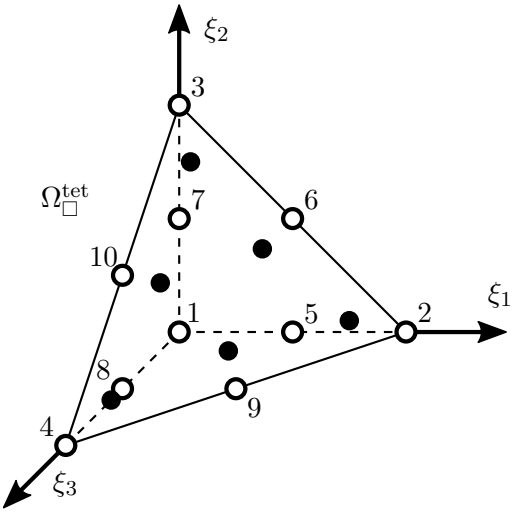


**(b)** Three-dimensional isoparametric 10-node tetrahedral element $\Omega_\square^{\text{tet}}$ with its natural coordinates $\boldsymbol{\xi} = [\xi_1, \xi_2, \xi_3]$ and the volume $V_\square^{\text{tet}} = 1/6$. Surface quadrature points are exemplarily depicted on the surface with their normal in $[1, 1, 1]$-direction.

**Figure 5.2:** Triangular and tetrahedral master elements with nodes (white circles), nodes numbers and $n_{\text{qp}} = 6$ quadrature points (black circles). The edge length is 1.

ing to Fig. 5.2b, the vertex nodes are defined as:

$$\boldsymbol{\xi}_{\text{tet}}^1 = \begin{bmatrix} 0 \\ 0 \\ 0 \end{bmatrix}, \quad \boldsymbol{\xi}_{\text{tet}}^2 = \begin{bmatrix} 1 \\ 0 \\ 0 \end{bmatrix}, \quad \boldsymbol{\xi}_{\text{tet}}^3 = \begin{bmatrix} 0 \\ 1 \\ 0 \end{bmatrix} \quad \text{and} \quad \boldsymbol{\xi}_{\text{tet}}^4 = \begin{bmatrix} 0 \\ 0 \\ 1 \end{bmatrix}. \tag{5.78}$$

In order to reproduce the volume of the master tetrahedral element, $V_\square^{\text{tet}} = 1/6$, the weights have to be adapted by

$$w_q^{\text{tet}} = \frac{1}{3} w_q^{\text{tri}} \quad q = 1, \ldots, n_{\text{qp}}, \tag{5.79}$$

so that the sum of the weights corresponds to the volume of the tetrahedral master element: $\sum_{q=1}^{n_{\text{qp}}} w_q^{\text{tet}} = V_\square^{\text{tet}}$.

Next, the transformation of quadrature points from a quadrilateral element to the surface of a hexahedral element is shown. Fig. 5.3a illustrates the quadrature points' positions within a quadrilateral element ($n_{\text{qp}} = 9$) and Tab. 5.2 summarizes their positions and weights. Their projection onto the surface of a hexahedral element is shown in Fig. 5.3b. Depending on the surface normal $\mathbf{N}$, the transformation of the quadrature

| $q$ | $v_1^q$ | $v_2^q$ | $v_3^q$ | $w_q^{\mathrm{tri}}$ |
|---|---|---|---|---|
| 1 | $a_1$ | $a_1$ | $1-2\,a_1$ | $0.5\,b_1$ |
| 2 | $a_1$ | $1-2\,a_1$ | $a_1$ | $0.5\,b_1$ |
| 3 | $1-2\,a_1$ | $a_1$ | $a_1$ | $0.5\,b_1$ |
| 4 | $a_2$ | $a_2$ | $1-2\,a_2$ | $0.5\,b_2$ |
| 5 | $a_2$ | $1-2\,a_2$ | $a_2$ | $0.5\,b_2$ |
| 6 | $1-2\,a_2$ | $a_2$ | $a_2$ | $0.5\,b_2$ |

**Table 5.1:** Quadrature points' positions and weights, $\mathbf{v}_q = [v_1^q, v_2^q, v_3^q]$ in barycentric coordinates and $w_q^{\mathrm{tri}}$, of the two-dimensional triangular element ($n_{\mathrm{qp}} = 6$, cf. [14]). With $a_1 = 0.445948490915965$, $a_2 = 0.091576213509771$, $b_1 = 0.223381589678010$ and $b_2 = 0.091576213509771$.

| $q$ | $\xi_1^{\mathrm{quad}}$ | $\xi_2^{\mathrm{quad}}$ | $w_q^{\mathrm{quad}}$ |
|---|---|---|---|
| 1 | $-\sqrt{3/5}$ | $-\sqrt{3/5}$ | $25/81$ |
| 2 | $0$ | $-\sqrt{3/5}$ | $40/81$ |
| 3 | $\sqrt{3/5}$c | $-\sqrt{3/5}$ | $25/81$ |
| 4 | $-\sqrt{3/5}$ | $0$ | $40/81$ |
| 5 | $0$ | $0$ | $64/81$ |
| 6 | $\sqrt{3/5}$ | $0$ | $40/81$ |
| 7 | $-\sqrt{3/5}$ | $\sqrt{3/5}$ | $25/81$ |
| 8 | $0$ | $\sqrt{3/5}$ | $40/81$ |
| 9 | $\sqrt{3/5}$ | $\sqrt{3/5}$ | $25/81$ |

**Table 5.2:** Positions and weights of the quadrature points, $\boldsymbol{\xi}^{\mathrm{quad}} = \left[\xi_1^{\mathrm{quad}}, \xi_2^{\mathrm{quad}}\right]$ and $w_q^{\mathrm{quad}}$, of the two-dimensional quadrilateral element (cf. [69]).

points is conducted by the following cases:

$$
\begin{aligned}
\mathbf{N} = \begin{bmatrix}1\\0\\0\end{bmatrix} &: \quad \boldsymbol{\xi}^{\mathrm{hex}} = \begin{bmatrix}1\\ \xi_1^{\mathrm{quad}}\\ \xi_2^{\mathrm{quad}}\end{bmatrix}, \qquad \mathbf{N} = \begin{bmatrix}-1\\0\\0\end{bmatrix} : \quad \boldsymbol{\xi}^{\mathrm{hex}} = \begin{bmatrix}-1\\ \xi_1^{\mathrm{quad}}\\ \xi_2^{\mathrm{quad}}\end{bmatrix},\\
\mathbf{N} = \begin{bmatrix}0\\1\\0\end{bmatrix} &: \quad \boldsymbol{\xi}^{\mathrm{hex}} = \begin{bmatrix}\xi_1^{\mathrm{quad}}\\ 1\\ \xi_2^{\mathrm{quad}}\end{bmatrix}, \qquad \mathbf{N} = \begin{bmatrix}0\\-1\\0\end{bmatrix} : \quad \boldsymbol{\xi}^{\mathrm{hex}} = \begin{bmatrix}\xi_1^{\mathrm{quad}}\\ -1\\ \xi_2^{\mathrm{quad}}\end{bmatrix},\\
\mathbf{N} = \begin{bmatrix}0\\0\\1\end{bmatrix} &: \quad \boldsymbol{\xi}^{\mathrm{hex}} = \begin{bmatrix}\xi_1^{\mathrm{quad}}\\ \xi_2^{\mathrm{quad}}\\ 1\end{bmatrix}, \qquad \mathbf{N} = \begin{bmatrix}0\\0\\-1\end{bmatrix} : \quad \boldsymbol{\xi}^{\mathrm{hex}} = \begin{bmatrix}\xi_1^{\mathrm{quad}}\\ \xi_2^{\mathrm{quad}}\\ -1\end{bmatrix}.
\end{aligned}
\tag{5.80}
$$

In order to reproduce the volume of the hexahedral element, $\sum_{q=1}^{n_{\mathrm{qp}}} w_q^{\mathrm{hex}} = V_{\square}^{\mathrm{hex}}$ has to

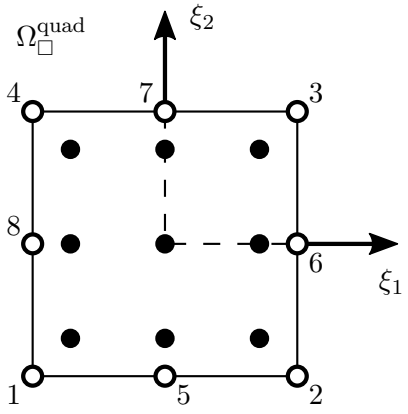


**(a)** Two-dimensional serendipity 8-node quadrilateral element $\Omega_\square^{\text{quad}}$ with its natural coordinates $\boldsymbol{\xi} = [\xi_1, \xi_2]$ and the surface area $A_\square^{\text{quad}} = 4$.

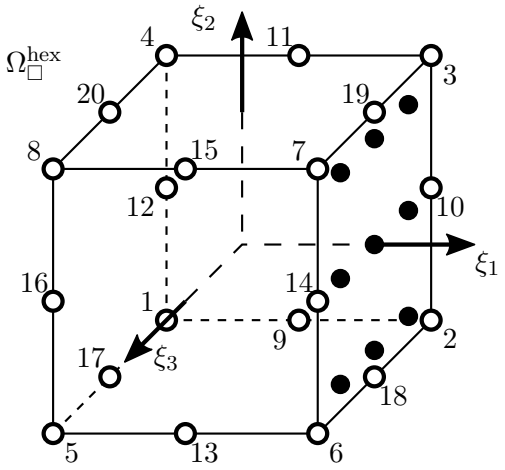


**(b)** Three-dimensional serendipity 20-node hexahedral element $\Omega_\square^{\text{hex}}$ with its natural coordinates $\boldsymbol{\xi} = [\xi_1, \xi_2, \xi_3]$ and the volume $V_\square^{\text{hex}} = 8$. Surface quadrature points are exemplarily depicted on the surface with their normal in $[1, 0, 0]$-direction.

**Figure 5.3:** Triangular and tetrahedral master elements with nodes (white circles), nodes numbers and $n_{\text{qp}} = 9$ quadrature points (black circles). The edge length is 2.

hold. Thus, the weights are converted by

$$w_q^{\text{hex}} = 2\, w_q^{\text{quad}} \quad q = 1, \ldots, n_{\text{qp}}. \tag{5.81}$$

During the numerical implementation, the associated area $\mathrm{d}A_q$ for each quadrature point $q$ on the surface has to be multiplied by the ratio between the side face area of the element including the surface quadrature points, $A_{\text{surf}}$, and the volume of bulk element, $V$. To be more precise, the associated area $\mathrm{d}a_q$ of a surface quadrature point $q$ reads

$$\mathrm{d}A_q = \det(\mathbf{J})\; w_q^{\mathcal{S}}\, \frac{A_{\text{surf}}}{V}. \tag{5.82}$$

Therein, $\mathbf{J}$ denotes the Jacobian matrix. $w_q^{\mathcal{S}}$ is the weight of the surface quadrature point $q$ and is replaced either by $w_q^{\text{tet}}$ or $w_q^{\text{hex}}$.

#### 5.3.2.2 Implementation into the finite element framework

This implementation corresponds to an energetic formulation that inherently contains the relaxation process, i.e., it corresponds to the formulation in Eq. (5.54) with dual conjugates $\mathbf{P}_{\text{r}} \leftrightarrow \mathbf{F}$. Also note that relaxation is independent of prior projection, $\psi_{\text{r}}(\mathbf{C}) = \psi_{\text{r}}\big(\overline{\mathbf{C}}\big)$, as will be proven later during the theoretical comparison in Eq. (5.93). The weak form Eq. (5.69) is transformed into the residual vector at the local node $i$ of

an element $e$ as

$$\mathbf{R}_e^i = \int_{\mathcal{B}_0^e} \mathbf{P} \cdot \operatorname{Grad} N^i \, \mathrm{d}V + \int_{\mathcal{S}_0^e} \mathbf{P}_\mathrm{r} \cdot \operatorname{Grad} N^i \, \mathrm{d}A, \tag{5.83}$$

where the relaxed surface approach $\mathbf{P}_\mathrm{r}$ has been employed for the surface stress $\mathbf{P}_\mathcal{S}$. The local tangent stiffness reads

$$\begin{aligned}\left\{\mathbf{K}_e^{ij}\right\}_{ac} = \int_{\mathcal{B}_0^e} \left\{\operatorname{Grad} N^i\right\}_b \left\{\frac{\partial \mathbf{P}}{\partial \mathbf{F}}\right\}_{abcd} \left\{\operatorname{Grad} N^i\right\}_d \mathrm{d}V \\ + \int_{\mathcal{S}_0^e} \left\{\operatorname{Grad} N^i\right\}_b \left\{\frac{\mathrm{d}\mathbf{P}_\mathrm{r}}{\mathrm{d}\mathbf{F}}\right\}_{abcd} \left\{\operatorname{Grad} N^i\right\}_d \mathrm{d}A.\end{aligned} \tag{5.84}$$

The global residual vector and global tangent stiffness are equal to Eqs. (5.72) and (5.74). $\partial \mathbf{P}/\partial \mathbf{F}$ is identical to bulk tangent $\mathbb{A}$. The tangent matrix of the relaxed surface energy $\mathrm{d}\mathbf{P}_\mathrm{r}/\mathrm{d}\mathbf{F} = \mathbb{A}_\mathrm{r}$ is derived in the following.

As a consequence, the linearization of the relaxed stresses can be written as

$$\mathrm{d}\mathbf{P}_\mathrm{r} = \frac{\partial^2 \psi(\widetilde{\mathbf{F}}(\mathbf{F}, \mathbf{a}))}{\partial \mathbf{F}^2} : \mathrm{d}\mathbf{F} + \frac{\partial^2 \psi(\widetilde{\mathbf{F}}(\mathbf{F}, \mathbf{a}))}{\partial \mathbf{F} \, \partial \mathbf{a}} \cdot \mathrm{d}\mathbf{a}. \tag{5.85}$$

Along relaxed states, the relaxed energy is always stationarity with respect to the jump vector (see Eq. (5.64)) such that the differential of $\partial \psi / \partial \mathbf{a}$ vanishes as well. Linearization of this differential with respect to $\mathbf{a}$ and $\mathbf{F}$ then allows a reformulation of $\mathrm{d}\mathbf{a}$ as

$$\mathrm{d}\left[\frac{\partial \psi(\widetilde{\mathbf{F}}(\mathbf{F}, \mathbf{a}))}{\partial \mathbf{a}}\right] = \mathbf{0} \quad \Rightarrow \quad \mathrm{d}\mathbf{a} = -\left[\frac{\partial^2 \psi(\widetilde{\mathbf{F}}(\mathbf{F}, \mathbf{a}))}{\partial \mathbf{a}^2}\right]^{-1} \cdot \frac{\partial^2 \psi(\widetilde{\mathbf{F}}(\mathbf{F}, \mathbf{a}))}{\partial \mathbf{a} \, \partial \mathbf{F}} : \mathrm{d}\mathbf{F}. \tag{5.86}$$

By inserting Eq. (5.86) into Eq. (5.85) one finally obtains

$$\mathrm{d}\mathbf{P}_\mathrm{r} = \left[\frac{\partial^2 \psi(\widetilde{\mathbf{F}}(\mathbf{F}, \mathbf{a}))}{\partial \mathbf{F}^2} - \frac{\partial^2 \psi(\widetilde{\mathbf{F}}(\mathbf{F}, \mathbf{a}))}{\partial \mathbf{F} \, \partial \mathbf{a}} \cdot \left[\frac{\partial^2 \psi(\widetilde{\mathbf{F}}(\mathbf{F}, \mathbf{a}))}{\partial \mathbf{a}^2}\right]^{-1} \cdot \frac{\partial^2 \psi(\widetilde{\mathbf{F}}(\mathbf{F}, \mathbf{a}))}{\partial \mathbf{a} \, \partial \mathbf{F}}\right] : \mathrm{d}\mathbf{F} \tag{5.87}$$

$$=: \mathbb{A}_\mathrm{r} : \mathrm{d}\mathbf{F}. \tag{5.88}$$

According to Eq. (5.88) and as a result of the underlying variational minimization principle, tangent $\mathbb{A}_\mathrm{r}$ shows major symmetry. Equivalently by replacing the deformation

gradient by the relaxed counterpart, the tangent $\mathbb{A}_\mathrm{r}$ can be rewritten as

$$\mathbb{A}_\mathrm{r} = \frac{\mathrm{d}\mathbf{P}_\mathrm{r}}{\mathrm{d}\mathbf{F}} \tag{5.89}$$

$$= \frac{\partial^2\psi(\widetilde{\mathbf{F}})}{\partial\mathbf{F}^2} - \left[\frac{\partial^2\psi(\widetilde{\mathbf{F}})}{\partial\mathbf{F}^2}\cdot\mathbf{N}\right]\cdot\left[\mathbf{N}\overset{(2)}{\cdot}\frac{\partial^2\psi(\widetilde{\mathbf{F}})}{\partial\mathbf{F}^2}\cdot\mathbf{N}\right]^{-1}\cdot\left[\mathbf{N}\overset{(2)}{\cdot}\frac{\partial^2\psi(\widetilde{\mathbf{F}})}{\partial\mathbf{F}^2}\right]. \tag{5.90}$$

The relaxed deformation gradient is numerically determined from the bulk deformation gradient $\mathbf{F}$ of the new set of quadrature points located at the surface domain $\mathcal{S}_0$ (see Sec. 5.3.2.1). A Newton scheme solves the minimization $\inf_\mathbf{a}\psi(\widetilde{\mathbf{F}}(\mathbf{F},\mathbf{a}))$ and the relaxed deformation gradient is applied to the surface free energy density $\psi_\mathrm{r}(\mathbf{F})$.

# 5.4 Comparison of projection and relaxation concept

## 5.4.1 Analytical results

### 5.4.1.1 Equivalence cases for isotropy and for anisotropy in surface tangent space

The projection and relaxation approach are only equivalent under specific conditions, which mainly requires uniqueness of relaxation and no anisotropy normal to the surface. These conditions can be identified by using principal invariants ($I_{\widetilde{\mathbf{C}}}$, $II_{\widetilde{\mathbf{C}}}$) affecting the isotropic material response and pseudo invariants ($J^{(4)}_{\widetilde{\mathbf{C}}}$, $J^{(5)}_{\widetilde{\mathbf{C}}}$) manipulating the anisotropic material behavior. Therefore, a surface Helmholtz free energy density such as $\psi_\mathrm{r}\left(I_{\widetilde{\mathbf{C}}}, II_{\widetilde{\mathbf{C}}}, J^{(4)}_{\widetilde{\mathbf{C}}}, J^{(5)}_{\widetilde{\mathbf{C}}}\right)$ is assumed. In order to restrict the anisotropy to the tangent space, $\mathbf{d}_0\cdot\mathbf{N}=0$ has to hold, where $\mathbf{d}_0$ defines the direction of the material anisotropy with respect to the undeformed configuration.

Projected and relaxed state coincide if the projection deformation gradient equals the relaxed deformation gradient, reading

$$\widetilde{\mathbf{F}} = \overline{\mathbf{F}} \quad\Leftrightarrow\quad \mathbf{F} - \mathbf{a}\otimes\mathbf{N} = \mathbf{F}\cdot\overline{\mathbf{I}} = \mathbf{F}\cdot[\mathbf{I}-\mathbf{N}\otimes\mathbf{N}] \quad\Leftrightarrow\quad \mathbf{a} = \mathbf{F}\cdot\mathbf{N}. \tag{5.91}$$

Relaxed energy states can be further identified by the necessary stationarity condition

$$\frac{\partial\psi(\widetilde{\mathbf{F}}(\mathbf{F},\mathbf{a}))}{\partial\mathbf{a}} = \frac{\partial\psi}{\partial I_{\widetilde{\mathbf{C}}}} : \frac{\partial I_{\widetilde{\mathbf{C}}}(\widetilde{\mathbf{F}}(\mathbf{F},\mathbf{a}))}{\partial\mathbf{a}} + \frac{\partial\psi}{\partial II_{\widetilde{\mathbf{C}}}} : \frac{\partial II_{\widetilde{\mathbf{C}}}(\widetilde{\mathbf{F}}(\mathbf{F},\mathbf{a}))}{\partial\mathbf{a}}$$
$$+ \frac{\partial\psi}{\partial J^{(4)}_{\widetilde{\mathbf{C}}}} : \frac{\partial J^{(4)}_{\widetilde{\mathbf{C}}}(\widetilde{\mathbf{F}}(\mathbf{F},\mathbf{a}))}{\partial\mathbf{a}} + \frac{\partial\psi}{\partial J^{(5)}_{\widetilde{\mathbf{C}}}} : \frac{\partial J^{(5)}_{\widetilde{\mathbf{C}}}(\widetilde{\mathbf{F}}(\mathbf{F},\mathbf{a}))}{\partial\mathbf{a}} = \mathbf{0}. \tag{5.92}$$

A projected surface deformation is always a compatible relaxed deformation if anisotropy lies in the surface tangent space, because all four derivatives of the invariants indeed vanish if $\mathbf{a}=\mathbf{F}\cdot\mathbf{N}$, see Sec. C.3.1. The reversed implication is not necessarily

true, though. For instance, $\partial J^{(5)}_{\widetilde{\mathbf{C}}}/\partial \mathbf{a} = \mathbf{0}$ leads to a linear set of equations with infinitely many solutions. A projected deformation is just one of them. More generally, one may also construct cases, in which stationarity for relaxation is achieved by non-zero contributions that cancel each other or by trivial energies not depending on any invariant, for which projection is not fulfilled ($\mathbf{a} \neq \mathbf{F} \cdot \mathbf{N}$). Nonetheless it can be stated that projection and relaxation coincide for convex Helmholtz free energy densities (for isotropy and superficial anisotropy), as the only relaxed state must be obtained by projection.

#### 5.4.1.2 Relaxation independent of prior projection

Because the infimum is independent of a shift in the argument, relaxation yields the same solution for the three-dimensional deformation state and for the projection of it

$$\begin{aligned}
\psi_{\mathrm{r}}(\mathbf{C}) &= \inf_{\mathbf{a}} \psi\Big(\big[\mathbf{F} - \mathbf{a} \otimes \mathbf{N}\big]^{\mathrm{T}} \cdot \big[\mathbf{F} - \mathbf{a} \otimes \mathbf{N}\big]\Big) \\
&= \inf_{\mathbf{a}} \psi\Big(\big[\mathbf{F} - [\mathbf{a} + \mathbf{F} \cdot \mathbf{N}] \otimes \mathbf{N}\big]^{\mathrm{T}} \cdot \big[\mathbf{F} - [\mathbf{a} + \mathbf{F} \cdot \mathbf{N}] \otimes \mathbf{N}\big]\Big) \\
&= \inf_{\mathbf{a}} \psi\Big(\big[\overline{\mathbf{F}} - \mathbf{a} \otimes \mathbf{N}\big]^{\mathrm{T}} \cdot \big[\overline{\mathbf{F}} - \mathbf{a} \otimes \mathbf{N}\big]\Big) \\
&= \psi_{\mathrm{r}}\big(\overline{\mathbf{C}}\big)
\end{aligned} \tag{5.93}$$

and the relaxed energy is always equal to or less than the projected energy

$$\psi_{\mathrm{r}}(\mathbf{C}) = \psi_{\mathrm{r}}\big(\overline{\mathbf{C}}\big) \leq \psi\big(\overline{\mathbf{C}}\big) = \psi_{\mathrm{p}}(\mathbf{C})\,.$$

The following proof of non-equivalence provides a specific example for a true inequality in the above equation.

#### 5.4.1.3 Nonequivalence between projection and relaxation

Two exemplarily cases will serve as counter examples that prove the nonequivalence between projection and relaxation. The first counter example is motivated by the deformation state. Combining the requirement for being a projection ($\mathbf{a} = \mathbf{F} \cdot \mathbf{N}$ in Eq. (5.91)) with invertible deformations ($\det(\mathbf{F}) \neq 0$ for physically admissible deformations) and with finite-length normal vectors ($\mathbf{N} \neq \mathbf{0}$), it can be deduced that $\mathbf{a}$ must not vanish for projections, reading: $\mathbf{a} = \mathbf{F} \cdot \mathbf{N} \wedge \det(\mathbf{F}) \neq 0 \wedge \mathbf{N} \neq \mathbf{0} \Rightarrow \mathbf{a} \neq \mathbf{0}$ for projections. Consequently, the relaxation state cannot be a projection if the opposite holds:

$$\text{inequivalence condition 1:} \quad \mathbf{a} = \mathbf{0}. \tag{5.94}$$

Inactive relaxation is thus a sufficient condition for non-equivalence. It coincides with no change in deformation, i.e. $\mathbf{F}_{\mathrm{r}} = \mathbf{F}$ and $\mathbf{C}_{\mathrm{r}} = \mathbf{C}$. This condition can be trivially fulfilled by very simple but physically often unsuitable formulations. Before a specific example is provided, hence another inequality condition that is closer to physical restrictions is

motivated. It is based on the structure of the stress tensor $\widetilde{\mathbf{S}}$.

By definition, the relaxed state requires stationarity with respect to $\mathbf{a}$ as stated in Eq. (5.65). This key condition splits into the following cases that are tested for the projection condition ($\mathbf{a} = \mathbf{F} \cdot \mathbf{N}$ in Eq. (5.91)).

- Case A: $\mathbf{F} \cdot \widetilde{\mathbf{S}} \cdot \mathbf{N} = \mathbf{0}$.
  Considering only physical states with $\det \mathbf{F} \neq 0$, $\widetilde{\mathbf{S}} \cdot \mathbf{N} = \mathbf{0}$ as well as $\widetilde{\mathbf{S}} = S^{\alpha\beta}\, \mathbf{G}_\alpha \otimes \mathbf{G}_\beta$ (in-plane stresses) can be inferred because of symmetry. Consequently, the right Cauchy-Green tensor possesses only an in-plane deformation in the form $\widetilde{\mathbf{C}} = C_{\alpha\beta}\, \mathbf{G}^\alpha \otimes \mathbf{G}^\beta$ and hence $\widetilde{\mathbf{C}} : [\mathbf{N} \otimes \mathbf{N}] = 0$ has to hold. According to Eq. (5.56), this is fulfilled for $\mathbf{a} = \mathbf{F} \cdot \mathbf{N}$ and thus relaxation coincides with projection for stresses with $\mathbf{F} \cdot \widetilde{\mathbf{S}} \cdot \mathbf{N} = \mathbf{0}$.

- Case B: $\mathbf{F} \cdot \widetilde{\mathbf{S}} \cdot \mathbf{N} \neq \mathbf{0}$.
  This case implies a non-vanishing out of-plane normal stress, $\widetilde{S}^{\mathrm{NN}} := \mathbf{N} \cdot \widetilde{\mathbf{S}} \cdot \mathbf{N} \neq 0$, and is further subdivided as follows:
  - Case B1: $\mathbf{F} \cdot \widetilde{\mathbf{S}} \cdot \mathbf{N} \neq \mathbf{0}$ and $\widetilde{\mathbf{S}} = \overline{\mathbf{S}} + \widetilde{S}^{\mathrm{NN}} \mathbf{N} \otimes \mathbf{N}$.

    $$\begin{aligned} & \mathbf{F} \cdot \left[ \overline{\mathbf{S}} + \widetilde{S}^{\mathrm{NN}} \mathbf{N} \otimes \mathbf{N} \right] \cdot \mathbf{N} = \left[ \mathbf{N} \cdot \left[ \overline{\mathbf{S}} + \widetilde{S}^{\mathrm{NN}} \mathbf{N} \otimes \mathbf{N} \right] \cdot \mathbf{N} \right] \mathbf{a} \\ \Rightarrow \quad & \widetilde{S}^{\mathrm{NN}} \mathbf{F} \cdot \mathbf{N} = \widetilde{S}^{\mathrm{NN}}\, \mathbf{a} \quad (\text{because } \overline{\mathbf{S}} \cdot \mathbf{N} = 0) \\ \Leftrightarrow \quad & \mathbf{a} = \mathbf{F} \cdot \mathbf{N} \end{aligned}$$

    Hence, relaxation coincides with projection for out-of-plane stresses that are purely normal to the surface.
  - Case B2: $\mathbf{F} \cdot \widetilde{\mathbf{S}} \cdot \mathbf{N} \neq \mathbf{0}$ and $\widetilde{\mathbf{S}} = \overline{\mathbf{S}} + \widetilde{S}^{\mathrm{NN}} \mathbf{N} \otimes \mathbf{N} + \widetilde{S}^{\mathrm{1N}} [\mathbf{G}_1 \otimes \mathbf{N} + \mathbf{N} \otimes \mathbf{G}_1]$.

    $$\begin{aligned} & \mathbf{F} \cdot \left[ \overline{\mathbf{S}} + \widetilde{S}^{\mathrm{NN}} \mathbf{N} \otimes \mathbf{N} + \widetilde{S}^{\mathrm{1N}} [\mathbf{G}_1 \otimes \mathbf{N} + \mathbf{N} \otimes \mathbf{G}_1] \right] \cdot \mathbf{N} \\ & \qquad = \left[ \mathbf{N} \cdot \left[ \overline{\mathbf{S}} + \widetilde{S}^{\mathrm{NN}} \mathbf{N} \otimes \mathbf{N} + \widetilde{S}^{\mathrm{1N}} \cdot [\mathbf{G}_1 \otimes \mathbf{N} + \mathbf{N} \otimes \mathbf{G}_1] \right] \cdot \mathbf{N} \right] \mathbf{a} \\ \Rightarrow \quad & \widetilde{S}^{\mathrm{NN}} \mathbf{F} \cdot \mathbf{N} + \widetilde{S}^{\mathrm{1N}} \mathbf{F} \cdot \mathbf{G}_1 = \widetilde{S}^{\mathrm{NN}}\, \mathbf{a} \quad (\text{because } \overline{\mathbf{S}} \cdot \mathbf{N} = 0, \mathbf{G}_1 \cdot \mathbf{N} = 0) \\ \Leftrightarrow \quad & \mathbf{a} = \mathbf{F} \cdot \mathbf{N} + \frac{\widetilde{S}^{\mathrm{1N}}}{\widetilde{S}^{\mathrm{NN}}}\, \mathbf{F} \cdot \mathbf{G}_1 \neq \mathbf{F} \cdot \mathbf{N} \end{aligned}$$

    Relaxation therefore does not coincide with projection for out-of-plane stresses that have both normal-normal components and normal-tangential shear components, yielding

    $$\text{inequality condition 2:} \quad \widetilde{S}^{\mathrm{NN}} \neq 0 \text{ and } \widetilde{S}^{\mathrm{1N}} \neq 0. \tag{5.95}$$

The following example indeed proves the nonequivalence between relaxation and projection combining both inequality conditions (5.94) and (5.95). For the sake of simplicity

orthonormal bases $\mathbf{G}^1 = \mathbf{G}_1 = \mathbf{e}_1$, $\mathbf{G}^2 = \mathbf{G}_2 = \mathbf{e}_2$ and $\mathbf{G}^3 = \mathbf{G}_3 = \mathbf{e}_3 = \mathbf{N}$ are assumed. Coefficients of the following example are given with respect to this basis. The example uses the quadratic energy potential

$$\psi = \frac{1}{2}\,\mathbf{E} : \mathbb{G} : \mathbf{E} = \frac{1}{2}\,E_{ij}[G\,\delta_{ik}\,\delta_{jl}]\,E_{kl} = \frac{1}{2}\,G\,E_{ij}^2 \geq 0, \tag{5.96}$$

where the Green-Lagrangian strain tensor is

$$\mathbf{E} = \frac{1}{2}[\mathbf{C} - \mathbf{I}] = \frac{1}{2}\left[\mathbf{F}^{\mathrm{T}} \cdot \mathbf{F} - \mathbf{I}\right], \tag{5.97}$$

and a sheared bulk of the form

$$\mathbf{F} = \mathbf{I} + \gamma\,\mathbf{G}^1 \otimes \mathbf{N} = \begin{bmatrix} 1 & 0 & \gamma \\ 0 & 1 & 0 \\ 0 & 0 & 1 \end{bmatrix} \quad \Rightarrow \quad \psi(\mathbf{F}) = \frac{1}{8}\,G\left[\gamma^4 + 2\,\gamma^2\right]. \tag{5.98}$$

The projected surface energy is a constant in this particular example, because the deformation gradient in normal direction is canceled:

$$\overline{\mathbf{F}} = \overline{\mathbf{I}} = \begin{bmatrix} 1 & 0 & 0 \\ 0 & 1 & 0 \\ 0 & 0 & 0 \end{bmatrix} \quad \Rightarrow \quad \psi_{\mathrm{p}}(\mathbf{F}) = \frac{1}{8}\,G > 0. \tag{5.99}$$

The relaxation for this example energy and deformation reads for arbitrary $\mathbf{a}$

$$\widetilde{\mathbf{F}} = \mathbf{F} - \mathbf{a} \otimes \mathbf{N} = \begin{bmatrix} 1 & 0 & \gamma - a_1 \\ 0 & 1 & -a_2 \\ 0 & 0 & 1 - a_3 \end{bmatrix} \tag{5.100}$$

$$\Rightarrow \quad \psi_{\mathrm{r}}(\mathbf{F}) = \frac{1}{8}\Big[2\,[\gamma - a_1]^2 + 2\,{a_2}^2 + \big[[\gamma - a_1]^2 + {a_2}^2 + [1 - a_3]^2 - 1\big]^2\Big]. \tag{5.101}$$

Relaxation yields the same result as projection if $\mathbf{a} = \mathbf{F} \cdot \mathbf{N}$. Nevertheless, an even lower energy can be achieved for another value of $\mathbf{a}$. The energy is in fact globally minimized at

$$\mathbf{a} = \begin{bmatrix} \gamma \\ 0 \\ 0 \end{bmatrix} \quad \Rightarrow \quad \widetilde{\mathbf{F}} = \mathbf{I} = \begin{bmatrix} 1 & 0 & 0 \\ 0 & 1 & 0 \\ 0 & 0 & 1 \end{bmatrix}, \quad \psi_{\mathrm{r}} = 0. \tag{5.102}$$

The above counter example thus proves that projection and relaxation are generally not equivalent as $\overline{\mathbf{F}} \neq \widetilde{\mathbf{F}}$ and $\psi_{\mathrm{p}} > \psi_{\mathrm{r}}$. It contains the two relevant characteristics mentioned by the two inequality conditions above. Condition Eq. (5.95) is physically more important: the out-of-plane shear component of the form $\boldsymbol{\alpha} \otimes \mathbf{N}$, $\boldsymbol{\alpha} \perp \mathbf{N}$, can be relaxed but is eliminated by projection. This may appear, e.g., by anchoring or

incorporated impurity atoms those do not only modify the tangential reconstruction but also redistribute the atoms in depth of the boundary [1, 27]. Inequality condition Eq. (5.95) is trivially fulfilled and more academic: the projection cannot eliminate all bulk strain measures of Seth-Hill type such as $E_{33} = [C_{33} - 1]/2$. In the limit of the equilibrium state, $\gamma = 0$, even the bulk energy is lower than the projected surface energy. This occurs trivially by applying bulk operators such as determinants to the surface deformation without adaption. Such adaption of the initially three-dimensional bulk energy is advisable for physical interpretation, even if it leads to a constant energy shift and thus does not affect stress and stiffness values. Numerical examples follow in the next section, activating the energy contributions by individual invariants.

## 5.4.2 Numerical analysis

### 5.4.2.1 Setup

The projection and the relaxation approach are illustrated by two numerical examples, a cube free of external loads (Fig. 5.4) and a stretched beam (Fig. 5.5). The systems are discretized by quadratic, serendipity hexahedral bulk elements ($n_{\mathrm{qp}} = 14$) and quadratic, serendipity quadrilateral surface elements ($n_{\mathrm{qp}} = 9$) (projection approach) and quadratic, serendipity hexahedral bulk elements ($n_{\mathrm{qp}} = 14$) with 9 additional surface quadrature points (relaxation approach), respectively. The cube discretization contains 125 uniformly distributed bulk elements and 150 surface elements. The beam discretization contains 256 bulk elements and 288 surface elements. Further note that a mesh bias for quadratic tetrahedral ($n_{\mathrm{qp}} = 5$ for pure bulk elements, $n_{\mathrm{qp}} = 6$ for additional surfaces) and quadratic triangle elements ($n_{\mathrm{qp}} = 6$) was observed. They induced a deformation bias between opposite edges depending on the element orientation and thus have been omitted. Computations are performed with the finite element code FEAP (cf. [65]). The derivations of the implemented tangents of the following energies are shown in Sec. C.3.2.

A compressible hyperelastic neo-Hooke free energy density is chosen for the bulk material as

$$\psi(\mathbf{C}) = \frac{1}{4}\,\lambda \log(\det \mathbf{C})^2 + \frac{1}{2}\,\mu\,[\operatorname{tr} \mathbf{C} - 3 - \log(\det \mathbf{C})] \tag{5.103}$$

$$= \frac{1}{4}\,\lambda \log(III_{\mathbf{C}})^2 + \frac{1}{2}\,\mu\,[I_{\mathbf{C}} - 3 - \log(III_{\mathbf{C}})]\,, \tag{5.104}$$

where $\lambda = 10\,\mathrm{N/mm^2}$ and $\mu = 0.1\,\mathrm{N/mm^2}$ are the Lamé parameters. The surface material response is determined by an objective Mooney-Rivlin free energy density extended

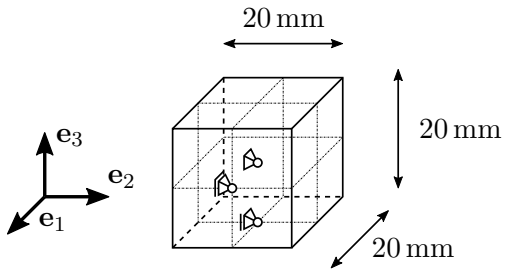


**Figure 5.4:** Geometry and boundary conditions of the cube.

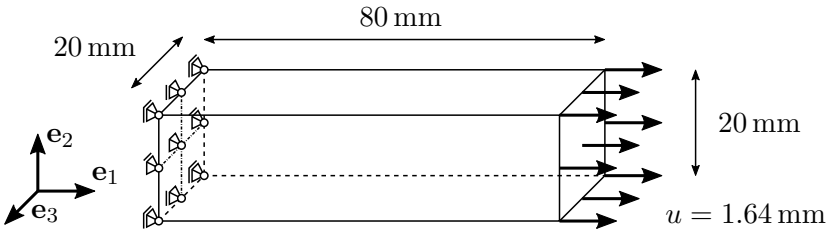


**Figure 5.5:** Geometry and boundary conditions of the beam. Arrows indicate prescribed displacement of the nodes.

by anisotropic terms. Projection and relaxation differ in terms of their derived notation

$$\psi_{\mathrm{p}}\big(\overline{\mathbf{C}}\big) = c_1\,[I_{\overline{\mathbf{C}}} - 3] + c_2\,[II_{\overline{\mathbf{C}}} - 3] + c_4\,J^{(4)}_{\overline{\mathbf{C}}} + c_5\,J^{(5)}_{\overline{\mathbf{C}}}\,, \tag{5.105}$$

$$\psi_{\mathrm{r}}(\mathbf{C}) = \inf_{\mathbf{a}}\,\psi(\widetilde{\mathbf{C}}) = \inf_{\mathbf{a}}\Big(c_1\,\big[I_{\widetilde{\mathbf{C}}} - 3\big] + c_2\,\big[II_{\widetilde{\mathbf{C}}} - 3\big] + c_4\,J^{(4)}_{\widetilde{\mathbf{C}}} + c_5\,J^{(5)}_{\widetilde{\mathbf{C}}}\Big)\,. \tag{5.106}$$

The surface material parameters $c_i$ are activated by a stepwise increase from 0 to 1 N/mm$^2$, showing a quadratic convergence of the Newton-Raphson scheme. Different combinations of surface contributions $c_i$ are activated to compare the individual influences, namely each contribution individually ($c_1$, $c_2$, $c_3$ and $c_4$) and $c_1$ in combination with $c_2$. The special case of similar bulk and surface energy formulations would be achieved for the incompressible Neo-Hooke limit at $c_1 = \mu/2$, but this intermediate setting did not show specific peculiarities among the range of variations. The first and second term $c_1$ and $c_2$ or the first and second principal invariants $I$ and $II$, respectively, represent an isotropic material behavior of the surface. In contrast to this, the material parameters $c_4$ and $c_5$ generate an anisotropic material response within the surface by activating the pseudo invariants $J^{(4)}$ and $J^{(5)}$. Thus, the influence of the different principal invariants (see Eq. (5.25)) and pseudo invariants (see Eq. (5.29)) can be investigated. In the following, the direction of the anisotropy is denoted by $\mathbf{d}_0$. Thus, the structural tensor reads ${}^{(1)}\mathbf{M} = \mathbf{d}_0 \otimes \mathbf{d}_0$. Two anisotropic cases are studied: $\mathbf{d}_0 \cdot \mathbf{N} = 0$, such that $\mathbf{d}_0$ is revolving around the $\mathbf{e}_1$-direction, and $\mathbf{d}_0 \cdot \mathbf{N} \neq 0$ with a constant $\mathbf{d}_0$.

#### 5.4.2.2 Numerical results

The isotropic energy reduces and convexifies the cube surface, while in-plane anisotropy yields both convex and concave curvatures, Fig. 5.6. Convex surfaces appear where the anisotropic energy is active in terms of $\mathbf{d}_0$. Concave surfaces develop on surfaces that are oriented with the revolving direction of $\mathbf{d}_0$, which is around $\mathbf{e}_1$ in the present example and where anisotropy vector $\mathbf{d}_0$ vanishes. Concave surfaces develop also for the stretched beam, Fig. 5.7, while convex surfaces are prevented by the boundary conditions for the case $\mathbf{d}_0 = \mathbf{e}_1 \times \mathbf{N}$. Changing the revolving direction to $\mathbf{d}_0 = \mathbf{e}_2 \times \mathbf{N}$, the long side faces of the beam perpendicular to $\mathbf{e}_2$ will develop a slight curvature.

Simulations of the relaxation approach did not find a unique relaxed energy state for in-plane anisotropy ($\mathbf{N} \cdot \mathbf{d}_0 = 0$). This issue has been anticipated in Sec. 5.4.1.1 and it has been shown that $\overline{\mathbf{C}} = \widetilde{\mathbf{C}}$ holds. To be more precise, the derivatives of the pseudo invariants $J^{(4)}_{\widetilde{\mathbf{C}}}$ and $J^{(5)}_{\widetilde{\mathbf{C}}}$ are independent of the deformation gradient jump $\mathbf{a}$ and identical with the invariants of the projection approach $J^{(4)}_{\overline{\mathbf{C}}}$ and $J^{(5)}_{\overline{\mathbf{C}}}$. However, the projection ($\mathbf{a} = \mathbf{F} \cdot \mathbf{N}$) is only one of infinitely many solutions. For the considered case, $\mathbf{N} \cdot \mathbf{d}_0 = 0$, the second derivative of the pseudo invariant $J^{(4)}_{\widetilde{\mathbf{C}}}$ vanishes automatically (see Eq. (C.28)) and the second derivative of the second pseudo invariant $\partial^2 J^{(5)}_{\mathbf{C}_\mathrm{r}} / \partial \mathbf{a}^2 = \mathbf{0}$ is rank-deficient (see Eq. (C.29)). This can be illustrated by the example case

$$\mathbf{d}_0 = \begin{bmatrix} 0 \\ 0 \\ 1 \end{bmatrix}, \quad \mathbf{N} = \begin{bmatrix} 0 \\ 1 \\ 0 \end{bmatrix}, \quad \mathbf{F} = \mathbf{I} \quad \text{and} \quad \mathbf{a} = \begin{bmatrix} a_1 \\ a_2 \\ a_3 \end{bmatrix} = \mathbf{F} \cdot \mathbf{N} = \begin{bmatrix} 0 \\ 1 \\ 0 \end{bmatrix}, \tag{5.107}$$

one obtains for the derivatives (see Eqs. (C.21) and (C.29))

$$\frac{\partial J^{(5)}_{\widetilde{\mathbf{C}}}}{\partial \mathbf{a}} = \begin{bmatrix} 0 \\ 0 \\ -a_3 \end{bmatrix} = \mathbf{0} \quad \text{and} \quad \frac{\partial^2 J^{(5)}_{\widetilde{\mathbf{C}}}}{\partial \mathbf{a}^2} = \begin{bmatrix} 0 & 0 & 0 \\ 0 & 0 & 0 \\ 0 & 0 & 2 \end{bmatrix}. \tag{5.108}$$

The second derivatives of the invariants with respect to the jump $\mathbf{a}$ are therefore singular

$$\det\left( \frac{\partial^2 J^{(4)}_{\widetilde{\mathbf{C}}}}{\partial \mathbf{a}^2} \right) = 0 \quad \text{and} \quad \det\left( \frac{\partial^2 J^{(5)}_{\widetilde{\mathbf{C}}}}{\partial \mathbf{a}^2} \right) = 0. \tag{5.109}$$

As a result, the numerical problem is ill-posed, more precisely the tangent $\mathbb{A}_\mathrm{r}$ in Eq. (5.90) is degenerate as anticipated by the theoretical analysis and by the example. Further modification of the numerical scheme is necessary to force a unique solution, e.g., numerical perturbations, inverse reformulation and/or stochastic imperfections, but this exceeds the scope of the work.

Projection and relaxation approach differ in the case of out-of-plane anisotropy. While projection onto the surface results in significant distortion, relaxation compensates the

anisotropy contribution in the cube and the stretched beam examples, Figs. 5.6 and 5.7. Out-of-plane anisotropy thus clearly distinguishes between the physical capabilities of projection and relaxation. Also in contrast to in-plane anisotropy, the numerical relaxation examples show convergence towards a unique minimum.

In summary, all numerical results are in exact agreement with the theoretical predictions: (i) projection and relaxation coincide for isotropy and in-plane anisotropy, (ii) the equivocality of the relaxed jump poses numerical difficulties for the relaxation simulations of in-plane anisotropy and (iii) out-of-plane anisotropy can be relaxed but yields distortion when projected.

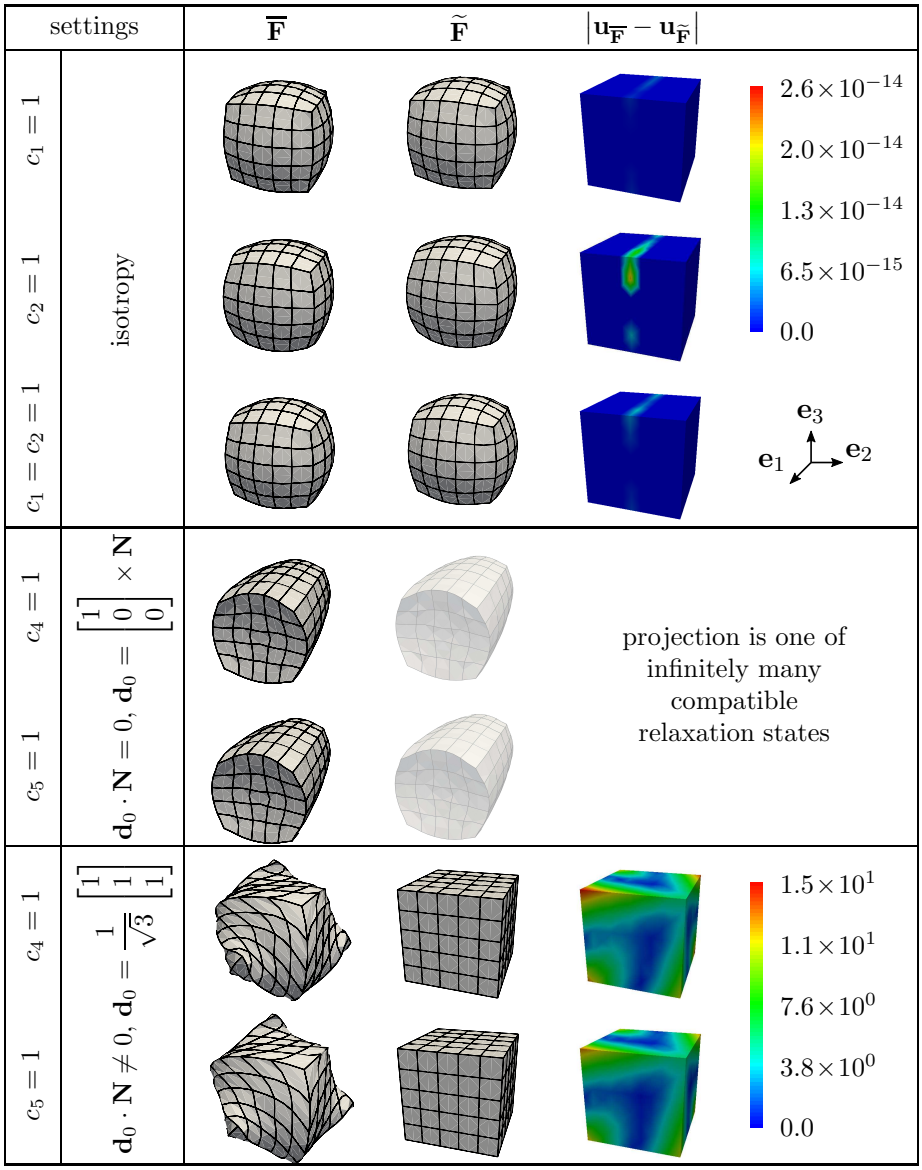


**Figure 5.6:** Deformation of the free cube by the projection approach, $\overline{\mathbf{F}}$, and the relaxation approach, $\widetilde{\mathbf{F}}$. Invariant weighting factors $c_i$ are given in [N/mm$^2$]. They are zero when no value is given. The difference of the displacement between both approaches, $|\mathbf{u}_{\overline{\mathbf{F}}} - \mathbf{u}_{\widetilde{\mathbf{F}}}|$, is given in [mm]. The anisotropy vector $\mathbf{d}_0$ revolves around $\mathbf{e}_1$ in the middle rows four and five. Also note for these cases that no unique minimum exists for relaxation of the deformation gradient jump $\mathbf{a}$, which is why a transparent plot of the projected solution is shown, which is one of the infinitely many solutions.

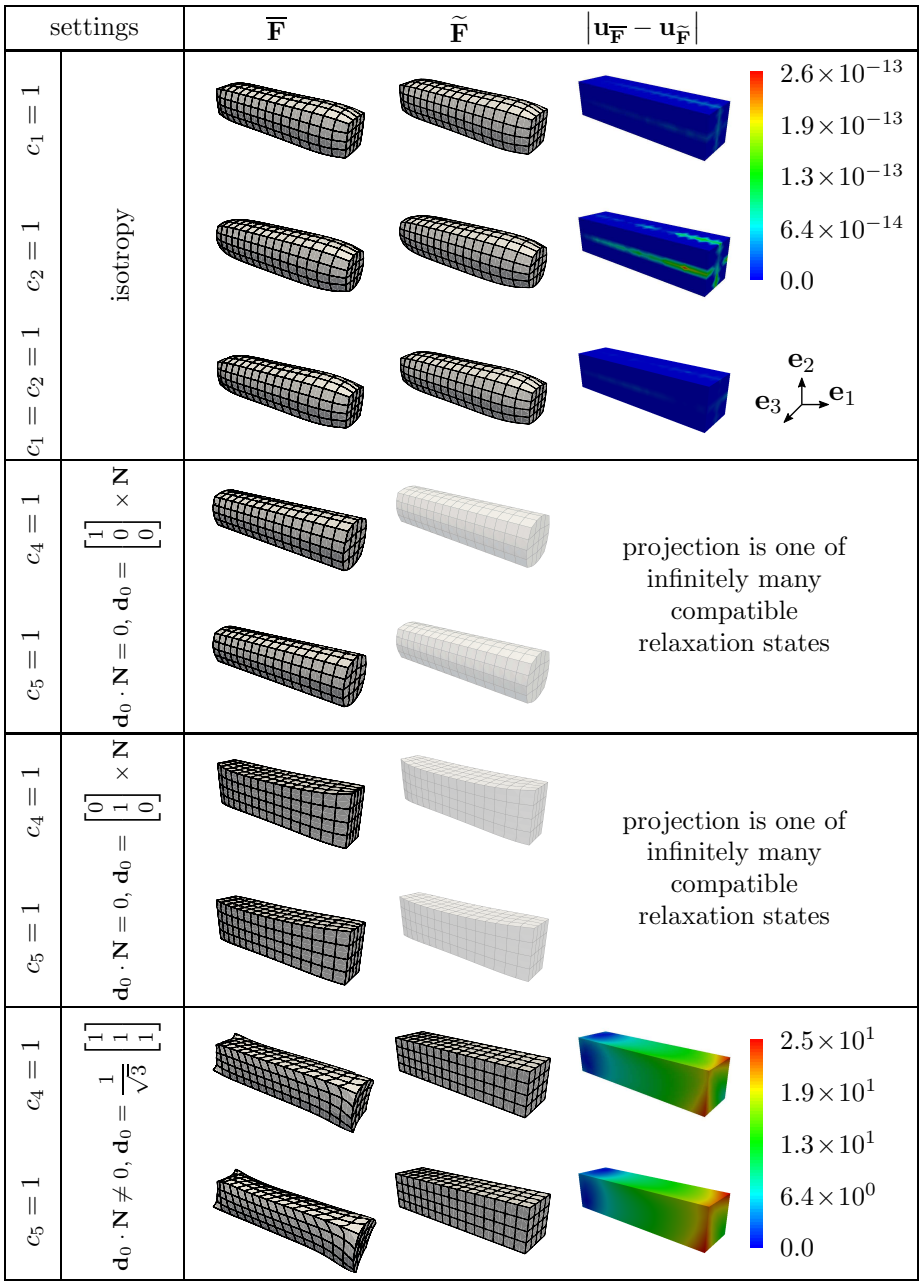


**Figure 5.7:** Deformation of the stretched beam by the projection approach, $\overline{\mathbf{F}}$, and the relaxation approach, $\widetilde{\mathbf{F}}$. Invariant weighting factors $c_i$ are given in [N/mm$^2$]. They are zero when no value is given. The difference of the displacement between both approaches, $|\mathbf{u}_{\overline{\mathbf{F}}} - \mathbf{u}_{\widetilde{\mathbf{F}}}|$, is given in [mm]. The anisotropy vector $\mathbf{d}_0$ revolves around $\mathbf{e}_1$ in rows four and five and around $\mathbf{e}_2$ in rows six and seven. Also note for these cases that no unique minimum exists for relaxation of the deformation gradient jump $\mathbf{a}$, which is why a transparent plot of the projected solution is shown, which is one of the infinitely many solutions.

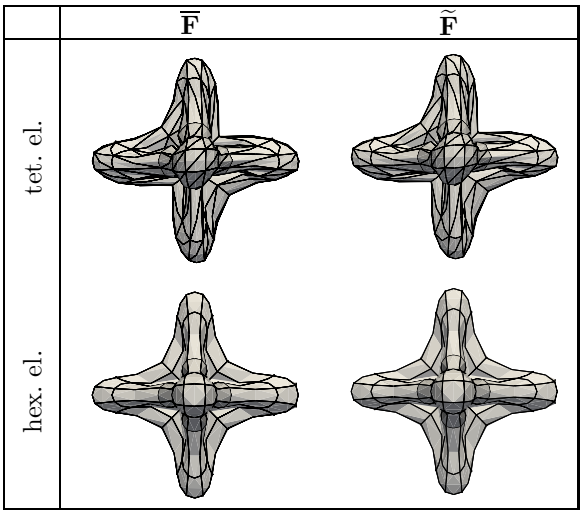


**Figure 5.8:** Deformation scaled with the factor 5 in the $\mathbf{e}_1$-$\mathbf{e}_2$-plane of the free cube by the projection approach, $\overline{\mathbf{F}}$, and the relaxation approach, $\widetilde{\mathbf{F}}$, meshed with a tetrahedral/triangular elements in the first row and hexahedral/quadrilateral elements in the second row. Only the first invariant $I$ is activated by $c_1 = 1\,\mathrm{N/mm^2}$.

As mentioned at the beginning of Sec. 5.4.2.1, a mesh bias is observed. This is shown for the free cube illustrated in Fig. 5.4 by meshing with tetrahedral and triangular elements as well as with hexahedral and quadrilateral elements. Fig. 5.8 clearly illustrates the deformation bias between opposite edges by the use of the tetrahedral and triangular elements for the projection and relaxed approach in the first row. Nevertheless, both approaches lead to the same results as can be seen in Fig. 5.9 in the first and second row. The same figures show that this deformation bias does not arise by using hexahedral and quadrilateral elements. The difference between the different meshes is pointed out in the third row in Fig. 5.9.

## 5.5 Conclusion & Outlook

Motivated by observations of local coupling between bulk and surface deformation, two methods to model surface elasticity using the underlying bulk deformation state were derived. Namely, projection and relaxation were introduced. Both approaches modify the deformation state as an argument of the energy potential and derive the surface stress as a thermodynamically consistent conjugate. The projection approach captures classic in-plane stresses. The relaxation approach adds another degree of freedom to capture reorientation of surface components that is known from liquid nematic crystals or from incorporation of atoms into the boundary region.

A projected deformation is always a relaxed deformation if anisotropy lies in the surface tangent space. Equivalence is however not guaranteed. On one hand, a unique

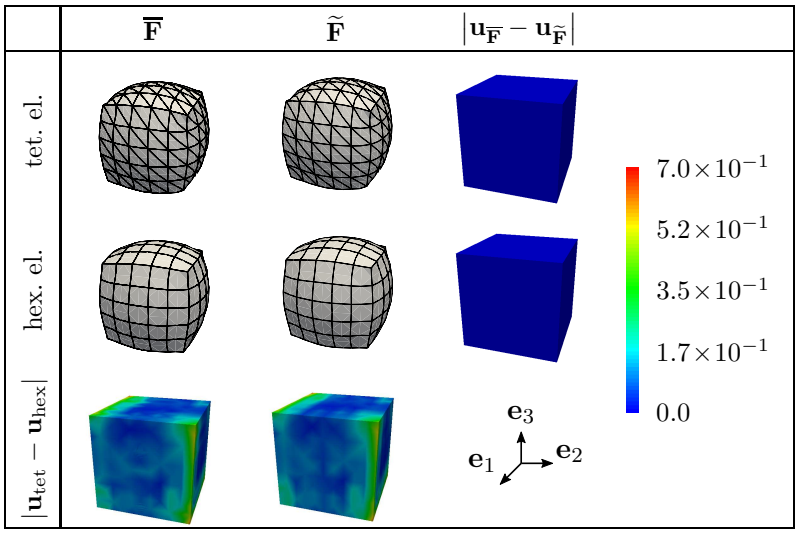


**Figure 5.9:** Deformation of the free cube by the projection approach, $\overline{\mathbf{F}}$, and the relaxation approach, $\widetilde{\mathbf{F}}$, meshed with a tetrahedral/triangular elements in the first row and hexahedral/quadrilateral elements in the second row. Only the first invariant $I$ is activated by $c_1 = 1\,\mathrm{N/mm^2}$. The differences between both approaches, $|\mathbf{u}_{\overline{\mathbf{F}}} - \mathbf{u}_{\widetilde{\mathbf{F}}}|$, and the difference between the meshes, $|\mathbf{u}_{\mathrm{tet}} - \mathbf{u}_{\mathrm{hex}}|$, are given in [mm].

solution may also not be available for the relaxation model due to the additional degree of freedom. On the other hand, relaxation is able to reduce the energy of out-of-plane shear components, which are ignored by projection. In addition to the theoretical investigations, the finite-element simulations of a load-free cube show the typical behavior of surface minimization for an isotropic surface energy. The anisotropic, stretched beam illustrates how relaxation is able to decrease and even eliminate energy contributions compared to direct projection.

Finally, both proposed methods constitute a valuable alternative to conventional surface models, providing their individual set of physical and computational capabilities. Their stress responses are not restricted by *ad-hoc* assumptions and derive from a bulk-type potential. This guarantees coupling to the underlying bulk physics and fulfills the principles of thermodynamically consistent continuum modeling. The examples underline the extra complexity of surface mechanics and the need for a comprehensive modeling framework. Future work will include application to experimental data of liquid and solid surfaces and more complex geometries. Moreover, inelastic surfaces will be studied with particular emphasis on the individual behavior of the projection and the relaxation approach.

# 6 Concluding remarks

This work has focused on the modeling of material interfaces and surfaces. Approaches for the atomistic-to-continuum transition of material parameters and the modeling of mechanical surfaces have been presented.

In contrast to previous frameworks, the novel Ritz-type homogenization approach described in Ch. 3 allows the determination of surface parameters informed by molecular dynamics simulations in which relaxation is taken into account. To be more precise, the respective configurations are in equilibrium – unlike, for instance, within the UBER model. The homogenization approach is based on the principle of energy equivalence. Using the example of copper, the homogenization approach leads to a very good agreement with literature data for the bulk material and surface material. Only the stiffness parameters of the surface material deviate. However, it has been shown that the contribution of the stiffness to the total energy is negligibly small in comparison to the ground state energy. In Ch. 4 the Ritz-type homogenization approach has been applied to thermoelastic bulk materials.

The modeling of mechanical surfaces presented in Ch. 5 deals with two approaches: projection and relaxation. In a nutshell, the projection approach considers classic in-plane stresses and the relaxation approach adds another degree of freedom to capture reorientation of surface components. Both approaches fulfill all fundamental principles of material modeling such as the first law of thermodynamics, balance of angular momentum and the principle of material frame indifference. It has been shown that both approaches coincide for isotropic and in-plane anisotropic material behavior. Only for out-of-plane anisotropy the results deviate. Thereby, the projection approach ignores the out-of-plane shear components which are reduced by the relaxation approach.

# A Ritz-type homogenization approach for surface material

## A.1 Numerics

This section adds technical details on the simulation settings. Atomistic simulations are carried out by the molecular dynamic code LAMMPS (cf. [52]). The underlying potential was developed by Oh & Johnson (cf. [45]). The minimization style is set to the Polak-Ribiere version of the conjugate gradient algorithm (LAMMPS command: `min_style cg`). The moving of any atom within a single line search is restricted to 1 pm and the line search algorithm is set to quadratic (`min_modify dmax 1.0e-2 line quadratic`). The minimize command is run with `minimize 1.0e-16 1.0e-10 1e6 1e6`. Two complete and executable input scripts for atomistic simulations with LAMMPS are given in Sec. A.2.

Continuum simulations are performed by the finite element code FEAP developed by Taylor & Govindjee (cf. [65]). The finite element computations are performed with 10-node-quadratic-tetrahedron-elements with five quadrature points for the bulk material and 6-node-quadratic-triangle-elements with six quadrature points for the surface material. The distribution of the quadrature points and the shape functions are defined in [69] and [14]. The order of the Voigt-notation in FEAP differs from [38] as used in Eq. (3.14), reading for instance $\sigma_{11}$, $\sigma_{22}$, $\sigma_{33}$, $\sigma_{12}$, $\sigma_{23}$ and $\sigma_{13}$.

The numeric minimization of the Ritz method is performed by using the simplex downhill algorithm developed by Nelder & Mead [43]. The numerical optimization by means of the Nelder-Mead algorithm is consecutively started several times with results from its last run until convergence.

## A.2 Input scripts for atomistic simulations

This section gives two exemplary, executable input scripts for LAMMPS. Only surface simulations with a thickness of $a_{\mathcal{B}} = 20\, n_{\mathrm{uc}}$ are considered. First, the input script of the load case $i = 1$ with $\bar{\mathbf{F}}^{(1)} = \mathbf{I}$ ("relaxation", zero-load) is presented. Subsequently, the input script for the load case $i = 10$ considering a combination of axial tension and

shear is shown. Therein, the strain amplitude is increased stepwise until the maximum of $\epsilon = 0.001$ is achieved.

```
log relaxation.log

units metal
dimension 3
boundary p p p
atom_style atomic

variable latparam equal 3.614859998
variable atomsx equal 5
variable atomsy equal 5
variable atomsz equal 20
variable atomsgap equal 20
variable atomsb equal 0.5*${atomsz}
variable lxx equal ${atomsx}*${latparam}
variable lyy equal ${atomsy}*${latparam}
variable lzz equal (${atomsz}+${atomsgap})*${latparam}
variable lbb equal ${atomsb}*${latparam}
variable geomtol equal 1.0e-4

variable etol equal 1.0e-16
variable ftol equal 1.0e-10
variable maxiter equal 1000000
variable maxeval equal 1000000
variable dmax equal 1.0e-2

region whole prism 0.0 $(v_lxx) 0.0 $(v_lyy) 0.0
   ↪ $(v_lzz) 0.0 0.0 0.0 units box
create_box 2 whole

region lower prism 0.0 $(v_lxx) 0.0 $(v_lyy) 0.0
   ↪ $(v_lbb-v_geomtol) 0.0 0.0 0.0 units box
lattice fcc $(v_latparam) orient x 1 0 0 orient y 0 1
   ↪ 0 orient z 0 0 1
create_atoms 1 region lower
group lower region lower

region upper prism 0.0 $(v_lxx) 0.0 $(v_lyy)
   ↪ $(v_lzz-v_lbb-v_geomtol) $(v_lzz) 0.0 0.0 0.0
   ↪ units box
```

```
35 lattice fcc $(v_latparam) orient x 1 0 0 orient y 0 1
     ↪ 0 orient z 0 0 1
36 create_atoms 2 region upper
37 group upper region upper
38
39 # Need to set mass to something, just to satisfy LAMMPS
40 mass * 1.0e-20
41
42 pair_style      eam/alloy
43 pair_coeff * * Cu_OhJohnson.eam.alloy Cu Cu
44 neighbor 2.0 bin
45 neigh_modify delay 10 check yes
46
47 min_style cg
48 min_modify dmax ${dmax} line quadratic
49
50 thermo 100
51 thermo_style custom step temp pe lx ly lz xy xz yz vol
     ↪ press pxx pyy pzz pxy pyz pxz
52 thermo_modify norm no
53 thermo_modify format float %16.15e
54
55 compute peng all pe/atom
56 compute stre all stress/atom NULL
57
58 dump 1 all custom 1000 dump.relaxation type x y z
     ↪ c_peng c_stre[1] c_stre[2] c_stre[3]
59 dump_modify 1 format line "%d %16.15e %16.15e %16.15e
     ↪ %16.15e %16.15e %16.15e %16.15e"
60
61 minimize ${etol} ${ftol} ${maxiter} ${maxeval}
62
63 write_restart relaxation.restart
```

```
1 log eps11_0.0_0.001_eps12_-0.0_-0.001_step_0.0001.log
2
3 units metal
4 dimension 3
5 boundary p p p
6 atom_style atomic
7 variable latparam equal 3.61486
8 variable atomsx equal 5
```

```
variable atomsy equal 5
variable atomsz equal 20
variable atomsgap equal 20
variable atomsb equal 0.5*${atomsz}
variable lxx equal ${atomsx}*${latparam}
variable lyy equal ${atomsy}*${latparam}
variable lzz equal (${atomsz}+${atomsgap})*${latparam}
variable lbb equal ${atomsb}*${latparam}
variable geomtol equal 1.0e-4

variable eps equal 0.0001
variable etol equal 1.0e-16
variable ftol equal 1.0e-10
variable maxiter equal 1000000
variable maxeval equal 1000000
variable dmax equal 1.0e-2

read_restart relaxation.restart

# Need to set mass to something, just to satisfy LAMMPS
mass * 1.0e-20

pair_style      eam/alloy
pair_coeff * * Cu_OhJohnson.eam.alloy Cu Cu
neighbor 2.0 bin
neigh_modify delay 10 check yes

min_style cg
min_modify dmax ${dmax} line quadratic

thermo 100
thermo_style custom step temp pe lx ly lz xy xz yz vol
   ↪ press pxx pyy pzz pxy pyz pxz
thermo_modify norm no
thermo_modify format float %16.15e

change_box all x delta 0 $(v_atomsx*v_latparam*v_eps)
   ↪ xy delta $(-v_eps*v_lxx) boundary p p p remap
   ↪ units box
minimize ${etol} ${ftol} ${maxiter} ${maxeval}

```

```
47 change_box all x delta 0 $(v_atomsx*v_latparam*v_eps)
     ↪ xy delta $(-v_eps*v_lxx) boundary p p p remap
     ↪ units box
48 minimize ${etol} ${ftol} ${maxiter} ${maxeval}
49
50 change_box all x delta 0 $(v_atomsx*v_latparam*v_eps)
     ↪ xy delta $(-v_eps*v_lxx) boundary p p p remap
     ↪ units box
51 minimize ${etol} ${ftol} ${maxiter} ${maxeval}
52
53 change_box all x delta 0 $(v_atomsx*v_latparam*v_eps)
     ↪ xy delta $(-v_eps*v_lxx) boundary p p p remap
     ↪ units box
54 minimize ${etol} ${ftol} ${maxiter} ${maxeval}
55
56 change_box all x delta 0 $(v_atomsx*v_latparam*v_eps)
     ↪ xy delta $(-v_eps*v_lxx) boundary p p p remap
     ↪ units box
57 minimize ${etol} ${ftol} ${maxiter} ${maxeval}
58
59 change_box all x delta 0 $(v_atomsx*v_latparam*v_eps)
     ↪ xy delta $(-v_eps*v_lxx) boundary p p p remap
     ↪ units box
60 minimize ${etol} ${ftol} ${maxiter} ${maxeval}
61
62 change_box all x delta 0 $(v_atomsx*v_latparam*v_eps)
     ↪ xy delta $(-v_eps*v_lxx) boundary p p p remap
     ↪ units box
63 minimize ${etol} ${ftol} ${maxiter} ${maxeval}
64
65 change_box all x delta 0 $(v_atomsx*v_latparam*v_eps)
     ↪ xy delta $(-v_eps*v_lxx) boundary p p p remap
     ↪ units box
66 minimize ${etol} ${ftol} ${maxiter} ${maxeval}
67
68 change_box all x delta 0 $(v_atomsx*v_latparam*v_eps)
     ↪ xy delta $(-v_eps*v_lxx) boundary p p p remap
     ↪ units box
69 minimize ${etol} ${ftol} ${maxiter} ${maxeval}
70
71 change_box all x delta 0 $(v_atomsx*v_latparam*v_eps)
     ↪ xy delta $(-v_eps*v_lxx) boundary p p p remap
```

```
    ↪ units box
minimize ${etol} ${ftol} ${maxiter} ${maxeval}
```

# B Ritz-type homogenization approach for thermoelastic material

## B.1 Numerical performance

This section describes the settings of the atomistic simulations required for the extension of the Ritz-type homogenization approach to a thermoelastic material. The atomistic simulations are performed with the molecular dynamics code LAMMPS (cf. [11, 52]). In order to reach a so-called "initial state" (in Tab. 4.1 defined as load case $i = 1$) as a starting point for all following simulations, the RVE is heated to the desired temperature $\Theta_0$ by the use of the $N\mathbf{t}T$ ensemble. In this ensemble, the pressure and the temperature of the RVE are specified and stated by the command `fix npt`. Due to prescribed deformations and thermal heating, load cases $i > 1$ (see Tab. 4.1) require an $NVT$ ensemble. Therefore, the `fix npt` command is replaced by `fix nvt` in order to specify the macroscopic deformation gradient and the temperature. Each simulation performs 100.000 time steps with a time step of 0.001 ps. Two executable input scripts are presented in Sec. B.2.

Due to oscillations of some quantities during atomistic simulations (see Figs. B.1 and B.2), the configuration used as input for the continuum computations is generated by the moving average. In order to obtain a large range of data for the moving average, the atomistic system is allowed to "relax" over a large number of time steps. Therefore, simulations with mechanical loads are split into two steps: (i) within the first 10% of the time steps, the RVE is deformed stepwise to the deformation $\bar{\mathbf{F}}^{(i)}$ and is heated to the temperature $\bar{\Theta}^{(i)}$, (ii) within the last 90% of the time steps, the deformation and temperature are kept constant in order to obtain a relaxation for the moving average. Simulations considering only thermal heating and no mechanical deformations, relax due to the damping factors within the `fix nvt` or `fix npt` command after less than 25% of the time steps. Finally, in order to avoid the influence of the stepwise deformation and heating, the moving average is generated over 75% of the time steps.

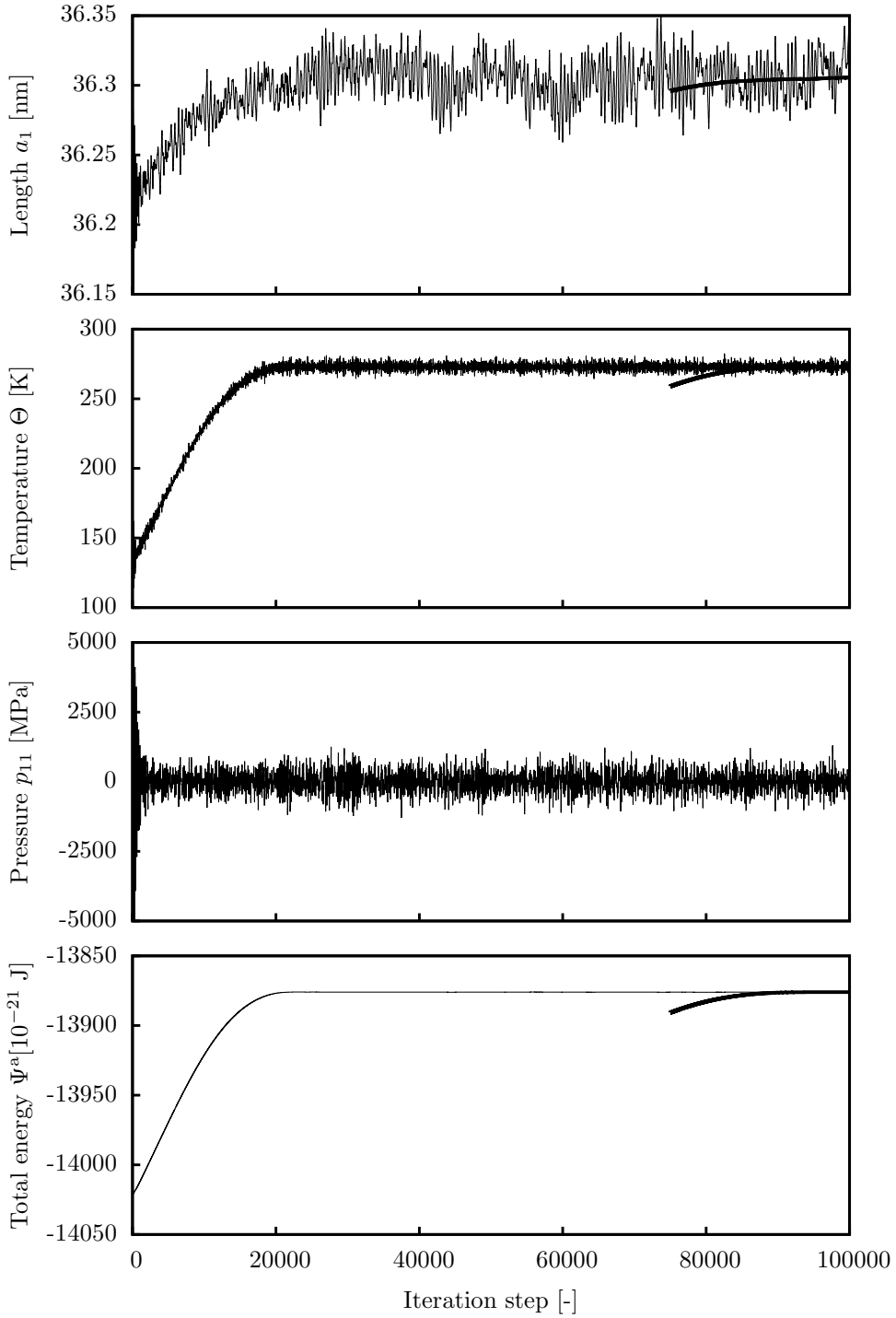


**Figure B.1:** Oscillation (thin lines) and moving average (thick lines) for selected quantities of the atomistic system for the load case $i = 1$ with $\Theta_0 = 273\,\mathrm{K}$ (cf. Tab. 4.1): edge length $a_1$, temperature $\Theta$, pressure $p_{11}$ in $\mathbf{e}_1$-direction and the total energy $\Psi^a$ over 100.000 time steps. The moving average overlaps with the oscillation in some charts.

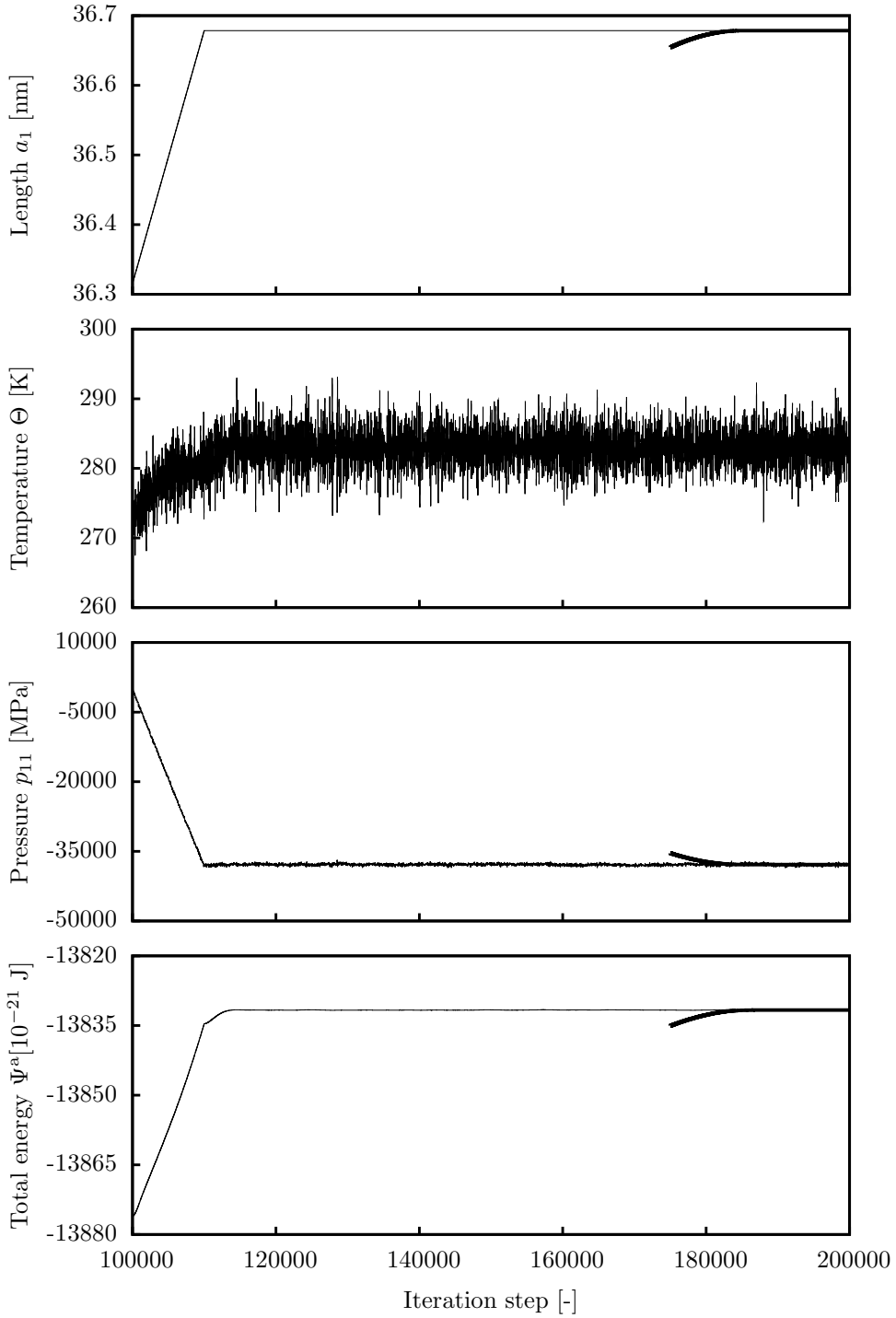


**Figure B.2:** Oscillation (thin lines) and moving average (thick lines) for selected quantities of the atomistic system for the load case $i = 6$ with $\epsilon = 0.01$, $\Theta_0 = 273\,\mathrm{K}$ and $\Delta\bar{\Theta}^{(i)} = 10\,\mathrm{K}$ (cf. Tab. 4.1): edge length $a_1$, temperature $\Theta$, pressure $p_{11}$ in $\mathbf{e}_1$-direction and the total energy $\Psi^a$ over 100.000 time steps. The moving average overlaps with the oscillation in some charts.

## B.2 Input scripts for atomistic simulations

This section shows two executable input scripts for LAMMPS. First, the input script in order to run the "relaxation" load case $i = 1$ for heating from 0 K to $\Theta_0 = 273$ K in the isothermal-isobaric ($N\mathbf{t}T$) ensemble. Subsequently, the input script for load case $i = 6$ using the canonical ($NVT$) ensemble follows. Therein, the temperature is increased to 283 K ($\Delta\Theta = 10$ K) and the strain amplitude is set to $\epsilon = 0.01$. Selected results of both load cases are already presented in Figs. B.1 and B.2.

```
log Cu_Tstart=0_Tend=273.log

units metal
dimension 3
boundary p p p
atom_style atomic
variable latparam equal 3.615
variable atoms equal 10
variable lxx equal ${atoms}*${latparam}
variable lyy equal ${atoms}*${latparam}
variable lzz equal ${atoms}*${latparam}

variable dt equal 0.001
variable nrun equal 100000
variable Tend equal 273

lattice fcc ${latparam}
region whole prism 0 ${lxx} 0 ${lyy} 0 ${lzz} 0 0 0
  ↪ units box
create_box 1 whole
lattice fcc ${latparam} orient x 1 0 0 orient y 0 1 0
  ↪ orient z 0 0 1
create_atoms 1 region whole

pair_style eam/alloy
pair_coeff * * Cu_mishin1.eam.alloy Cu
neighbor 2.0 bin
neigh_modify delay 10 check yes

compute disp all displace/atom
compute peng all pe/atom
compute keng all ke/atom
```

```
compute str all stress/atom NULL virial
compute flux all heat/flux keng peng str

timestep $(v_dt)

velocity all create $(v_Tend) 12345 mom yes rot no
fix 1 all npt temp $(v_Tend) $(v_Tend) 1 x 0 0 1 y 0 0 1 z 0 0 1 xy 0 0 1 xz 0 0 1 yz 0 0 1 drag 1

thermo 1
thermo_style custom step lx ly lz xy xz yz temp press pxx pyy pzz pxy pxz pyz pe ke etotal enthalpy
thermo_modify format float %16.15e

run $(v_nrun)

write_restart Cu_Tstart=0_Tend=273.restart
```

```
log Cu_Tstart=273_Tend=283_eps11=eps22=eps33=0.01.log

units metal
dimension 3
boundary p p p
atom_style atomic
variable latparam equal 3.165
variable atoms equal 10
variable lxx equal ${atoms}*${latparam}
variable lyy equal ${atoms}*${latparam}
variable lzz equal ${atoms}*${latparam}

variable dt equal 0.001
variable nrun equal 100000
variable Tend equal 283
variable eps equal 0.01

read_restart Cu_Tstart=0_Tend=273.restart

pair_style eam/alloy
pair_coeff * * Cu_mishin1.eam.alloy Cu
neighbor 2.0 bin
neigh_modify delay 10 check yes

```

```
25 compute disp all displace/atom
26 compute peng all pe/atom
27 compute keng all ke/atom
28 compute stre all stress/atom NULL virial
29 compute flux all heat/flux keng peng stre
30
31 timestep $(v_dt)
32
33 fix 1 all deform 1 x scale $(1+v_eps) y scale
     ↪ $(1+v_eps) z scale $(1+v_eps) remap v
34 fix 2 all nvt temp $(v_Tend) $(v_Tend) 1 drag 1
35
36 thermo 1
37 thermo_style custom step lx ly lz xy xz yz temp press
     ↪ pxx pyy pzz pxy pxz pyz pe ke etotal enthalpy
38 thermo_modify format float %16.15e
39
40 run $(0.1*v_nrun)
41
42 unfix 1
43 unfix 2
44 fix 3 all deform 1 x scale 1.0 y scale 1.0 z scale 1.0
     ↪ remap v
45 fix 4 all nvt temp $(v_Tend) $(v_Tend) 1 drag 1
46
47 thermo 1
48 thermo_style custom step lx ly lz xy xz yz temp press
     ↪ pxx pyy pzz pxy pxz pyz pe ke etotal enthalpy
49 thermo_modify format float %16.15e
50
51 run $(0.9*v_nrun)
52
53 write_restart Cu_Tstart=273_Tend=283_eps11=eps22=eps33
     ↪ =0.01.restart
```

# C Surface elasticity

## C.1 Surface determinant

The surface determinant of the surface deformation gradient reads (cf. [25])

$$\overline{\det}\,\overline{\mathbf{F}} = \frac{\left|\overline{\mathbf{F}}\cdot\mathbf{G}_1\times\overline{\mathbf{F}}\cdot\mathbf{G}_2\right|}{\left|\mathbf{G}_1\times\mathbf{G}_2\right|}. \tag{C.1}$$

Using the Levi-Civita symbol and the co- and contravariant metrics, one obtains

$$\begin{aligned}\left|\overline{\mathbf{F}}\cdot\mathbf{G}_1\times\overline{\mathbf{F}}\cdot\mathbf{G}_2\right| &= \sqrt{\left[\mathbf{C}:\mathbf{G}_1\otimes\mathbf{G}_1\right]\left[\mathbf{C}:\mathbf{G}_2\otimes\mathbf{G}_2\right]-\left[\mathbf{C}:\mathbf{G}_1\otimes\mathbf{G}_2\right]^2} &\text{(C.2)}\\ &= \sqrt{g_{11}\,g_{22}-g_{12}^2}, &\text{(C.3)}\end{aligned}$$

where

$$\overline{\mathbf{C}}:\mathbf{G}_i\otimes\mathbf{G}_j = g_{\alpha\beta}\,\mathbf{G}^\alpha\otimes\mathbf{G}^\beta:\mathbf{G}_i\otimes\mathbf{G}_j = g_{\alpha\beta}\,\delta_{\alpha i}\,\delta_{\beta j} = g_{ij}, \tag{C.4}$$

and

$$\begin{aligned}\left|\mathbf{G}_1\times\mathbf{G}_2\right| &= \sqrt{\left[\mathbf{G}_1\cdot\mathbf{G}_1\right]\left[\mathbf{G}_2\cdot\mathbf{G}_2\right]-\left[\mathbf{G}_2\cdot\mathbf{G}_2\right]^2} &\text{(C.5)}\\ &= \sqrt{G_{11}\,G_{22}-G_{12}^2}. &\text{(C.6)}\end{aligned}$$

Finally, Eq. (C.1) reads

$$\overline{\det}\,\overline{\mathbf{F}} = \sqrt{\frac{g_{11}\,g_{22}-g_{12}^2}{G_{11}\,G_{22}-G_{12}^2}}, \tag{C.7}$$

being the square root of the determinant of the right Cauchy-Green stress tensor

$$\overline{\det}\,\overline{\mathbf{C}} = \left[\overline{\det}\,\overline{\mathbf{F}}\right]^2 = \frac{g_{11}\,g_{22}-g_{12}^2}{G_{11}\,G_{22}-G_{12}^2}. \tag{C.8}$$

Likewise, with $I_{\overline{\mathbf{C}}} = \overline{\mathrm{tr}}\,\overline{\mathbf{C}} = g_{\alpha\beta}\,G^{\alpha\beta}$ and $\overline{\mathrm{tr}}\left(\overline{\mathbf{C}}^2\right) = g_{\alpha\beta}\,g_{\gamma\delta}\,G^{\alpha\gamma}\,G^{\beta\delta}$ at hand, the second surface invariant reads

$$II_{\overline{\mathbf{C}}} = \frac{1}{2}\left[\left[\mathrm{tr}\,\overline{\mathbf{C}}\right]^2 - \mathrm{tr}\left(\overline{\mathbf{C}}^2\right)\right] = \frac{1}{2}\,g_{\alpha\beta}\,g_{\gamma\delta}\left[G^{\alpha\beta}\,G^{\gamma\delta} - G^{\alpha\gamma}\,G^{\beta\delta}\right]. \tag{C.9}$$

Inserting $\alpha, \beta, \gamma, \delta \in \{1, 2\}$ and transferring the contravariant metrics to covariant metrics, the identity $II_{\overline{\mathbf{C}}} = \overline{\det}\,\overline{\mathbf{C}}$ is finally achieved.

## C.2 Consistency of the relaxed surface model

### C.2.1 Symmetry of the relaxed second Piola-Kirchhoff stress tensor

According to the principle of material frame indifference, the bulk's energy has to fulfill

$$\psi(\mathbf{Q}\cdot\mathbf{F}) = \psi(\mathbf{F}) \qquad \forall \mathbf{Q} \in SO(3)\,. \tag{C.10}$$

Thus, by inserting the relaxed deformation gradient $\widetilde{\mathbf{F}}$ into Eq. (C.10) and computing the time derivative for a pure change of observer (i.e., $\dot{\widetilde{\mathbf{F}}} = \mathbf{0}$, $\dot{\mathbf{a}} = \mathbf{0}$) one obtains

$$\frac{\partial\psi}{\partial\widetilde{\mathbf{F}}^*} : \left[\dot{\mathbf{Q}}\cdot\widetilde{\mathbf{F}}\right] = \widetilde{\mathbf{P}}^* : \left[\dot{\mathbf{Q}}\cdot\widetilde{\mathbf{F}}\right] = \mathbf{0}, \tag{C.11}$$

where notation $\widetilde{\mathbf{F}}^* = \mathbf{Q}\cdot\widetilde{\mathbf{F}}$ has been used. Since the relaxed first Piola-Kirchhoff stress tensor $\widetilde{\mathbf{P}}^*$ transforms as the deformation gradient, i.e., $\widetilde{\mathbf{P}}^* = \mathbf{Q}\cdot\widetilde{\mathbf{P}}$, Eq. (C.11) can be rewritten as

$$\left[\widetilde{\mathbf{P}}\cdot\widetilde{\mathbf{F}}^{\mathrm{T}}\right] : \left[\mathbf{Q}^{\mathrm{T}}\cdot\dot{\mathbf{Q}}\right] = \mathbf{0}. \tag{C.12}$$

Due to skew-symmetry of $\mathbf{Q}^{\mathrm{T}}\cdot\dot{\mathbf{Q}}$, Eq. (C.12) is equivalent to

$$\left[\widetilde{\mathbf{P}}\cdot\widetilde{\mathbf{F}}^{\mathrm{T}}\right] = \left[\widetilde{\mathbf{P}}\cdot\widetilde{\mathbf{F}}^{\mathrm{T}}\right]^{\mathrm{T}}, \tag{C.13}$$

which has the same form as balance of angular momentum for bulk materials. It bears emphasis that strictly speaking, Eq. (C.13) is not equivalent to the conventional balance of angular momentum, which requires $\widetilde{\mathbf{F}}$ to be replaced by $\mathbf{F}$ in Eq. (C.13). Nevertheless, Eq. (C.13) is equivalent to symmetry of the relaxed second Piola-Kirchhoff stress tensor $\widetilde{\mathbf{S}}$ with transformation $\widetilde{\mathbf{P}} = \widetilde{\mathbf{F}}\cdot\widetilde{\mathbf{S}}$.

### C.2.2 Balance of angular momentum

As mentioned before, Eq. (C.13) is not equivalent to balance of angular momentum which requires

$$\left[\widetilde{\mathbf{P}} \cdot \mathbf{F}^{\mathrm{T}}\right] = \left[\widetilde{\mathbf{P}} \cdot \mathbf{F}^{\mathrm{T}}\right]^{\mathrm{T}}. \tag{C.14}$$

However, the stationarity condition infers $\widetilde{\mathbf{P}} \cdot \mathbf{N} = \mathbf{0}$ for relaxed states (see Eq. (5.64)) and

$$\widetilde{\mathbf{P}} \cdot \widetilde{\mathbf{F}}^{\mathrm{T}} = \widetilde{\mathbf{P}} \cdot \left[\mathbf{F}^{\mathrm{T}} - \mathbf{N} \otimes \mathbf{a}\right] = \widetilde{\mathbf{P}} \cdot \mathbf{F}^{\mathrm{T}}. \tag{C.15}$$

Eq. (C.13) is thus indeed equivalent to balance of angular momentum (C.14) for relaxed states.

### C.2.3 Stress power

In the case of hyperelasticity, the stress power $\mathcal{P} = \partial\psi/\partial\mathbf{F} : \dot{\mathbf{F}} = \mathbf{P} : \dot{\mathbf{F}}$ is equivalent to the material time derivative of the Helmholtz free energy. The stress power of the surface along relaxed states can be written as

$$\widetilde{\mathcal{P}} = \frac{\partial\widetilde{\psi}}{\partial\widetilde{\mathbf{F}}} : \frac{\mathrm{d}}{\mathrm{d}t}\left[\widetilde{\mathbf{F}}\right]_{\mathbf{a}=\mathrm{const}} = \widetilde{\mathbf{P}} : \dot{\widetilde{\mathbf{F}}}. \tag{C.16}$$

Because $\widetilde{\mathbf{P}} \cdot \mathbf{N} = \mathbf{0}$ holds for relaxed states (see Eq. (5.64)), only in-plane surface contributions of the deformation rate finally enter the stress power, i.e. only the in-plane projection of the relaxed deformation gradient $\overline{\widetilde{\mathbf{F}}}$,

$$\tilde{\mathcal{P}} = \widetilde{\mathbf{P}} : \dot{\overline{\widetilde{\mathbf{F}}}}. \tag{C.17}$$

## C.3 Derivatives for numerical implementation

### C.3.1 Derivatives of invariants

This section shows the derivatives of the invariants with respect to the jump $\mathbf{a}$ used in the stationarity condition of the relaxed energy in Eq. (5.92). Eventually, it is shown that each derivative vanishes for $\mathbf{a} = \mathbf{F} \cdot \mathbf{N}$.

The derivatives of the invariants with respect to the jump $\mathbf{a}$ have the form

$$\frac{\partial I_{\widetilde{\mathbf{C}}}}{\partial \mathbf{a}} = -2\left[\mathbf{F}\cdot\mathbf{N}-\mathbf{a}\right], \tag{C.18}$$

$$\frac{\partial II_{\widetilde{\mathbf{C}}}}{\partial \mathbf{a}} = 2\left[\mathbf{F}:\left[\mathbf{F}-\mathbf{a}\otimes\mathbf{N}\right]\left[\mathbf{a}-\mathbf{F}\cdot\mathbf{N}\right]-\left[\mathbf{F}-\mathbf{a}\otimes\mathbf{N}\right]\cdot\mathbf{F}^{\mathrm{T}}\cdot\left[\mathbf{a}-\mathbf{F}\cdot\mathbf{N}\right]\right], \tag{C.19}$$

$$\frac{\partial J^{(4)}_{\widetilde{\mathbf{C}}}}{\partial \mathbf{a}} = 2\left[\mathbf{N}\cdot\mathbf{d}_0\right]\left[\mathbf{a}\otimes\mathbf{N}-\mathbf{F}\right]\cdot\mathbf{d}_0 \quad \text{and} \tag{C.20}$$

$$\begin{aligned}\frac{\partial J^{(5)}_{\widetilde{\mathbf{C}}}}{\partial \mathbf{a}} = {} & -2\left[\mathbf{N}\cdot\mathbf{d}_0\right]\left[\mathbf{F}-\mathbf{a}\otimes\mathbf{N}\right]\cdot\left[\mathbf{F}^{\mathrm{T}}-\mathbf{N}\otimes\mathbf{a}\right]\cdot\left[\mathbf{F}-\mathbf{a}\otimes\mathbf{N}\right]\cdot\mathbf{d}_0 \\ & -2\left[\left[\mathbf{F}-\mathbf{a}\otimes\mathbf{N}\right]\cdot\mathbf{d}_0\right]\left[\left[\mathbf{F}^{\mathrm{T}}-\mathbf{N}\otimes\mathbf{a}\right]\cdot\left[\mathbf{F}-\mathbf{a}\otimes\mathbf{N}\right]\cdot\mathbf{d}_0\right]\cdot\mathbf{N}.\end{aligned} \tag{C.21}$$

Each derivative of the invariant with respect to the jump $\mathbf{a}$ vanishes for $\mathbf{a}=\mathbf{F}\cdot\mathbf{N}$:

$$\frac{\partial I_{\widetilde{\mathbf{C}}}}{\partial \mathbf{a}} = \mathbf{0} \quad \text{if} \quad \mathbf{a}=\mathbf{F}\cdot\mathbf{N}, \tag{C.22}$$

$$\frac{\partial II_{\widetilde{\mathbf{C}}}}{\partial \mathbf{a}} = \mathbf{0} \quad \text{if} \quad \mathbf{a}=\mathbf{F}\cdot\mathbf{N}, \tag{C.23}$$

$$\frac{\partial J^{(4)}_{\widetilde{\mathbf{C}}}}{\partial \mathbf{a}} = \mathbf{0} \quad \text{if} \quad \mathbf{a}=\mathbf{F}\cdot\mathbf{N} \wedge \mathbf{N}\cdot\mathbf{d}_0 \neq 0 \quad (\text{or if } \mathbf{N}\cdot\mathbf{d}_0=0) \quad \text{and} \tag{C.24}$$

$$\frac{\partial J^{(5)}_{\widetilde{\mathbf{C}}}}{\partial \mathbf{a}} = \mathbf{0} \quad \text{if} \quad \mathbf{a}=\mathbf{F}\cdot\mathbf{N}. \tag{C.25}$$

For the second derivatives of the invariants with respect to the jump $\mathbf{a}$ one obtains

$$\frac{\partial^2 I_{\widetilde{\mathbf{C}}}}{\partial \mathbf{a}^2} = 2\,\mathbf{I}, \tag{C.26}$$

$$\frac{\partial^2 II_{\widetilde{\mathbf{C}}}}{\partial \mathbf{a}^2} = 2\left[\mathbf{F}\cdot\mathbf{N}\otimes\mathbf{F}\cdot\mathbf{N}-\mathbf{F}\cdot\mathbf{F}^{\mathrm{T}}+\left[\mathbf{F}:\mathbf{F}-\mathbf{N}\cdot\mathbf{F}^{\mathrm{T}}\cdot\mathbf{F}\cdot\mathbf{N}\right]\mathbf{I}\right], \tag{C.27}$$

$$\frac{\partial^2 J^{(4)}_{\widetilde{\mathbf{C}}}}{\partial \mathbf{a}^2} = 2\left[\mathbf{N}\cdot\mathbf{d}_0\right]^2\mathbf{I} \quad \text{and} \tag{C.28}$$

$$\begin{aligned}\frac{\partial^2 J^{(5)}_{\widetilde{\mathbf{C}}}}{\partial \mathbf{a}^2} = {} & -2\left[\left[\mathbf{N}\cdot\mathbf{d}_0\right]\left[-\mathbf{F}\cdot\mathbf{N}\otimes\mathbf{F}\cdot\mathbf{d}_0-\mathbf{F}\cdot\mathbf{d}_0\otimes\mathbf{F}\cdot\mathbf{N}\right.\right. \\ & -2\left[\mathbf{N}\cdot\mathbf{F}^{\mathrm{T}}\cdot\mathbf{F}\cdot\mathbf{d}_0\right]\mathbf{I}-2\left[\mathbf{a}\cdot\mathbf{F}\cdot\mathbf{d}_0\right]\mathbf{I}+2\,\mathbf{a}\otimes\mathbf{F}\cdot\mathbf{d}_0+2\,\mathbf{F}\cdot\mathbf{d}_0\otimes\mathbf{a} \\ & +\left[\mathbf{N}\cdot\mathbf{d}_0\right]\left[-\mathbf{F}\cdot\mathbf{F}^{\mathrm{T}}+2\,\mathbf{F}\cdot\mathbf{N}\otimes\mathbf{a}+2\left[\mathbf{N}\cdot\mathbf{F}^{\mathrm{T}}\cdot\mathbf{a}\right]\mathbf{I}\right. \\ & \left.\left.+2\,\mathbf{a}\otimes\mathbf{F}\cdot\mathbf{N}-2\left[\mathbf{a}\cdot\mathbf{a}\right]\mathbf{I}-4\,\mathbf{a}\otimes\mathbf{a}\right]\right]-\mathbf{F}\cdot\mathbf{d}_0\otimes\mathbf{F}\cdot\mathbf{d}_0\right].\end{aligned} \tag{C.29}$$

## C.3.2 Derivatives of energies

This section presents the stress tensors and tangents required for the numerical implementation of the bulk energy as well as the projected and relaxed surface energies. The

numerical implementation is derived in Secs. 2.5 and 5.3. The energies are given in Sec. 5.4.2.1.

### C.3.2.1 Bulk material

The bulk Helmholtz free energy in Eq. (5.103) depends on the right Cauchy-Green tensor $\mathbf{C}$. For the numerical implementation it is rewritten as a function of the bulk deformation gradient $\mathbf{F}$:

$$\psi(\mathbf{C}) = \frac{1}{4}\lambda \log(\det \mathbf{C})^2 + \frac{1}{2}\left[\operatorname{tr}\mathbf{C} - 3 - \log(\det \mathbf{C})\right] \tag{C.30}$$

$$\Leftrightarrow \psi(\mathbf{F}) = \frac{1}{2}\lambda \log(\det \mathbf{F})^2 + \frac{1}{2}\left[\operatorname{tr}\left(\mathbf{F}^{\mathrm{T}}\cdot\mathbf{F}\right) - 3 - 2\log(\det \mathbf{F})\right]. \tag{C.31}$$

From this point the first Piola-Kirchhoff stress $\mathbf{P}$ is expressed as

$$\frac{\partial\psi(\mathbf{F})}{\partial\mathbf{F}} = [\lambda \log(\det \mathbf{F}) - \mu]\ \mathbf{F}^{-\mathrm{T}} + \mu\,\mathbf{F} \tag{C.32}$$

and the tangent $\mathbb{A}$ reads

$$\frac{\partial^2\psi(\mathbf{F})}{\partial\mathbf{F}^2} = \lambda\,\mathbf{F}^{-\mathrm{T}}\otimes\mathbf{F}^{-\mathrm{T}} + [\mu - \lambda\log(\det\mathbf{F})]\ \mathbf{F}^{-\mathrm{T}}\underline{\otimes}\,\mathbf{F}^{-1} + \mu\,[\mathbf{I}\,\overline{\otimes}\,\mathbf{I}]. \tag{C.33}$$

### C.3.2.2 Surface material – projected deformation gradient

According to Eqs. (5.41) and (5.52), the following identities $\partial\psi\left(\overline{\mathbf{F}}\right)/\partial\mathbf{F} = \partial\psi\left(\overline{\mathbf{F}}\right)/\partial\overline{\mathbf{F}}$ and $\partial^2\psi\left(\overline{\mathbf{F}}\right)/\partial\mathbf{F}^2 = \partial^2\psi\left(\overline{\mathbf{F}}\right)/\partial\overline{\mathbf{F}}^2$ hold for a surface Helmholtz free energy depending on the four invariants: $\psi = \psi\left(I_{\overline{\mathbf{C}}}, II_{\overline{\mathbf{C}}}, J^{(4)}_{\overline{\mathbf{C}}}, J^{(5)}_{\overline{\mathbf{C}}}\right)$. The energy is given in Eq. (5.105) as

$$\psi_{\mathrm{p}}\left(\overline{\mathbf{C}}\right) = \psi_{\mathrm{p}}\left(\overline{\mathbf{C}}\left(\overline{\mathbf{F}}\right)\right) = c_1\left[I_{\overline{\mathbf{C}}} - 3\right] + c_2\left[II_{\overline{\mathbf{C}}} - 3\right] + c_4\,J^{(4)}_{\overline{\mathbf{C}}} + c_5\,J^{(5)}_{\overline{\mathbf{C}}}. \tag{C.34}$$

Using the chain rule, the first derivative of the surface energy, in the following denoted only as $\psi_{\mathrm{p}}$, with respect to the projected deformation gradient $\overline{\mathbf{F}}$, being identical with the projected surface stress $\mathbf{P}_{\mathrm{p}}$, reads

$$\frac{\partial\psi_{\mathrm{p}}}{\partial\overline{\mathbf{F}}} = \frac{\partial\psi_{\mathrm{p}}}{\partial I_{\overline{\mathbf{C}}}}\frac{\partial I_{\overline{\mathbf{C}}}}{\partial\overline{\mathbf{F}}} + \frac{\partial\psi_{\mathrm{p}}}{\partial II_{\overline{\mathbf{C}}}}\frac{\partial II_{\overline{\mathbf{C}}}}{\partial\overline{\mathbf{F}}} + \frac{\partial\psi_{\mathrm{p}}}{\partial J^{(4)}_{\overline{\mathbf{C}}}}\frac{\partial J^{(4)}_{\overline{\mathbf{C}}}}{\partial\overline{\mathbf{F}}} + \frac{\partial\psi_{\mathrm{p}}}{\partial J^{(5)}_{\overline{\mathbf{C}}}}\frac{\partial J^{(5)}_{\overline{\mathbf{C}}}}{\partial\overline{\mathbf{F}}}. \tag{C.35}$$

Therein, the derivatives of each invariant have the form

$$\frac{\partial I_{\overline{\mathbf{C}}}}{\partial \overline{\mathbf{F}}} = 2\,\overline{\mathbf{F}}, \tag{C.36}$$

$$\frac{\partial II_{\overline{\mathbf{C}}}}{\partial \overline{\mathbf{F}}} = 2\left[I_{\overline{\mathbf{C}}}\,\overline{\mathbf{F}} - \overline{\mathbf{F}}\cdot\overline{\mathbf{C}}\right], \tag{C.37}$$

$$\frac{\partial J^{(4)}_{\overline{\mathbf{C}}}}{\partial \overline{\mathbf{F}}} = 2\,\overline{\mathbf{F}}\cdot\mathbf{d}_0\otimes\overline{\mathbf{I}}\cdot\mathbf{d}_0 \quad \text{and} \tag{C.38}$$

$$\frac{\partial J^{(5)}_{\overline{\mathbf{C}}}}{\partial \overline{\mathbf{F}}} = 2\left[\overline{\mathbf{F}}\cdot\overline{\mathbf{C}}\cdot\mathbf{d}_0\otimes\overline{\mathbf{I}}\cdot\mathbf{d}_0 + \overline{\mathbf{F}}\cdot\mathbf{d}_0\otimes\overline{\mathbf{C}}\cdot\mathbf{d}_0\right]. \tag{C.39}$$

Finally, Eq. (C.35) is expressed as

$$\Rightarrow \frac{\partial \psi_{\mathrm{p}}}{\partial \overline{\mathbf{F}}} = c_1\,\frac{\partial I_{\overline{\mathbf{C}}}}{\partial \overline{\mathbf{F}}} + c_2\,\frac{\partial II_{\overline{\mathbf{C}}}}{\partial \overline{\mathbf{F}}} + c_4\,\frac{\partial J^{(4)}_{\overline{\mathbf{C}}}}{\partial \overline{\mathbf{F}}} + c_5\,\frac{\partial J^{(5)}_{\overline{\mathbf{C}}}}{\partial \overline{\mathbf{F}}}. \tag{C.40}$$

The second derivative of the surface energy with respect to the projected deformation gradient or the tangent $\overline{\mathbb{A}}$, respectively, reads

$$\frac{\partial^2 \psi_{\mathrm{p}}}{\partial \overline{\mathbf{F}}^2} = c_1\,\frac{\partial^2 I_{\overline{\mathbf{C}}}}{\partial \overline{\mathbf{F}}^2} + c_2\,\frac{\partial^2 II_{\overline{\mathbf{C}}}}{\partial \overline{\mathbf{F}}^2} + c_4\,\frac{\partial^2 J^{(4)}_{\overline{\mathbf{C}}}}{\partial \overline{\mathbf{F}}^2} + c_5\,\frac{\partial^2 J^{(5)}_{\overline{\mathbf{C}}}}{\partial \overline{\mathbf{F}}^2} \tag{C.41}$$

with

$$\frac{\partial^2 I_{\overline{\mathbf{C}}}}{\partial \overline{\mathbf{F}}^2} = 2\,\mathbf{i}\,\overline{\otimes}\,\overline{\mathbf{I}}, \tag{C.42}$$

$$\frac{\partial^2 II_{\overline{\mathbf{C}}}}{\partial \overline{\mathbf{F}}^2} = 2\left[2\,\overline{\mathbf{F}}\otimes\overline{\mathbf{F}} + I_{\overline{\mathbf{C}}}\,\mathbf{i}\,\overline{\otimes}\,\overline{\mathbf{I}} - \mathbf{i}\,\overline{\otimes}\,\overline{\mathbf{C}} - \overline{\mathbf{F}}\,\underline{\otimes}\,\overline{\mathbf{F}}^{\mathrm{T}} - \left[\overline{\mathbf{F}}\cdot\overline{\mathbf{F}}^{\mathrm{T}}\right]\,\overline{\otimes}\,\overline{\mathbf{I}}\right], \tag{C.43}$$

$$\frac{\partial^2 J^{(4)}_{\overline{\mathbf{C}}}}{\partial \overline{\mathbf{F}}^2} = 2\,\mathbf{i}\,\overline{\otimes}\left[\overline{\mathbf{I}}\cdot\mathbf{d}_0\otimes\overline{\mathbf{I}}\cdot\mathbf{d}_0\right] \quad \text{and} \tag{C.44}$$

$$\begin{aligned}\frac{\partial^2 J^{(5)}_{\overline{\mathbf{C}}}}{\partial \overline{\mathbf{F}}^2} = {} & 2\,\mathbf{i}\otimes\left[\overline{\mathbf{I}}\cdot\mathbf{d}_0\otimes\overline{\mathbf{C}}\cdot\mathbf{d}_0\right] + 2\,\overline{\mathbf{F}}\,\underline{\otimes}\left[\overline{\mathbf{I}}\cdot\mathbf{d}_0\otimes\overline{\mathbf{F}}\cdot\mathbf{d}_0\right] \\ & + 2\left[\overline{\mathbf{F}}\cdot\overline{\mathbf{F}}^{\mathrm{T}}\right]\,\overline{\otimes}\left[\overline{\mathbf{I}}\cdot\mathbf{d}_0\otimes\overline{\mathbf{I}}\cdot\mathbf{d}_0\right] + 2\,\mathbf{i}\,\overline{\otimes}\left[\overline{\mathbf{C}}\cdot\mathbf{d}_0\otimes\overline{\mathbf{I}}\cdot\mathbf{d}_0\right] \\ & + 2\left[\overline{\mathbf{F}}\cdot\mathbf{d}_0\otimes\overline{\mathbf{F}}\cdot\mathbf{d}_0\right]\,\overline{\otimes}\,\overline{\mathbf{I}} + 2\left[\overline{\mathbf{F}}\cdot\mathbf{d}_0\otimes\overline{\mathbf{I}}\cdot\mathbf{d}_0\right]\,\underline{\otimes}\,\overline{\mathbf{F}}^{\mathrm{T}}.\end{aligned} \tag{C.45}$$

#### C.3.2.3 Surface material – relaxed deformation gradient

Starting from the relaxed Helmholtz free surface energy $\psi = \psi(\widetilde{\mathbf{C}})$ depending on the invariants given in Eq. (5.106)

$$\psi(\widetilde{\mathbf{C}}) = \psi(\widetilde{\mathbf{C}}(\widetilde{\mathbf{F}})) = c_1\left[I_{\widetilde{\mathbf{C}}} - 3\right] + c_2\left[II_{\widetilde{\mathbf{C}}} - 3\right] + c_4\,J^{(4)}_{\widetilde{\mathbf{C}}} + c_5\,J^{(5)}_{\widetilde{\mathbf{C}}} \tag{C.46}$$

and using the chain rule for the derivative of the relaxed surface energy, in the following only denoted as $\psi$, with respect to the relaxed deformation gradient $\widetilde{\mathbf{F}}$, one obtains the relaxed surface stress $\mathbf{P}_\mathrm{r}$ as

$$\frac{\partial \psi}{\partial \mathbf{F}} = \frac{\partial \psi}{\partial I_{\widetilde{\mathbf{C}}}} \frac{\partial I_{\widetilde{\mathbf{C}}}}{\partial \mathbf{F}} + \frac{\partial \psi}{\partial II_{\widetilde{\mathbf{C}}}} \frac{\partial II_{\widetilde{\mathbf{C}}}}{\partial \mathbf{F}} + \frac{\partial \psi}{\partial J^{(4)}_{\widetilde{\mathbf{C}}}} \frac{\partial J^{(4)}_{\widetilde{\mathbf{C}}}}{\partial \mathbf{F}} + \frac{\partial \psi}{\partial J^{(5)}_{\widetilde{\mathbf{C}}}} \frac{\partial J^{(5)}_{\widetilde{\mathbf{C}}}}{\partial \mathbf{F}}. \tag{C.47}$$

Therein, the derivative of each invariant is computed as

$$\frac{\partial I_{\widetilde{\mathbf{C}}}}{\partial \mathbf{F}} = 2\,\widetilde{\mathbf{F}}, \tag{C.48}$$

$$\frac{\partial II_{\widetilde{\mathbf{C}}}}{\partial \mathbf{F}} = 2\left[I_{\widetilde{\mathbf{C}}}\,\widetilde{\mathbf{F}} - \widetilde{\mathbf{F}} \cdot \widetilde{\mathbf{C}}\right], \tag{C.49}$$

$$\frac{\partial J^{(4)}_{\widetilde{\mathbf{C}}}}{\partial \mathbf{F}} = 2\,\widetilde{\mathbf{F}} \cdot \mathbf{d}_0 \otimes \mathbf{d}_0 \quad \text{and} \tag{C.50}$$

$$\frac{\partial J^{(5)}_{\widetilde{\mathbf{C}}}}{\partial \mathbf{F}} = 2\left[\widetilde{\mathbf{F}} \cdot \widetilde{\mathbf{C}} \cdot \mathbf{d}_0 \otimes \mathbf{d}_0 + \widetilde{\mathbf{F}} \cdot \mathbf{d}_0 \otimes \widetilde{\mathbf{C}} \cdot \mathbf{d}_0\right]. \tag{C.51}$$

Eventually, Eq. (C.47) reads

$$\Rightarrow \frac{\partial \psi}{\partial \mathbf{F}} = c_1 \frac{\partial I_{\widetilde{\mathbf{C}}}}{\partial \mathbf{F}} + c_2 \frac{\partial II_{\widetilde{\mathbf{C}}}}{\partial \mathbf{F}} + c_4 \frac{\partial J^{(4)}_{\widetilde{\mathbf{C}}}}{\partial \mathbf{F}} + c_5 \frac{\partial J^{(5)}_{\widetilde{\mathbf{C}}}}{\partial \mathbf{F}}. \tag{C.52}$$

The tangent $\mathbb{A}_\mathrm{r}$ (cf. Eq. (5.90)) requires the second derivative of the relaxed surface energy with respect to the relaxed deformation gradient

$$\frac{\partial^2 \psi}{\partial \mathbf{F}^2} = c_1 \frac{\partial^2 I_{\widetilde{\mathbf{C}}}}{\partial \mathbf{F}^2} + c_2 \frac{\partial^2 II_{\widetilde{\mathbf{C}}}}{\partial \mathbf{F}^2} + c_4 \frac{\partial^2 J^{(4)}_{\widetilde{\mathbf{C}}}}{\partial \mathbf{F}^2} + c_5 \frac{\partial^2 J^{(5)}_{\widetilde{\mathbf{C}}}}{\partial \mathbf{F}^2}, \tag{C.53}$$

where

$$\frac{\partial^2 I_{\widetilde{\mathbf{C}}}}{\partial \mathbf{F}^2} = 2\,\mathbf{i} \,\overline{\otimes}\, \mathbf{I}, \tag{C.54}$$

$$\frac{\partial^2 II_{\widetilde{\mathbf{C}}}}{\partial \mathbf{F}^2} = 2\left[2\,\widetilde{\mathbf{F}} \otimes \widetilde{\mathbf{F}} + I_{\widetilde{\mathbf{C}}}\,\mathbf{i} \,\overline{\otimes}\, \mathbf{I} - \mathbf{i} \,\overline{\otimes}\, \widetilde{\mathbf{C}} - \widetilde{\mathbf{F}} \,\underline{\otimes}\, \widetilde{\mathbf{F}}^\mathrm{T} - \left[\widetilde{\mathbf{F}} \cdot \widetilde{\mathbf{F}}^\mathrm{T}\right] \,\overline{\otimes}\, \mathbf{I}\right], \tag{C.55}$$

$$\frac{\partial^2 J^{(4)}_{\widetilde{\mathbf{C}}}}{\partial \mathbf{F}^2} = 2\,\mathbf{i} \,\overline{\otimes}\, [\mathbf{d}_0 \otimes \mathbf{d}_0] \quad \text{and} \tag{C.56}$$

$$\begin{aligned}\frac{\partial^2 J^{(5)}_{\widetilde{\mathbf{C}}}}{\partial \mathbf{F}^2} = {} & 2\,\mathbf{i} \otimes \left[\mathbf{d}_0 \otimes \widetilde{\mathbf{C}} \cdot \mathbf{d}_0\right] + 2\,\widetilde{\mathbf{F}} \,\underline{\otimes}\, \left[\mathbf{d}_0 \otimes \widetilde{\mathbf{F}} \cdot \mathbf{d}_0\right] \\ & + 2\left[\widetilde{\mathbf{F}} \cdot \widetilde{\mathbf{F}}^\mathrm{T}\right] \,\overline{\otimes}\, [\mathbf{d}_0 \otimes \mathbf{d}_0] + 2\,\mathbf{i} \,\overline{\otimes}\, \left[\widetilde{\mathbf{C}} \cdot \mathbf{d}_0 \otimes \mathbf{d}_0\right] \\ & + 2\left[\widetilde{\mathbf{F}} \cdot \mathbf{d}_0 \otimes \widetilde{\mathbf{F}} \cdot \mathbf{d}_0\right] \,\overline{\otimes}\, \mathbf{I} + 2\left[\widetilde{\mathbf{F}} \cdot \mathbf{d}_0 \otimes \mathbf{d}_0\right] \,\underline{\otimes}\, \widetilde{\mathbf{F}}^\mathrm{T}.\end{aligned} \tag{C.57}$$

# Bibliography


[1] M. Alfredsson, R. Catlow, A. Paulidou, and R.M. Nix. Evidence of surface reconstructions and incorporation of oxygen into the oxide framework on the hydroxylated $La_2O_3$ {001} surface. *Chemical communications*, 38:2128–9, 10 2002. doi:10.1039/B205528G.

[2] S.M. Allen and J.W. Cahn. A microscopic theory for antiphase boundary motion and its application to antiphase domain coarsening. *Acta Metallurgica*, 27(6):1085–1095, 1979. ISSN 0001-6160. doi:10.1016/0001-6160(79)90196-2.

[3] A. Bartels and J. Mosler. Efficient variational constitutive updates for Allen-Cahn-type phase field theory coupled to continuum mechanics. *Computer Methods in Applied Mechanics and Engineering*, 317:55–83, 2017. ISSN 0045-7825. doi:10.1016/j.cma.2016.11.024.

[4] K.-J. Bathe and P. Zimmermann. *Finite-Elemente-Methoden*. Springer-Verlag, 2002. ISBN 3-540-66806-3.

[5] N. Bleier and J. Mosler. A hybrid variationally consistent homogenization approach based on Ritz's method. *International Journal for Numerical Methods in Engineering*, 94(7):625–647, 2013. ISSN 1097-0207. doi:10.1002/nme.4465.

[6] J.W. Cahn and J.E. Hilliard. Free Energy of a Nonuniform System. I. Interfacial Free Energy. *The Journal of Chemical Physics*, 28(2):258–267, 1958. doi:10.1063/1.1744102.

[7] M. Canadija and J. Mosler. On the thermomechanical coupling in finite strain plasticity theory with non-linear kinematic hardening by means of incremental energy minimization. *International Journal of Solids and Structures*, 48(7):1120–1129, 2011. ISSN 0020-7683. doi:10.1016/j.ijsolstr.2010.12.018.

[8] P. Ciarlet. *Mathematical elasticity. Volume I: Three-dimensional elasticity*. North-Holland Publishing Company, Amsterdam, 1988.

[9] B.D. Coleman. Thermodynamics of materials with memory. *Archive for Rational Mechanics and Analysis*, 17(1):1–46, 1964. ISSN 1432-0673. doi:10.1007/BF00283864.

[10] B.D. Coleman and M.E. Gurtin. Thermodynamics with Internal State Variables. *The Journal of Chemical Physics*, 47(2):597–613, 1967. doi:10.1063/1.1711937.

[11] Sandia Corporation. LAMMPS Documentation, 2019. URL `https://lammps.sandia.gov/doc/Manual.html`.

[12] M.S. Daw and M.I. Baskes. Embedded-atom method: Derivation and application to impurities, surfaces, and other defects in metals. *Phys. Rev. B*, 29:6443–6453, Jun 1984. doi:10.1103/PhysRevB.29.6443.

[13] R. Dingreville and J. Qu. A semi-analytical method to compute surface elastic properties. *Acta Materialia*, 55(1):141–147, 2007. ISSN 1359-6454. doi:10.1016/j.actamat.2006.08.007.

[14] A. Ern and J.-L. Guermond. *Theory and Practice of Finite Elements*. Springer-Verlag, 2004. doi:10.1007/978-1-4757-4355-5.

[15] R. Gao, Z.L. Wang, Z. Bai, W.A. de Heer, L. Dai, and M. Gao. Nanomechanics of individual carbon nanotubes from pyrolytically grown arrays. *Phys. Rev. Lett.*, 85: 622–625, Jul 2000. doi:10.1103/PhysRevLett.85.622.

[16] X. Gao, Z. Huang, J. Qu, and D. Fang. A curvature-dependent interfacial energy-based interface stress theory and its applications to nano-structured materials: (i) General theory. *Journal of the Mechanics and Physics of Solids*, 66:59–77, 2014. ISSN 0022-5096. doi:10.1016/j.jmps.2014.01.010.

[17] Goodfellow. Copper (Cu) – Material Information, 2019. URL `http://www.goodfellow.com/E/Kupfer.html`.

[18] T. Heitbreder, N.S. Ottosen, M. Ristinmaa, and J. Mosler. Consistent elastoplastic cohesive zone model at finite deformations - variational formulation. *International Journal of Solids and Structures*, 106–107:284–293, 2017. ISSN 0020-7683. doi:10.1016/j.ijsolstr.2016.10.027.

[19] T. Heitbreder, N.S. Ottosen, M. Ristinmaa, and J. Mosler. On damage modeling of material interfaces: Numerical implementation and computational homogenization. *Computer Methods in Applied Mechanics and Engineering*, 337:1–27, 2018. ISSN 0045-7825. doi:10.1016/j.cma.2018.03.023.

[20] Y. Hiki and A.V. Granato. Anharmonicity in noble metals; higher order elastic constants. *Phys. Rev.*, 144:411–419, Apr 1966. doi:10.1103/PhysRev.144.411.

[21] G.A. Holzapfel. *Nonlinear solid mechanics*. John Wiley & Sons, 2010.

[22] K. Hutter. The foundations of thermodynamics, its basic postulates and implications. A review of modern thermodynamics. *Acta Mechanica*, 27(1-4):1–54, 1977. ISSN 0001-5970. doi:10.1007/BF01180075.

[23] K. Hutter and K. Jöhnk. *Continuum Methods of Physical Modeling*. Springer-Verlag, 2004. doi:10.1007/978-3-662-06402-3.

[24] A. Javili and P. Steinmann. A finite element framework for continua with boundary energies. Part II: The three-dimensional case. *Computer Methods in Applied Mechanics and Engineering*, 199(9):755–765, 2010. ISSN 0045-7825. doi:10.1016/j.cma.2009.11.003.

[25] A. Javili, P. Steinmann, and J. Mosler. Micro-to-macro transition accounting for

general imperfect interfaces. *Computer Methods in Applied Mechanics and Engineering*, 317:274–317, 2017. ISSN 0045-7825. doi:10.1016/j.cma.2016.12.025.

[26] A. Javili, N.S. Ottosen, M. Ristinmaa, and J. Mosler. Aspects of interface elasticity theory. *Mathematics and Mechanics of Solids*, 23(7):1004–1024, 2018. doi:10.1177/1081286517699041.

[27] B. Jérme, A. Bosseboeuf, and P. Pieranski. Anchoring of nematic liquid crystals on terraced silicon surfaces. *Phys. Rev. A*, 42:6032–6041, Nov 1990. doi:10.1103/PhysRevA.42.6032.

[28] V. Joekar-Niasar, S.M. Hassanizadeh, and A. Leijnse. Insights into the Relationships Among Capillary Pressure, Saturation, Interfacial Area and Relative Permeability using Pore-Network Modeling. *Transport in Porous Media*, 74(2):201–219, 2008.

[29] P. Kurzeja. The criterion of subscale sufficiency and its application to the relationship between static capillary pressure, saturation and interfacial areas. *Proc. R. Soc. A*, 472:20150869, 2016. doi:10.1098/rspa.2015.0869.

[30] P. Kurzeja and H. Steeb. Variational formulation of oscillating fluid clusters and oscillator-like classification. I. Theory. *Physics of Fluids*, 26:042106, 04 2014. doi:10.1063/1.4871486.

[31] P. Kurzeja and H. Steeb. Variational formulation of oscillating fluid clusters and oscillator-like classification. II. Numerical study of pinned liquid clusters. *Physics of Fluids*, 26(4):042107, 2014. doi:10.1063/1.4871489.

[32] H.M. Ledbetter and E.R. Naimon. Elastic properties of metals and alloys. ii. copper. *Journal of Physical and Chemical Reference Data*, 3(4):897–935, 1974. doi:10.1063/1.3253150.

[33] H. Liang, M. Upmanyu, and H. Huang. Size-dependent elasticity of nanowires: Nonlinear effects. *Phys. Rev. B*, 71:241403, Jun 2005. doi:10.1103/PhysRevB.71.241403.

[34] J.E. Mardsen and T.J.R. Hughes. *Mathematical foundation of elasticity*. Dover, New York, 1994.

[35] G. J. Martyna, M. L. Klein, and M. Tuckerman. Nosé-hoover chains: The canonical ensemble via continuous dynamics. *The Journal of Chemical Physics*, 97(4):2635–2643, 1992. doi:10.1063/1.463940.

[36] G. J. Martyna, D. J. Tobias, and M. L. Klein. Constant pressure molecular dynamics algorithms. *The Journal of Chemical Physics*, 101(5):4177–4189, 1994. doi:10.1063/1.467468.

[37] G. J. Martyna, M. E. Tuckerman, D. J. Tobias, and M. L. Klein. Explicit reversible integrators for extended systems dynamics. *Molecular Physics*, 87(5):1117–1157, 1996. doi:10.1080/00268979600100761.

[38] M.M. Mehrabadi and S.C. Cowin. Eigentensors of linear anisotropic elastic mate-

rials. *Q. J. Mech. appl. Math.*, 43:15–41, 1990. doi:10.1093/qjmam/43.1.15.

[39] S. Melchionna, G. Ciccotti, and B. L. Holian. Hoover NPT dynamics for systems varying in shape and size. *Molecular Physics*, 78(3):533–544, 1993. doi:10.1080/00268979300100371.

[40] J.C. Michel and P. Suquet. Nonuniform transformation field analysis. *International Journal of Solids and Structures*, 40(25):6937–6955, 2003. ISSN 0020-7683. doi:10.1016/S0020-7683(03)00346-9.

[41] Y. Mishin, M. J. Mehl, D. A. Papaconstantopoulos, A. F. Voter, and J. D. Kress. Structural stability and lattice defects in copper: Ab initio, tight-binding, and embedded-atom calculations. *Phys. Rev. B*, 63:224106, May 2001. doi:10.1103/PhysRevB.63.224106.

[42] J. Mosler and I. Scheider. A thermodynamically and variationally consistent class of damage-type cohesive models. *Journal of the Mechanics and Physics of Solids*, 59(8):1647–1668, 2011. ISSN 0022-5096. doi:10.1016/j.jmps.2011.04.012.

[43] J.A. Nelder and R. Mead. A simplex method for function minimization. *The Computer Journal*, 7(4):308–313, 1965. doi:10.1093/comjnl/7.4.308.

[44] W. Noll. A new mathematical theory of simple materials. *Archive for Rational Mechanics and Analysis*, 48(1):1–50, 1972. ISSN 1432-0673. doi:10.1007/BF00253367.

[45] D.J. Oh and R.A. Johnson. Simple embedded atom method model for fec and hcp metals. *Journal of Materials Research*, 3:471–478, 6 1988. ISSN 2044-5326. doi:10.1557/JMR.1988.0471.

[46] M. Parrinello and A. Rahman. Polymorphic transitions in single crystals: A new molecular dynamics method. *Journal of Applied Physics*, 52(12):7182–7190, 1981. doi:10.1063/1.328693.

[47] periodictable.com. Technical data for Copper, 2019. URL `https://periodictable.com/Elements/029/data.html`.

[48] A.C. Pipkin. The relaxed energy density for isotropic elastic membranes. *IMA Journal of Applied Mathematics*, 36:85–99, 1986.

[49] A.C. Pipkin. Convexity conditions for strain-dependent energy functions for membranes. *Arch. Rational Mech. Anal.*, 121:361–376, 1993.

[50] A.C. Pipkin. Relaxed energy densities for large deformations of membranes. *IMA Journal of Applied Mathematics*, 52:297–308, 1994.

[51] H.N. Pishkenari, F.S. Yousefi, and A. Taghibakhshi. Determination of surface properties and elastic constants of FCC metals: a comparison among different EAM potentials in thin film and bulk scale. *Materials Research Express*, 6(1):015020, oct 2018. doi:10.1088/2053-1591/aae49b.

[52] S. Plimpton. Fast parallel algorithms for short-range molecular dynamics. *Journal of Computational Physics*, 117(1):1–19, 1995. ISSN 0021-9991.

doi:10.1006/jcph.1995.1039.

[53] J.H. Rose, J.R. Smith, and J. Ferrante. Universal features of bonding in metals. *Phys. Rev. B*, 28:1835–1845, Aug 1983. doi:10.1103/PhysRevB.28.1835.

[54] J. Schröder. *Homogenisierungsmethoden der Kontinuumsmechanik unter Beachtung von Stabilitätsproblemen*. Habilitationsschrift, Universität Stuttgart, 2000.

[55] J. Shantilal Shah. *Thermal lattice expansion of various types of solids*. Dissertation, University Of Missouri-Rolla, 1971.

[56] V.B. Shenoy. Atomistic calculations of elastic properties of metallic fcc crystal surfaces. *Phys. Rev. B*, 71:094104, Mar 2005. doi:10.1103/PhysRevB.71.094104.

[57] W. Shinoda, M. Shiga, and M. Mikami. Rapid estimation of elastic constants by molecular dynamics simulation under constant stress. *Phys. Rev. B*, 69:134103, Apr 2004. doi:10.1103/PhysRevB.69.134103.

[58] C. Sievers, J. Mosler, L. Brendel, and P. Kurzeja. Computational homogenization of material surfaces: From atomistic simulations to continuum models. *Computational Materials Science*, 175:109431, 2020. doi:10.1016/j.commatsci.2019.109431.

[59] N.J. Simon, E.S. Drexler, and R.P. Reed. *Properties of Copper and Copper Alloys at Cryogenic Temperatures*. NIST Monograph 177. National Institute of Standards and Technology, 1992.

[60] A.J.M. Spencer. Ronald Rivlin and invariant theory. *International Journal of Engineering Science*, 47:1066–1078, 11 2009. doi:10.1016/j.ijengsci.2009.01.004.

[61] D.J. Steigmann. *Elements of the Theory of Elastic Surfaces*, pages 268–304. London Mathematical Society Lecture Note Series. Cambridge University Press, 2001. doi:10.1017/CBO9780511526466.009.

[62] P. Steinmann. On boundary potential energies in deformational and configurational mechanics. *Journal of the Mechanics and Physics of Solids*, 56(3):772–800, 2008. ISSN 0022-5096. doi:10.1016/j.jmps.2007.07.001.

[63] R. Sunyk and P. Steinmann. On higher gradients in continuum-atomistic modelling. *International Journal of Solids and Structures*, 40(24):6877–6896, 2003. ISSN 0020-7683. doi:10.1016/j.ijsolstr.2003.07.001.

[64] E.B. Tadmor and R.E. Miller. *Modeling Materials: Continuum, Atomistic and Multiscale Techniques*. Cambridge University Press, 2011. ISBN 9780521856980.

[65] R.L. Taylor. FEAP - A Finite Element Analysis Program, 2014. URL `http://projects.ce.berkeley.edu/feap/`.

[66] C. Truesdell and W. Noll. *The Non-Linear Field Theories of Mechanics*, pages 1–541. Springer Berlin Heidelberg, Berlin, Heidelberg, 1965. ISBN 978-3-642-46015-9. doi:10.1007/978-3-642-46015-9_1.

[67] M.E. Tuckerman, J. Alejandre, R. López-Rendón, A.L. Jochim, and G.J. Martyna.

A liouville-operator derived measure-preserving integrator for molecular dynamics simulations in the isothermal–isobaric ensemble. *Journal of Physics A: Mathematical and General*, 39(19):5629–5651, apr 2006. doi:10.1088/0305-4470/39/19/s18.

[68] A. Weuster, S. Strege, L. Brendel, H. Zetzener, D. E. Wolf, and A. Kwade. Shear flow of cohesive powders with contact crystallization: experiment, model and calibration. *Granular Matter*, 17(2):271–286, Apr 2015. ISSN 1434-7636. doi:10.1007/s10035-015-0555-3.

[69] P. Wriggers. *Nonlinear Finite Element Methods*. Springer-Verlag, 2008. doi:10.1007/978-3-540-71001-1.

[70] Q. Yang, L. Stainier, and M. Ortiz. A variational formulation of the coupled thermo-mechanical boundary-value problem for general dissipative solids. *Journal of the Mechanics and Physics of Solids*, 54(2):401–424, 2006. ISSN 0022-5096. doi:10.1016/j.jmps.2005.08.010.

[71] Q.-S. Zheng. Two-dimensional tensor function representation for all kinds of material symmetry. *Proceeding of the Royal Society A*, 199:127–138, 1993. doi:10.1098/rspa.1993.0135.

# Publication series of the Institute of Mechanics

## published to date:

2010/01 Palnau, V.: Implementierung eines netzfreien Diskretisierungsverfahrens und seine Anwendung auf die Scherbandanalyse. ISBN 978-3-921823-51-4

2010/02 Klusemann, B.: Application of homogenization methods and crystal plasticity to the modeling of heterogeneous materials of technological interest. ISBN 978-3-921823-53-8

2011/01 Hortig, C.: Local and non-local thermomechanical modeling and finite-element simulation of high-speed cutting. ISBN 978-3-921823-54-5

2011/02 Parvizian, F.: Modeling of microstructure evolution in aluminum alloys during hot extrusion. ISBN 978-3-921823-56-9

2011/03 Noman, M.: Characterization and model identification for the simulation of the forming behavior of ferritic steels. ISBN: 978-3-921823-55-2

2011/04 Kayser, T.: Characterization of microstructure in aluminum alloys based on electron backscatter diffraction. ISBN: 978-3-921823-57-6

2011/05 Bargmann, S.: Computational modeling of material behavior on different scales based on continuum mechanics. ISBN: 978-3-921823-58-3

2013/01 Waffenschmidt, T.: Modelling and simulation of adaptation and degradation in anisotropic biological tissues. ISBN: 978-3-921823-61-3

2015/01 Ostwald, R.: Modelling and simulation of phase-transformations in elasto-plastic polycrystals. ISBN: 978-3-921823-66-8

2016/01 Subramanian, M.: Phenomenological modelling and simulation of ferro-electric ceramics. ISBN: 978-3-921823-74-3

2016/02 Clausmeyer, T.: Evolution of plastic anisotropy in metals: Material models, experiments and applications. ISBN: 978-3-921823-76-7

2017/01 Holtermann, R.: Computational multiscale modelling of grinding processes. ISBN: 978-3-921823-86-6

2017/02 Bartels, A.: Modelling of evolving microstructures at different scales. ISBN: 978-3-921823-93-4

2017/03 Dusthakar Kumar Rao, D. K.: Computational modelling of single and polycrystalline ferroelectric materials. ISBN: 978-3-921823-94-1

2019/01 Buckmann, K.: Microstructure evolution in functional magnetic materials. ISBN: 978-3-947323-09-8

2019/02 Kaiser, T.: Computational modelling of non-simple and anisotropic materials. ISBN: 978-3-921823-14-2

2019/03 Heitbreder, T.: Modelling of material interfaces at different length scales. ISBN: 978-3-947323-18-0

2020/01 Berthelsen, R.: Computational homogenisation of thermomechanical problems. ISBN: 978-3-947323-19-7

2020/02 Sievers, C.: Describing the macroscopic behavior of surfaces based on atomistic models. ISBN: 978-3-947323-24-1